

Back-end Design of the Readout System for Cryogenic Particle Detectors

Zur Erlangung des akademischen Grades eines

DOKTORS DER INGENIEURWISSENSCHAFTEN (Dr.-Ing.)

von der KIT-Fakultät für Elektrotechnik und Informationstechnik des
Karlsruher Instituts für Technologie (KIT)

angenommene

DISSERTATION

von

Dipl.-Ing. Luciano Ferreyro

geboren in: Buenos Aires, Argentina

Tag der mündlichen Prüfung:

12.12.2023

Hauptreferent:

Prof. Dr. Marc Weber

Korreferent:

Prof. Dr.-Ing. Manuel Platino

Back-end Design of the Readout System for Cryogenic Particle Detectors

Para obtener el título académico de

DOCTOR EN CIENCIAS APLICADAS Y DE LA INGENIERÍA

de la Escuela de Ciencia y Técnica de la
Universidad Nacional de San Martín (UNSAM)

DISERTACIÓN

aceptada

de

Ing. Luciano Ferreyro

nacido en: Buenos Aires, Argentina

Fecha de la defensa oral:

12.12.2023

Director:

Prof. Dr. Marc Weber

Co-Director:

Prof. Dr.-Ing. Manuel Platino

Abstract

This thesis is dedicated to the design and development of the digital back-end (D-BE) for room temperature read-out electronics used in cryogenic quantum detectors. The primary focus is on applications related to Cosmic Microwave Background (CMB) experiments, although the technology is adaptable for particle detection experiments. Two key projects are the main focus of this research: the QUBIC project, designed to detect the B-mode polarization of the CMB, and the ECHo experiment, aimed at setting a new upper limit for neutrino mass determination in the sub-eV range. In these projects Transition Edge Sensors (TES) and Magnetic Microcalorimeters (MMCs) are employed.

In the case of the QUBIC project, the TES are multiplexed using time division multiplexing (TDM). However, a proposal for a new type of bolometer, known as the Magnetic Microbolometer (MMB), was presented in the QUBIC Collaboration which opens the door to implementing a Frequency Division Multiplexing (FDM) system. This could be achieved through the use of a Microwave Superconducting Quantum Interference Device (SQUID) Multiplexer (μ MUX), similar to the MMCs in the ECHo Experiment. To facilitate the read-out of the multiplexed detectors, a multi-tonal signal is generated, with each frequency tone component monitoring a μ MUX channel within the cryostat. This signal then passes through a Low-Noise Amplifier (LNA), typically located in the 4 K stage, before reaching the Radio-Frequency Front-End (RF-FE). The RF-FE comprises high-frequency electronics that interface with both the D-BE and the cold electronics.

This work introduces a novel application of the Goertzel Filter for channelizing multi-tonal signals. Through simulations conducted using a Python-based software package developed in this thesis, the most favorable arrangements for both signal generation and acquisition have been successfully identified, taking into consideration factors such as noise performance, cross-talk isolation, and system linearity. This thesis demonstrates how this approach can be efficiently implemented in a Field Programmable Gate Array (FPGA), allowing for scalability in reading multiple sensors. This capability is particularly crucial in various applications, including radio telescopes for Cosmic Microwave Background (CMB) surveys, cryogenic calorimeters for particle detection, and quantum computing. Extensive validation experiments showcase how the implementation of a filter bank enables the channelization of the multi-tonal input signal to retrieve the imprinted data from the detectors.

Zusammenfassung

Diese Arbeit widmet sich dem Design und der Entwicklung des digitalen Back-Ends (D-BE) für Raumtemperatur-Ausleseelektronik, die in kryogenen Quantendetektoren verwendet wird. Der Schwerpunkt liegt auf Anwendungen im Zusammenhang mit Experimenten zur Kosmischen Hintergrundstrahlung (CMB, im Englischen *Cosmic Microwave Background radiation* genannt), jedoch ist die Technologie anpassbar für Partikeldetektionsexperimente. Zwei Schlüsselprojekte stehen im Mittelpunkt dieser Forschung: das QUBIC-Projekt zur Erkennung der B-Mode-Polarisation des CMB und das ECHO-Experiment, das darauf abzielt, eine neue Obergrenze für die Bestimmung der Neutrinomasse im Sub-eV-Bereich festzulegen. In diesen Projekten werden Übergangskanten-Sensoren (TES) und magnetische Mikrokalorimeter (MMCs) eingesetzt.

Im Fall des QUBIC-Projekts werden die TES unter Verwendung von Zeitaufteilungsmultiplexing (TDM) gemultiplext. Es wurde jedoch ein Vorschlag für einen neuen Bolometer-Typ namens Magnetischer Mikrobolometer (MMB) in der QUBIC-Kollaboration vorgestellt, der die Implementierung eines Frequenzaufteilungsmultiplexing (FDM)-Systems ermöglicht. Dies könnte durch die Verwendung eines Mikrowellen-Supraleiter-Quanteninterferenzgerät (SQUID)-Multiplexers (μ MUX) erreicht werden, ähnlich wie bei den MMCs im ECHO-Experiment. Zur Erleichterung der Auslese der gemultiplexten Detektoren wird ein mehrtoniges Signal erzeugt, wobei jede Frequenztonkomponente einen μ MUX-Kanal innerhalb des Kryostaten überwacht. Dieses Signal passiert dann einen rauscharmen Verstärker (LNA, im Englischen *Low-Noise Amplifier* genannt), der in der Regel in der 4K-Stufe liegt, bevor es das Hochfrequenz-Front-End (RF-FE) erreicht. Das RF-FE umfasst Hochfrequenzelektronik, die sowohl mit dem D-BE als auch mit der Elektronik im Kryostaten verbunden ist.

Diese Arbeit stellt eine neuartige Anwendung des Goertzel-Filters zur Kanalisierung von mehrtonigen Signalen vor. Durch Simulationen, die mit einem in dieser Arbeit entwickelten auf Python basierendem Softwarepaket durchgeführt wurden, wurde die optimale Konfiguration für die Signalgenerierung und -erfassung in Bezug auf Rauschleistung, Abschirmung gegen Übersprechen und Systemlinearität ermittelt. Diese Arbeit zeigt, wie dieser Ansatz effizient in einem Field Programmable Gate Array (FPGA) implementiert werden kann, was die Skalierbarkeit bei der Auslese mehrerer Sensoren ermöglicht. Diese Skalierung ist im Besonderen in Anwendungen wie Radioteleskopen für CMB-Messungen, kryogenen Kalorimetern für die Partikeldetektion und Quantencomputing entscheidend. Umfangreiche Validierungsexperimente zeigen, wie die Implementierung dieses Filtersatzes die Kanalisierung des mehrtonigen Eingangssignals zur Wiederherstellung der von den Detektoren aufgezeichneten Daten ermöglicht.

Resumen

Esta tesis está dedicada al diseño y desarrollo del *back-end* digital (D-BE) para la electrónica de lectura a temperatura ambiente utilizada en detectores cuánticos criogénicos. El enfoque principal se centra en aplicaciones relacionadas con experimentos de Fondo Cósmico de Microondas (CMB), aunque la tecnología es adaptable para experimentos de detección de partículas. Dos proyectos clave son el enfoque principal de esta investigación: el proyecto QUBIC, diseñado para detectar la polarización de modo B del CMB, y el experimento ECHO, dirigido a establecer un nuevo límite superior para la determinación de la masa del neutrino en el rango sub-eV. En estos proyectos se utilizan Detectores de Borde de Transición (TES) y Microcalorímetros Magnéticos (MMCs).

En el caso del proyecto QUBIC, los TES se multiplexan utilizando multiplexación por división de tiempo (TDM). Sin embargo, se presentó una propuesta para un nuevo tipo de bolómetro, conocido como Microbolómetro Magnético (MMB), en la colaboración QUBIC, lo que abre la posibilidad de implementar un sistema de multiplexación por división de frecuencia (FDM). Esto podría lograrse mediante el uso de un Multiplexor de Dispositivos de Interferencia Cuántica Superconductores (SQUID) de Microondas (μ MUX), similar a los MMCs en el experimento ECHO. Para realizar la lectura de los detectores multiplexados, se genera una señal multi-tonal, con cada componente de tono de frecuencia monitoreando un canal del μ MUX dentro del criostato. Esta señal luego pasa por un Amplificador de Bajo Ruido (LNA), generalmente ubicado en la etapa de 4 K, antes de llegar al *Front-End* de Radio-Frecuencia (RF-FE). El RF-FE comprende electrónica de alta frecuencia que se conecta tanto con el D-BE como con la electrónica dentro del criostato (usualmente denominada *cold electronics*).

En este trabajo, una nueva aplicación del filtro de Goertzel para la canalización de señales multi-tonales es presentado. Se determinó la configuración ideal en términos de rendimiento de ruido, aislamiento de crosstalk y linealidad del sistema mediante simulaciones realizadas con un paquete de software basado en Python, desarrollado durante esta tesis, para la generación y adquisición de señales. Esta tesis demuestra cómo este enfoque puede implementarse de manera eficiente en una Matriz de Celdas Programables (FPGA, por sus siglas en inglés), lo que permite la escalabilidad en la lectura de múltiples sensores, un requisito crítico en aplicaciones como radio telescopios para experimentos de CMB, calorímetros criogénicos para la detección de partículas y computación cuántica. Se realizaron numerosos experimentos de validación que muestran cómo la implementación de un conjunto de estos filtros permite la canalización de la señal de entrada multi-tonal para recuperar los datos añadidos por los detectores.

Acknowledgments

Danksagung

Agradecimientos

First of all, I want to thank Prof. Manuel Platino, Prof. Marc Weber, and Prof. Alberto Etchegoyen for giving me an incredible opportunity to conduct bi-national research in my favorite fields of science, including digital signal processing, digital electronics, cosmology, and particle physics. Their unwavering support and understanding, made of this experience, one it will remain in my memory forever.

To my colleagues at the Institut für Prozessdatenverarbeitung, a very special message of gratitude, definitely and without any doubts, goes to Nick Karcher and Oliver Sander. Our extensive and fruitful discussions have been instrumental in completing this thesis, saving me countless hours. Without their input, I couldn't have achieved the progress I've made thus far. To Timo Muscheid, who gave unconditional support during this project, especially when the Vivado versions, the Linux kernel and drivers, and the hardware support became a nightmare for both of us. To Luis Ardila for his guidance and support in various situations. And to Robert Gartmann for his technical support. Thank you to all for the enjoyable coffee breaks, long post-lunch walks, and barbecues.

To my dear colleagues at the Instituto de Tecnologías en Detección y Astropartículas, I feel fortunate to have such exceptional individuals around me since I began working at ITeDA in 2014. Specifically, I want to express my gratitude to Matías Hampel and Alan Fuster, my office mates and friends. Without our technical discussions, your constant support and guidance, this task would have been much more challenging than anticipated. Thank you. To Manuel García and Juan Salum, with whom I began this journey five years ago. We have had many productive and technical discussions, and they kindly helped me with the last measurements. To Belen Andrada, for the delightful distractions and continuous supply of chocolate candies.

Also, I want to express my gratitude to Prof. Sebastian Kempf from the Institut für Mikro- und Nanoelektronische Systeme, as well as Jesus Bonilla, Nahuel Müller, and Alejandro Almela, for providing an excellent Microwave SQUID Multiplexer device to work with during the past few months. Having access to it allowed me to take a

significant step forward in the suitability validation studies of the proposed channelizer in this work. Without this amazing device, the section on measurements would not be as comprehensive and strong.

To the Helmholtz International Research School for Astroparticle Physics and Enabling Technologies, not only for the financial support but also for this opportunity where I was able to meet such remarkable people. Also, to the Universidad Nacional de San Martín, UNSAM, and Consejo Nacional de Investigaciones Científicas y Técnicas, CONICET, for the financial contribution of this years.

To my friends back home, thanks for understanding when I had to be away for a few days because of work, and for the long distance support while I was in the beautiful city of Karlsruhe.

A special thanks is for my parents and my sister, for their patience, and who understood me as nobody could. To my dearest wife Agustina, for her listening ear, the support (especially during my first stay in Karlsruhe), her friendship, the delightful distractions, and the extraordinary patience throughout the thesis writing process.

Contents

Abstract	i
Acknowledgments	iii
1 Physics Motivation	1
2 Particle Detectors	9
2.1 Cooper pairs and phonons	10
2.2 Josephson junction	11
2.3 Superconducting Quantum Interference Device	12
2.4 Cryogenic calorimeters and bolometers	16
2.4.1 Transition Edge Sensors	16
2.4.2 Microwave Kinetic Inductance Detectors	17
2.4.3 Magnetic Microcalorimeters	19
2.4.4 Magnetic Microbolometers	21
3 Multiplexing Systems	23
3.1 Time-Division Multiplexing	23
3.2 Code-Division Multiplexing	24
3.3 Frequency-Division Multiplexing	25
3.4 Microwave SQUID Multiplexer	27
4 Data Acquisition Architecture	31
4.1 Noise in the DAQ system	31
4.1.1 Quantization Noise	31
4.1.2 Aperture Jitter	35
4.2 Channelization of Wideband Signals	35
4.3 System-On-Chip Architectures	38
4.4 Proposed Data Acquisition system	41
4.5 Hardware prototype selection	42
4.5.1 Available hardware	42
4.5.2 Digital electronics	43
4.5.3 AD - DA Converters	43
4.5.4 High Frequency electronics	44
4.5.5 Operative System, software and firmware integration	45

5	Digital Down Conversion Stage	47
5.1	CIC - Cascaded Integrator Comb Filter	48
5.2	CFIR - Compensation Finite Impulse Response Filter	50
6	Goertzel Filter Bank Channelizer	55
6.1	The Discrete Fourier Transform	55
6.2	The Goertzel Algorithm	56
6.3	The Goertzel Filter derivation	56
6.4	Window Functions for Spectral Analysis with the Goertzel Filter	64
6.5	A simple modulation model	64
6.5.1	No modulation nor detector signal: $m(t) = 0$ and $d(t) = 0$	65
6.5.2	No detector signal: $m(t) \neq 0$ and $d(t) = 0$	66
6.5.3	With detector signal: $m(t) \neq 0$ and $d(t) \neq 0$	67
6.6	Targeting a Sliding Goertzel Filter Bank	67
6.7	Computational simulations	70
6.7.1	Goertzel Filter Frequency response	70
6.7.2	Goertzel Filter vs Sliding Goertzel Filter	70
6.7.3	Goertzel Filter demodulation capabilities	72
7	Signal Generation Algorithms	75
7.1	Multi-tone Signal	75
7.2	Peak-to-Average Power Ratio Optimization	76
7.2.1	General concepts	76
7.2.2	Optimization algorithms	78
7.2.3	Expected problem	78
7.3	Complex baseband and bandpass signal	79
7.3.1	IQ Imbalance and the error model	82
7.3.2	Considerations	83
7.4	Computational simulations	84
8	Firmware Implementation and Readout Electronics integration	87
8.1	Signal Generation	87
8.2	Goertzel Filter Bank	88
8.2.1	Goertzel Filter Core	89
8.2.2	Digital Down Converter design	91
8.2.3	Window Function	93
8.3	Signal-to-Noise Ratio (SNR)	94
8.4	Arithmetic treatment	96
8.4.1	Window function compensation and Goertzel Filter overflow control	96
8.4.2	Fixed Point arithmetic	97
8.5	Complete prototype firmware implementation	99

9	Prototype Measurements	103
9.1	Goertzel Filter Bank Channelizer validation	103
9.1.1	Channelizer Frequency response	103
9.1.2	Demodulation capabilities	105
9.2	Power calibration	110
9.2.1	Frequency response of the Digital-to-Analog Converter (DAC) . .	111
9.2.2	Output power calibration	112
9.3	Power Spectral Density	117
9.4	Signal Generation	118
9.4.1	Slope / Ripple correction	118
9.4.2	IQ Imbalance correction	118
9.5	Cryostat measurements	121
9.5.1	Experimental setup	121
9.5.2	Microwave SQUID Multiplexer characterization	122
10	Summary and perspective	129
	List of Figures	133
	List of Tables	137
	List of Algorithms	139
	List of Acronyms	143
	Bibliography	145

Chapter 1

Physics Motivation

There are many unanswered questions in the scientific community. In particle physics, research into the absolute scale of neutrino masses is of great interest, and the mass of the neutrino has yet to be determined. Recently, the KATRIN project [1, 2] established a new upper limit of $0.8 \text{ eV}/c^2$ by studying the beta decay of tritium and measuring the energy of the electrons released in the process. Using a different approach, the Electron Capture in ^{163}Ho Experiment (ECHO) [3] aims to achieve sub-eV sensitivity for the effective electron neutrino mass by analyzing the calorimetric electron capture spectrum of ^{163}Ho .

Another example of still unanswered questions are those related to the Cosmic Microwave Background Radiation (CMB). The CMB was predicted in 1948 by Ralph Alpher and Robert Herman, and first observed in 1964 by Arno Penzias and Robert Woodrow Wilson using a radiometer originally designed for radio astronomy and satellite communications. They measured unexpected electromagnetic *noise* that matched a black body radiating at 3.5 K [4], which was indeed accounted for by the CMB. More recently, results from the Cosmic Background Explorer (COBE) [5] showed that 50 % of the luminosity and 98 % of the photons emitted by the CMB are in the sub-millimeter and far-infrared range. Experiments so far suggest a big bang model for a hot and dense universe in the past, cooling adiabatically as it expands. The CMB represents the oldest picture, the last scattering, we can take of the universe when it was only $\sim 380,000$ years old. A period of exponential expansion called "inflation" [6] in the early universe has been proposed as a solution to major problems with the standard Big Bang model: the horizon, flatness and monopole problems. One observable effect of this process is the production of B-modes of polarization in the CMB, which are tensorial perturbations in the metric [7]. Experiments such as LABOCA [8], Bicep2 [9], Boomerang and Maxima [10], SPT [11], SPT-3G [12], LiteBIRD [13], POLARBEAR-2 and The Simons Observatory [14, 15], and Q&U Bolometric Interferometer for Cosmology Project (QUBIC) [16] aim to observe and quantify the B-modes.

Both the neutrino mass experiments and the CMB measurements implement low-temperature detectors: calorimeters and bolometers, respectively; and they operate typically below 1 K. For neutrino mass experiments, the detectors must guarantee high energy resolution, fast response and a detection efficiency close to 100 %; for ECHO, this is achieved by using Metallic Magnetic Calorimeters (MMC) [17, 18] or as they are cur-

rently called Magnetic Microcalorimeters (MMC). In CMB experiments, it is desirable to work with background-limited detectors, such as the most commonly used Transition Edge Sensor (TES) [19].

The direct connection of each *sensor* or *pixel* to a read-out electronics with an individual signal cable is possible as long as the number of sensors is small, mainly due to the complexity of having many cables coming out of the cryostat which impacts the heat load on the different cooling stages. The need to improve the sensitivity of the experiment requires an increase in the number of sensors, making this direct connection no longer suitable as the complexity added by the large number of cables required increases considerably. Different techniques are used to solve this problem: Time Division Multiplexing (TDM) [20], Frequency Division Multiplexing (FDM) [21], Code Division Multiplexing (CDM) [22, 23] at MHz frequencies, while at GHz frequencies using a Microwave SQUID Multiplexer (μ MUX) [24–26] or using superconducting microwave resonators with Microwave Kinetic Inductance Detector (MKID) [27]. These techniques reduce the number of cables needed to read a large number of sensors, achieving multiplexing factors, because of the Shannon Limit channel capacity [28], of ~ 40 for TDM, ~ 40 for FDM at MHz and ~ 1000 at GHz, ~ 256 for CDM; and ~ 4000 for μ MUX.

The growing demand for larger detector arrays in these experiments drives advances not only in the low temperature devices but also in the associated room temperature electronics. The latter involves the challenging tasks of generating the sensors monitoring signals, followed by the acquisition of these signals and processing. This work is involved in two projects in particular, QUBIC and ECHO, which will be introduced in the following.

QUBIC - The Q&U Bolometric Interferometer for Cosmology Project

QUBIC [16, 29] is an observational cosmology project and is dedicated to the exploration of the inflation era of the Universe [30, 31]. By detecting and characterizing the CMB B-mode polarization, QUBIC will contribute to finding the so called *smoking gun* of inflation.

The Big Bang Theory appears as a suitable model for describing the known Universe upon based on the current observations. It proposes a hot and dense primordial Universe 13.800 millions years ago, which cools down as it expands. In this way, the Universe should be filled with radiation which is literally the remanent of this hot state, known as the CMB. Even though the Big Bang Theory successfully explains different aspects of the observable Universe, it presents three major problems: planicity, horizon and magnetic monopoles.

1. **Planicity problem:** experiments so far have demonstrated that the geometry of the Universe is almost plain, and because of that it presents a global curvature close to 0 (this is not true locally, for example, close to black holes or supermassive stars). However, the proposed Big Bang model leads to an increase in the space curvature as the time evolves. The cosmological density parameter, Ω , is related with the space curvature (among other parameters) and is currently established near 1. This implies that at the very beginning of the Universe Ω was much more closer to 1: it seems extremely improbable that Ω currently remains close to 1 just by

simple causality,

2. **Horizon problem:** it arises from trying to determine why the known Universe seems to be statistically homogeneous and isotropic, in concordance with the cosmological principle. Because of the intrinsic concept of expansion (everything was collapsed in a tiny space and then started to expand) of the Universe due to the Big Bang, a Universe where only the known matter and radiation of the standard model exist, two widely separated regions of the observable Universe could never have been equilibrated because they never being in causal contact. The gravitational expansion did not give sufficient time to the primordial Universe to equilibrate,
3. **Magnetic Monopoles problem:** the Big Bang Theory predicts the existence of a large number of heavy and stable magnetic monopoles, and that they should have been produced during the early Universe. However, they have never being observed yet, so in the case that the magnetic monopoles really exist, they occur much more rarely than at the rate they were predicted.

As a solution to these problems and other open questions in Cosmology, Alan Guth, Andrei Linde, Paul Steinhardt and Andy Albrecht developed the Inflation Theory [30–32]. This theory proposes a period of an extremely rapid expansion (exponential) of the Universe before a more gradual expansion like the Big Bang. During this period, the energy density of the Universe was dominated by a vacuum energy of cosmological constant type that later decayed to produce the matter and radiation that completes the current Universe. In this way, it also explains the origin of structures of the Universe: before Inflation, the portion of the Universe that can be observed was microscopic, and because of the quantum fluctuations in the matter density at these microscopic scales expanded to astronomic scales during this inflationary period. During the following hundreds of millions of years, the more dense regions condensed in stars, galaxies, and galaxies clusters. These quantum fluctuations would have generated two types of *perturbations* or *waves* (primordials ones): gravitational waves and density waves, which must have left a characteristic imprint in the CMB. So, the inflation model explains in a simple way the Universe’s peculiar initial conditions [33–35], and all current observations are consistent with the universal inflation paradigm, specially the Planck telescope CMB temperature and polarization observations (see Figure 1.1).

The most direct evidence for inflation is the presence of a tensorial perturbation in the primordial metrics as a consequence of primordial gravitational waves. These primordial gravitational waves produced a particular polarization in the CMB, that because it is produced by this type of waves it is known as *B mode polarization* [6, 7]. Observing this polarization is the only way to explore the inflation epoch and its associated physics. Still, and due to the low intensity of the signal to be detected, a very sensitive instrument is required to be developed. B-modes turns out to be very difficult to detect because of their small amplitude: a tensor-to-scalar ratio of 0.01 corresponds to polarization fluctuations of the CMB of a few nK while the well observed temperature fluctuations are around 100 μ K. Even if such a sensitivity can be achieved using background-limited detectors such as bolometers from low-atmospheric emission suborbital locations or from

a satellite, the challenge to face for this detection remains huge because of two main reasons: instrumental systematics and foregrounds.

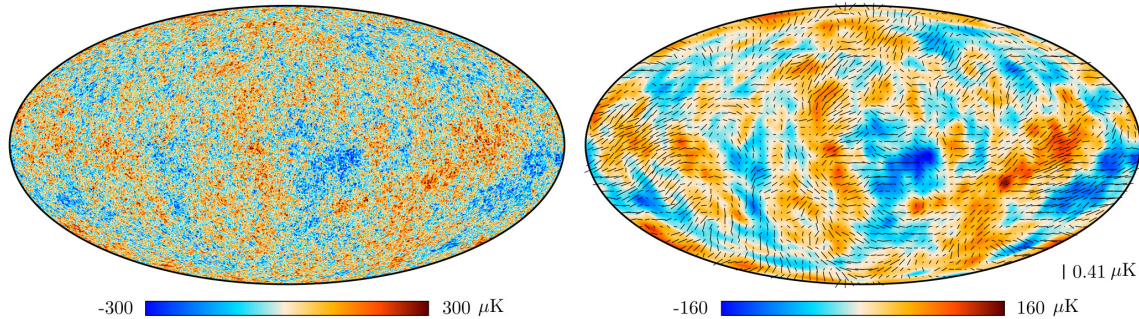


Figure 1.1: Planck Telescope 2018 results. CMB temperature anisotropies map (left). Map of the polarized CMB anisotropies shown as black rods representing the direction and amplitude of the polarization. Background is the CMB anisotropies map smoothed to 5 degrees (right) [36].

With the measurement of the Cosmic Microwave B-mode Polarization in two bands at 150 GHz and 220 GHz, with two years of continuous observations from Alto Chorillos near San Antonio de los Cobres, Salta Province, Argentina, at an altitude of 4820 m over the sea level, the first QUBIC module would be able to constrain the ratio of the primordial tensor to scalar perturbations power spectra amplitudes with a conservative projected uncertainty of $\sigma(r) = 0.02$, while having a good control of foregrounds contamination thanks to its dual band nature [16]: the CMB is dominant in the 150 GHz band, and the foregrounds are stronger in the 220 GHz band. A sketch of the instrument can be appreciated in Figure 1.2. It will observe interference fringes formed altogether by a large number of receiving horns with two arrays of bolometric detectors operating at 150 GHz and 220 GHz. The instrument is a radio-interferometer [37] and consists of a rotatory Half-Wave Plate (HWP) [38], infrared filters (IR), a polarizing grid [39], a back-to-back antenna horn array [40] (a matrix of 8x8 horns for the Technical Demonstrator (TD), and of 20x20 horns for the Final Instrument (FI) version), two mirrors and a dichroic which sends the input radiation towards both focal planes. The combination of the horns array and the optical system [41] conform the interferometric system of QUBIC. Finally, two focal planes take place which operates at a temperature of 320 mK and consist of [42]:

1. for the TD, where only one quarter of one of the focal planes is available: 256 cryogenic detectors based on TES of which only 248 are exposed to the incoming radiation and the rest are used for systematics errors studies,
2. for the FI, where the two focal planes will be available: each focal plane will have 1024 detectors, where only 992 will be exposed to the sky radiation and the rest will be used for systematics errors studies.

The TD is currently installed in the observation site and performing testing measurements since November 2022.

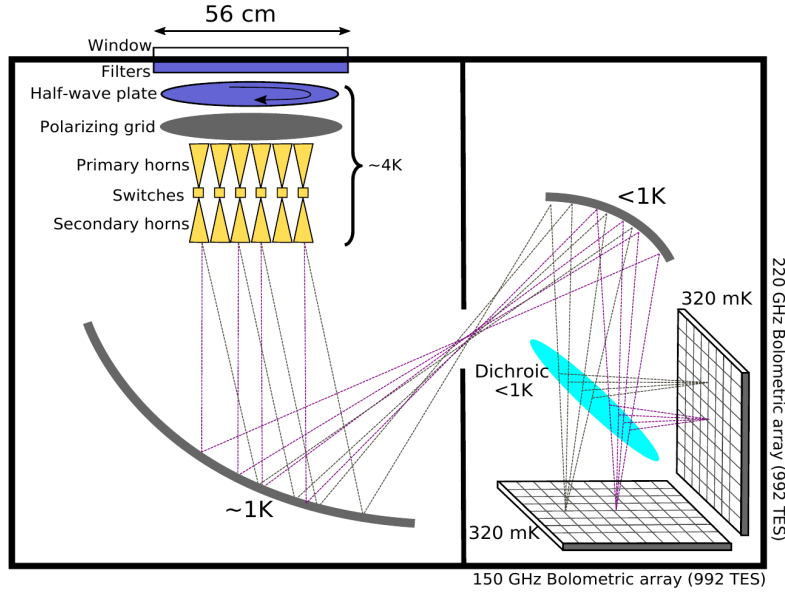


Figure 1.2: The QUBIC Telescope internal sketch [16]. Each focal plane consists of 1024 TES bolometers, of which only 992 are exposed to the incoming radiation and the rest are used for temperature monitoring and calibration.

ECHo - Electron Capture in ^{163}Ho experiment

ECHo is designed to investigate the electron neutrino mass in the sub-eV region by the analysis of the calorimetrically measured electron capture spectrum of ^{163}Ho . The nucleus of ^{163}Ho decays into a nucleus of ^{163}Dy , by capturing an electron (EC) from an inner atomic shell, see Figure 1.3, ①. According to the latest result of the ECHo collaboration, the Q-Value (defined as the mass difference between the neutral ^{163}Ho and ^{163}Dy atoms) is $Q_{\text{EC}} = 2.833 \pm 0.030_{\text{stat}} \pm 0.015_{\text{sys}}$ keV [3, 43], and in this EC process it emits an electron-neutrino ②.

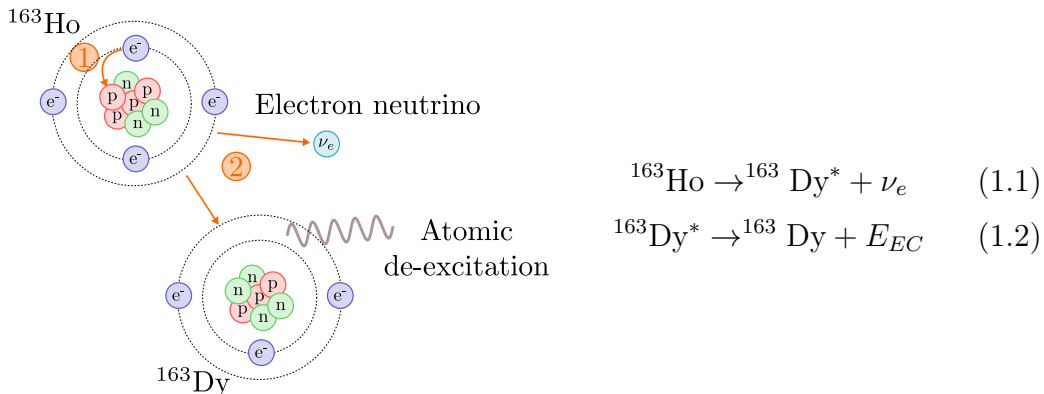


Figure 1.3: Electron Capture in Holmium, emitting an electron-neutrino in the process.

The ^{163}Dy daughter atom is left in an excited state and it subsequently reaches the

ground state emitting cascades of X-rays and Auger electrons. The available decay energy (Q_{EC}) is shared by the atomic de-excitations of the ^{163}Dy atom and by the electron neutrino, neglecting the tiny nuclear recoil contribution. This makes ^{163}Ho a good candidate to perform an experiment to investigate the neutrino mass in the sub-eV region. The direct measurement of the mass of the neutrino emitted during decay is not possible because it rarely interacts with other matter. However, the measurable energy E_{EC} released during decay reflects the mass difference Q_{EC} excluding the mass of the neutrino.

$$E_{EC}^{Max} = Q_{EC} - m_{\nu_e} c^2 \quad (1.3)$$

The released energy E_{EC} generates a continuous energy spectrum disappearing towards the end-point region near the Q_{EC} , as depicted in Figure 1.4. The non-zero neutrino mass, since effectively reduces the energy available, shifts the end-point of the spectrum.

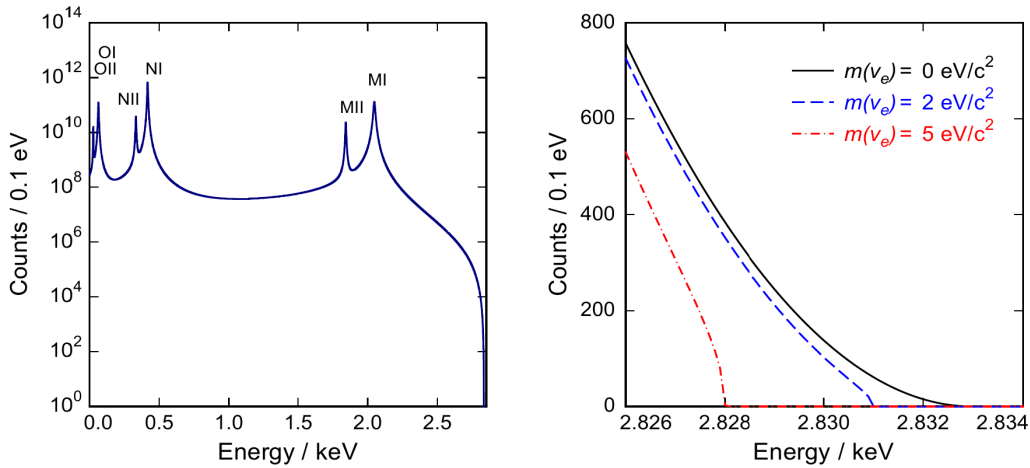


Figure 1.4: Calculated ^{163}Ho EC spectrum for a total number of 10^{14} events using the $Q_{EC} = 2.833$ keV, considering only first order excitations for the daughter ^{163}Dy assuming zero neutrino mass, left. Shape of the spectrum near the endpoint calculated for neutrino masses of 0, 2 and $5 \text{ eV}/c^2$, respectively, showing the effect of a finite electron neutrino mass on a linear scale [3], right.

As can be seen in the previous figure, in the end-point region is where the largest effect of a non-zero neutrino mass on the spectral shape is appreciable. It was demonstrated by De Rujula and Lusignoli in 1982, that in order to enhance the sensitivity on the effective neutrino mass, the EC spectrum must be measured with a calorimetric approach including all the contributions to the de-excitation energy [44]. This can be achieved if the source, the ^{163}Ho , is completely contained within the detector itself.

Then, in this case of an embedded source in the detector, each ^{163}Ho decay in the detector generates a signal with finite time resolution. This means that an intrinsic source of background in the measured spectrum exists [3, 45] leading to an unresolved pile-up. A pile-up is an event that occurs when two or more individual decays happen within a time interval that is shorter than the time resolution of the detector. The visible pulse in such detector will look like a single event but the height (proportional to the energy)

will be equivalent to these two or more decays. For two events the pile-up spectrum is given by the auto-convolution of the ^{163}Ho normal spectrum, see Figure 1.5.

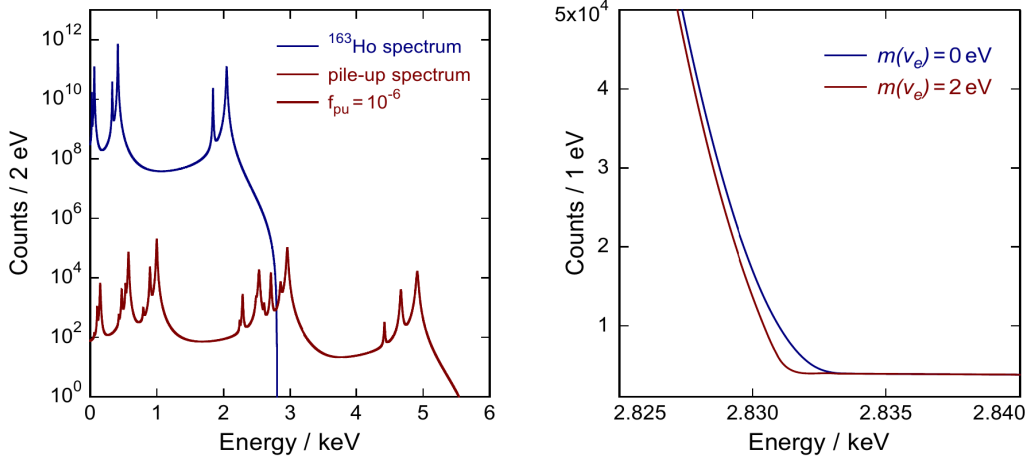


Figure 1.5: Calculated ^{163}Ho EC pile-up spectrum (solid red line) assuming an unresolved pile-up fraction of 10^{-6} and the corresponding ^{163}Ho EC spectrum (solid blue line) without pile-up using the same parameters as in Figure 1.4, left. Sum of both contributions shown for the end-point region calculated for two different values of the neutrino mass $0 \text{ eV}/c^2$ and $2 \text{ eV}/c^2$, right. [3]

The unresolved pile-up fraction (defined as: $f_{PU} = A \cdot \tau_{res}$, with A , the activity of the source and τ_{res} , the time resolution of the detector) constrain the maximum ^{163}Ho activity which can be enclosed in a single detector. Moreover, this defines the number of detectors which are required in the experiment aiming at a given total activity. Currently, the target is a ^{163}Ho total activity of the order of MBq to reach a neutrino mass sensitivity in the sub-eV region, which requires in the order of 10^5 single pixels.

Finally, the neutrino mass sensitivity is strongly affected by the energy resolution of the detector, defined as the full width at half maximum of the Gaussian detector response, ΔE_{FWHM} . A few eV allows to resolve all the structures present in the ^{163}Ho spectrum, thus reducing possible systematic errors.

All the aforementioned requirements can be very well satisfied using MMC arrays with implanted ^{163}Ho . The ECHo experiment is organized in up-scaling phases, gradually increasing the total statistics and therefore the sensitivity on the effective electron neutrino mass. The next phase, ECHo-100k, aims to lower the sensitivity below 3 eV operating about 12,000 MMC pixels. The modular approach of the ECHo experiment will allow the collaboration to scale up to further phases with larger number of pixels [46].

This Thesis proposes the development and possible implementation for particle physics, astrophysics and cosmology experiments of a digital backend for the readout electronics of cryogenic sensors, focused in particular in QUBIC and ECHo, showing its performance at warm and cold temperatures in a laboratory setup, examining the different available hardware.

The main focus of this work is on the digital signal processing chain, which will extract the sensors signals from the large input data stream in real time, and thus reduce the data rate by several orders of magnitude.

In particular, this Thesis proposes the demodulation of the input signal, by calculating the desired Discrete Fourier Transform (DFT) bin consistent with each monitoring signal, while in a further step demodulate the sensor signal component. This work proposes as a novel channelizing technique for this application, the computing of a single DFT bin by using the Goertzel Filter [47, 48]. This should give an extra degree of configuration flexibility to the warm read-out electronics, upon based in several parameters like the tuning frequency of the filter, the window type and size, among others. The selection of a window function and the arithmetic treatment are critical steps in this work.

As for any novel method, several validation experiments were carried out in order to verify its suitability for being applied to any of the aforementioned experiments, presenting remarkable performance results.

Chapter 2

Particle Detectors

Superconductivity was discovered in 1911 by Kamerlingh Onnes while studying the resistivity of pure metals, and during his investigation of a mercury sample, he noticed how the resistance of this material suddenly dropped when the temperature was below 4.2 K [49], see Figure 2.1. The temperature point where the resistance of a metal abruptly drops when is cooled down is called *transition temperature* or *critical temperature*, T_c . This value differs among different materials. In 1933, Meissner and Ochsenfeld discovered that superconductors are not only characterized by the absence of resistance but also by their ideal diamagnetism [50]. This led to the classification of, in principle, two types of superconductors. Type I, where there is only one critical value for the magnetic field that deactivates the superconductive state; and Type II, where there are two critical values (but only the highest one destroys the superconductivity and restores the normal conducting state).

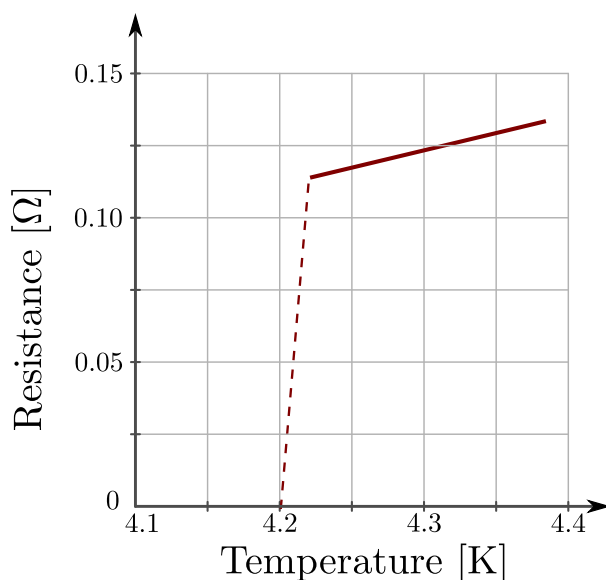


Figure 2.1: Discovery of superconductivity. Historical data on the temperature dependence of the electrical resistance of a thread of mercury [49, 51].

Ginzburg and Landau proposed a phenomenological theory of superconductivity in 1950 [52]. They were able to give an explanation for the existence of the two types of superconductors. Subsequent works from Abrikosov in 1957 [53] and Gorkov in 1959 [54] complemented Ginzburg-Landau Theory showing that this theory is not only applicable at temperatures close to T_c , but at all temperatures. The general concept developed by this group is often named GLAG theory. This theory basically uses thermodynamic principles to describe superconductors without depending on microscopic models. Finally, in 1957, Bardeen, Cooper, and Schrieffer developed a theory of superconductivity [55] (named BCS Theory after their names) that described the microscopic origin of superconductivity.

In 1986 Bednorz and Müller [56] made a crucial step forward in the direction of developing (or discovering) superconductors with higher T_c : looking for superconductivity in a new class of ceramics (copper oxide, or *cuprates*) they found a particular copper oxide compound which resistance dropped to zero at a $T_c = 35.1$ K. These materials are called high- T_c superconductors (HTS). It was in 1987 that Philip Anderson gave the first theoretical description of HTS materials, based on the Resonating Valence Bond (RVB) theory [57], although still nowadays these materials are still not fully understood because their composition and structure is rather complex. Most HTS materials are Type II superconductors.

2.1 Cooper pairs and phonons

In 1932, Igor Tamm introduced the concept of the phonon as the quantum mechanical description of an elementary vibrational motion in which a lattice of atoms or molecules uniformly oscillates at a single frequency. They are analogous to photons as they have an energy $\hbar\omega$ as the quanta of excitation of the lattice vibration. Since their momentum p is exact, due to the Heisenberg uncertainty principle, the position of phonons cannot be determined; thus, they are not localized particles. In 1956 it was shown by Cooper that the ground state of a Fermi gas becomes unstable if a small attractive interaction between a pair of electrons exists [58]. The attractive interaction can be interpreted as an exchange of virtual phonons, since at low temperatures electrons cannot undergo sufficient energy changes to create phonons of short wave-length. In other words, he demonstrated that an arbitrarily small attraction between electrons in a metal can cause a paired state of electrons to have a lower energy than the Fermi energy level, which implies that the pair is bounded; and that for superconductors in particular, this attraction is due to the electron-phonon interaction [51], as depicted in Figure 2.2.

The BCS ground state represents a coherent many-particle state within which all Cooper pairs occupy a common quantum state. This state may be described by the macroscopic wave function of the form:

$$\Psi(r) = \Psi_0 e^{j\varphi(r)} \quad (2.1)$$

where the magnitude of the wave function is given by $|\Psi_0|^2 = n_s$, which is the concentration of Cooper pairs. The existence of such a wave function with a well-defined phase

in the whole sample has remarkable consequences for the behavior of superconductors and gives rise to peculiar effects in magnetic fields [51].

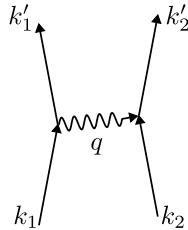


Figure 2.2: Electron-electron interaction via phonon exchange. The interacting electrons exchange a virtual phonon with the wave vector \mathbf{q} . The center of mass momentum $k_1 + k_2 = k_1' + k_2' = K$ is conserved [51].

2.2 Josephson junction

In 1962, Brian Josephson observed that super-current tunnelling through a Superconductor-Insulator-Superconductor (SIS) junction should be a periodic function of the phase difference between the superconducting wave-functions on either side of the junction [59, 60]. This super-current is derived from the tunnelling of superconducting Cooper pairs and is present even though there is no voltage applied between the superconductors. This is the Josephson effect.

This phenomenon occurs due to the possibility of the existence of a gradient in the phase, which can cause a current, and the time variation of that phase can cause a voltage.

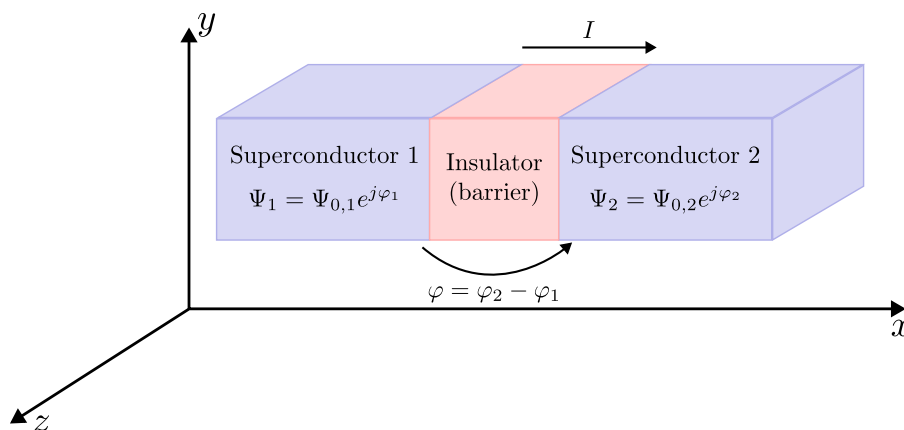


Figure 2.3: Josephson Junction diagram

As there is a current I along the device through a cross section A_j , a current density constant $j_s(x)$ exists. The weak link (barrier) is characterized by a phase difference φ . The supercurrent density, J_s , is a function of the gauge-invariant phase difference, φ , of the two superconductors:

$$\varphi = \varphi_2 - \varphi_1 - \frac{2\pi}{\Phi_0} \int_1^2 \mathbf{A}(\mathbf{r}) d\mathbf{l} \quad (2.2)$$

where Φ_0 is the fundamental quantum flux, being $\Phi_0 = \frac{h}{2e} = 2.07 \times 10^{-15} \text{ Tm}^2$ and $\mathbf{A}(\mathbf{r})$ the magnetic vector potential inside the tunnel barrier of the JJ.

There are two principal Josephson relations. One is the dependence of J_s with φ and the other one is related to the evolution of φ in time. The first one is the Current-Phase Relation (CPR) and is defined by:

$$J_s(\varphi) = J_c \sin(\varphi) \quad (2.3)$$

where J_c represents the critical current density. This expression is also found in the bibliography in terms of current (and not current density):

$$I_s(\varphi) = I_c \sin(\varphi) \quad (2.4)$$

The other equation is the Voltage-Phase Relation (VPR) and is defined by:

$$\frac{d\varphi}{dt} = \dot{\varphi} = \frac{2\pi}{\Phi_0} V \quad (2.5)$$

where V represents the voltage across the junction. Considering an alternating current with an amplitude I_s smaller than the critical current of the junction, taking the time derivative of eq. 2.4 and inserting it in eq. 2.5, the voltage drop across the junction can be re-written like:

$$\begin{cases} I_s \dot{\varphi} = I_c \cos(\varphi) \frac{d\varphi}{dt} \Rightarrow \frac{d\varphi}{dt} = \frac{I_s \dot{\varphi}}{I_c \cos(\varphi)} \Rightarrow \\ \frac{d\varphi}{dt} = \frac{2\pi}{\Phi_0} V \end{cases} \quad (2.6)$$

$$\Rightarrow \frac{2\pi}{\Phi_0} V = \frac{I_s \dot{\varphi}}{I_c \cos(\varphi)} \Rightarrow V = \frac{\Phi_0}{2\pi I_c \cos(\varphi)} I_s \dot{\varphi} \quad (2.7)$$

$$L(\varphi) = \frac{\Phi_0}{2\pi I_c \cos(\varphi)} = \frac{L_{JJ}}{\cos(\varphi)} \quad (2.8)$$

where $L(\varphi) = V/I_s(\varphi)$, indicating a phase-dependant non-linear inductance, and $L_{JJ} = \Phi_0/2\pi I_c$, the Josephson inductance.

2.3 Superconducting Quantum Interference Device

When a superconducting ring is exposed to a magnetic field and cooled down below T_c , the field is not expelled [51]. When this external field is removed, the internal magnetic flux will remain trapped. Since the phase $\varphi(r)$ in eq. (2.1) is well-defined, the phase difference $\Delta\phi$ that exists between two points can be obtained by calculating the contour integral:

$$\Delta\varphi = \int_1^2 \nabla\varphi(r) \cdot ds \quad (2.9)$$

To demonstrate the existence of flux quantization, consider the superconducting ring in Figure 2.4, left.

The existence of a macroscopic wave function has an important consequence for the trapped magnetic flux. It can be demonstrated that for this scenario the quantum mechanical expression for the circulating density current where cooper pairs are involved, \mathbf{j} , in a magnetic field \mathbf{A} is [51, 61]:

$$\mu_0\lambda_L^2\mathbf{j} = \left(\frac{\hbar}{e}\nabla\varphi - 2\mathbf{A}\right) \quad (2.10)$$

where λ_L is the London penetration depth, e is the charge of the electron and μ_0 is the vacuum magnetic permeability. Carrying out the integration along the closed contour, the line L illustrated in Figure 2.4 left, of this superconducting ring:

$$\mu_0\lambda_L^2 \oint_L \mathbf{j} \cdot d\mathbf{s} = \frac{\hbar}{e} \oint_L \nabla\varphi \cdot d\mathbf{s} - 2 \oint_L \mathbf{A} \cdot d\mathbf{s} \quad (2.11)$$

Because of the Meissner effect, the current on the surface creates a magnetic field which cancels the external one. This means that there exists a path where $\mathbf{j} = 0$ around the entire loop, simplifying eq. 2.11.

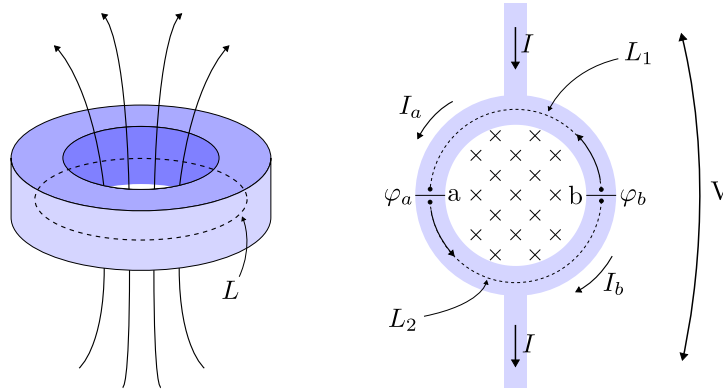


Figure 2.4: Superconducting ring penetrated by a magnetic field. The integration line contour is shown in a dashed black line (left). Superconducting ring interrupted by two Josephson Junctions (JJs) and penetrated by a magnetic field, represented by the crosses. L_1 and L_2 represents the contour lines along which the integration is performed. We can appreciate the two JJs, a and b , with the currents I_a and I_b (right).

Transforming the line integral to a surface integral using the Stokes' theorem yields to the total magnetic flux Φ :

$$\Phi = \oint_L \mathbf{A} \cdot d\mathbf{s} = \int_{\Sigma} \mathbf{B} \cdot d\mathbf{f} \quad (2.12)$$

Finally, from this last expression:

$$\Phi = n \frac{h}{2e} = n\Phi_0 \quad (2.13)$$

where $n \in \mathbb{N}$. From the quantization of the magnetic flux it immediately follows that the current in a closed loop is quantized as well. A continuous variation of the current is not possible since the phase of the wave function can only be changed by a multiple of 2π . This comes from the fact that since a wave function is single-valued, after one turn in a ring the phase change is 2π [62].

A Superconducting Quantum Interference Device (SQUID) consists of a superconducting loop that can be interrupted by one or more Josephson Junctions (JJs). If it is interrupted by one JJ, it corresponds to an rf-SQUID [63], while interrupted by two JJs, corresponds to a dc-SQUID [64].

In a dc-SQUID, the wave function is separated by two weakly coupled wave functions over the two legs of the rings, see Figure 2.4, right. Connecting this dc-SQUID to a current source, the component of the current carried by the Cooper pairs can be calculated using the JJ equations as follows:

$$I = I_c[\sin(\varphi_a) + \sin(\varphi_b)] = 2I_c \cos\left(\frac{\varphi_a - \varphi_b}{2}\right) \sin\left(\frac{\varphi_a + \varphi_b}{2}\right) \quad (2.14)$$

with φ_a and φ_b being the phase changes at the junctions a and b respectively.

A current is also induced when the ring is in the presence of a magnetic flux Φ_{ext} . The difference $\varphi_a - \varphi_b$ depends on the magnetic flux Φ enclosed by the device. It can be demonstrated that:

$$\varphi_a - \varphi_b = \frac{2e\Phi}{\hbar} \quad (2.15)$$

Inserting the previous equation in (2.14):

$$I = 2I_c \cos\left(\frac{2e\Phi}{\hbar}\right) \sin\left(\frac{\varphi_a + \varphi_b}{2}\right) \quad (2.16)$$

Here $\Phi = \Phi_{ext} + \Phi_L$, where Φ_L is the flux related to the resulting shielding currents. Introducing no significant errors we can approximate $\Phi \simeq \Phi_{ext}$ (neglecting the SQUID self inductance), which applied to equation (2.16) gives [61]:

$$I = I_{max} \sin\left(\frac{\varphi_a + \varphi_b}{2}\right) \quad (2.17)$$

where I_{max} is obtained by finding the extremum value doing $dI/d\varphi_I = 0$ in eq.2.16 for $\Phi \simeq \Phi_{ext}$:

$$I_{max} = 2I_c \cos\left|\frac{2e\Phi_{ext}}{\hbar}\right| \quad (2.18)$$

From this last equation, we can derive that the external magnetic flux Φ_{ext} is translated into a current change with a factor $1/\Phi_0$, which allows us to use it as a very accurate magnetometer. To do so, the current I can be set by applying an external bias current.

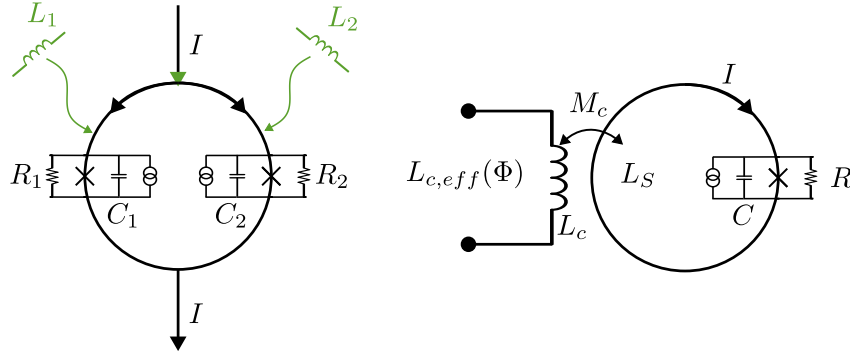


Figure 2.5: The JJs are represented by their Resistively and Capacitively shunted Junction (RCSJ) model. Equivalent circuit for the dc-SQUID (left). Equivalent circuit for the rf-SQUID (right). The JJ is illustrated as the *cross* symbol and the current source represents the noise contribution to the model.

Using the RCSJ model [65, 66] taking $R_1 = R_2 = \frac{R}{2}$, $C_1 = C_2 = 2C$ and a critical current $2I_c \cos(\pi\Phi_{ext})$, see Figure 2.5 left, we can express the voltage-flux characteristic [61] as:

$$V(\Phi_{ext}) = I_c R \sqrt{\left(\frac{I}{2I_c}\right)^2 - \left[\cos\left(\frac{\pi\Phi_{ext}}{\Phi_0}\right)\right]^2} \quad (2.19)$$

The dc-SQUID is not the only device that can be used for magnetic flux measurements. In contrast to the dc-SQUID, the rf-SQUID extracts the magnetic flux using the change in the inductance of the JJ in a superconducting ring. This is achieved using an inductor L_c coupled to the SQUID, as can be seen in the Figure 2.5 right. The JJ is illustrated as the *cross* symbol and the current source represents the noise contribution to the model.

For the rf-SQUID the magnetic flux can be read out via the effective inductance $L_{c,eff}$:

$$L_{c,eff}(\Phi) = L_c - \frac{M_c^2}{L_S} \frac{\beta_L \cos(2\pi \frac{\Phi}{\Phi_0})}{1 + \beta_L \cos(2\pi \frac{\Phi}{\Phi_0})} \quad (2.20)$$

where β_L is the screening parameter defined as $\beta_L = 2\pi L_S I_c / \Phi_0$. As very sensitive magnetometers, the dc-SQUID and the rf-SQUID, can be used to read out low-temperature detectors, such as the ones described in the following sections.

2.4 Cryogenic calorimeters and bolometers

The bolometer was proposed by Langley in 1878 [67, 68] as an instrument for the quantitative measurement of electromagnetic radiation, by means of resistive sensitive elements like thermistors. The working principle consists of observing a change of the resistance of this sensitive element as a function of a change in temperature.

The invention of the calorimeter is attributed to the French chemist Antoine Lavoisier. He developed the first calorimeters in the late 18th century as part of his research on the nature of heat and combustion. From the observed temperature change it is possible to calculate the amount of heat generated or absorbed by the system.

The natural next step for these sensors was to move to lower temperatures in order to improve one or more of their intrinsic characteristics. Working at cryogenic temperatures, typically below 400 mK for bolometers [16] and below 100 mK for calorimeters [3, 17, 18], improves the energy resolution of the calorimeters, while in the case of the bolometers, it allows higher sensitivity. In both cases, working at very low temperatures lowers the noise of the detectors.

Since the discovery of superconductivity, paramagnetic materials have been widely utilized and effectively employed in various applications, such as serving as sensor materials for high-precision susceptibility thermometers. This section will present a concise summary of the TES, MKID, MMC, and the newly introduced Magnetic Microbolometers (MMB). These detector types are relevant to this Thesis.

2.4.1 Transition Edge Sensors

A superconducting TES consists of a superconducting film operated in a narrow temperature region between the normal and superconducting state, where the electrical resistance varies from zero to its normal value, see Figure 2.6.

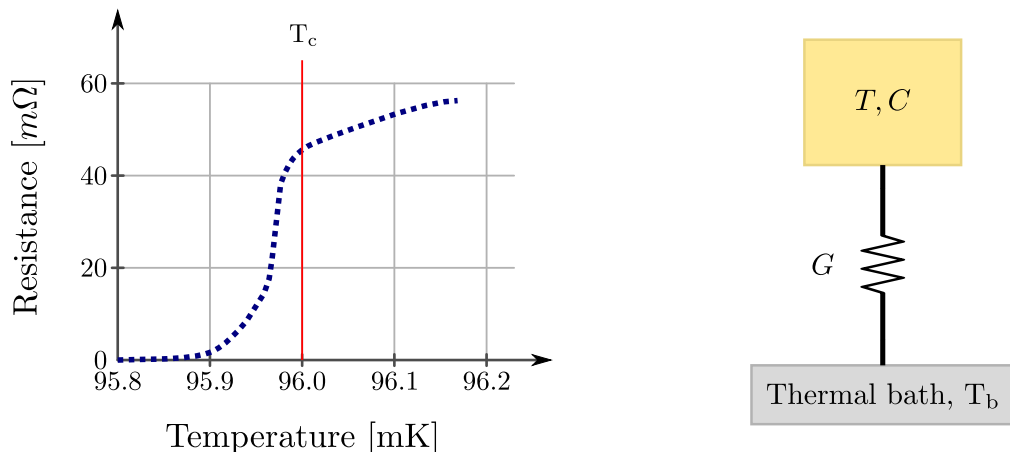


Figure 2.6: Transition of a superconducting film (a Mo/Cu proximity bilayer) from the normal to the superconducting state near 96 mK [19]. (left). Simple sketch of the TES where C is the thermal capacitance and G the thermal conductance of the weak thermal link (right). The time constant, without feedback, is defined as: $\tau = C/G$.

Compared to typical semiconductor thermistors, TES can resolve smaller energies with faster rise times [19, 69] due to their inherent working principle: the electrothermal feedback (ETF), dR/dT , which arises from the Joule heating. In the case of the semiconductors, the ETF is negative so an increase in temperature yields to a decrease in the resistance. For superconductors is positive, an increase in temperature results in an increase in the resistance.

The TES can be operated in two ways: current-biased or voltage-biased. The former one yields to a positive ETF operation of the device ($P = I^2R \Rightarrow$ if $T \uparrow \Rightarrow R \uparrow \Rightarrow P \uparrow$), while the latter (the mostly used mechanism) gives a negative ETF operation ($P = V^2/R \Rightarrow$ if $T \uparrow \Rightarrow R \uparrow \Rightarrow P \downarrow$). Negative ETF gives a constant dissipated power P operated device.

Some of their majors weaknesses are the Johnson noise in the operation region, and the requirement of operating the sensor in a small temperature region (a sharp transition exists between the superconducting and normal conducting state, which leads to a greater tendency for instability and lower saturation energy).

Fortunately, this problem can be resolved with the addition of a SQUID magnetometer as a current amplifier which can easily be impedance-matched to the TES and implementing a negative ETF (voltage-biased) [19]. This also gave the possibility to multiplex the readout of several TES detectors [70]. TESs are still the main device for CMB experiments due to the maturity of the technology (and consequently, its reliability) [71, 72].

However, the transition between the superconducting and normal states is non-linear, and the rise time also depends on the pulse height. This non-linearity limits the applicability of TES for scenarios where a large dynamic range is required [73, 74].

For the TES used as a bolometer, the sensitivity is given by the following expression for the Noise Equivalent Power (NEP):

$$\text{NEP}_{\text{TES}} = \sqrt{4K_B T^2 G} \quad (2.21)$$

where K_B is the Boltzmann constant, and G is the thermal conductance. In the case of being used as a calorimeter, the energy resolution is given by:

$$\Delta_{\text{FWHM}} = 2.35\sqrt{K_B T^2 C} \quad (2.22)$$

where C is the thermal capacitance.

2.4.2 Microwave Kinetic Inductance Detectors

Kinetic inductance detectors operate on the principle that a change in the number of quasiparticles (broken Cooper pairs) in a superconductor will change the kinetic inductance. This occurs because the quasiparticles block Cooper pairs from occupying some of the electron states. Photons (or particles) absorbed in the superconductor produce quasiparticles, and the resulting change in the inductance is measured at the detector output. In a superconductor, the surface impedance Z_s is primarily inductive [75–78], therefore we can represent that impedance by:

$$Z_s = R_s + j\omega L_s \quad (2.23)$$

An equivalent circuit of this device is shown in Figure 2.7, left. Z_s is represented by the variable inductor in Figure 2.7, which is part of a resonant circuit where L_s varies the total inductance L of the circuit, while the surface resistance R_s makes the inductor slightly lossy (adding a series resistance). This produces a resonator circuit that will change its response as a function of the input power / energy $P(t)$. The surface resistance R_s is a consequence of quasiparticles in the superconductor experiencing accelerations due to time variable electromagnetic field and subsequent scattering processes causing ohmic losses, analogously to conduction electrons in normal conducting metals. In contrast, Cooper pairs, are not subject to those scattering mechanisms and, hence, they flow dissipationless through the superconductor. Due to their inertia, they cannot follow the time variable electromagnetic field instantaneously, which manifests in the kinetic inductance L_{kin} . Thus, the surface inductance L_s is comprised not only of the magnetic inductance related to the geometry of the superconductor, but also of the kinetic inductance: $L_s = L_m + L_{kin}$.

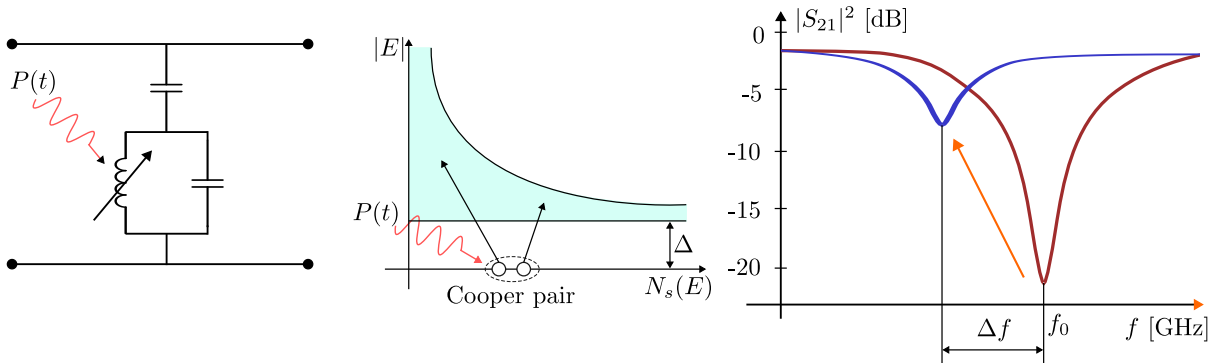


Figure 2.7: MKID equivalent circuit. The surface impedance Z_s of the superconducting film changes with the impact of a photon with power or energy $P(t)$ (left). A photon is absorbed breaking Cooper pairs (shown at the Fermi energy level) which creates a number of quasiparticle excitations. $N_s(E)$ is the density of states for quasiparticles, and E is the quasiparticle energy (center). The absorbed photon breaks cooper-pairs, changing the kinetic inductance and hence, the frequency response of the device shifting the f_0 (red curve) normal state resonance frequency, towards a minor frequency (blue curve) (right).

The incident photon with an energy $hf > 2\Delta$ (with Δ the superconducting gap energy), is absorbed in a superconducting film cooled to $T \ll T_c$ which will break Cooper pairs creating a number of quasiparticle excitations, and hence introducing a frequency shift in the MKID response, see Figure 2.7 right. It is worth to mention that the efficiency of creating quasiparticles will be less than one since some energy of the photon will end up as phonons.

2.4.3 Magnetic Microcalorimeters

The use of paramagnetic materials for calorimetric particle detectors was pioneered by Bühler and Umlauf [79–81] in 1988. Very promising results were obtained with these first detectors, showing that this scheme is well suited for the development of high resolution detectors. A weakness of these first devices was the relatively slow signal rise time. When dielectrics are doped with a paramagnetic material (*dielectric host materials*), the relaxation time for the energy content of the spin system after energy deposition is limited by the spin-phonon relaxation time. This time varies between milliseconds to tens of milliseconds for many of the dielectric materials at temperatures below 100 mK. Simon R. Bandler [82] suggested the use of diluted paramagnetic alloys such as gold (Au) doped with a rare-earth material like Erbium (Er) (*metallic host materials*) or silver (Ag) as the metallic host [83], which gives a measured Korringa constant for the electron-spin relaxation times below 1 μ s at 100 mK [84]. As a trade-off, the presence of conduction electrons considerably increases the heat capacity of the sensor and leads to enhanced interaction among the magnetic moments.

A MMC employs a para-magnet placed in a small magnetic field as a temperature sensor. An absorber suitable for stopping the particle to be detected is in strong thermal contact with the sensor. These two components are weakly coupled to a thermal bath. An energy deposition, δE , in the absorber produces a temperature change, δT , in the absorber/sensor system, which can be monitored by measuring the change of magnetization, δM , of the paramagnetic sensor using a sensitive SQUID magnetometer [17], see Figure 2.8. The corresponding temperature information is retrieved from the change of magnetization of the paramagnetic sensor.

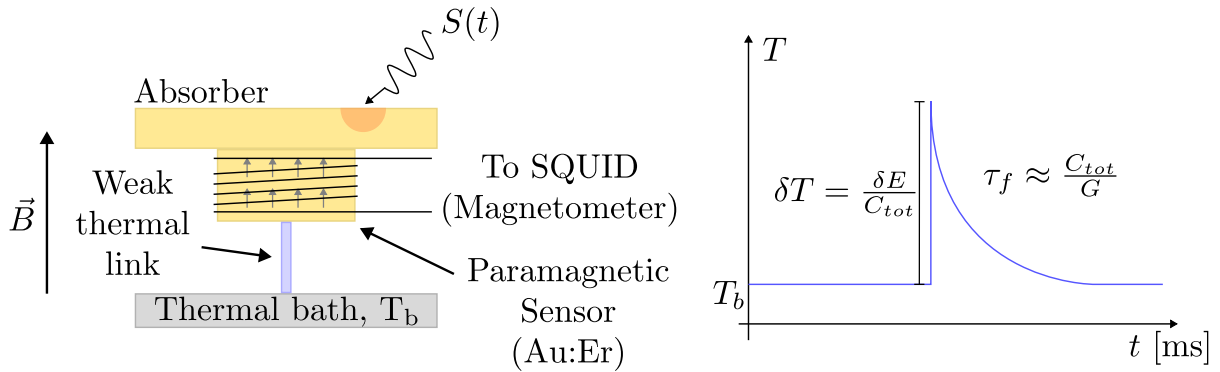


Figure 2.8: Magnetic Microcalorimeter model. Au:Er refers to the gold - erbium dilute alloy. The darker region in the absorber represents the energy deposition, $S(t)$, and an increase in the temperature (left). Conceptual temperature response of the sensor (right).

From the laws of thermodynamics the change in temperature can be obtained by the following relationship:

$$\delta T = \frac{\delta E}{C_{tot}} \quad (2.24)$$

and thus:

$$\delta M = \frac{\partial M}{\partial T} \delta T \Rightarrow \delta M = \frac{\partial M}{\partial T} \frac{\delta E}{C_{tot}} \quad (2.25)$$

with C_{tot} the total heat capacity of the system: sensor and absorber.

At sufficiently low temperatures (between 10 mK and 1.5 K) and small magnetic fields, it is possible to describe the magnetic behavior of erbium in gold by a Two-Level System (TLS) whose quasi-spin $\tilde{S} = 1/2$ and whose effective isotropic gyromagnetic ratio $\tilde{g} = 34/5$ [85], see Figure 2.9 left. Below 0.9 mK a phase transition to spin glass occurs. This helps to do the analysis of the working principle of the sensor and the noise contributions [17]. The performance of MMCs strongly depends on the heat capacity and magnetization of the Au:Er or Ag:Er sensor. There are three principal effects that contribute to a thermal fluctuation analysis in order to obtain the energy resolution: the magnetic dipole-dipole interaction, the Ruderman-Kittel-Kasuya-Yosida (RKKY) interaction (which in the case of Au:Er, the exchange is through the localized $4f$ electrons of the erbium ions with the gold conduction electrons) and the Zeeman effect (related with the magnetic field in which the sensor is immersed) [17, 51].

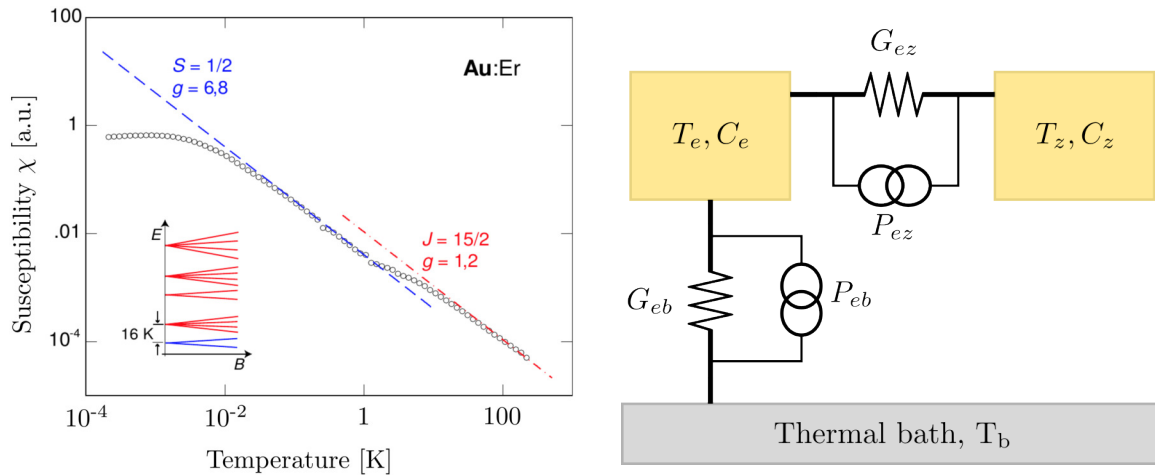


Figure 2.9: Paramagnetic contribution to the magnetic susceptibility of Au containing 600 ppm Er as a function of temperature. The two straight lines represent the Curie susceptibility assuming Er^{+3} ions in the Γ_7 -groundstate doublet and Er^{+3} ions without crystal field splitting [17] (left). Canonical ensemble for the MMC with two subsystems. One subsystem represents the electron system (the absorber), with T_e and C_e . The other one represents the spin system with T_z and C_z (the paramagnetic sensor). The thermal link between these two subsystems is represented by G_{ez} , and between them and the thermal bath with G_{eb} . Finally, P_{eb} and P_{ez} model the noise sources appreciated in the energy fluctuations between the systems (right).

The energy resolution is given by the following equation [18]:

$$\Delta_{\text{FWHM}} \simeq 2.35 \sqrt{4K_B C_e T^2} \left[\frac{1}{\beta(1-\beta)} \frac{\tau_r}{\tau_d} \right]^{1/4} \quad (2.26)$$

where C_e is the absorbers heat capacity, T is the operation temperature, τ_r is the rise time, τ_d is the decay time (and $\tau_r \ll \tau_d$) and $\beta = C_s/(C_e + C_s)$, where C_s is the heat capacity of the paramagnetic sensor, see Figure 2.9. It is worth to mention that this last expression does not include the magnetic johnson noise, the erbium $1/f$ excess noise and the readout SQUID noise.

The key points of this sensor are the high sensitivity and its dissipationless characteristic. Combined with the possibility of being read-out by a SQUID (a near quantum-limited noise device) this results in the MMC's remarkable characteristics: very fast signal rise time, an excellent energy resolution, a large dynamic range, a quantum efficiency close to 100% as well as an almost linear detector response [83].

2.4.4 Magnetic Microbolometers

The MMB emerged as an idea for exploring the applicability of a paramagnetic thermometer using metallic host materials like the ones used in MMCs, aiming to relax in some sense the complexities that the actual refrigerators need to fulfill in order to cool-down devices with several TESs or MKIDs arrays, exploiting the dissipationless characteristic of such thermometer. The proposal and theoretical discussion of this sensor concept can be found here [86].

The thermal model for this detector is the same as the one presented for the MMC in Figure 2.8. Again, a change in the magnetization due to the incoming radiation which was absorbed, induces an excess magnetic flux signal that is collected by a pick-up coil and connected to a SQUID magnetometer (ultimately, an rf-SQUID, as will be introduced later for the microwave SQUID multiplexer in 3.4). In Figure 2.10 the expected signal shape is shown.

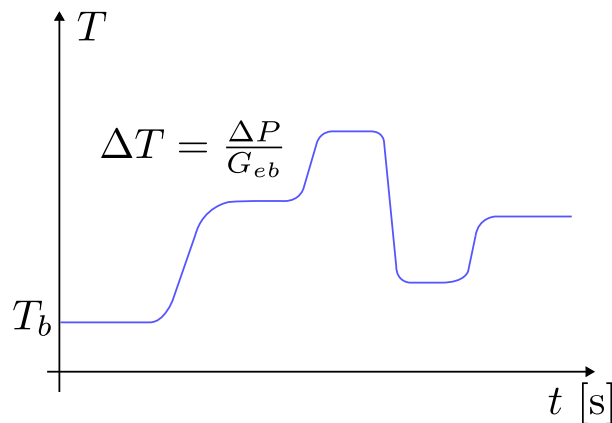


Figure 2.10: Magnetic Microbolometer expected signal.

The time scales between this expected signal and the one for the MMCs as can be seen in Figure 2.8, are in quite different orders of magnitude: the first one is a pulsed

shape one where important high frequency components are present, while the second one is a low frequency dominated signal.

In the case of QUBIC, the instrument scan the sky at a rate of 1 deg/s and have a synthetic beam width of 0.39 deg [16]. As indicated in the formula from [86], the decay time constant τ (which essentially defines the bolometer's speed) is around 62 ms. Consequently, CMB signal imprinted in the focal plane spans from approximately 0 Hz (DC) to 2.5 Hz ($1/2\pi\tau$).

The possible sketches for the MMB are shown in Figure 2.11, for a radiation coupling version that can be based on either an absorber-coupling [87] or antenna-coupling scheme [88, 89].

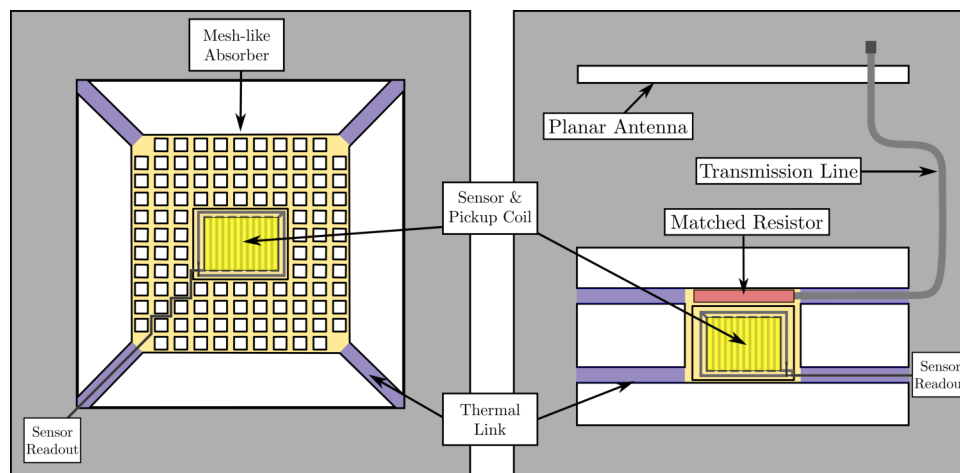


Figure 2.11: Conceptual detector layout of a MMB. The version based on a thin metal mesh-like absorber with a surface resistivity tuned to the impedance of free space that absorbs incoming optical radiation. The subsequent rise in temperature is measured by a paramagnetic sensor and magnetically coupled pickup coil (left). The Antenna-coupled bolometer scheme, consisting of a planar antenna that couples radiation onto a microstrip transmission line terminated with a matched resistor thermally coupled to a paramagnetic material placed over a meander-shaped pickup coil which in both cases reads out the magnetization and simultaneously introduces the biasing magnetic field (right).

Chapter 3

Multiplexing Systems

In communication theory, various multiplexing techniques are employed to allow multiple signals to be transmitted over a common medium. This facilitates the efficient utilization of resources and bandwidth. Multiplexing can be achieved through different means, including time-division, frequency-division, or encoding via orthogonal functions, among other methods. In the following sections, a brief overview of some of the most relevant multiplexing techniques, for multiplexing superconducting cryogenic detectors will be provided. Furthermore, an introduction will be given to two specific techniques: frequency-division through the Microwave SQUID Multiplexer and the Flux-Ramp Modulation (FRM) technique.

3.1 Time-Division Multiplexing

Time Division Multiplexing, is a technique used to transmit multiple signals over a shared communication channel by dividing them into discrete time slots. The transmission channel, see Figure 3.1, is divided into equal-duration time intervals, and during each interval, one given signal is transmitted, as each channel is assigned to one time slot.

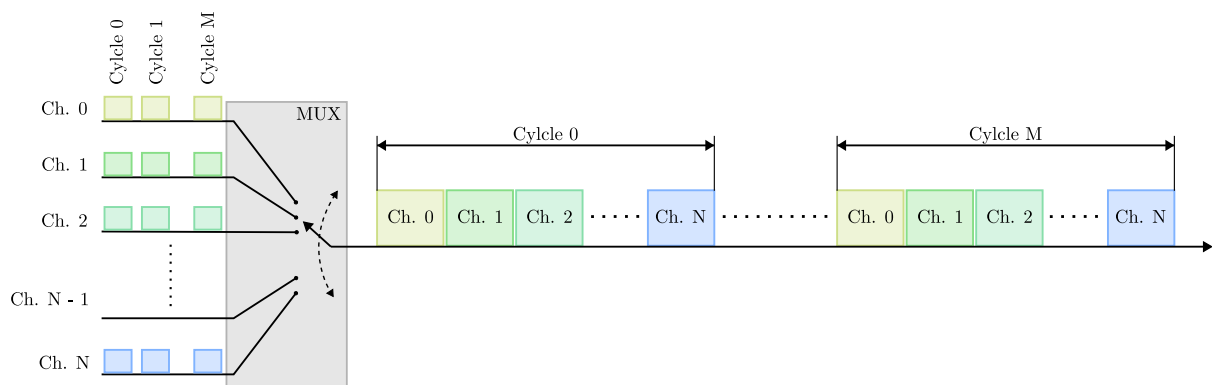


Figure 3.1: This is a typical TDM schematic. The multiplexer (MUX) is connected to each input channel sending each channel to a common transmission medium. The number of channels fixes the minimum time of each cycle.

A single common electrical connection serves as the output line. A direct result of this method is the reduction in the number of connections required for the total amount of channels [90, 91]. One of the major advantage of this method (when compared to other methods) is the required low signal processing effort. However, this approach is limited (mainly) by two factors: the sampling time and the switching time. The former strongly depends on the amount of channels to be read. The latter impacts the sampling time because each channel can be read only after the previous ones. Furthermore, during the switching time and a few moments after, readout has to be inhibited due to stabilization processes that have to take place. There are many examples on how this approach is applied to the readout of superconducting TES [42, 91, 92]. In example, for the QUBIC project technical demonstrator, see Figure 3.2, each quarter of the focal plane consist of two SQUID multiplexers of 128 channels each (128:1 ratio):

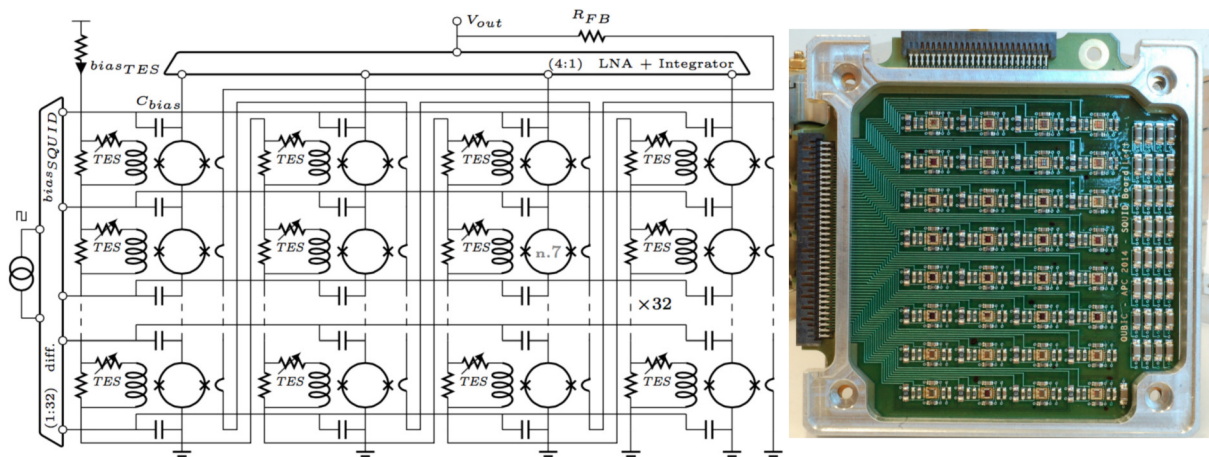


Figure 3.2: The SQUID multiplexer used in the QUBIC project (left). Top view of the circuit (picture taken from [42]) (right).

3.2 Code-Division Multiplexing

Code Division Multiplexing, is a technique where multiple signals are transmitted by means of spread spectrum communication. In this method, a narrow-band signal is spread across multiple channels via division of the transmission channel, see Figure 3.3 left. The information is projected onto individual orthogonal functions, and can be separated through receiver-side correlation with the individual functions. The Walsh functions [22, 23, 93] are commonly used as the orthogonal basis, as they can be easily generated, implying a low demand on circuitry and hardware. In this system, the information of a sample or bit is spread over the period length of the orthogonal basis [90]. In simple words, it allots a unique code to every channel so that each of these channels can use the same spectrum simultaneously at the same time, making use of the bandwidth very efficient with reasonable high immunity to interference.

Applying this technique to reading superconducting sensors, the Walsh functions are used to control the flux coupling of the sensors to the SQUID amplifiers. This can be

done in different ways as described in [23, 94–96]. The works from Stiehl and Doriese combines both TDM and CDM in order to increase the number of reading channels, but also improves the readout noise considerably. Moreover, the data transmission is low and post-processing is much complex than for TDM. While a raw data recording does not need to be significantly modified in the CDM process, post-processing or decoding of the data is necessary [94, 95]. However, when facing real-time analysis, the correlation must be carried out on the readout device, in order to be able to separate the sensors signals.

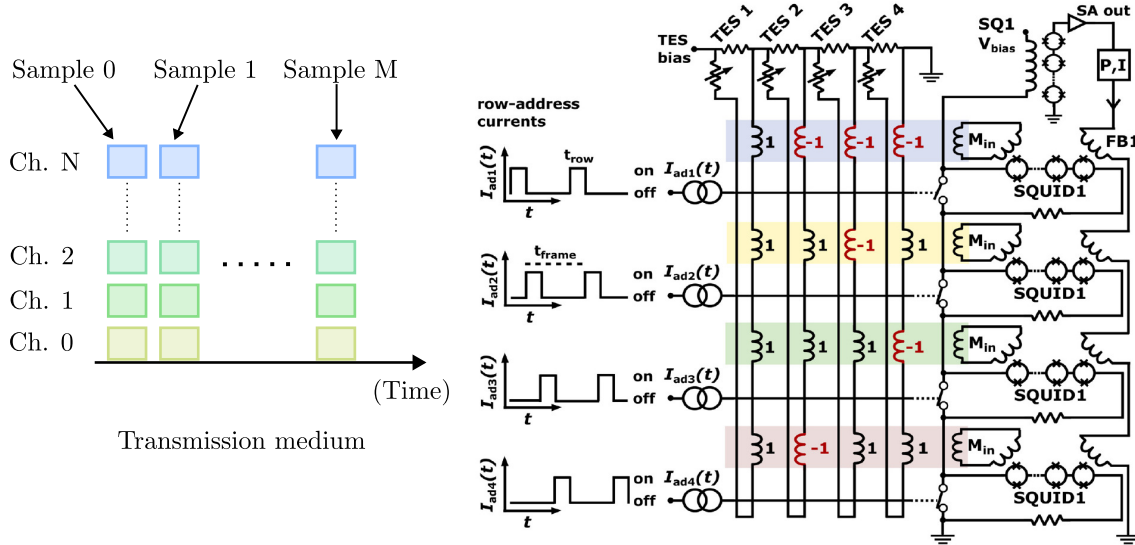


Figure 3.3: This is a typical CDM schematic. Each channel is assigned a unique code so that each of these channels can use the same spectrum simultaneously at the same time (left). An implementation example of a 4-channel example of a CDM circuit. Bias to each SQUID channel is controlled by applying address current (I_{ad}) to a flux-actuated switch. A common feedback signal (FB1) is applied to all channels. Current signals from each TES are coupled positively or negatively to each SQUID channel [23] (right).

3.3 Frequency-Division Multiplexing

Frequency Division Multiplexing, is a technique where multiple signals are transmitted simultaneously over a shared communication channel by dividing the available frequency spectrum into non-overlapping frequency bands, see Figure 3.4. Transmission takes place simultaneously by modulating the signals onto different carrier frequencies along the reserved frequency band. The maximum number of channels that can be transmitted over a single line is determined by taking into account the total useful bandwidth of each channel, the distance among them (Δf) and the total bandwidth of the readout system.

Figure 3.5 shows a very basic schematic of MHz FDM as is used, for example, in POLARBEAR [14, 97] experiment. There, each bolometer is connected through a series resonant LC circuit that defines the bias frequency. Only two wires are needed to connect the bolometers of a readout module on the sub-Kelvin stage to the 4 K stage on which

the SQUIDs are mounted.

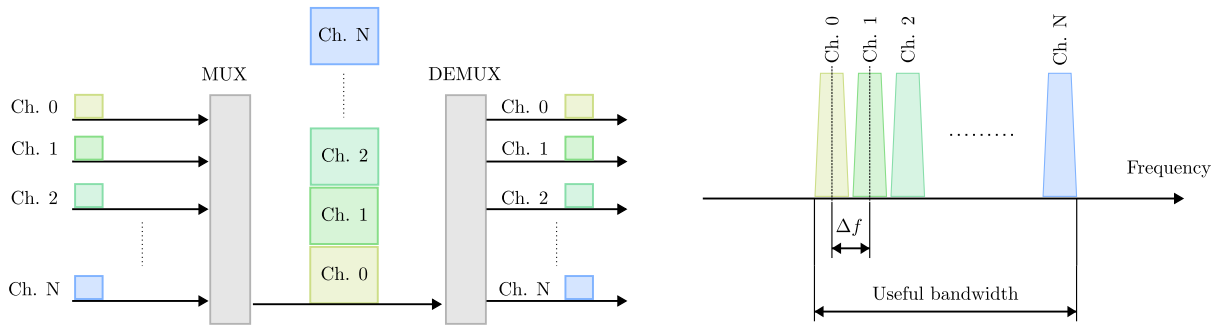


Figure 3.4: This is a typical FDM schematic. The multiplexer and the de-multiplexer are very different from the ones used for TDM. Here a process called *channelization* has to be performed, consisting on different demodulation techniques such as Direct Down Conversion (left). Frequency representation of each channel with its corresponding bandwidth (right).

A bank of N fixed amplitude sine-wave generators operating at room temperature provides a *comb* or *carrier* of detector voltage bias carriers (synthesized with a Digital Multi-Frequency Synthesizer (DMFS)), each operating at a frequency tuned to match the resonance of the individual $LCR_{\text{bolometer}}$ channels. Sky signals modulate the TES resistance, amplitude modulating the current of the carrier. This encodes the sky-signal in symmetrical sidebands above and below the carrier. Since the signal currents from the individual bolometers detectors are at different frequencies, they can all be summed together and transmitted to a single low-impedance input amplifier operating at the 4 K stage.

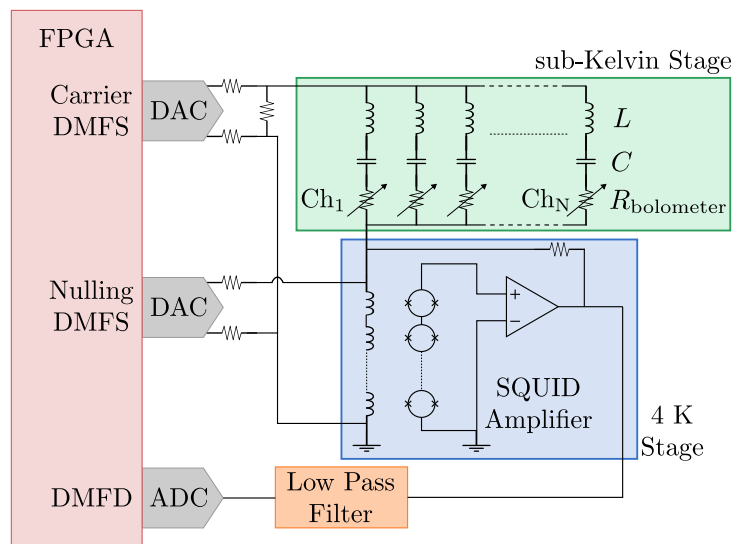


Figure 3.5: This is a typical FDM schematic for MHz frequency values [97, 98]. FPGA stands for Field Programmable Gate Array.

A series array of SQUID is employed operating in a flux-locked loop (FLL) for this transimpedance amplification stage. To reduce the SQUID dynamic range requirements, an inverted version of the carrier comb, referred to as the *nulling comb* is injected at the SQUID input to cancel the carriers. The comb of amplitude modulated carriers is transmitted from the SQUID output to a bank of room temperature demodulators (the Digital Multi-Frequency Demodulator (DMFD)). A low-pass antialiasing filter is applied to the resultant timestream before it is digitized. The signal amplitude is proportional to the photon power deposited on the bolometer photon absorber [98].

3.4 Microwave SQUID Multiplexer

A Microwave SQUID Multiplexer (μ MUX) is a device consisting of N superconducting quarter-wave resonators which implements a FDM technique. Each resonator represents a channel i , with $i = 1, \dots, N$, and is comprised by a superconducting Coplanar Waveguide (CPW) quarter-wave resonator type inductively terminated by a load inductor L_t , and coupled to a common microwave transmission line via a coupling capacity C_c , see Figure 3.6 [46]. The transmission line and the resonator exhibit the same characteristic impedance Z_0 .

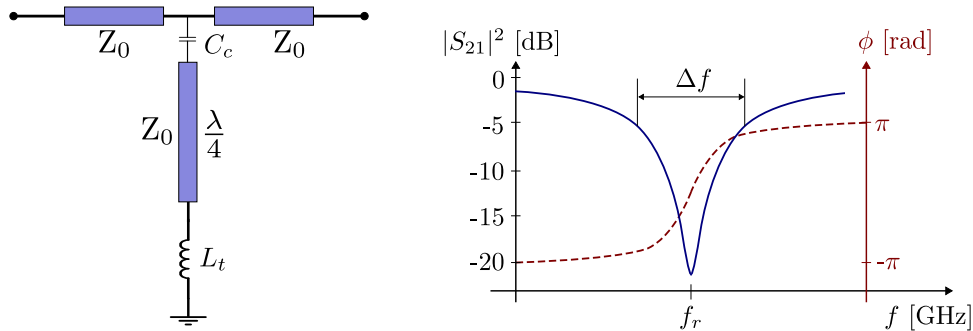


Figure 3.6: Schematic of a CPW quarter-wave resonator, coupled to a transmission line via a capacity C_c and terminated with a load inductor L_t (left), and its frequency response (qualitative plot) can be located in the GHz region, typically between 4 GHz to 8 GHz (right).

The resonance frequency of this device is determined by the following formula:

$$f_r = \frac{f_0}{1 + 4f_0(C_c Z_0 + L_t/Z_0)} \quad (3.1)$$

Where $f_0 = 1/4l_r\sqrt{LC}$ (l_r is the length of the CPW resonator, from which L and C depends) [46, 99]. The scatter parameter $S_{21}(f)$ is defined by:

$$S_{21}(f) = \frac{S_{21}^{min} + 2jQ_l \frac{f-f_r}{f_r}}{1 + 2jQ_l \frac{f-f_r}{f_r}} \quad (3.2)$$

Where $S_{21}^{min} = Q_l/Q_i$, Q_l is the loaded quality factor and Q_i is the intrinsic quality factor. For a detailed calculation of these parameters see [46, 78, 100, 101]. Finally, the resonators bandwidth Δf is determined by $\Delta f = f_r/Q_l$. In a real measurement, the scatter parameter S_{21} is not only determined by the resonator parameters f_r , Q_l and Q_i , but it is also subject to environmental influences, introduced by components in between the resonator and the measurement device, such as cables, attenuators and amplifiers.

The modulation in the μ MUX is achieved by means of an rf-SQUID which limits the power dissipation into the experimental setup to a few pW per channel (much lower when compared to a dc-SQUID approach, which is in the order of 1 to 10 nW [102, 103]), enabling a high order of multiplexing factor ($\sim 10^5$ channels) keeping the power dissipation well below the available cooling power in this kind of experimental setups of $\sim 10 \mu$ W at around 20 mK.

The rf-SQUID introduces a non-linear inductance to achieve the modulation of high-frequency carrier signals in the μ MUX, thanks to the presence of the Josephson junction, see eq.2.8. In particular, a non-hysteretic unshunted rf-SQUID is used, as it can be considered as quasi-dissipationless and the loaded quality factor becomes flux-independent [46, 104]. The rf-SQUID is coupled to the CPW quarter-wave resonator presented before, see Figure 3.7 bottom right.

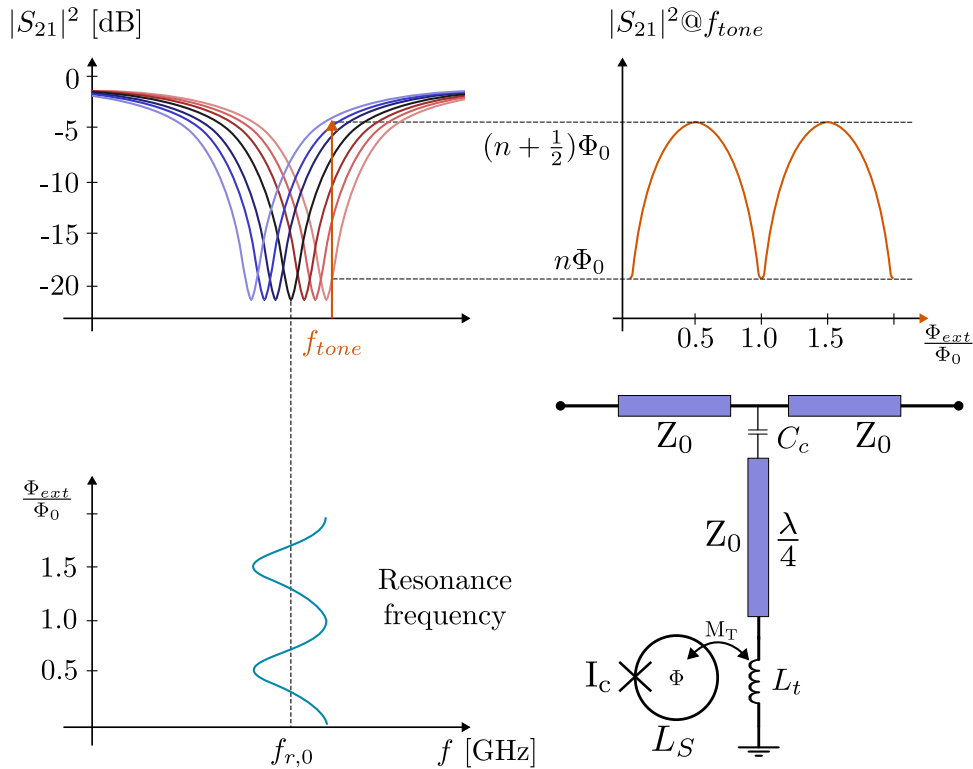


Figure 3.7: An rf-SQUID coupled to a CPW quarter-wave resonator (bottom right). A change that in the concatenated flux Φ occurs, changes the resonance frequency position $f_{r,0}$ (left plots). Because of this, a microwave carrier signal, f_{tone} , will exhibit an amplitude (top right) and phase modulation.

The resonance frequency will depend on the effective load inductor as can be seen in the following equation [105], due the rf-SQUID which is acting as a parametric inductance:

$$f_r(\Phi_{\text{tot}}) = \frac{f_0}{1 + 4f_0(C_c Z_0 + L_{t,\text{eff}}(\Phi_{\text{tot}})/Z_0)} \quad (3.3)$$

In a μMUX consisting of N of the introduced resonator type, each channel exhibits a unique resonance frequency which can be adjusted by the resonator length. Figure 3.8 displays a simple schematic of a μMUX :

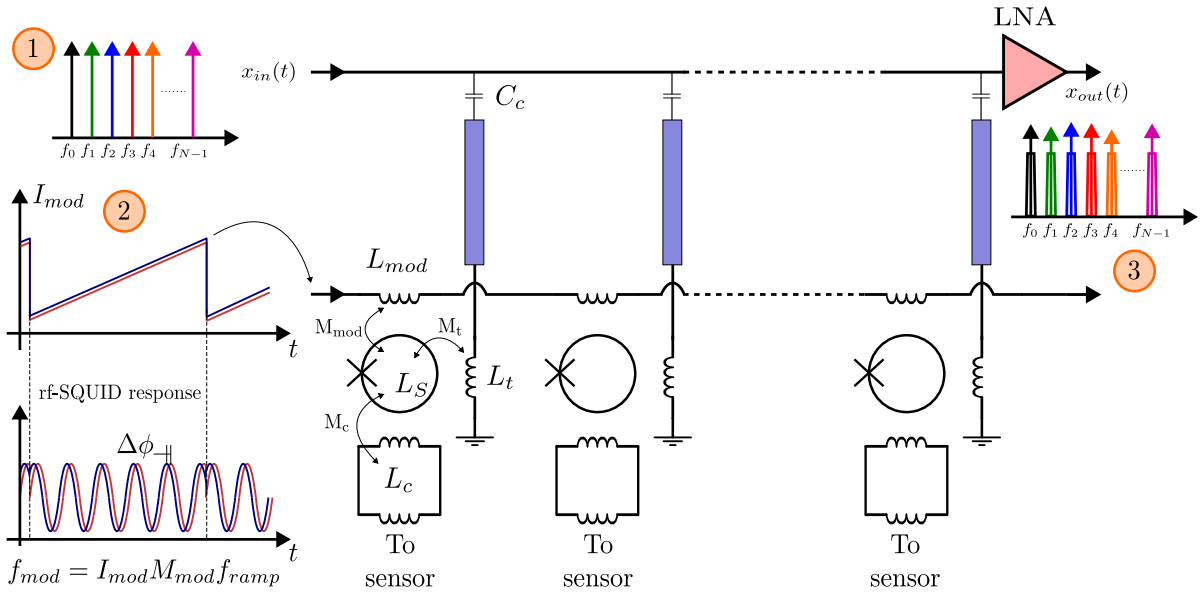


Figure 3.8: μMUX schematic with the FRM line. This device is placed inside of a cryostat typically between 10 mK and 100 mK. C_c is the coupling capacitor, L_t and the blue rectangle represent the superconducting microwave resonator. L_s represents the rf-SQUID inductance, L_{frm} the coupling inductor between the FRM lane and the rf-SQUID, L_c is the coupling inductor to the required sensor and LNA stands for Low-Noise Amplifier. The multitonal input signal is modified after passing through the μMUX .

A sensor is coupled to each rf-SQUID and a change on it will modify the magnetic flux within the rf-SQUID, hence, modifying the resonance frequency of the associated resonator by changing its inductance. By reading this frequency shift one can measure the variation of magnetic flux in the rf-SQUID and therefore the sensor signal.

The monitoring of each channel is achieved by introducing a microwave multi-carrier signal, of which each frequency component targets a unique resonator ($f_{\text{tone},i} = f_{r,i}$), (1) and reading it back. The linear read-out of the μMUX is carried out by implementing the Flux-Ramp Modulation (FRM) technique, which consists of applying a periodic ramp signal to all the rf-SQUIDs [106] (2), which are coupled to a common modulation coil. The FRM may be considered as a phase modulation technique because the rf-SQUIDs have a periodic response, in which case the input signal determines the instantaneous phase of the periodic response to the flux ramp. If the rf-SQUIDs response is essentially

sinusoidal it may also be considered a frequency modulation technique. Each resonator affects its corresponding RF tone, and modulates its phase and amplitude depending on the absorbed electromagnetic radiation by the detector. In Figure 3.8 the natural state of the system is represented by the red curve, while the blue curve shows an state where an event in a sensor occurred, generating $\Delta\varphi$.

At the output of the μ MUX the same microwave multi-carrier signal appears but with each component modulated in phase and amplitude by each detector [3](#). The challenge in these kind of setups is the recovery of the different $\Delta\varphi$ (one for each detector) from this signal. The μ MUX allows the read-out of large arrays of cryogenic sensors [\[24, 46, 64, 107, 108\]](#).

Chapter 4

Data Acquisition Architecture

Working with a μ MUX requires the generation of a multi-tonal microwave frequency signal. These devices operate within a cryostat, maintaining temperatures below 100 mK. They require a carrier power input signal ranging from approximately -70 to -80 dBm per channel [109, 110], and span in the 4 to 8 GHz frequency range. The signal generated in the digital back-end undergoes considerable attenuation. Current research efforts in the field of μ MUXs are shifting the operational region toward higher frequencies for two primary reasons: 1) noise reduction and 2) increased integration, achieved by adding more resonators in closer proximity to each other. Conversely, within room temperature electronics, endeavors focus on minimizing the number of components required to enhance electronic integration. These efforts are driving research areas such as direct synthesis and direct conversion [111, 112]. The fundamental topology for μ MUX readout comprises a high-frequency converter board (employing mixers for upward and downward frequency translation), digital converter devices (including DACs and Analog-to-Digital Converter (ADC)s), and a digital backend responsible for signal generation and pre-processing of the digitized signal from the ADC. The central component of the digital backend is a System-on-Chip (SoC) device equipped with a micro-processor (μ P) and an Field Programmable Gate Array (FPGA).

4.1 Noise in the DAQ system

For the understanding of the following chapters it is important to know how the noise in the digital backend was studied, in terms of the quantization noise, in order to achieve a proper word length in every stage of the acquisition chain.

4.1.1 Quantization Noise

The process of converting a continuous-valued signal into a discrete-valued signal is known as quantization, essentially an approximation process that can be achieved through rounding or truncation [113]. This task is facilitated by an ADC, and it can be conceptually split into three key steps: sampling, quantization, and codification, see Figure 4.1. In the initial step, the conversion from a continuous-time signal to a discrete-time signal occurs,

adhering to the Nyquist-Shannon sampling theorem [114–116]: $f_{max} \leq F_s/2$, where F_s refers to the sampling frequency. Quantization takes place in the second step, assigning a discrete digital value to the sampled data. Each sample value is represented by a selection from a finite set of possible values, for example, 256 possible values for an 8-bit ADC. Finally, in the third step, the discrete value derived from the quantization process is translated into an N-bit binary sequence [113, 117].

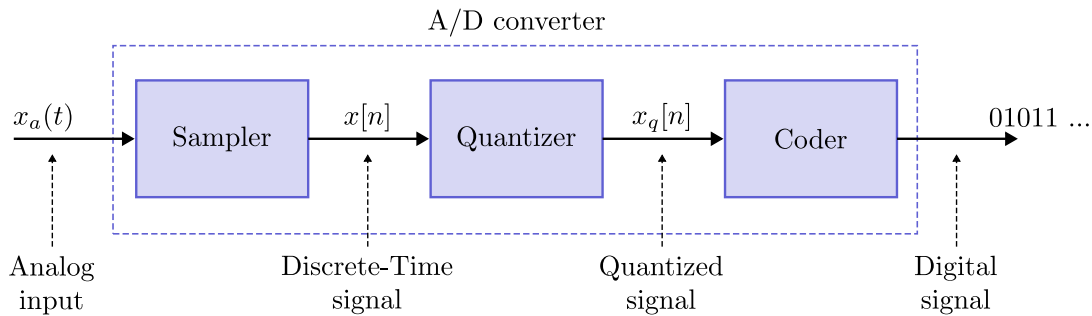


Figure 4.1: Basic ADC conversion steps.

During the quantization process, there will be a difference between the quantized output and the unquantized input value, and this difference is called *quantization error* and, consequently, will be associated with a quantization noise. Denoting $x_q[n]$ as the quantized samples of an input sequence $x[n]$, the error of the quantization procedure can be defined as follows:

$$e_q[n] = x_q[n] - x[n] \quad (4.1)$$

The values allowed in the digital signals are called quantization levels, and the distance between two consecutive quantization levels is called resolution, q . The quantization error, then, is limited to the interval:

$$-\frac{q}{2} \leq e_q[n] \leq \frac{q}{2} \quad (4.2)$$

We can calculate the variance, mean-square error power P_q , of (4.1) assuming a uniformly distributed probability density function, f_{e_q} over a quantization step q [118]:

$$P_q = E\{e_q^2(t)\} = \int_{-\infty}^{\infty} e_q^2 \cdot f_{e_q} de_q = \frac{1}{q} \int_{-q/2}^{q/2} e_q^2 de_q \Rightarrow E\{e_q^2(t)\} = \frac{q^2}{12} \quad (4.3)$$

Quantization is an irreversible process because all samples that are in a distance $q/2$ about certain quantization level are assigned the same value [113]. Unfortunately, the quantization process of an analog signal results in an inevitable loss of information, but always fulfilling the Quantization Theorem [117]. This, in consequence, makes the analysis of the quantization noise extremely difficult. However, a sinusoidal signal can be used for performing an analysis, which provides accurate results for most practical purposes [113, 117, 119, 120]. A key point is that the quantization noise is approximately Gaussian and spread more or less uniformly over the Nyquist bandwidth (DC to $F_s/2$, with F_s the

Sampling Frequency), assuming that the noise is uncorrelated to the input signal. Even though that under certain conditions the quantization noise becomes correlated (when the sampling clock and the signal are harmonically related) and the energy is concentrated at the harmonics signal, the Root-Mean-Squared (RMS) value of the this noise remains approximately: $q/\sqrt{12}$. Therefore the analysis performed so far is based in the following assumptions [121]:

1. The error sequence $e_q[n]$ is a sample sequence of a stationary random process,
2. the error sequence is uncorrelated with the sequence $x[n]$,
3. the random variables of the error process are uncorrelated, thus the error is a white-noise process as was previously described,
4. the probability distribution of the error process is uniform over the range of quantization error.

The theoretical Signal-to-Noise Ratio (SNR) is now calculated with a full-scale sinusoidal signal:

$$x(t) = A \sin(2\pi ft) \rightarrow P_x = \frac{1}{T} \int_0^T x(t)^2 dt = \frac{A^2}{2} \quad (4.4)$$

with A the full-scale amplitude and P_x the signal average power. The quantization noise power will be determined considering a quantizer that has N bits of accuracy and that covers the entire range of $2A$ giving a quantization step of $q = 2A/2^N$:

$$P_q = \frac{q^2}{12} = \left(\frac{2A}{2^N}\right)^2 \cdot \frac{1}{12} \Rightarrow P_q = \left(\frac{4A^2}{2^{2N}}\right) \cdot \frac{1}{12} = \frac{A^2}{3 \cdot 2^{2N}} \quad (4.5)$$

Finally, the SNR defined as the quotient of signal power and noise power in:

$$\text{SNR} = \frac{P_x}{P_q} = \frac{A^2}{2} \cdot \frac{3 \cdot 2^{2N}}{A^2} = \frac{3 \cdot 2^{2N}}{2} \quad (4.6)$$

The SNR expressed in dB is:

$$\text{SNR}|_{\text{dB}} = 10 \log_{10} \left(\frac{3 \cdot 2^{2N}}{2} \right) = 10 \log_{10} \left(\frac{2}{3} \right) + 10 \log_{10} (2^{2N}) \quad (4.7)$$

$$\text{SNR}|_{\text{dB}} = 1.76 + 6.02N \quad (4.8)$$

If the signal of interest is contained in a smaller bandwidth B than the Nyquist bandwidth and a digital filtering is carried out to filter noise components outside of this smaller bandwidth B (see Figure 4.2), then a correction factor denominated *process gain* has to be included and must be applied to (4.8) [120]:

$$\text{SNR}|_{\text{dB}} = 1.76 + 6.02N + 10 \log_{10} \left(\frac{F_s}{2B} \right) \quad (4.9)$$

The process of sampling a signal at a rate greater than twice its bandwidth is often referred to as *oversampling*.

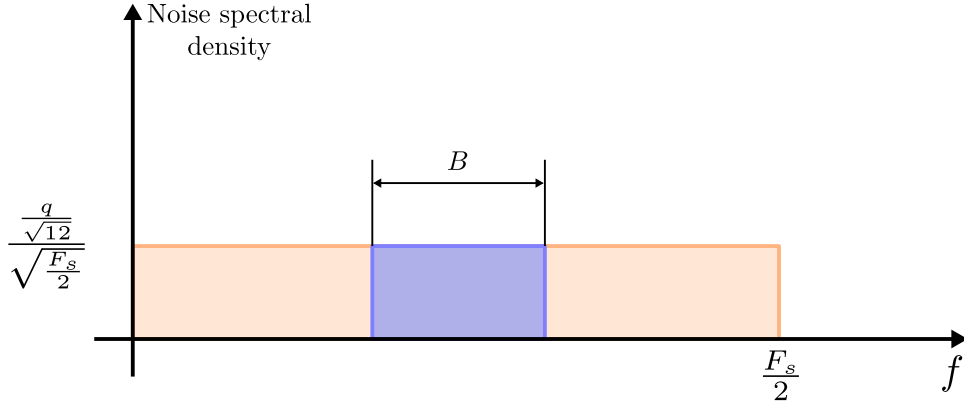


Figure 4.2: Quantization noise spectrum, for a sampling frequency F_s and a signal bandwidth B . The noise is measured over the full Nyquist bandwidth (DC to $F_s/2$). The noise RMS value is $q/\sqrt{12}$.

As was explained in Section 3.4, the monitoring of the μ MUX is carried out using multi-tonal signals. This topic will be properly addressed in chapter 7, but the SNR of the system is drastically affected by the number M of tones in the input multi-tonal signal. Formula (4.9) can be rewritten in terms of the crest factor (k_s) (defined as a signal's peak value and the RMS value ratio) and the number of bits N [122]:

$$\text{SNR}\Big|_{\text{dB}} = 4.771 + 6.02N + 10 \log_{10} \left(\frac{F_s}{2B} \right) - 20 \log_{10}(k_s) \quad (4.10)$$

Applying some algorithm to diminish k_s or Peak-to-Average Power Ratio (PAPR) (defined as a signal's peak power and the average power ratio) according to [122, 123] will improve the SNR. In the case no optimization is performed, $k_s = \sqrt{2M}$ yielding to the expression:

$$\text{SNR}\Big|_{\text{dB}} = 4.771 + 6.02N + 10 \log_{10} \left(\frac{F_s}{2B} \right) - 20 \log_{10} \left(\sqrt{2M} \right) \Rightarrow \quad (4.11)$$

$$\Rightarrow \text{SNR}\Big|_{\text{dB}} = 4.771 + 6.02N + 10 \log_{10} \left(\frac{F_s}{2B} \right) - \underbrace{10 \log_{10}(2)}_{\sim 1.76} - 10 \log_{10}(M) \Rightarrow \quad (4.12)$$

$$\Rightarrow \text{SNR}\Big|_{\text{dB}} = 6.02N + 1.76 + 10 \log_{10} \left(\frac{F_s}{2B} \right) - 10 \log_{10}(M) \quad (4.13)$$

Formula (4.13) also applies for DACs, but without the *process gain* term:

$$\text{SNR}\Big|_{\text{dB}} = 6.02N + 1.76 - 10 \log_{10}(M) \quad (4.14)$$

4.1.2 Aperture Jitter

Aperture Jitter, also known as aperture Uncertainty, is the sample-to-sample variation in the encoding process. It can contribute to three different effects that reduce system performance: increase system noise, increase the error vector magnitude and heighten the Inter-Symbol-Interference (ISI) [124]. Considering an input signal:

$$v(t) = A \sin(2\pi ft) \Rightarrow \frac{\partial v(t)}{\partial t} = 2A\pi f \cos(2\pi ft) \quad (4.15)$$

The maximum error occurs when the cosine is equal to 1 (at $t = 0$):

$$\left. \frac{\partial v(t)}{\partial t} \right|_{max} = 2A\pi f \Rightarrow dv(0) = 2A\pi f dt \rightarrow v_{err} = 2A\pi f t_a \rightarrow v_{err} \Big|_{rms} = \frac{2A\pi f t_a}{\sqrt{2}} \quad (4.16)$$

Then the SNR is degraded to:

$$\text{SNR} = \frac{A}{\sqrt{2} v_{err} \Big|_{rms}} \Rightarrow \text{SNR} \Big|_{dB} = 20 \log_{10} \left[\frac{A/\sqrt{2}}{2A\pi f t_a/\sqrt{2}} \right] \Rightarrow \quad (4.17)$$

$$\Rightarrow \text{SNR} \Big|_{dB} = -20 \log_{10}(2A\pi f t_a) \quad (4.18)$$

This last formula shows that depending on the final application of the system, the aperture time uncertainty takes a critical role in the system's performance [120].

4.2 Channelization of Wideband Signals

For FDM multiplexing schemes, digital channelization is a critical step in warm readouts for cryogenic applications as it makes wideband signal processing possible. Different techniques were designed, in order to solve the problems of signal attenuation at sub-band edge, spectral leakage and aliasing effects. The most implemented approaches are based on Polyphase Filter Banks (PFBs) [110, 118, 125–127] in its Critically Sampled (Critically Sampled Polyphase Filter Bank (CS-PFB)) version or Overlap (Over Sampled) (Over Sampled Polyphase Filter Bank (OS-PFB)) version; either implemented by classical HDL design [118] or using High-Level Synthesis (HLS) [127]. Another common method is based in a multi channel Digital Down Converters (DDCs) [128].

The main core of any of the aforementioned methods and cited works is some application of Fourier Theory and in particular, the Fast Fourier Transform (FFT). The DDC topic is addressed in more detail in chapter 5 as it is part of this Thesis work.

A channelizer is a system that takes a signal consisting of several frequency components (FDM scheme), or channels, and generates output signals corresponding to each channel converted to baseband. This channel *split* requires isolating adjacent channels from each other and suppressing the noise from other frequency ranges. This can be achieved by digital filters with high selectivity and order. However, this has to be carefully done because the higher the order, the more resources and/or multiplications are

required. Therefore, the channel separation must be optimized in order to achieve a scalable approach.

In Digital Signal Processing (DSP) filtering can be performed by two different types of filters: Finite Impulse Response (FIR) filters and Infinite Impulse Response (IIR) filters [113]. The FIR filters depend on a finite number of input values because of the finite number of coefficients. In contrast, the IIR filters achieve its response through the feedback of the output values. This recursive characteristic in the filter response of an IIR filter enables a frequency-selective filter with comparatively few multiplications and thus high resource efficiency consumption. However, IIR filters are generally avoided due to the nonlinear phase characteristics which distort the signal, but there are cases where the phase characteristic in the pass-band of the filter can be well controlled, especially if the pass-band is very narrow. In this case, it might suffer more from stability problems than those with a wider pass-band. Due to all of these, the FIR filters are more generally chosen, because of the linear phase and its natural stability [129].

FIR filters consist of a finite number of coefficients, K , and a digital structure that processes a corresponding number of input samples of a sequence $x[n]$, performing the discrete convolution between the input signal and its impulse response $h[n]$ [113]:

$$y[n] = \sum_{k=0}^{K-1} h[k] \cdot x[n - k] \quad (4.19)$$

In a FDM scheme it is necessary to extract a narrowband signal from a broadband spectrum, thus if all foreign signal components can be removed by filtering, the sampling rate can be reduced without aliasing effects. Moreover, if the ratio between the input spectrum and the signal bandwidth is large enough, FIR filters with many filter coefficients must be used to achieved the necessary selectivity. An efficient approach is the use of multirate filters like the polyphase FIR filter, which can be used for low-pass filtering and decimation [130, 131].

If the output signal $y[n]$ is decimated by a factor M , the subsampled output signal will be [113]:

$$v[m] = y[mM] = \sum_{k=0}^{K-1} h[k] \cdot x[mM - k] \quad (4.20)$$

And this addition can be rewritten in the form:

$$v[m] = \sum_{i=0}^{M-1} \sum_{k=0}^{K/M-1} h[kM + i] \cdot x[mM - (kM + i)] = \sum_{i=0}^{M-1} v_i[m] \quad (4.21)$$

Finally, the filter's transfer function $H(z)$ can be written as [132]:

$$H(z) = \sum_{i=0}^{M-1} z^{-i} \sum_{k=0}^{K/M-1} h[kM + i] z^{-kM} \quad (4.22)$$

where z the complex variable of the Z-Transform (the conversion of discrete-time signals into the complex frequency-domain). This results in M sub-filters as an inner summatory, whose output is added by an outer addition. The Polyphase Channelizer, the channelization process using PFB, consists of an extension of the polyphase FIR filter with a mixing operation using a DFT and its functionality is vastly explained in many sources [113, 131–133]. An extremely efficient implementation of a PFB channelizer can be found in Karcher’s thesis [118].

At this point, it is evident that channelization techniques used in a FDM system are an efficient approach for conducting a wideband FFT on smaller sections of the input bandwidth. These techniques demonstrate a clear and objective means of achieving this goal. The different named methods so far (PFB, DDC, direct FIR) or others based on direct DFTs by means of FFT algorithms, were designed to solve problems like signal attenuation at sub-band edge, spectral leakage, aliasing effects, among others [134]. Even though these methods are found to be really effective and very efficiently implemented in hardware in cases like the PFB, they might lack of flexibility regarding on how much re-configurable are in run-time. The FIR filters have a fixed length once they are synthesized and implemented in hardware. One example arises from analysing the situation in which a cryogenic experimental setup houses more than one μ MUX (connected by a cryogenic switch) like the one described in section 3.4. Certainly, the resonance frequency might change, or in a more extreme situation, have the double of channels. The aforementioned methods would face a scenario hard to solve, and in almost all cases will require a re-design, re-synthesis, and re-implementation in hardware, which takes a long time in large designs. Moreover, the controlling of the spectral leakage is not so well addressed as the baseband translation of each channel is not perfect in this approaches.

Another approach, also based on Fourier, would consist in single tone detection. Historically speaking, single tone detection was widely used for telecommunications: Dual-Tone Multi-Frequency (DTMF) was for several years the telecommunication signaling system used all around the world; of course, until it was dethroned by digital telecommunication systems. DTMF was originally decoded by a set of filter banks until digital signal processing became the predominant technology for decoding. Here methods like the Goertzel Algorithm [47], Multiple Signal Classification (MUSIC) [135, 136] or Estimation of Signal Parameters via Rotational Invariant Techniques (ESPRIT) [136], among others, started to be applied for carrying this detection tasks.

The Goertzel Filter enables the calculation of a single bin of a signal’s DFT, and can be represented by a 2nd order IIR filter. In principle, using this filter it would be possible to address the different problems that were previously enumerated: i) the frequency-selective characteristic of an IIR filter combined with the use of window functions, helps to mitigate the spectral leakage problems, ii) the low number of required variables (coefficients) in order to perform the single-bin DFT calculation enables an easy to solve hardware implementation for run-time re-configuration. In chapter 6, an in-depth exploration of the suitability of the Goertzel Filter for signal demodulation in an FDM system is undertaken. In chapter 8, its implementation is addressed.

4.3 System-On-Chip Architectures

The methods described so far for the specific application of multi-tonal signal processing are computationally intensive. Digital signal processing filters and algorithms require digital logic capable of fast parallel computation. Processors are less suitable for high continuous data rates and sample-by-sample processing [137]. Digital logic allocated in FPGAs can be used for this application, as it provides a large number of processing units for DSP tasks and can be flexibly interconnected. In contrast, calibrations that require control flow and complex evaluation can be more easily performed by a μP , and an FPGA is not suitable for this task. A brief presentation of AMD's heterogeneous SoC architecture is given below. This architecture integrates both an FPGA, a μP and in other cases also include A/D converters.

The Multiprocessor System-on-Chip (MPSoC) [138, 139] and the Radio Frequency System-on-Chip (RFSoc) [140] are two of the current workhorses of AMD's SoC chips, as they deliver high integration level and great performance characteristics. These devices can be split in two main parts: the Processing System (PS) and the Programmable Logic (PL), see Figure 4.3. The PS might house, depending on the chip grade and series, a Dual-core or Quad-core ARM Cortex-A53 64-bit superscalar application processor in the case of the MPSoC, and a Quad-core ARM Cortex-A53 in the RFSoc case. The Cortex-A53 cores use the ARM-v8-A instruction set and is normally clocked at 1.5 GHz. The PS also has a Dual-core ARM Cortex-R5F 32-bit real-time processor, using ARM-v7 instruction set with a dedicated tightly couple memory (TCM). It also provides a Mali-400 graphics processing unit (GPU), with pixel and geometry processor, and 64 KB L2 cache (for the EG and EV MPSoC devices).

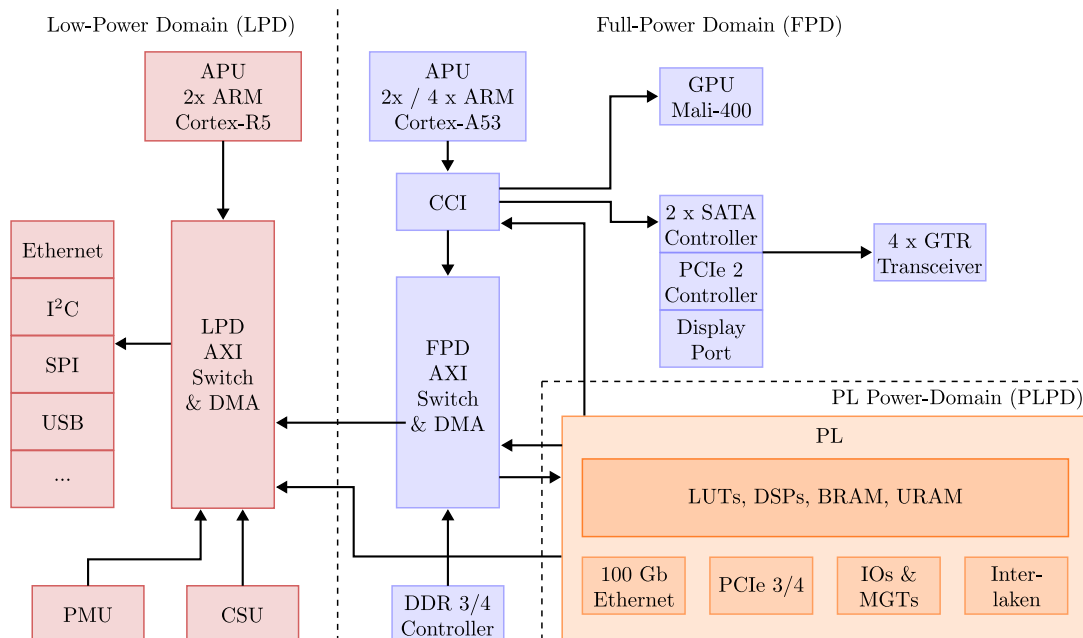


Figure 4.3: MPSoC and RFSoc simplified block diagram of the PS and PL regions [118, 139].

There are four main power domains: Low-Power Domain (LPD), Full-Power Domain (FPD), PL Power Domain (PLPD), and Battery Power Domain (BPD). Each power domain can be individually isolated. The Platform Management Unit (PMU) on the LPD, facilitates the isolation of each of the power domains.

The processor is connected to a Cache Coherent Interconnect (CCI), which is also coupled to other bus masters, such as the SATA3 controllers, the PCIe 2.1 controller, and the Mali-400 GPU. From there, the processor and the other devices can make use of the address-based AXI4 bus to access to the FPD switch, which is connected to the Double Data Rate (DDR) controller, among other things. The DDR controller supports up to 34 GB DDR3 and DDR4 memory. The FPD switch connects the processor to the PL and to the LPD [139].

On the other hand, the PL side consists of a Zynq UltraScale+ series which are high-end FPGAs. FPGAs are user-programmable circuits, which consists of universal smaller primitives: the Configurable Logic Block (CLB), which include Look-Up Table (LUT) and Flip-Flop (FF). These elements can be combined (or interconnected) to form a more complex circuit using configurable switching matrices. Depending on the FPGA version and series it might include very powerful elements known as Digital Signal Processing (DSP) Slices [141, 142], DSP Slice hereinafter, which extend the capabilities of the FPGA to perform complex arithmetic calculations. The DSP Slices can perform fast addition, multiplication and accumulation (like the MACC instructions of a typical DSP processor, for example the Analog Devices Blackfin processors). In particular, the DSP48E2 [142] version is available in the Zynq UltraScale+ series, an improved version of the DSP48E1 [141]. It consists of four registered input ports, a 27-bit pre-adder, a 27 x 18 two's complement multiplier, a 48-bit accumulator that can be cascaded to build a 96-bit and larger accumulators, adders, and counters; a 48-bit logic unit, and a pattern detector, among other features, see Figure 4.4.

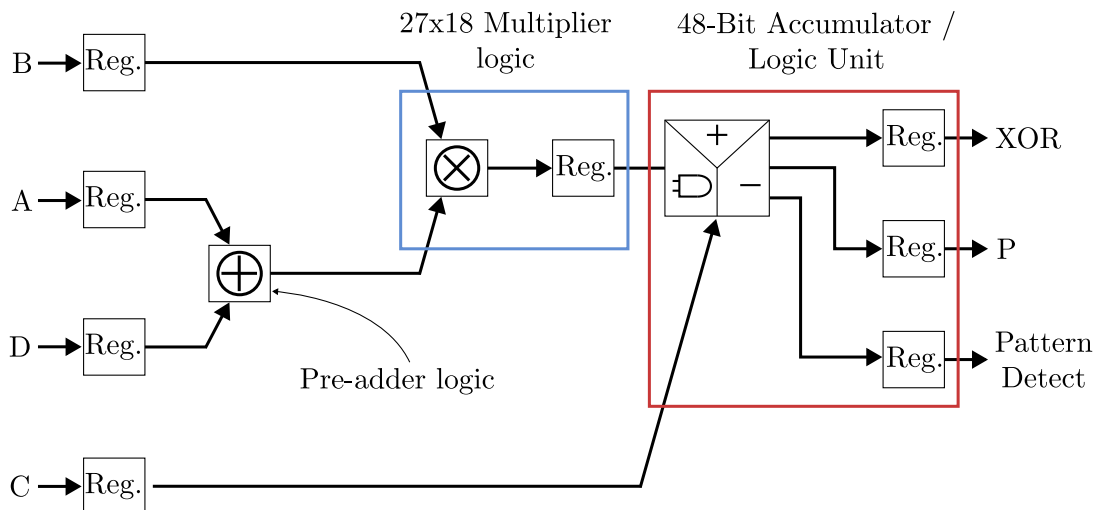


Figure 4.4: DSP48E2 Slice schematic and basic functionality.

There is also a so-called block RAM (BRAM), which allows data to be temporarily

stored after processing or passed between two clock domains. Larger IP Cores are available like for PCIe and Ethernet. The PL can be connected to external components via IO Blocks (IOBs). It can be possible to choose between different standards, such as LVCMOS or LVDS [143]. The maximum speed for these banks is in the range from 0.5 to 2 Gbit [144]. The option of using high-speed transceivers is available and depends on the Zynq model, up to 16 Gbits⁻¹ through GTH transceivers [145], and up to 30 Gbits⁻¹ through GTY transceivers [146].

In the case of the RFSoc, it also integrates key subsystems which include, a Soft-Decision Forward Error Correction (SD-FEC) engine and up to 16 channels of 14-bit RF-ADCs and 14-bit RF-DACs. The RF-ADCs can sample input frequencies up to 4 GHz at up to 4.096 Gsps. The RF-DACs generate output carrier frequencies up to 4 GHz using the 2nd Nyquist zone at 6.554 Gsps, see Figure 4.5. The RF data converters also include DDCs and Digital Up Converters (DUCs), with programmable decimation and interpolation ratios, Numerical Controlled Oscillators (NCOs), and complex mixers. They also support dual-band operation [139, 147].

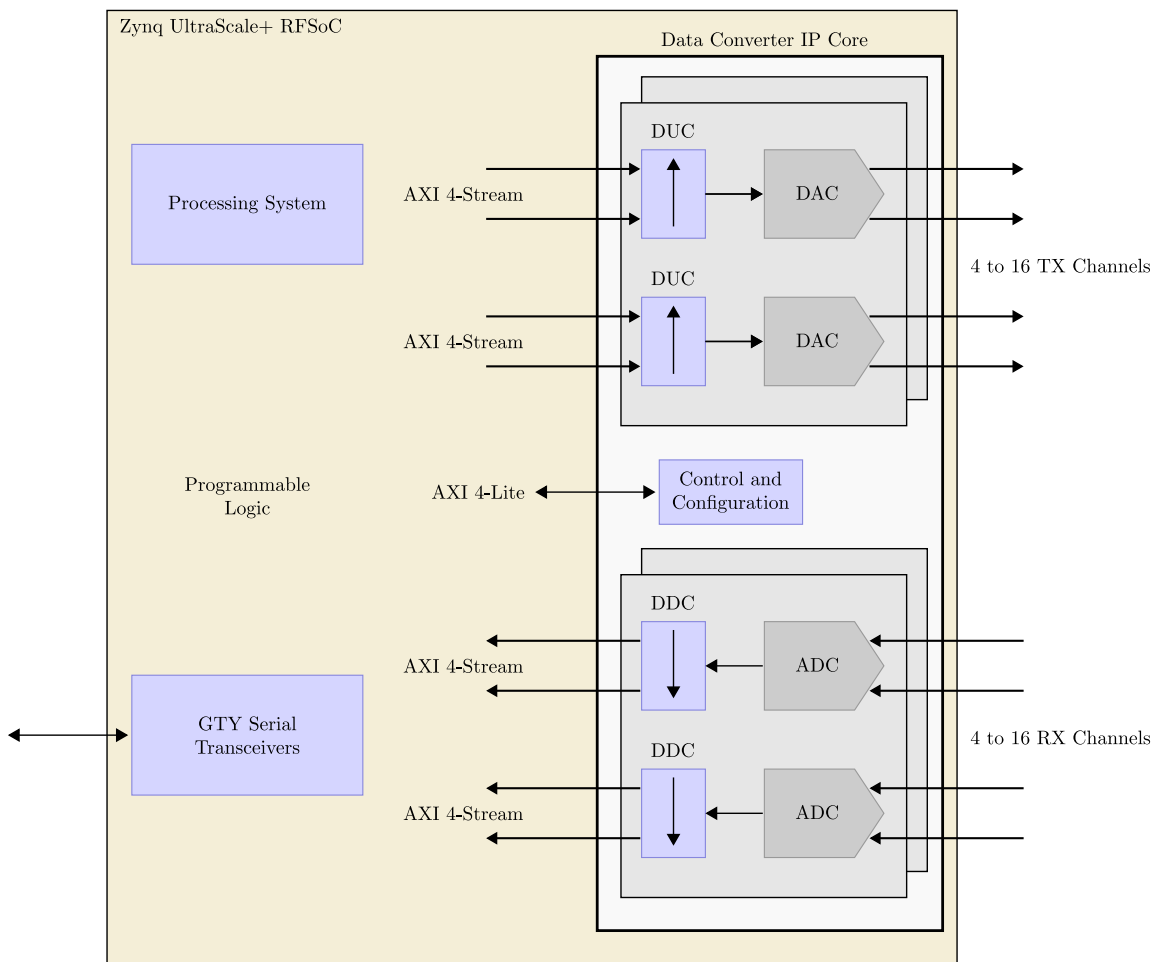


Figure 4.5: RFSoc RF Data Converter [147]. Each DAC and ADC symbol represents two of them (therefore the two arrows).

4.4 Proposed Data Acquisition system

Reading sensors that are multiplexed in the frequency domain requires the generation of multi-tonal signals in the microwave range (2 and 3). A Software-defined Radio (SDR) system is required for carrying out this intricate task. A SDR system is able to generate and digitize broadband analog signals and process them accordingly. This is a good moment to point out a difference between Software-defined Radio and Software Radio (SR) before continuing. SR is a device in which the digitization occurs, in the receiver, before the intermediate frequency (IF) down-conversion stage; with the terminology of software radio denoting a completely reconfigurable radio that can be programmed in software and its physical layer behavior can be significantly changed through software changes. SDR is a device in which digitization of the data is performed, in the receiver, after wideband filtering, low noise amplification, and down conversion to an IF [148, 149].

The basic elements of an SDR system are a so called radio-frequency front-end (RF front-end) which performs the tasks of signal up-conversion and down-conversion (the translation from baseband (BB) to the microwave range and vice-versa), spectrum splitting and merging. DAC and ADC converters which basically communicates the digital domain with the analog domain; and the digital electronics where the intensive processing occurs and that can be an FPGA, an Application Specific Integrated Circuit (ASIC) or a μP .

A very conceptual diagram for the read-out of cryogenic sensors multiplexed in the frequency domain by means of a μMUX with a SDR system is sketched in Figure 4.6 (a more detailed sketch of the cryogenic setup will be shown in chapter 9).

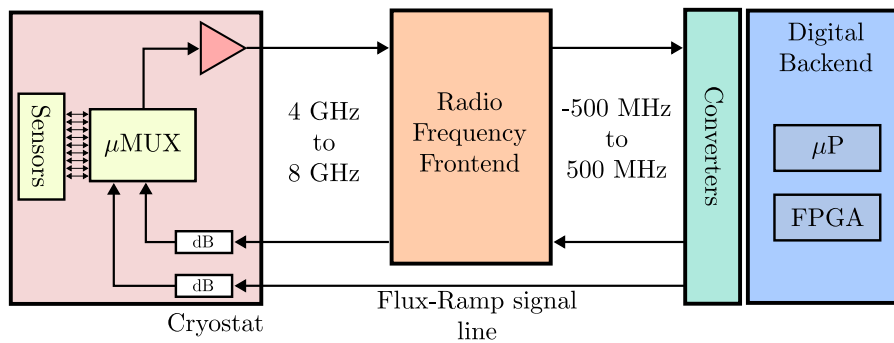


Figure 4.6: The read-out system. The cryostat consists of different temperature stages, not sketched in this diagram. The Low-Noise Amplifier (LNA), represented by the red triangle, works in the 4 K stage. The μMUX and the sensors are operating in the lowest temperature stage.

The transmission path must introduce some attenuators in order to condition the input signal to the μMUX requirements (typically between -70 dBm and -90 dBm [46, 99, 110, 150]). A cryogenic LNA is placed in the 4 K stage for conditioning the very attenuated signal before returning it to the RF front-end. The operating region for the μMUX falls within the range between 4 GHz and 8 GHz [46, 99, 109, 110, 118, 150, 151]. The sawtooth signal that realizes the flux-ramp modulation required for the μMUX is

generated by the digital back-end (without requiring frequency translation). Ideally, as remarked in [118] this signal should be generated by the readout system simplifying the synchronization, specially in the demodulation procedure. This idea will be clarified with the presented results in chapter 9.

This work is involved in two major projects, QUBIC and ECHo, as it was introduced in chapter 1 and thus focused on them. The detectors' signals to be processed are very different (see sections 2.4.3 and 2.4.4), especially in the frequency content. For ECHo, the readout system is already well established and this Thesis will contribute in potential firmware improvements. QUBIC is designed to operate with two focal planes, each equipped with 1024 cryogenic bolometers. The current technology employed by QUBIC centers in TES channels which are read-out in TDM [42]. Therefore, the introduction of MMBs represents a totally disruptive approach from the existing design. As a result, a new suite of electronics must be developed to support the MMBs. Given that the state-of-the-art bandwidth for μ MUXs is 4 GHz, the channel spacing would be approximately 3.9 MHz. This requires the creation of a set of cold and warm electronics. Additionally, synchronization with a GPS signal is required for positioning and acquisition, including timestamp values.

4.5 Hardware prototype selection

4.5.1 Available hardware

Several works exist for bolometric applications of TESs and MKIDs [27, 107, 151], and for their calorimetric applications [152, 153]. In the last year, an ad-hoc read-out for MMCs also emerged [118] with a newer generation of electronics. Even though first MMBs prototypes will appear the next year, it is fundamental to have an ad-hoc read-out for them too, which also allows the reading of several sensors (as required by CMB experimental projects). The ECHo read-out was, in principle, specifically designed for MMCs readout (in particular, targeting thousands of them). As MMBs share the same fundamental working principle (the paramagnetic sensor), and therefore, similar multiplexing requirements, the ECHo read-out electronics is a feasible and reliable hardware for being used and applied for MMBs read-out. However, two issues arise: firstly, the firmware needs to be conditioned for the acquisition and processing of the extremely weak and slow signals of QUBIC; and secondly, there is still no available definitive set of electronics.

The RFSoc architecture described in section 4.3 appears as an excellent alternative for combining the digital backend, the converter board and the removal of the first conversion stage of the RF front-end (see section 4.5.4) of the read-out system in Figure 4.6. By the time this Thesis started, only the Gen 1 architecture was released. There are a few works related with the readout of Quantum Bits (Qubits) using Gen 1 and 2 of the RFSoc architectures [154–156], and some related work for MKIDs [127]. However, Gen 3 was released during the third quarter of 2020, and the evaluation for the suitability of the RFSoc's RF converters for bolometric and calorimetric applications is still an open research topic, exceeding the scope of this work. Even though RFSoc Gen 3 seems to

be a strong candidate for the future of the read-out electronics for cryogenic bolometers and calorimeters, the hardware selection was done by technology maturity.

4.5.2 Digital electronics

In view of this scenario, the decision was made to opt for AMD's ZCU102 board. This board is equipped with the MPSoC Zynq UltraScale+ ZU9EG device, features two FMC+ connectors, an Ethernet connection, and more. Indeed, this specific evaluation board can be traced back to as the very starting point of the ECHo SDR project [118]. The compatibility between the characteristics of the ZU9EG, the features of the ZCU102 board and the project's requirements have led to the selection of the ZCU102 for prototyping (see Figure 4.7).



Figure 4.7: Selected digital electronics for prototyping, AMD's (ex Xilinx) ZCU102 Evaluation board.

4.5.3 AD - DA Converters

The converters board will be the Analog Devices AD-FMCDQA2-EBZ [157] which houses a DAC AD9144 and an ADC AD9680-1000 (see Figure 4.8). The DAC can be operated at up to 2.8 Gsps, has four channels (but two are available in the FMCDQA2 board) and 16-bit resolution [158]. The data are transmitted via eight high-speed connections according to the JESD204B standard at 10 Gbps. They will be configured to sample at 1 Gsps and two Crystek Low Pass Filters of 500 MHz are placed in its corresponding output channels.

The ADC has two channels and samples at 1 Gsps, and it has a resolution of 14-bit [159]. However, depending on the input frequency, it achieves an Effective Number-of-Bits (ENOB) between 10.3 and 10.8 bits. It has four integrated DDCs for pre-processing the incoming data. The available JESD204B standard in the ADC requires four high-speed lines for data transport, operated at 10 Gbps. The useful input bandwidth is roughly 800 MHz when using a decimation ratio by 2, and roughly 770 MHz when decimating by 4.

The clock chip is the AD9523 which have 8 outputs, and sources both converters and the implemented firmware in the FPGA PL side. It also generates the SYSREF signal required by the JESD204B standard for subclass 1 [160].



Figure 4.8: Selected converter board for prototyping: Analog Devices FMCDQA2 evaluation board.

4.5.4 High Frequency electronics

Another vital stage of the SDR system is the frequency translation electronics (see 4.4). This electronics will take the complex BB signals and convert them to the μ MUX frequency operating region. Frequency conversion can be performed either by single-stage IQ mixers or a two-stage superimposed mixer stage [90]. A direct method for the mixing stage is challenging in terms of component tolerances: they can considerably affect frequency-dependent amplitude distortions of all components and the phase imbalance of the mixers. However, a two-stage heterodyne mixer stage which creates an IF band can relax the bandwidth requirements [118] (see Figure 4.9). According to the available last results of [118, 161], the designed RF front-end for ECHO SDR also fulfills the requirements for QUBIC. Thus, this will be the used electronics for the RF front-end with the same strategy: each channel of this high-frequency electronics accepts an input BB frequency of 800 MHz. As a consequence, covering 4 GHz will require a spectrum merge section (and a split section for the receiver part) for five bands.

In this board, the input complex BB is first mixed to an intermediate frequency band from 0.5 to 4.5 GHz, and then converted to the high-frequency region of 4 to 8 GHz. The receiver part performs its counterpart operation. The initial frequency of 0.5 GHz aligns with the lower region of the BB signal: each DAC produces 1 GHz of complex bandwidth, which when shifted by 0.5 GHz, locates it in the appropriate starting region. The same logic applies for the receiver part and the ADC.

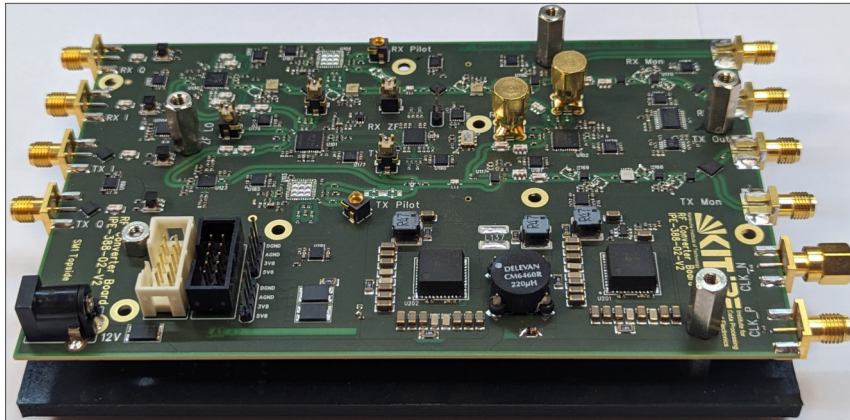


Figure 4.9: ECHO high frequency board [161].

4.5.5 Operative System, software and firmware integration

The warm electronics consists of several distributed acquisition systems, therefore, they have to be controllable remotely. The acquired data will be delivered from the measurement system via a network connection to a remote server. The warm electronics requires, for its functionality, several processes running within the μ P which will be in charge of administrating the whole system. Hence, the integration of firmware and software is not a trivial task. In light of these, the IPE-KIT group developed a set of tools which accomplish this task in a very powerful and versatile manner. It is based in the Yocto Project [162] and a big collection of Python and TCL scripts [118].

For the control of the different modules of the firmware, the ServiceHub environment is used. ServiceHub forms a configurable, modular plugin loader offering a standardized interface for gRPC [163, 164] function registration, logging, health and plugin management. A plugin is an entity for controlling a specific device or software class, including FPGA Intellectual Property (IP) cores with AXI interface, external devices attached to the SoC or even other plugins within the ServiceHub. Examples are manifold, like the control of external bias voltages, a data fetcher using Direct Memory Access (DMA), complex envelope generation or the configuration of FPGA logic [165].



Figure 4.10: Sketch of the basic ServiceHub scheme call hierarchy from user to hardware.

Chapter 5

Digital Down Conversion Stage

The DDC stage facilitates the translation of the targeted frequency band towards the baseband, thereby enabling a reduction in the sample rate. This operation comes with the benefit of reducing the filtering and further processing requirements. When working with complex signals, the DDC frequency domain translation and demodulation into I and Q components of the input signal can be achieved. The basic DDC operation encompasses a two-fold process: a complex mixing stage succeeded by the application of a low-pass filter. In a high level it can be described by the schematic in Figure 5.1 left.

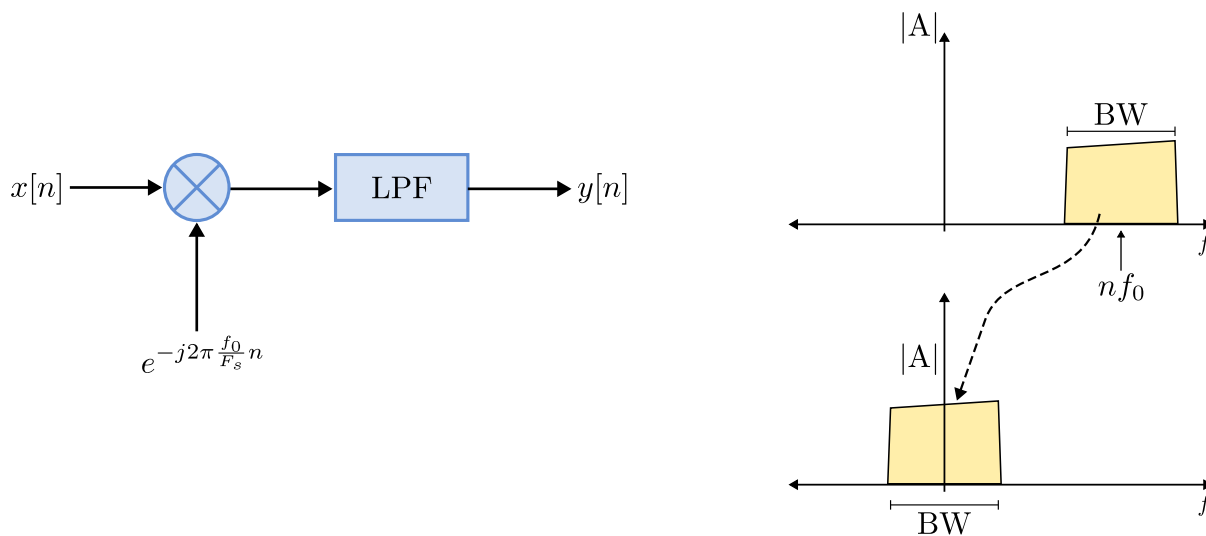


Figure 5.1: Digital Down Converter schematic. $x[n]$ is multiplied by a complex signal with nf_0 , followed by a low-pass filter (LPF) (left). Frequency translation concept performed with a DDC (right).

As the sampling frequency is much higher than the one required for the maximum frequency in the band of interest, it is possible to perform a decimation without incurring any loss of information. In the following sections, the basic concepts for understanding how the DDC was built, accompanied by accurate Python script simulations, are presented. The simulation results in this chapter can subsequently be cross-referenced with

the validation measurements presented in Section 9.1.1.

5.1 CIC - Cascaded Integrator Comb Filter

The Cascaded Integrator-Comb (CIC) filter, is a linear phase FIR filter, composed by three main elements: an integrator circuit, a derivator circuit and a rate changer. It was proposed by Hogenauer [166] as an efficient way to implement digital filters for decimation (Figure 5.2) and interpolation (Figure 5.3), requiring no multipliers and low memory storage. The cascaded integrator stages operate at the high sampling rate, F_s , and the cascaded derivator (comb) stages operate at the low sampling rate, $\frac{F_s}{R}$, where R is an integer rate change factor.

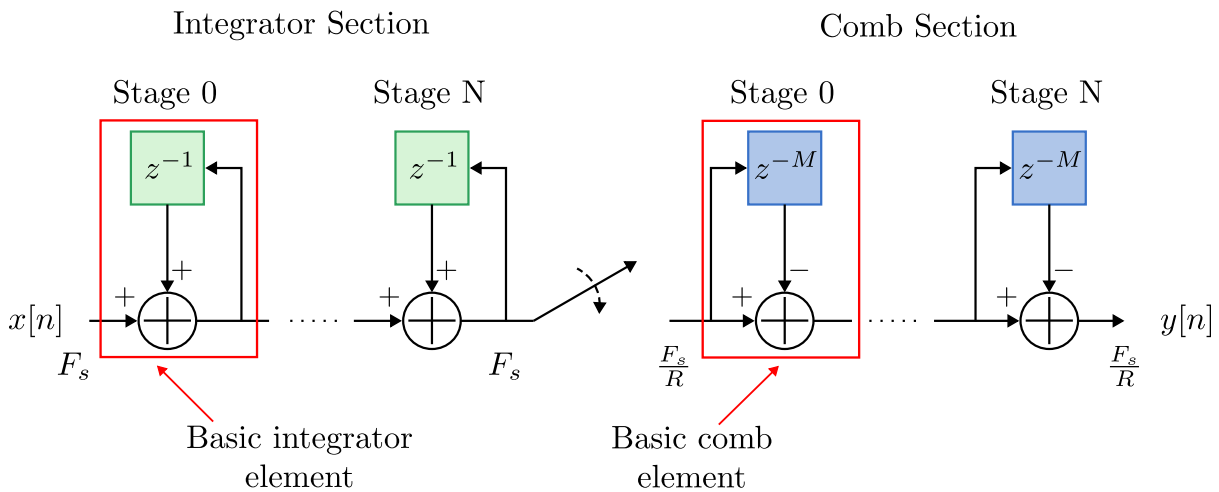


Figure 5.2: CIC decimator filter

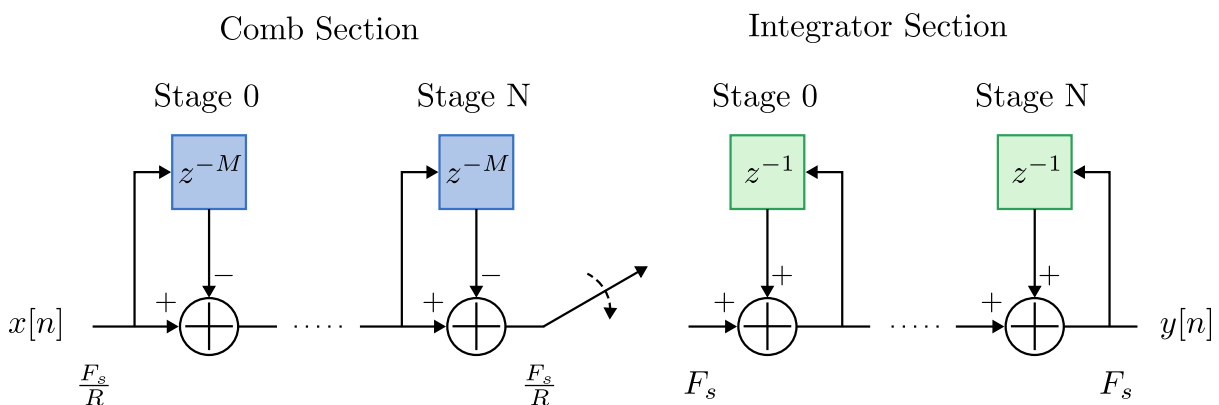


Figure 5.3: CIC interpolator filter

Typical FIR and IIR filters utilize chains of delay, multiplication, and addition elements [113]. The coefficients of the filter must be multiplied with the input value in

each clock cycle. As there are only a finite number of DSP slices on an FPGA, this approach is not adequate for scaling designs. Here is where the CIC filter wins against the classical FIR filters, because it operates with poles and zeros (its coefficients) on the unit circle [166], thereby all of its coefficients have a magnitude of one simplifying multiplications to straightforward additions.

The CIC filter can be adjusted by three parameters: the number of stages N , the decimation ratio R and the delay M in the comb section, which increase the number of zeros in the transfer function leading to an improved attenuation in the stop-band. The transfer function of this filter for one stage only is [166]:

$$\left. \begin{aligned} H_I(z) &= \frac{1}{1 - z^{-1}} \\ H_C(z) &= 1 - z^{-RM} \end{aligned} \right\} \Rightarrow \boxed{H_{CIC}(z) = \frac{1 - z^{-RM}}{1 - z^{-1}}} \quad (5.1)$$

where H_I stands for the integrator stages transfer function, and H_C for the comb stages. Here $H_C(z)$ refers to the high sampling rate region by introducing R . For N stages H_{CIC} becomes:

$$H_{CIC}(z) = \left(\frac{1 - z^{-RM}}{1 - z^{-1}} \right)^N = \left[\sum_{k=0}^{RM-1} z^{-k} \right]^N \quad (5.2)$$

Equation 5.2 depicts the transfer function of the CIC filter. The number of stages and delays modifies the response of the filter. The higher the number of stages, the higher the attenuation for aliasing components. For the purposes of this work, the decimation version of the structure is used. The frequency response is derived by evaluating equation 5.2 with $z = e^{j2\pi f/R}$:

$$H_{CIC}(f) = \left[\frac{\sin(\pi M f)}{\sin(\frac{\pi f}{R})} \right]^{2N} \quad (5.3)$$

The frequency response resembles a sinc(x) function. Figure 5.4 shows the CIC filter response for different numbers of stages and decimation ratios, for an input sampling frequency of 250 MHz. It can be seen that if the CIC filter has a large number of stages, the frequency response will not have a broad and flat pass-band. Although increasing delay in the comb stage improves alias rejection for the same number of stages and decimation ratio, it substantially decreases the useful bandwidth, see Figure 5.5. These problems can be overcome by using an FIR filter, whose magnitude response compensates the CIC filter response. As this FIR filter operates in the low-rate region of the CIC filter, it becomes more efficient in terms of hardware.

One thing that has to be taken into account is the bit growth (accumulator arithmetic register overflow) in the integrators section (unity feedback at each stage). Thus, the bit width must be properly designed to accommodate this situation. The bit growth can be calculated using the following equation [166]:

$$B_{out} = \lceil N \log_{10}(RM) \rceil + B_{in} \quad (5.4)$$

It is possible to perform a pruning (remove some Least Significant bits (LSB)) in the registers width in the different stages at the expense on reducing the precision (increasing the quantization noise) a little [131, 166].

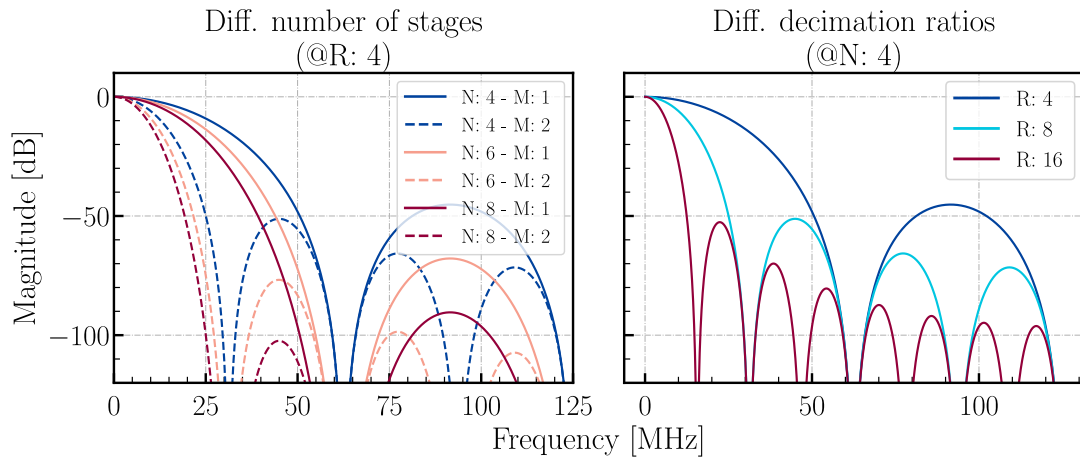


Figure 5.4: CIC filter decimator magnitude frequency response simulation. Different number of stages N (for same decimation ratio) (left). Different decimation ratios R (for the same number of stages and for $M = 1$) (right).

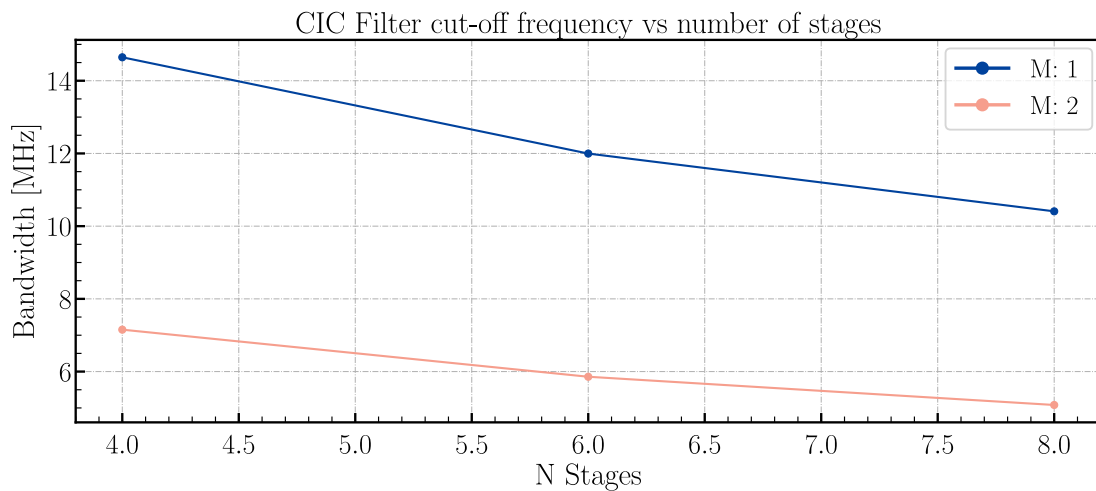


Figure 5.5: CIC filter cut-off frequency vs number of stages, for two different delay values in the comb stage.

5.2 CFIR - Compensation Finite Impulse Response Filter

Is desired in filtering applications to achieve a flat pass-band gain and a narrow transition region width, an ideal brickwall. As seen in the previous section, the early attenuation in

the band-pass of the CIC filter is a problem to be accounted for because it has a natural droop gain in the mainlobe and wide transition regions, as can be seen from Figure 5.4. Improving the transition region with more stages, makes the droop even worse.

To compensate for these effects, it is suggested to use a FIR filter, whose magnitude frequency response is ideally the inverted version of the CIC filter pass-band magnitude response to be compensated. There are many methods for achieving this task, like the ones based on a sharpening technique developed by Kaiser and Hamming [167], for example, the works from Kwentus [168], Stephen [169], or several works from Dolecek like [170–172] (among others). A different approach was proposed by Li [173] implementing the inverse response of the CIC filter.

Kaiser and Hamming (and later used by Kwentus) proposed the realization of the sharpened CIC (SCIC) by using the relationship [167]:

$$H_{\text{SCIC}}(z) = 3H_{\text{CIC}}^2(z) - 2H_{\text{CIC}}^3(z) \quad (5.5)$$

However, the integrators of these implementations of the CIC and the SCIC filters cannot be pipelined because they run at the input sample rate, limiting the speed at which the design can be clocked [169]. Stephen's work starts from factorising equation 5.2 affecting the previous equation 5.5. He proposes a modification for achieving a non-recursive structure more efficient for hardware implementations. The factorisation by 2^p for a decimation factor $R = 2^p F$ is:

$$H_{\text{CIC}}(z) = [H_1(z^{2^p})]^N [H_2(z)]^S \quad (5.6)$$

Where:

$$H_1(z^{2^p}) = \frac{1}{F} \frac{1 - z^{-2^p F}}{1 - z^{-2^p}} \quad (5.7)$$

$$H_2(z) = \frac{1}{2^p} \sum_{i=0}^{2^p-1} z^{-i} \quad (5.8)$$

which yields to the partially sharpened CIC (PSCIC) filter transfer function:

$$H_{\text{PSCIC}}(z) = [H_2(z)]^S [3H_1^{2N}(z^{2^p}) - 2H_1^{3N}(z^{2^p})] \quad (5.9)$$

where N represents the number of sections in the recursive portion of the filter, S is the number of cascades of the non-recursive portion, and p the number of non-recursive separated sections, each decimating by 2. In the PSCIC the integrators run at a speed 2^p slower than those in the SCIC; and in the input, the non-recursive sections can be implemented using the polyphase decomposition which enables high-speed implementations [169]. However, in this approach the compensation of the pass-band droop is performed in the narrow pass-band. The best performance is achieved for high decimation ratios but the best alias rejection ratio is in the order of ~ -62 dB (for $R = 4$) and ~ -59 dB (for R greater than 4).

Dolecek starts from proposing a form of the second-order polynomial interpolation filter, which is based on a sine function. The magnitude frequency response of such filter is:

$$|H(e^{j\omega M})| = \left| 1 + 2^{-b} \sin^2 \left(\frac{\omega M}{2} \right) \right| \quad (5.10)$$

which arises from the following transfer function:

$$H(z^M) = A (1 + Bz^{-M} + z^{-2M}) \quad (5.11)$$

with M the differential delay of the comb section, b is decided by the order of the filter and used to change the extent of the amplitude compensation, $A = -2^{-b-2}$ and $B = -2^{b+2} - 2$. This compensation method improves the previous works results, at the expense of an increased complexity [172].

Finally, Li's work implements the compensation using the inverse response of the CIC filter to compensate. The coefficients of this FIR filter can be determined by the sampling frequency method [174], available in Python and MatLab. This compensation method significantly reduces the pass-band droop and improves the stop-band rejection. Kwentus shown that adding a decimation in the compensation filter, improves the useful bandwidth of the overall response and increases the alias rejection [168]. Thus. the decimation in the compensation FIR filter (which is the second decimation factor in the DDC) determines the frequency at which the worst-case aliasing and the pass-band edge frequency where the worst-case pass-band distortion takes place. This is derived from the following equations:

$$\frac{\omega_c}{\pi} = \frac{1}{NM} \quad (5.12)$$

$$\frac{\omega_a}{\pi} = \frac{2N - 1}{NM} \quad (5.13)$$

where ω_c is the pass-band edge normalized with respect to the the high sampling rate region, ω_a is for the worst-case aliasing, M is the decimation factor of the CIC filter and N is the decimation factor of the compensation FIR filter (the total decimation ratio is $R = NM$). This is the implemented method in this Thesis, introducing a decimation ratio of two in the Compensation Finite Impulse Response (CFIR) filter and taking special care in the order of the filter as it impacts directly in the required hardware resources. Figure 5.6 presents different CFIR frequency responses that vary depending on the number of coefficients for the same number of CIC stages that need to be compensated.

When the quantization is fixed to a 16-bit width for each coefficient, there is no additional improvement in the attenuation and transition region. For example, keeping a 16-bit word width and the alias rejection at 80 dB, it is not possible to achieve a ripple of 0.1 dB when aiming for a sharper transition region. It is important to consider that fewer stages to be compensated will lead to a lower number of taps in the CFIR. However, this comes at the cost of a lower alias rejection. In Figure 5.6 it is possible to appreciate that the aliasing attenuation is limited by the coefficients' quantization.

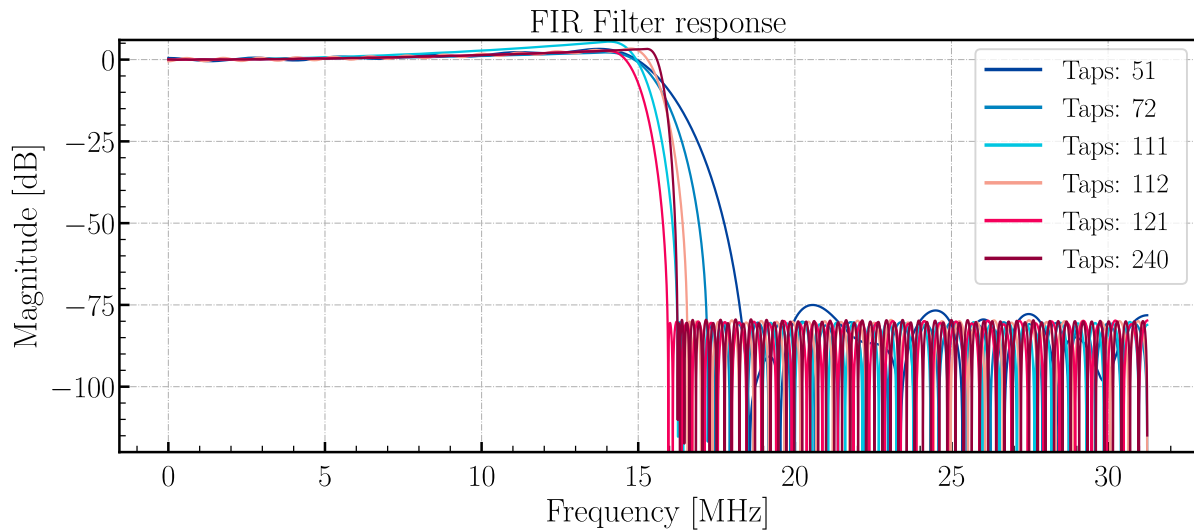


Figure 5.6: Compensation FIR filter for different number of taps and 16-bit width word for each coefficient, aliasing attenuation of 80 dB and decimation ratio of 2.

The frequency response of the CIC and CFIR filters, together with the overall response can be appreciated in Figure 5.7. This result shows that no aliasing component above -80 dB is expected, a good flatness in the pass-band and a useful bandwidth of approx. 94 %.

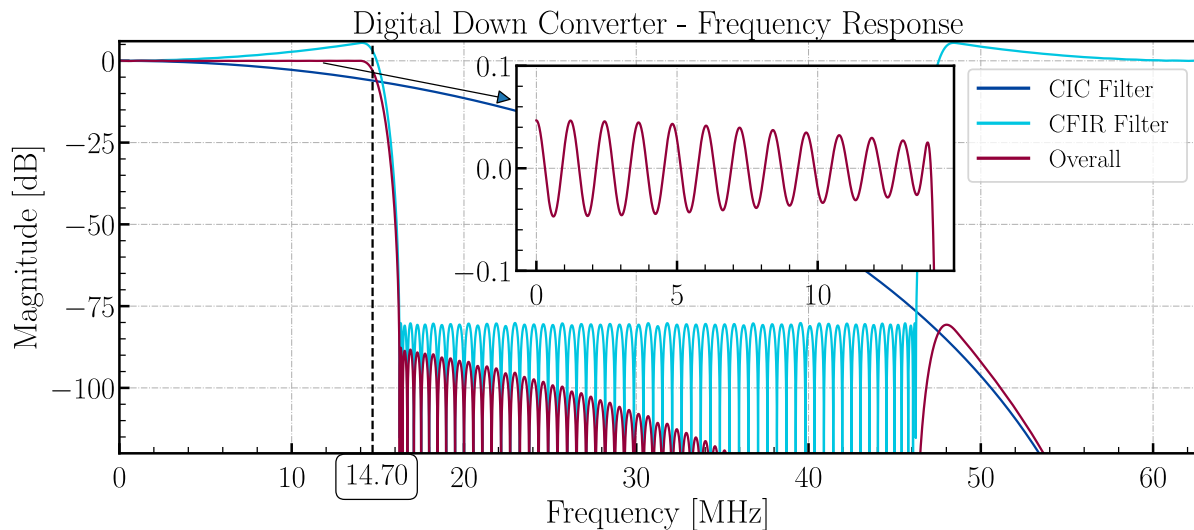


Figure 5.7: Digital Down Converter: python simulated frequency response of the whole filter chain where the CIC, CFIR and overall response are plotted. The 3 dB frequency cut, f_{cut} , marked with the dashed black vertical line is 14.70 MHz. A ripple of less than 0.1 dB can be observed.

The final firmware implementation of the DDC is explained in Section 8.2.2.

Chapter 6

Goertzel Filter Bank Channelizer

In order to fully understand how the proposal of the Goertzel Filter Bank (GFB) Channelizer for the read-out of cryogenic sensors multiplexed in FDM works, it is necessary to start from basic concepts of the Fourier Transform and Discrete Fourier Transform. This will give insight into how the Goertzel Algorithm is derived, following by the IIR filter interpretation of it. An adaptation with different window functions for reducing spectral leakage and improving crosstalk isolation is explained and added to the filter, including the compensation for it. The arithmetic scaling in the algorithm is contemplated. Finally, the mathematical demonstration on how this filter can be used to demodulate the input signals in this kind of systems is presented.

6.1 The Discrete Fourier Transform

The Fourier Analysis can be divided in four groups: continuous-time aperiodic, continuous-time periodic, discrete-time aperiodic and discrete-time periodic. Fourier Series (FS) and the Fourier Transform (FT) are mathematical tools that allows the mapping of a signal (function), from the time domain to the frequency domain and vice versa. The FT can be applied to continuous-time aperiodic signals, while for continuous-time periodic signals the FS is used.

	$\mathcal{F}\{\}$	$\mathcal{F}^{-1}\{\}$
FT	$X(\omega) = \int_{-\infty}^{+\infty} x(t)e^{-j\omega t} dt$	$x(t) = \frac{1}{2\pi} \int_{-\infty}^{+\infty} X(\omega)e^{j\omega t} d\omega$
	$X(f) = \int_{-\infty}^{+\infty} x(t)e^{-j2\pi ft} dt$	$x(t) = \frac{1}{2\pi} \int_{-\infty}^{+\infty} X(f)e^{j2\pi ft} df$
DTFT	$X(\omega) = \sum_{n=-\infty}^{+\infty} x[n]e^{-j\omega n}$	$x(t) = \frac{1}{2\pi} \int_{-\pi}^{+\pi} X(\omega)e^{j\omega n} d\omega$
DFT	$X[k] = \sum_{n=0}^{N-1} x[n]e^{-j\frac{2\pi k}{N}n}$	$x[n] = \frac{1}{N} \sum_{k=0}^{N-1} X[k]e^{j\frac{2\pi k}{N}n}$
	$k = 0, 1, 2, \dots, N - 1$	$n = 0, 1, 2, \dots, N - 1$

Table 6.1: Fourier Transform for the continuous and discrete cases.

The Discrete Fourier Series (DFS) is used for discrete-time periodic signals, and for discrete-time aperiodic signals the Discrete Time Fourier Transform (DTFT) is used, both giving a periodic frequency spectrum. Certainly, these are not the entirely correct tools for the analysis to be done. However, the sampled version of the DTFT, known as the DFT where both time domain and frequency domain are discrete and finite, is used in digital signal processing. Table 6.1 shows the different mathematical expressions for the relevants of the aforementioned transforms for this Thesis.

6.2 The Goertzel Algorithm

From the previous chapters the idea of calculating a single bin of a DFT seems quite attractive. In principle, and without any further analysis, the approach suggest minor computation requirements than applying a complete DFT (lets say, for “all” frequency bins). In 1950, Gerald Goertzel introduced the Goertzel Algorithm, where he proposed the simultaneous numerical evaluation of the values C and S , which are the magnitude and phase of the input signal (respectively), based on the values a_k , $\cos(x)$ and $\sin(x)$ [47]:

$$C = \sum_{k=0}^N a_k \cos(kx) \quad S = \sum_{k=1}^N a_k \sin(kx) \quad (6.1)$$

The algorithm is defined as:

Algorithm 1: Goertzel Algorithm

- 1 $U_{N+2} = U_{N+1} = 0;$
 - 2 $U_k = a_k + 2 \cos(x)U_{k+1} - U_{k+2} \quad \triangleright k = N, N-1, \dots, 1$
 - 3 $C = a_0 + U_1 \cos(x) - U_2 \wedge S = U_1 \sin(x)$
-

Where a_k is the k^{th} sample and x , is the target frequency. In this way, it is possible to calculate the k^{th} element of the DFT of a sequence $x[n]$ with N samples. In the following section, a synthetizable Goertzel Filter expression is derived.

6.3 The Goertzel Filter derivation

Starting from the forward DFT expression, (see table 6.1):

$$X[k] = \sum_{n=0}^{N-1} x[n] e^{-j \frac{2\pi k}{N} n} \quad k = 0, 1, 2, \dots, N - 1$$

From this expression, following [175] and using the Euler’s identity $1 = e^{j2\pi} = e^{j2\pi \frac{N}{N}}$ it is possible rewrite it like:

$$X[k] = \sum_{n=0}^{N-1} x[n] \cdot 1 \cdot e^{-j \frac{2\pi k}{N} n} = \sum_{n=0}^{N-1} x[n] e^{j \frac{2\pi k}{N} N} e^{-j \frac{2\pi k}{N} n} \Rightarrow X[k] = \sum_{n=0}^{N-1} x[n] e^{-j 2\pi k \frac{n-N}{N}} \quad (6.2)$$

Equation (6.2) can be interpreted as the linear discrete convolution between a signal $x[n]$ and some response $h_k[n]$. In this way, it is possible to write:

$$\left. \begin{aligned} y_k[m] &= \sum_{-\infty}^{+\infty} x[n]h_k[m-n], \\ h_k[l] &= e^{-j2\pi k \frac{l}{N}} u[l] \end{aligned} \right\} \Rightarrow \boxed{y_k[m] = \sum_{-\infty}^{+\infty} x[n]e^{-j2\pi k \frac{m-n}{N}} u[m-n]} \quad (6.3)$$

Comparing equations (6.2) and (6.3), keeping the N^{th} sample of (6.3), the result is $X[k]$:

$$\boxed{X[k] = y_k[N]} \quad (6.4)$$

for an arbitrary, but fixed, value of $k = 0, 1, \dots, N - 1$.

Now, applying the Z-Transform to the equation (6.3) it is possible to get the filter's transfer function:

$$\begin{cases} h_k[n] = e^{-j2\pi k \frac{n}{N}} u[n], \\ \mathcal{Z}\{h_k[n]\} = H_k(z) \end{cases} \Rightarrow H_k(z) = \sum_{n=-\infty}^{+\infty} h_k[n]z^{-n} \Rightarrow \quad (6.5)$$

$$\begin{aligned} \Rightarrow H_k(z) &= \sum_{n=-\infty}^{+\infty} e^{-j2\pi k \frac{n}{N}} u[n]z^{-n} \\ &= \sum_{n=0}^{+\infty} e^{-j2\pi k \frac{n}{N}} z^{-n} \\ &= \sum_{n=0}^{+\infty} (e^{-j2\pi k \frac{1}{N}} z^{-1})^n \end{aligned} \quad (6.6)$$

The convergence case of the geometric series, is:

$$\sum_{n=0}^{+\infty} ar^n = \frac{a}{1-r} \quad (6.7)$$

Where, replacing $a = 1$ and $r = e^{j2\pi k \frac{1}{N}} z^{-1}$, the equation (6.6) can be written as:

$$\boxed{H_k(z) = \frac{1}{1 - e^{j\frac{2\pi k}{N}} z^{-1}}} \quad (6.8)$$

which is the Goertzel's Filter **first order IIR** transfer function. In order to get the appropriate formulation for writing a computer algorithm, it is necessary to get the difference equation of $H_k(z)$:

$$\begin{aligned}
 H_k(z) &= \frac{Y_k(z)}{X(z)} \Rightarrow \\
 \Rightarrow Y_k(z) &= H_k(z)X(z) \\
 &= \frac{1}{1 - e^{j\frac{2\pi k}{N}} z^{-1}} X(z) \Rightarrow \\
 \Rightarrow (1 - e^{j\frac{2\pi k}{N}} z^{-1})Y_k(z) &= X(z) \\
 \Rightarrow Y_k(z) - Y_k(z)e^{j\frac{2\pi k}{N}} z^{-1} &= X(z) \Rightarrow \mathcal{Z}^{-1}\{\} \Rightarrow \\
 y_k[n] - y_k[n-1]e^{j\frac{2\pi k}{N}} &= x[n]
 \end{aligned} \tag{6.9}$$

Here \mathcal{Z}^{-1} represents the inverse Z-transform. Re-ordering the result:

$$\boxed{y_k[n] = x[n] + y_k[n-1]e^{j\frac{2\pi k}{N}}} \tag{6.10}$$

with $y_k[-1] = 0$.

The problem with this last expression is the complex multiplication, which is computationally demanding as is cyclically applied. In order to reduce its impact, the transfer function $H_k(z)$ (6.8) can be multiplied and divided by: $1 - e^{-j\frac{2\pi k}{N}} z^{-1}$, the denominator's conjugate:

$$\begin{aligned}
 H_k(z) &= \frac{1}{1 - e^{j\frac{2\pi k}{N}} z^{-1}} \frac{(1 - e^{-j\frac{2\pi k}{N}} z^{-1})}{(1 - e^{-j\frac{2\pi k}{N}} z^{-1})} \\
 &= \frac{1 - e^{-j\frac{2\pi k}{N}} z^{-1}}{1 - e^{-j\frac{2\pi k}{N}} z^{-1} - e^{j\frac{2\pi k}{N}} z^{-1} + z^{-2}}
 \end{aligned} \tag{6.11}$$

Through Euler's formula:

$$\begin{cases} e^{-j\frac{2\pi k}{N}} = \cos\left(\frac{2\pi k}{N}\right) - j \sin\left(\frac{2\pi k}{N}\right) \\ e^{j\frac{2\pi k}{N}} = \cos\left(\frac{2\pi k}{N}\right) + j \sin\left(\frac{2\pi k}{N}\right) \end{cases} \tag{6.12}$$

Replacing in (6.11):

$$\boxed{H_k(z) = \frac{1 - e^{-j\frac{2\pi k}{N}} z^{-1}}{1 - 2 \cos\left(\frac{2\pi k}{N}\right) z^{-1} + z^{-2}}} \tag{6.13}$$

Which is the Goertzel's Filter **second order IIR** transfer function. The same mechanism for getting the difference equation, the inverse Z-Transform it is applied:

$$\begin{aligned}
 H_k(z) &= \frac{Y_k(z)}{X(z)} \Rightarrow \\
 \Rightarrow y_k(z)[1 - 2 \cos\left(\frac{2\pi k}{N}\right) z^{-1} + z^{-2}] &= X(z)(1 - e^{-j\frac{2\pi k}{N}} z^{-1}) \Rightarrow \\
 \Rightarrow Y_k(z) - 2 \cos\left(\frac{2\pi k}{N}\right) Y_k(z)z^{-1} + Y_k(z)z^{-2} &= X(z) - X(z)e^{-j\frac{2\pi k}{N}} z^{-1} \Rightarrow \\
 \Rightarrow \mathcal{Z}^{-1}\{\} &\Rightarrow
 \end{aligned} \tag{6.14}$$

$$\Rightarrow y_k[n] - 2 \cos\left(\frac{2\pi k}{N}\right) y_k[n-1] + y_k[n-2] = x[n] - x[n-1]e^{-j\frac{2\pi k}{N}} \tag{6.15}$$

Re-ordering the result:

$$\boxed{y_k[n] = x[n] - x[n-1]e^{-j\frac{2\pi k}{N}} + 2 \cos\left(\frac{2\pi k}{N}\right) y_k[n-1] - y_k[n-2]} \tag{6.16}$$

with $y_k[-1] = y_k[-2] = x[-1] = 0$ (due to causality). A block diagram of this second order IIR filter can be appreciated in the next Figure 6.1.

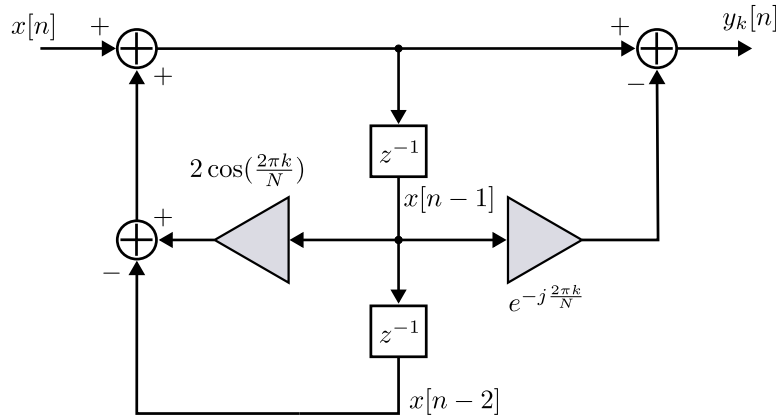


Figure 6.1: Goertzel Filter - IIR Filter representation block diagram.

In order to accurately visualize how this model is less computationally demanding than the first order one and understand the algorithm deduction, it is good to get the **Discrete-Time State Space** form of the described system. Formally speaking, determine the state variables by:

$$\begin{cases} \vec{x}[l+1] = \mathbf{A}\vec{x}[l] + \mathbf{B}\vec{u}[l] \\ \vec{y}[l] = \mathbf{C}\vec{x}[l] + \mathbf{D}\vec{u}[l] \end{cases} \tag{6.17}$$

where the bold typography represents matrices. In the literature, it is common to find that the used letter for the discretization of the State Space Variables is k , as: $\vec{x}[k+1]$;

but here k stands for the discrete frequency, so letter “ l ” is used instead. An n -th order difference equation is defined by the following general expression:

$$\begin{aligned} y[l+n] + a_{n-1}y[l+n-1] + \cdots + a_1y[l+1] + a_0y[l] = \\ b_nx[l+n] + b_{n-1}x[l+n-1] + \cdots + b_1x[l+1] + b_0x[l] \end{aligned} \quad (6.18)$$

and the general matrix formulation for this controllable canonical form:

$$A = \begin{pmatrix} 1 & 0 & \cdots & 0 \\ 0 & 1 & \cdots & 0 \\ \vdots & \vdots & \ddots & \vdots \\ -a_0 & -a_1 & \cdots & -a_{n-1} \end{pmatrix} B = \begin{pmatrix} 0 \\ 0 \\ \vdots \\ 1 \end{pmatrix} \quad (6.19)$$

$$C = ((b_0 - a_0b_n) \quad (b_1 - a_1b_n) \cdots (b_{n-1} - a_{n-1}b_n)) \quad D = (b_n) \quad (6.20)$$

The described system yields to the following state space representation:

$$\begin{aligned} \begin{bmatrix} x_1[l+1] \\ x_2[l+1] \end{bmatrix} &= \begin{bmatrix} 0 & 1 \\ -a_{n-2} & -a_{n-1} \end{bmatrix} \begin{bmatrix} x_1[l] \\ x_2[l] \end{bmatrix} + \begin{bmatrix} 0 \\ 1 \end{bmatrix} u[l] \\ y_k[l] &= [\beta_2 \quad \beta_1] \begin{bmatrix} x_1[l] \\ x_2[l] \end{bmatrix} + b_0u[l] \end{aligned}$$

Comparing the general expression (6.18) with (6.15) it is possible to write:

$$\begin{cases} b_0 = a_0 = 1 \\ b_{n-1} = -e^{-j\frac{2\pi k}{N}} \\ a_{n-1} = -2 \cos\left(\frac{2\pi k}{N}\right) \\ a_{n-2} = 1 \\ \beta_1 = b_{n-1} - b_0a_{n-1} = -e^{-j\frac{2\pi k}{N}} + 2 \cos\left(\frac{2\pi k}{N}\right) \\ \beta_2 = b_{n-2} - b_0a_{n-2} = -1 \end{cases} \quad (6.21)$$

Solving the representation to get the state space equation for the Goertzel Filter:

$$\begin{cases} x_1[l+1] = x_2[l] \\ x_2[l+1] = -x_1[l] + 2 \cos\left(\frac{2\pi k}{N}\right) x_2[l] + u[l] \\ y_k[l+1] = -x_1[l] + \left[-e^{-j\frac{2\pi k}{N}} + 2 \cos\left(\frac{2\pi k}{N}\right)\right] x_2[l] + u[l] \end{cases} \Rightarrow \quad (6.22)$$

$$\Rightarrow \begin{cases} x_1[l+1] = x_2[l] \\ x_2[l+1] = u[l] - x_1[l] + 2 \cos\left(\frac{2\pi k}{N}\right) x_1[l+1] \\ y_k[l] = -x_1[l] + \left[-e^{-j\frac{2\pi k}{N}} + 2 \cos\left(\frac{2\pi k}{N}\right)\right] x_1[l+1] + u[l] \end{cases} \Rightarrow \quad (6.23)$$

$$x_2[l+1] = u[l] - x_1[l] + 2 \cos\left(\frac{2\pi k}{N}\right) x_1[l+1] \quad (6.24)$$

$$y_k[l] = u[l] - x_1[l+1]e^{-j\frac{2\pi k}{N}} \quad (6.25)$$

These final equations can be represented in the next signal flow graph diagram, Figure 6.2:

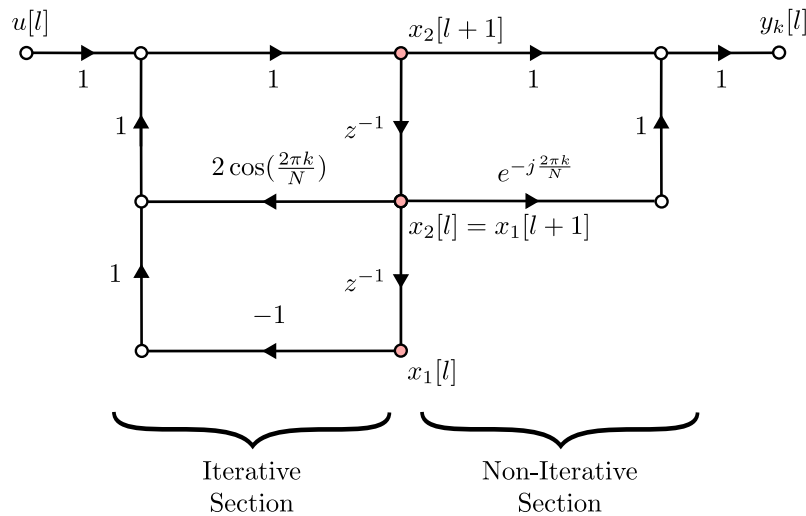


Figure 6.2: Goertzel Filter State-Space variables signal flow diagram. The coloured (light red) dots (states) represent the internal state variables of the system.

It is worth clarifying that the used nomenclature here is referred to the use of delay elements (z^{-1}): the output of a delay element is the present value (current state) stored in a *register*, and the input represents the next value to be stored in that *register* [176]. Consequently, in Figure 6.2 representing the done state-space analysis, it is possible to see that the expression $[l+1]$ is used instead of a more *natural* expression like the one used in the block diagram of Figure 6.1. To improve the readability of the algorithms, the state variables were renamed as follows: $x[n] = u[l]$, $y_k[n] = y_k[l]$, $\omega_0 = x_2[l+1]$, $\omega_1 = x_2[l] = x_1[l+1]$ and $\omega_2 = x_1[l]$.

Algorithm 2: Standard Goertzel Algorithm

```

1  $A = \frac{2\pi k}{N}$ 
2  $B = 2 \cos(A)$ 
3  $C = e^{-jA}$ 
4  $\omega_0 = \omega_1 = \omega_2 = 0$ 
5 for  $n = 0$  to  $N - 1$  do
6    $\omega_0 = x[n] + B\omega_1 - \omega_2$ 
7    $\omega_2 = \omega_1$ 
8    $\omega_1 = \omega_0$ 
9  $\omega_0 = B\omega_1 - \omega_2$ 
10  $y = \omega_0 - \omega_1 C$ 
    
```

It can be concluded from here that the algorithm for implementing this IIR filter iterates (6.24) for $N + 1$ times (starting from index $n = 0$). Afterwards $y_k(N)$ is calculated with (6.25), performing in this way only one complex multiplication. The problem with expressions (6.2) and the DFT, is that they are only in agreement for integer values of the discrete frequency k . In fact, for real values of k in accordance with Section 6.1, the DFT is no longer applicable and we should go back to the DTFT:

$$X(\omega) = \sum_{n=-\infty}^{+\infty} x[n]e^{-j\omega n} \quad (6.26)$$

noting that for $\omega_k = 2\pi \frac{k}{N}$ we can rewrite (6.26) as:

$$X(\omega_k) = \sum_{n=0}^{N-1} x[n]e^{-j2\pi k \frac{n}{N}} \quad (6.27)$$

with $\omega_k, k \in \mathfrak{R}$. Defining unity similarly like in (6.2): $1 = e^{j2\pi k \frac{N}{N}} e^{-j2\pi k \frac{N}{N}}$, then:

$$X(\omega_k) = \sum_{n=0}^{N-1} x[n]e^{-j2\pi k \frac{n}{N}} \cdot e^{j2\pi k \frac{N}{N}} \cdot e^{-j2\pi k \frac{N}{N}} \Rightarrow \quad (6.28)$$

$$\Rightarrow X(\omega_k) = e^{-j2\pi k} \sum_{n=0}^{N-1} x[n]e^{-j2\pi k \frac{N-n}{N}} \quad (6.29)$$

This last expression only differs from (6.2) in the element previous to the summation, $e^{-j2\pi k}$, which depends on the frequency of interest and is correcting the phase of the calculated bin. The correct value for the module estimation is not affected by the non-integer value of k ; however the phase is affected and needs to be corrected by it. Performing the same state-space variables deduction, yields to a new set of equations which only differs in the phase correction factor (so (6.24) remains exactly the same):

$$y_k[l] = e^{-j2\pi k} \left\{ u[l] - x_1[l + 1]e^{-j\frac{2\pi k}{N}} \right\} \quad (6.30)$$

The new generalized Goertzel Algorithm for non-integer values and introducing a reduction in the number of iterations, according to [175], is:

Algorithm 3: Generalized Goertzel Algorithm for non-integer k values and shortened iteration loop

```

1  $A = \frac{2\pi k}{N}$ 
2  $B = 2 \cos(A)$ 
3  $C = e^{-jA}$ 
4  $D = e^{-j2\pi k \frac{N-1}{N}}$ 
5  $\omega_0 = \omega_1 = \omega_2 = 0$ 
6 for  $n = 0$  to  $N - 1$  do
7    $\omega_0 = x[n] + B\omega_1 - \omega_2$ 
8    $\omega_2 = \omega_1$ 
9    $\omega_1 = \omega_0$ 
10  $\omega_0 = x[N - 1] + B\omega_1 - \omega_2$ 
11  $y = \omega_0 - \omega_1 C$ 
12  $y = yD$ 

```

This version, despite of showing an improvement in the number of iterations, is not suitable for the purposes of this work as this improvement is only by one iteration, at the cost of requiring an extra complex multiplication (which increases the required resources in an FPGA). The number of iterations is substantially important as it will be shown in the following sections. For the purposes of this work, the generalized Goertzel algorithm version from Richard Lyons [48] was implemented, which besides reducing the computational workload of the last complex multiplication, allows a better parallelization for multiple frequency components when mapping the algorithm to an FPGA:

Algorithm 4: Goertzel algorithm generalized to non-integer multiples of fundamental frequency k

```

1  $\alpha = \frac{2\pi k}{N}$ 
2  $\beta = \frac{2\pi k(N-1)}{N}$ 
3  $a = \cos(\beta)$ 
4  $b = -\sin(\beta)$ 
5  $c = \sin(\alpha) \sin(\beta) - \cos(\alpha) \cos(\beta)$ 
6  $d = \sin(2\pi k)$ 
7  $\omega_0 = \omega_1 = \omega_2 = 0$ 
8 for  $N = 0$  to  $N - 1$  do ▷ Iterative Section
9    $\omega_0 = x[n] + 2 \cos(\alpha)\omega_1 - \omega_2$ 
10   $\omega_2 = \omega_1$ 
11   $\omega_1 = \omega_0$ 
12  $X_k = a\omega_1 + c\omega_2 + j(b\omega_1 + d\omega_2)$  ▷ Non-iterative Section
13  $|X_k| = \sqrt{(a\omega_1 + c\omega_2)^2 + (b\omega_1 + d\omega_2)^2}$ 
14  $\Phi(X_k) = \arctan\left(\frac{b\omega_1 + d\omega_2}{a\omega_1 + c\omega_2}\right)$ 

```

6.4 Window Functions for Spectral Analysis with the Goertzel Filter

When studying (6.3), $h_k[n]$ was distinguished as the impulse response of some filter which then lead to the second order IIR filter model. In the same expression, $h_k[n]$ was affected, naturally, by the step function $u[m - n]$ which allows the interpretation that the very basic Goertzel Filter is *using* a rectangular window of size N . Window functions in general have their own time-domain and frequency-domain responses [177]. The DFT can be generalized to different window function types by adding $w[n]$ to the DFT pipeline deduction starting from (6.2):

$$x_w[n] = x[n] \cdot w[n] \quad (6.31)$$

$$X[k] = \sum_{n=0}^{N-1} x_w[n] e^{-j2\pi k \frac{n-N}{N}} \quad (6.32)$$

As it will be shown later, in Section 6.7.1, this allows an important improvement in the filter regarding three main aspects: a) mitigating the spectral leakage effects due to the inherent windowing procedure of applying a FT method, b) improving the isolation between adjacent channels, and c) filtering spurious and inter-modulation products. Figure 6.3 shows the inclusion of the window function in the Goertzel Filter (GF) block diagram:

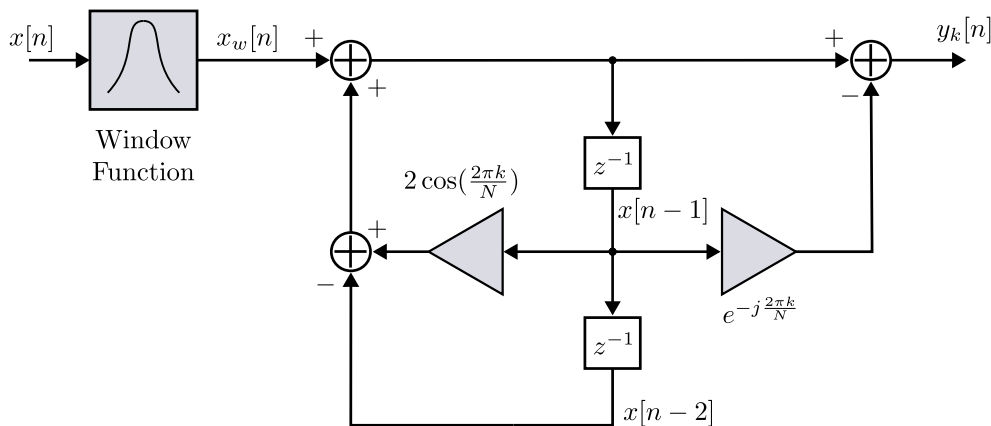


Figure 6.3: GF - IIR Filter representation block diagram with the Window Function block, representing the windowing of the input signal.

6.5 A simple modulation model

So far, the GF was presented and deeply mathematically studied. In the previous section the spectral response of the system was also presented. Now, it is important to determine whether this filter is capable of achieving the required task for this development. This is a good moment to remember that according to Mates [106] (and already introduced in

Section 3.4), the FRM technique may be considered as a phase modulation (PM) technique. Actually, even if there is no FRM in the experimental setup but some mechanism exists for modulating the resonance frequency of the resonators affecting the input carrier amplitude, an amplitude modulation (AM) would be expected. In light of this, it seems reasonable to simply demonstrate how the GF can retrieve the desired scientific data even in this context of AM and PM signals, through the DFT analysis.

For doing so, three different situations are analyzed: a) without modulation and detector signals, b) with modulation signal but no detector, and c) with both components. The different modulation effects are described by the following expressions:

- $m(t)$: for the modulation signal for the input tone to the cryostat (basically, the flux variation effects over the tone due to the μ MUX's resonators modulation),
- $d(t)$: the detector signal which is related with the sensors response and that affects the SQUID's flux through the resonator,
- $x_{in}(t) = A_{in} \cos(2\pi f_{in} \cdot t + \phi_{in})$: the input carrier signal to the cryostat but from the base-band point of view. Analogously, for the output carrier signal, it will be referenced as $x_{out}(t)$.

6.5.1 No modulation nor detector signal: $m(t) = 0$ and $d(t) = 0$

When none of the modulation effects are present, the input carrier signal $x_{in}(t)$ remains unaltered by the system (except perhaps by an attenuation factor). In this particular case it happens that $x_{out}(t) = x_{in}(t)$, and the DFT evaluations yields:

$$\left. \begin{aligned} x_{out}[n] &= A_{out} \cos \left[\frac{2\pi k_{out} \cdot n}{N} + \phi_{out} \right] \\ X[k] &= \sum_0^{N-1} x_{in}[n] \cdot w[n] e^{j2\pi k \frac{n}{N}} \end{aligned} \right\} \Rightarrow \quad (6.33)$$

$$\Rightarrow X[k] = \sum_0^{N-1} A_{out} \cos \left\{ \frac{2\pi k_{out} \cdot n}{N} + \phi_{out} \right\} w[n] e^{-j2\pi k \frac{n}{N}} \quad (6.34)$$

As this demonstrations are meanly illustrative, the case where $w[n]$ represents a *rectangular window* and $\phi_{out} = 0$ is analyzed:

$$\begin{aligned} X[k] &= \sum_0^{N-1} A_{out} \left[\frac{e^{j2\pi k_{out} \frac{n}{N}} + e^{-j2\pi k_{out} \frac{n}{N}}}{2} \right] \cdot 1 \cdot e^{-j2\pi k \frac{n}{N}} \Rightarrow \\ \Rightarrow X[k] &= \frac{A_{out}}{2} \left[\sum_0^{N-1} e^{j2\pi \frac{n}{N} (k_{out}-k)} + \sum_0^{N-1} e^{-j2\pi \frac{n}{N} (k_{out}+k)} \right] \end{aligned} \quad (6.35)$$

In concordance with the analysis of the previous sections, the GF output for $k = k_{out}$ will be in fact: $X[k_{out}] = \frac{A_{out}}{2} N$ (for the ideal case with no spectral leakage, meaning that k_{out} is an integer value) and analogously for $k = -k_{out}$. The N factor in the result can

be derived from solving the case of the closed-form geometric series of $\sum_0^{N-1} e^{nq} = \frac{1-e^{qN}}{1-e^q}$ with $e^q \neq 1$, where for example, for the positive frequency case, $q = -j2\pi\frac{n}{N}(k_{out} - k)$.

6.5.2 No detector signal: $m(t) \neq 0$ and $d(t) = 0$

In this case, the flux-ramp modulation is present in the model which will make the resonators in the μ MUX change their response (magnitude and phase). This model, as was explained before, can be thought as an AM and PM system:

$$m(t) = A_m \cos(2\pi f_m \cdot t + \phi_m) \rightarrow m[n] = A_m \cos\left[\frac{2\pi k_m}{N}n\right] \quad (6.36)$$

The resultant output signal from the cryostat will be:

$$x_{out}(t) = m(t) \frac{x_{in}(t)}{A_{in}} + x_{in}(t) \Rightarrow x_{out}[n] = m[n] \frac{x_{in}[n]}{A_{in}} + x_{in}[n] \quad (6.37)$$

$$\begin{aligned} \Rightarrow x_{out}[n] &= A_m \cos\left[\frac{2\pi k_m}{N}n\right] \frac{A_{in}}{A_{in}} \cos\left[\frac{2\pi k_{in}}{N}n + m[n]\right] + A_{in} \cos\left[\frac{2\pi k_{in}}{N}n + m[n]\right] \Rightarrow \\ \Rightarrow x_{out}[n] &= A_m \cos\left[\frac{2\pi k_m}{N}n\right] \cos\left[\frac{2\pi k_{in}}{N}n + m[n]\right] + A_{in} \cos\left[\frac{2\pi k_{in}}{N}n + m[n]\right] \end{aligned} \quad (6.38)$$

In order to simplify the analysis of the PM, the narrow-band case is contemplated, so that $\beta \ll 1$, skipping the Bessel functions step [178]. However, the understanding for that more generic case is straight forward. Applying the DFT to this last expression:

$$\begin{aligned} X_{out}[k] &= \sum_0^{N-1} \left\{ A_m \cos\left[\frac{2\pi k_m}{N}n\right] \cos\left[\frac{2\pi k_{in}}{N}n + m[n]\right] + A_{in} \cos\left[\frac{2\pi k_{in}}{N}n + m[n]\right] \right\} e^{-j2\pi k \frac{n}{N}} \\ X_{out}[k] &= X_{out_a}[k] + X_{out_b}[k] \end{aligned} \quad (6.39)$$

$$\begin{cases} X_{out_a}[k] = \sum_0^{N-1} A_m \cos\left[\frac{2\pi k_m}{N}n\right] \cos\left[\frac{2\pi k_{in}}{N}n + m[n]\right] e^{-j2\pi k \frac{n}{N}} \\ X_{out_b}[k] = \sum_0^{N-1} A_{in} \cos\left[\frac{2\pi k_{in}}{N}n + m[n]\right] e^{-j2\pi k \frac{n}{N}} \end{cases} \Rightarrow \quad (6.40)$$

$$\Rightarrow \begin{cases} X_{out_a}[k] = A_{in} \left\{ \sum_0^{N-1} \frac{\cos \left[\frac{2\pi}{N} (k_m - k_{in})n - m[n] \right]}{2} \right. \\ \left. + \frac{\cos \left[\frac{2\pi}{N} (k_m + k_{in})n + m[n] \right]}{2} \right\} e^{-j2\pi k \frac{n}{N}} \\ X_{out_b}[k] = \frac{A_{in}}{2} \left[\sum_0^{N-1} e^{j2\pi \frac{n}{N} (k_{in}-k)} + \sum_0^{N-1} e^{-j2\pi \frac{n}{N} (k_{in}+k)} \right] \end{cases} \quad (6.41)$$

Here $X_{out_b}[k]$ is the DFT of a single cosine function as was depicted in the previous subsection 6.5.1, clearly representing the carrier component, k_{in} , which is the monitoring tone. On the other hand, $X_{out_a}[k]$ represents the side bands of the carrier component (as in a typical AM system). Using the cosine expressions gives a better insight on how the magnitude of the Fourier bin is changing: when this functions are multiplied by $e^{-j2\pi \frac{k_{in}n}{N}}$ a frequency translation occurs as expected (which is basically what the filter is doing); the output should present a cosine function at k_m frequency and an offset consistent with the carrier power (x_{in}).

As will be shown in Section 6.7.3, the model is contemplating both magnitude and phase variation due to $m(t)$.

It is clear by now, that for recovering the data of interest in the module of $m(t)$ no further processing is required. But if it is in the phase, the extraction of the phase from the GF output is necessary by some post-processing method.

6.5.3 With detector signal: $m(t) \neq 0$ and $d(t) \neq 0$

Finally, considering the case where $d(t) \neq 0$ (which can be a pulse, or a continuously changing function) is not so different from the previous section. A detector signal into the modulating function $m(t)$ is added, as it is affecting its phase:

$$m(t) = A_m \cos[2\pi f_m \cdot t + \phi_m + d(t)] \quad (6.42)$$

The result is the same as before, but a post-processing step is mandatory in order to recover $d(t)$ from the phase of the GF output. In principle there are two ways to achieve this task: a typical IQ demodulation technique [106] or the Hilbert Transform [121, 178]. These post-processing steps will be addressed later.

6.6 Targeting a Sliding Goertzel Filter Bank

At this point, the analysis was done to a windowed (finite-length) time-domain sequence without taking into account the DFT shift theorem as a consequence of attempting a real-time acquisition and processing. This theorem, also known as *Circular Shifting* [121], can be stated as:

$$x[n \pm n_0] \xrightarrow{N} e^{\pm j\omega_k n_0} X(\omega_k) \quad (6.43)$$

where as described before, $w_k = \frac{2\pi nk}{N}$. An intuitive interpretation of this effect can be appreciated in the following figure:

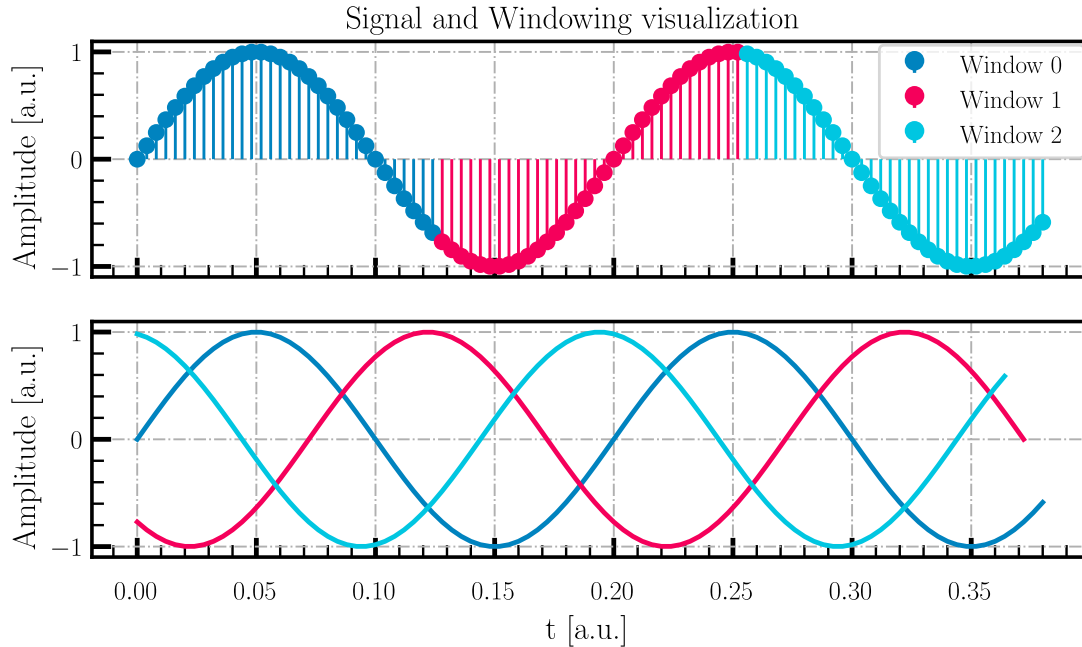


Figure 6.4: Window effect in real-time acquisition systems. The figure represents the N samples that are taken in each window application, and how the signal is then interpreted by a Fourier method.

The top graph of Figure 6.4, represents how after N samples there is a new window applied to the input signal. As the window size is not a multiple of the input signal frequency (as it will happen in a channelizer because we do not use a different window function module for every different input signal, due to the required FPGA resources), the effect we can see is that the subsequent stages of the processing chain, will interpret a signal of the same frequency characteristics but different phase (bottom graph of Figure 6.4). That certainly will give a correct magnitude value for the GF but a totally inconsistent result for the phase. In order to address this problem, in [179, 180] a sliding DFT and a sliding GF are proposed. The solution shows the incorporation of a comb filter before applying either the DFT or the GF. The expression for this mathematical operation is presented below:

$$H_k(z) = \frac{(1 - e^{-j\frac{2\pi k}{N}} z^{-1})(1 - z^{-N})}{1 - 2 \cos(\frac{2\pi k}{N}) z^{-1} + z^{-2}} \quad (6.44)$$

This model is represented in Figure 6.5. The inconvenient with this expression is that it expects the shift between applied windows of only one sample, otherwise the result is a FT with the incorrect phase recovered. However it is possible to still overcome this situation: the property 6.43 shows that a determined, constant value of phase is added

6.7 Computational simulations

6.7.1 Goertzel Filter Frequency response

Figure 6.6 depicts the simulated GF frequency response, evaluated for different window functions and sizes. The simulation parameters are: a sampling frequency of 31.25 Msps, window size of 256 samples and the GF tuned at 6.865 MHz. The simulation was carried out in Python and in full-precision arithmetic (floating-point).

The statements described in Section 6.4 are now clearly seen. The window size is a parameter that will be used for establishing the separation between channels and the final decimation ratio; the window function will improve the cross-talk isolation (leaving an open topic here regarding of a better selection for a window function or a custom design for it).

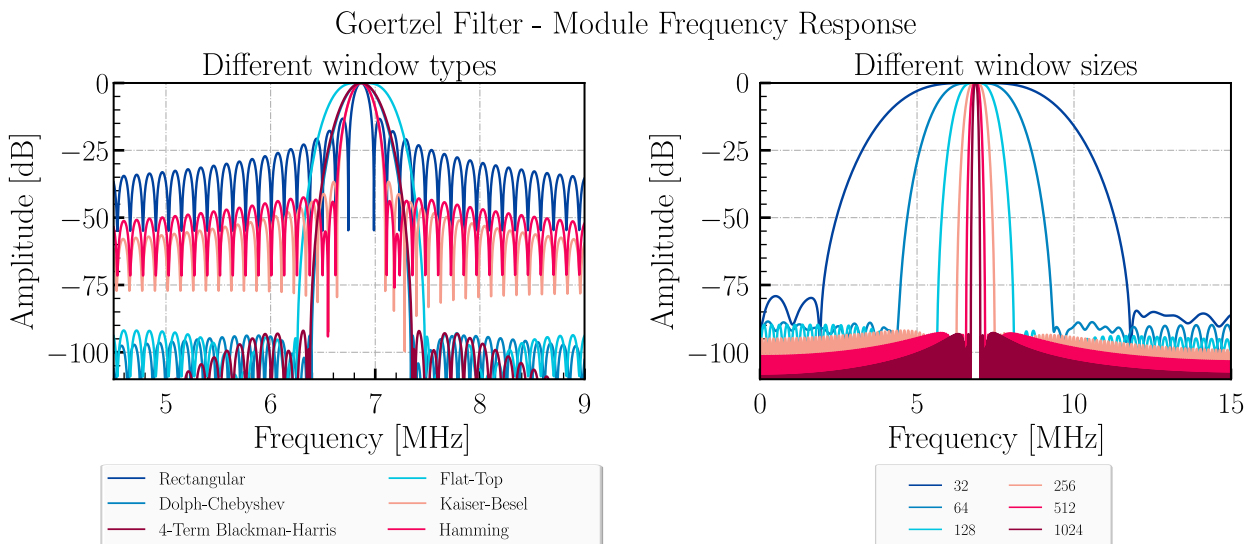


Figure 6.6: GF frequency response. $F_s = 31.25$ Msps, 256 samples window size and $f_{gf} = 6.865$ MHz.

6.7.2 Goertzel Filter vs Sliding Goertzel Filter

According to what was discussed in Section 6.6, Figure 6.7 shows how the circular property of the DFT / GF, directly impacts in the phase estimation even though the magnitude is not affected. This can be also appreciated looking in the complex plane and see how the X_k (the calculated DFT bin) is turning around instead of being, ideally, a steady point in that plane. Figure 6.8 shows how the correction presented in equation (6.44) and implemented in algorithm 5 considerably improves the performance of the filter in the phase estimation. The small “ringing” effect, also observable in the magnitude estimation, can be attributed to a limitation of the algorithm in the calculation of a non-integer multiple of the fundamental frequency or an arithmetic error (limited by the default width of the floating-point arithmetic managed by Python).

In both figures, the coloured rectangle marks the magnified subfigure present inside the plots. The relative error in the magnitude estimation is of 0.00116% and in the phase estimation 0.000741%.

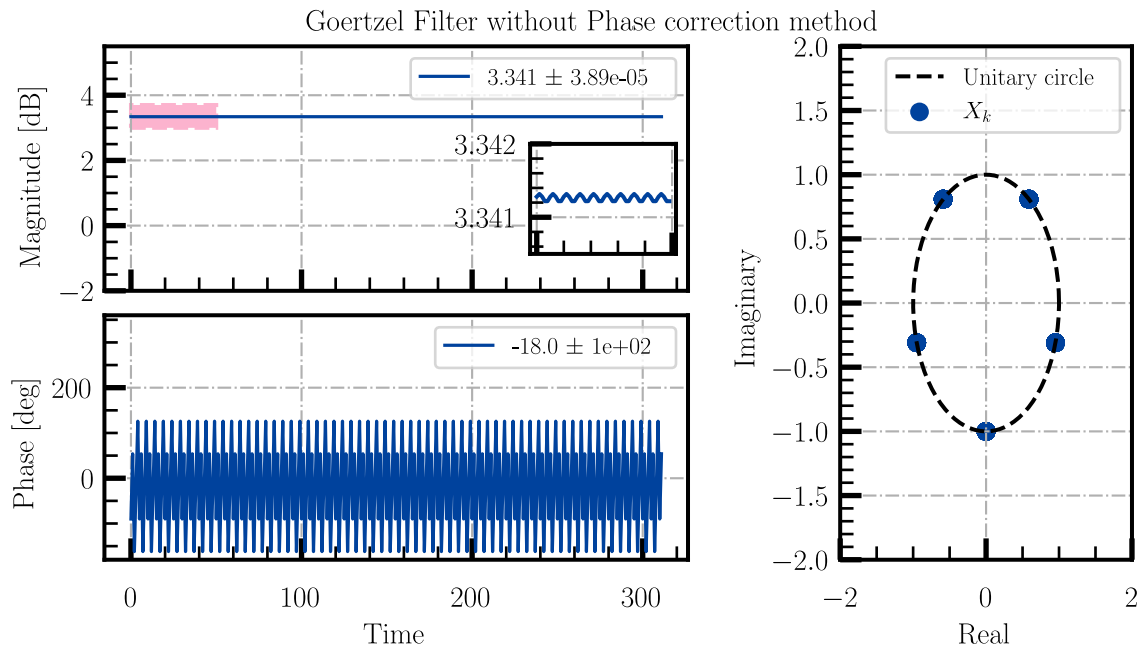


Figure 6.7: GF without phase correction method.

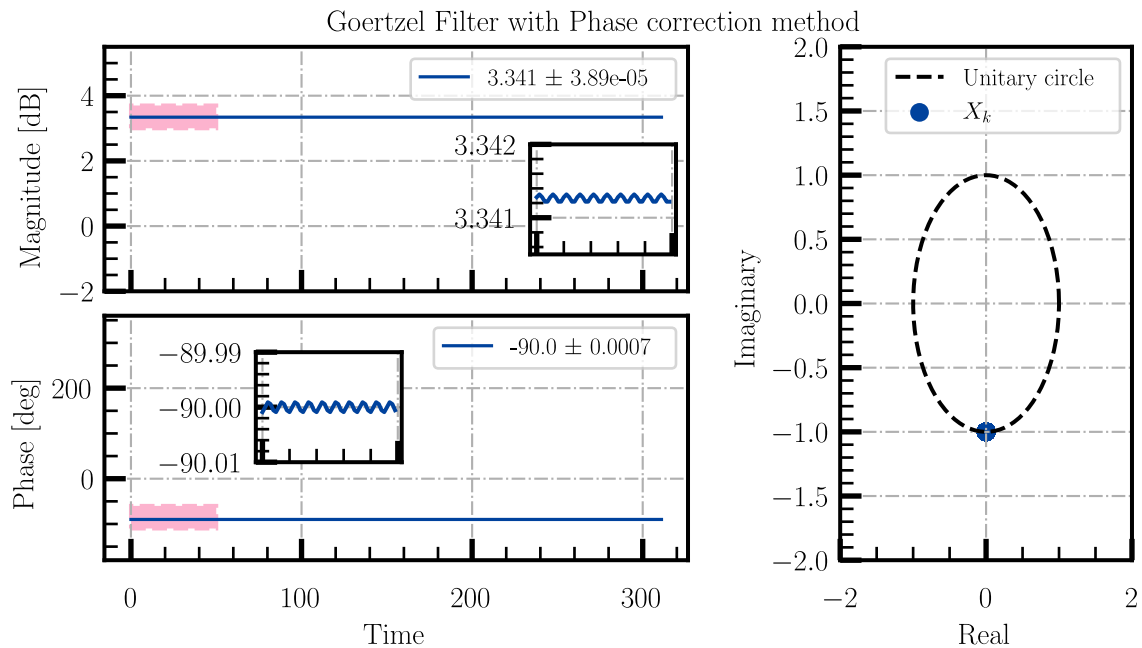


Figure 6.8: GF with phase correction method: Sliding GF.

6.7.3 Goertzel Filter demodulation capabilities

A sinusoidal signal of 5 MHz as the carrier (with the filter tuned at that frequency), which will be the *input signal* for the GF, was generated. The flux-ramp modulation is simulated by a sinusoidal signal of 50 kHz creating the AM components next to the main carrier, see Figure 6.9. To simulate a detector response, a sinusoidal signal at 200 Hz. The amplitude (peak value) was of 0.5 rad (roughly 28°) for the detector signals. The sampling frequency was $F_s = 20$ Msps. Figure 6.10 presents the spectrum of the aforementioned input signal.

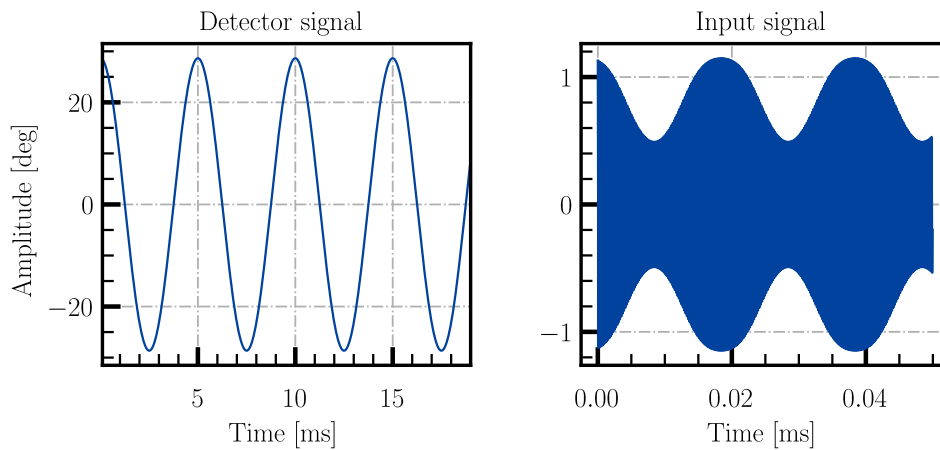


Figure 6.9: Computational simulations of the GF demodulation capabilities. A 200 Hz sinusoidal signal was used for the detector signal, with 28° peak value (left). A carrier signal of 5 MHz was used (right).

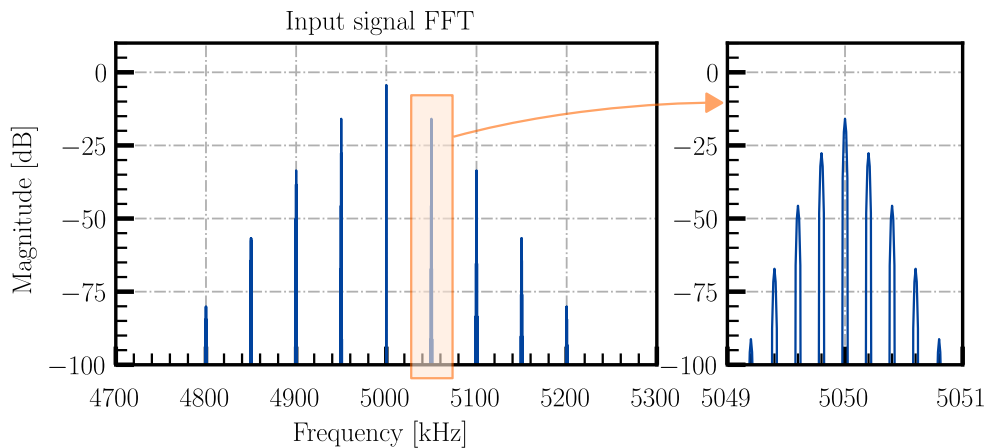


Figure 6.10: Spectrum of the input signal. The 5 MHz carrier signal, with the 50 kHz AM and the 200 Hz PM components.

It is worth to mention that this simple modulation model does not take into account

the effects of phase jumps introduced by the sawtooth modulation signal at every reset cycle, which will be clearly seen while presenting the measurements results later in chapter 9. Figure 6.11 provides illustrations of both magnitude and phase information of the GF FFT outputs. These plots indicate that the detector signal can be demodulated from any of these outputs.

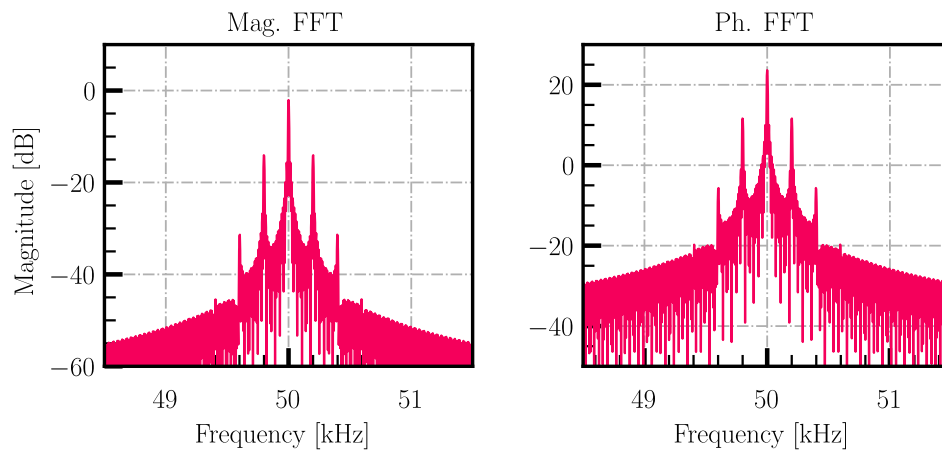


Figure 6.11: Magnitude and phase FFT of the GF output. The expected 50 kHz signal (the AM demodulation) with the 200 Hz PM components, was recovered.

In this simulation a quadrature demodulation [106] was performed for recovering the detector signal, see Figure 6.12.

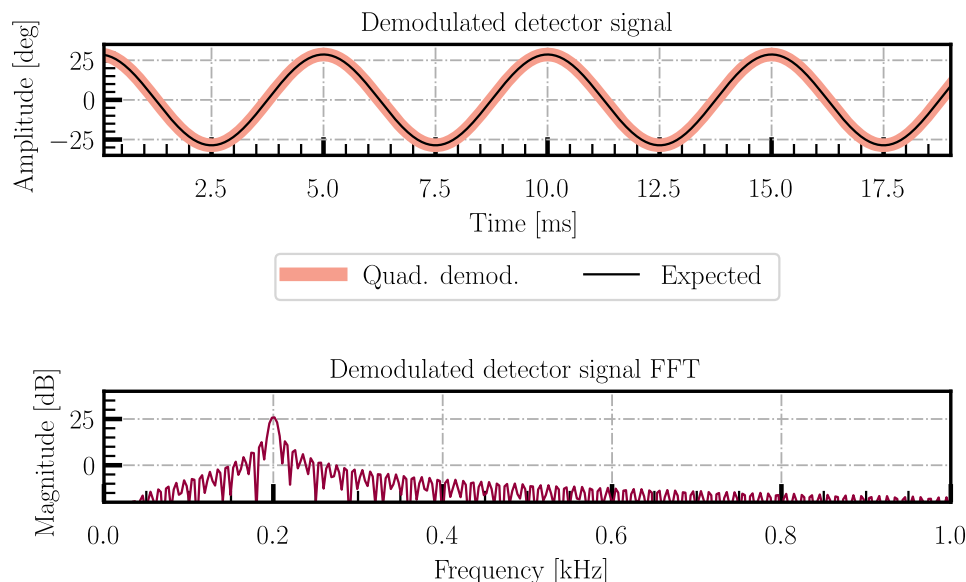


Figure 6.12: Quadrature demodulation of the GF output. The detector signal was possible to recover as expected after the GF was applied for the channelization of the input signal.

These results demonstrate the suitability of the GF to be used for the recovery of the detectors signal; detectors which are multiplexed in the frequency domain by means of a μ MUX using the Flux-Ramp Modulation technique. The developed simulation software for this task also accepts any kind of detector signal, such as a squared or a periodic pulse, for different frequencies.

Chapter 7

Signal Generation Algorithms

This chapter presents a summary of typically used methods for multi-tonal signal generation with controlled PAPR, their corresponding computational simulations and the IQ imbalance analysis.

7.1 Multi-tone Signal

The general idea for reading an ideal μ MUX (where all the resonators are equally spaced along the operation frequency) consists of introducing a so called *frequency comb signal*, where each component is associated to each μ MUX's resonator.

We can create an ideal real multi-tonal signal by implementing the following formula:

$$y(t)_{real} = \sum_{n=0}^{\infty} A_n \cos(n\omega_0 t + \phi_n) \quad (7.1)$$

which can be extrapolated for the creation of a complex multi-tonal signal. This real and complex signals can be expanded using the Exponential Fourier Series (EFS):

$$\begin{cases} x(t) = \sum_{n=-\infty}^{\infty} C_n e^{jn\omega_0 t + \phi_n} \\ C_n = \frac{1}{T} \int_{-T/2}^{T/2} y(t) e^{-jn\omega_0 t} dt \end{cases} \quad (7.2)$$

Using the EFS expansion is easy to get the Fourier Transform of this multi-tonal signal:

$$X(\omega) = \sum_{n=-\infty}^{\infty} C_n 2\pi \delta(\omega - n\omega_0) \quad (7.3)$$

7.2 Peak-to-Average Power Ratio Optimization

7.2.1 General concepts

When analyzing the dynamic range or peak values of a signal, we have mainly two metrics for accomplishing this task: Crest Factor (CF) and PAPR [122, 181]. Their definitions, for complex signals, are described below:

$$CF = \frac{s_{peak}}{s_{rms}} = \frac{\max\{|x(t)|\}}{\sqrt{\frac{1}{T} \int_0^T |x(t)|^2 dt}} \quad (7.4)$$

$$PAPR = CF^2 = \frac{P_{peak}}{P_{avg}} = \frac{\max\{|x(t)|\}^2}{\frac{1}{T} \int_0^T |x(t)|^2 dt} \quad (7.5)$$

Even though both metrics are equivalent, the PAPR is more relevant for our application as we are working with devices which performances are characterized in terms of power. For example, for a constant value in time, CF is 1 and the PAPR is 0 dB, while for a pure sine wave, CF is $\sqrt{2}$ and PAPR is 3.01 dB.

Another useful metric is the Complementary Cumulative Distribution Function (CCDF) [182]. The CCDF is a statistical measure used to characterize the probability distribution of peak amplitudes of a signal: represents the probability that the instantaneous peak power exceeds a certain level. In other words:

$$CCDF = \text{Prob}\{PAPR > z\} \quad (7.6)$$

In multi-tonal signals, formulas (7.1) and (7.2) show that the parameter ϕ_n is extremely critical. If every component of $x(t)$ retains an initial phase value $\phi_n = 0$, the result is a signal where all the components interfere in a constructive manner. It can be demonstrated that the maximum value of such a signal is $\sqrt{2N}$, with N the number of components (or frequency tones). This formula assumes unitary amplitudes for each component, but the concept is that each component is linearly added [122]:

$$v_{peak} = \sqrt{\sum_{n=0}^{N-1} A_n} \quad (7.7)$$

It is interesting to acknowledge that as long as N gets bigger, which implies a bigger number of frequency tones (a wider frequency comb signal) the time domain behavior tends to look like a Dirac Delta; being this consistent with Fourier's theory. The following Figures, 7.1 and 7.2, shows a simple sketch where a complex multi-tonal signal of 80 tones without any phase assignment optimization (so all $\phi_n = 0$) is presented both in the time domain and frequency domain, respectively:

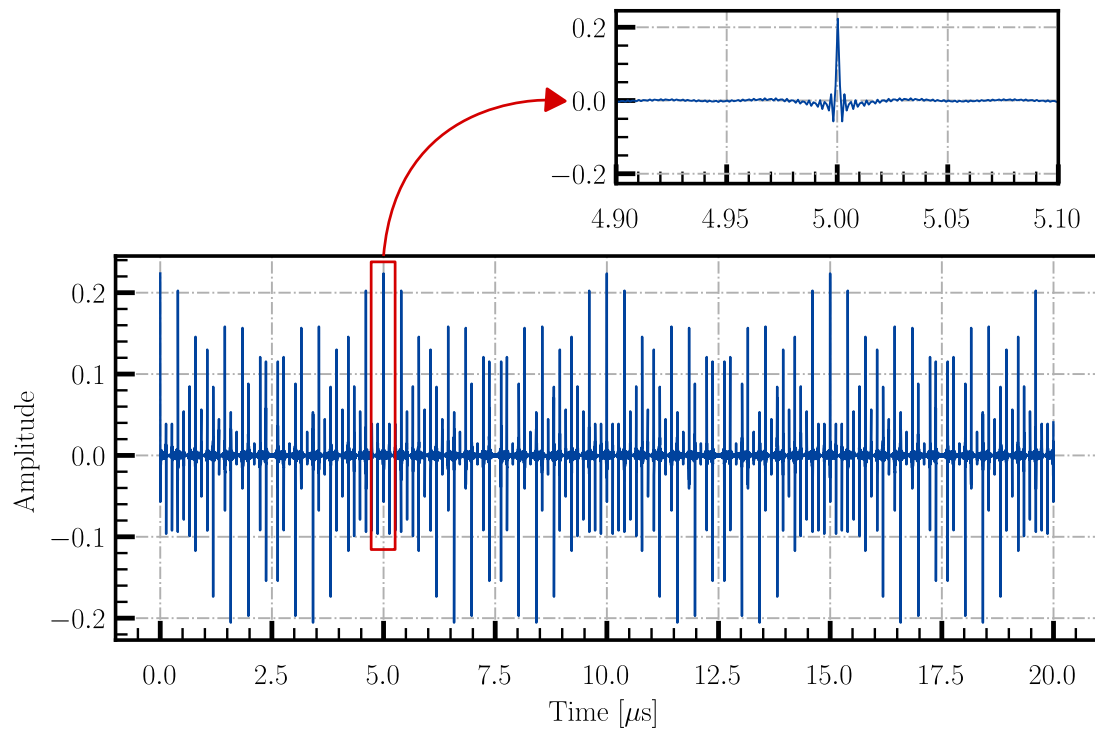


Figure 7.1: Multi-tonal signal without optimization for PAPR reduction, composed of 100 tones, equally spaced, with an $F_s = 1$ Gps, and a target power of -40 dBm per frequency component. The Dirac Delta behavior alike can be appreciated in the zoom image.

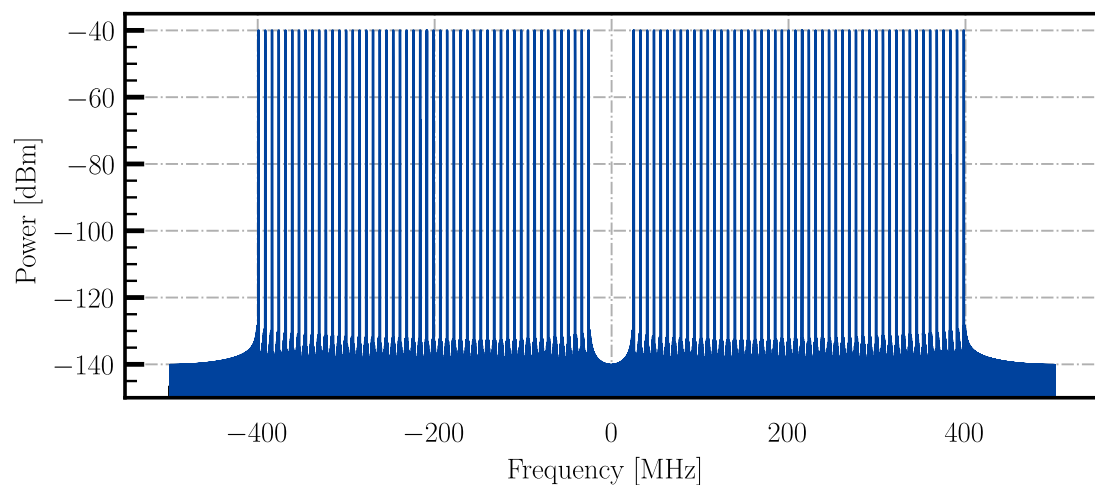


Figure 7.2: Fourier transform of the previous figure. A frequency guard of a total of 40 MHz (from -20 MHz to 20 MHz) is placed, as the typical implementation for this Thesis work scope.

7.2.2 Optimization algorithms

To improve PAPR, several algorithms were and are still under developed. The classical deterministic ones are those written by Schroeder [183], Rudin-Shapiro [122, 184, 185], Newman [186], among others. There also exist other types like the well know Random Phases [187] method. More modern algorithms uses machine learning techniques like Genetic Algorithms [188]. For the purposes of this work, a comparison of four of the most classical methods is carried out. Below, a summary of how the phases are assigned with some methods is presented:

Schroeder

$$\phi_n = \frac{\pi}{N}(n-1)n \quad (7.8)$$

Rudin-Shapiro

A sequence of signs, 1s and -1s is defined. Then K_{th} Rudin sign r_k is the K_{th} element of the generated sequence [122]:

$$\begin{cases} \phi_n = 0, r_k = 1 \\ \phi_n = \pi, r_k = -1 \end{cases} \quad (7.9)$$

Newman

$$\phi_n = \frac{\pi}{N}(n-1)^2 \quad (7.10)$$

Random Phases

In this case, ϕ_n is assigned by a number between 0 and 2π randomly generated with a uniform distribution function.

7.2.3 Expected problem

These algorithms, as will be seen in section 7.4, perform at their full potential when the frequencies tones are equally spaced, Δf . Unfortunately, nothing can be further from the ideal situation than when working with a μ MUX where the resonators, after the fabrication process, are not equally spaced. Generate a multi-carrier signal taking this effect into account (non-equally spaced frequency components), has a direct impact in detriment of the performance of these multi-tonal signals generation algorithms. Modifying equation (7.2) for including a *perturbance factor* to the frequency assignment in the developed simulation framework helps to understand the implications of this situation, with which a range is created for a uniformly distributed frequency assignment:

$$\begin{cases} x(t) = \sum_{n=-\infty}^{\infty} C_n e^{jn2\pi f'_{tone} t + \phi_n} \\ C_n = \frac{1}{T} \int_{-T/2}^{T/2} y(t) e^{-jn2\pi f'_{tone} t} dt \\ f'_{tone} = f_{tone} + \delta_f(\delta_0, \Delta f) \end{cases} \quad (7.11)$$

where δ_0 is a small percentage (the *perturbance factor*) of the distance Δf , between the desired tones from which the random number is generated:

$$\delta_f(\delta_0, \Delta f) = X_U \wedge X_U \sim U(-\delta_0 \Delta f, \delta_0 \Delta f) \quad (7.12)$$

This parameters will be used for the simulations performed in section 7.4.

7.3 Complex baseband and bandpass signal

As was explained in Sections 3.4 and 4.4, the read-out signals of the μ MUX are typically in the microwave range (GHz). Currently there are high speed converters targeting direct synthesis and sampling of signals, for working directly in the operation frequency range. This is a topic of interest in this community as it simplifies the warm read-out electronics, specially avoiding the use of complex mixers. However this implies more costs and, until recently from the 3rd generation of the AMD's RFSoc devices, the SNR was not matching the requirements of the experiments where this work is involved [112]. Therefore the used RF Front-end for this read-out electronics prototype consists of a two-stage superheterodyne scheme [161], where two mixers are involved in the up-conversion and the down-conversion.

Mixing can be mathematical defined as the multiplication of two signals (convolution in the frequency domain):

$$x_{bb}(t) \cdot x_{LO}(t) \xrightarrow{\circ} X_{bb}(\omega) * X_{LO}(\omega) \quad (7.13)$$

where $x_{bb}(t)$ denotes the *baseband signal*, and $x_{LO}(t)$ the *local oscillator signal* or *carrier signal*, which will perform the frequency translation. The result of this operation, towards high frequency translations, creates a signal which is called *bandpass signal*. Having a real signal and multiplying it for another real signal, will shift this signal to the frequency of the carrier one, f_{LO} :

$$x_{bb}(t) \sin(2\pi f_{LO} t) \xrightarrow{\circ} X_{bb}(f) * \frac{j}{2} [\delta(f + f_{LO}) - \delta(f - f_{LO})] \Rightarrow \quad (7.14)$$

$$\Rightarrow \frac{j}{2} [X_{bb}(f + f_{LO}) - X_{bb}(f - f_{LO})] \quad (7.15)$$

The frequency spectrum of baseband real signals is symmetrical, which implies that it also is symmetrical in the translated region, above and below the carrier frequency.

Because of this, only the half of the bandwidth is useful: one of the sidebands of the carrier frequency will have to be filtered.

This complication is addressed by baseband complex signals using IQ modulation. This signal can be created from two real signals, commonly named I and Q (*In-Phase* and *Quadrature-Phase*):

$$\tilde{x}(t) = x_I(t) + jx_Q(t) \tag{7.16}$$

where $\tilde{x}(t)$ is called the *complex envelope* of the carrier signal, $x(t)$ [189, 190]. This can be seen by replacing in eq. 7.16 the I and Q components for sinusoidal signals, and then by their Euler's identity:

$$x_I(t) = A_I \cos(2\pi f_0 t) = A_I \frac{e^{j2\pi f_0 t} + e^{-j2\pi f_0 t}}{2} \tag{7.17}$$

$$x_Q(t) = A_Q \sin(2\pi f_0 t) = A_Q \frac{e^{j2\pi f_0 t} - e^{-j2\pi f_0 t}}{2j} \tag{7.18}$$

Which yields to the expression:

$$\tilde{x}(t) = A_I \frac{e^{j2\pi f_0 t} + e^{-j2\pi f_0 t}}{2} + j \left(A_Q \frac{e^{j2\pi f_0 t} - e^{-j2\pi f_0 t}}{2j} \right) \Rightarrow \tag{7.19}$$

$$\Rightarrow \tilde{x}(t) = (A_I + A_Q) e^{j2\pi f_0 t} \tag{7.20}$$

Eq. 7.20 shows how the complex signal is only present in one side of the spectrum, depending only of f_0 sign. An intuitive explanation of quadrature signals can be found here [191]. In SDR systems this is called the *complex baseband*. The bandpass signal, $x(t)$, is generated by an IQ modulator (or mixer), see Figure 7.3. An IQ mixer consists of two mixers and an adder, where the mixers have a common high frequency reference, and for one of them this reference is shifted 90° . The 90° offset suppresses the image frequencies components during the mixing process [90], allowing the bandwidth to be efficiently used as this allows to select each band independently.

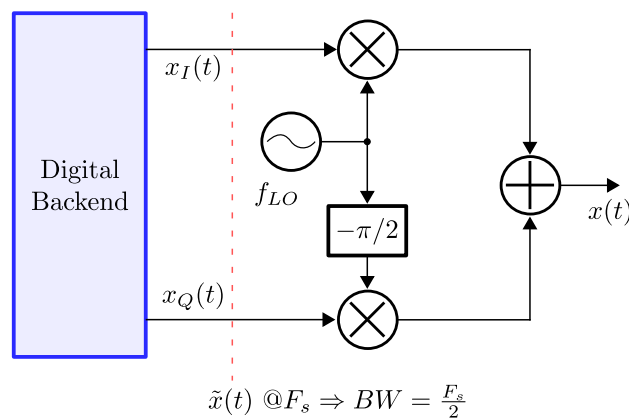


Figure 7.3: Complex envelope and bandpass signal generation.

The final result is that the positive frequencies appear in the upper sideband (above f_{LO}) and the negative ones in the lower side-band (below f_{LO}); meanwhile, $x(t)$ is a real-valued signal thanks to the conjugate term as it make $x(t)$ an Hermitian function, as can be seen in the equation (7.25) and illustrated in Figure 7.4:

$$x(t) = \Re [\tilde{x}(t)e^{j2\pi f_{LO}t}] \Rightarrow \quad (7.21)$$

$$x(t) = x_I(t) \cos(2\pi f_{LO}t) - x_Q(t) \sin(2\pi f_{LO}t) \Rightarrow \mathcal{F}\{\} \quad (7.22)$$

$$\Rightarrow \frac{1}{2}[X_I(f + f_{LO}) + X_I(f - f_{LO})] - \frac{j}{2}[X_Q(f + f_{LO}) - X_Q(f - f_{LO})] \Rightarrow \quad (7.23)$$

$$\Rightarrow \underbrace{\frac{1}{2}X_I(f - f_{LO}) + \frac{j}{2}X_Q(f - f_{LO})}_{X(f-f_{LO})} + \underbrace{\frac{1}{2}X_I(f + f_{LO}) - \frac{j}{2}X_Q(f + f_{LO})}_{X^*(f+f_{LO})} \Rightarrow \quad (7.24)$$

$$\Rightarrow X(f) = \frac{1}{2}[X(f - f_{LO}) + X^*(f + f_{LO})] \quad (7.25)$$

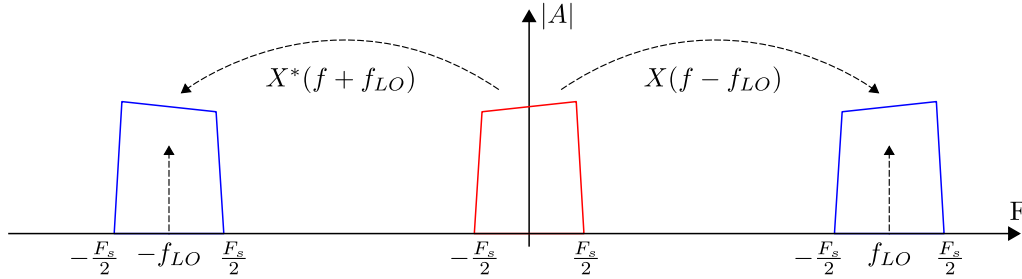


Figure 7.4: IQ Modulator / Mixer frequency shift, of the complex baseband towards the bandpass signal at f_{LO} .

For the usual case of using sinusoidal signals for the complex envelope, continuing with eq. (7.17) and (7.18), it can be demonstrated by the expression (7.25) the frequency shift ($A_I = A_Q = 1$, for simplicity):

$$x(t) = \cos(2\pi f_0t) \cos(2\pi f_{LO}t) - \sin(2\pi f_0t) \sin(2\pi f_{LO}t) \Rightarrow \mathcal{F}\{\} \quad (7.26)$$

$$\begin{aligned} \Rightarrow X(f) &= \frac{1}{2} [\delta(f + f_0) + \delta(f - f_0)] * \frac{1}{2} [\delta(f + f_{LO}) + \delta(f - f_{LO})] \\ &\quad - \frac{j}{2} [\delta(f + f_0) - \delta(f - f_0)] * \frac{j}{2} [\delta(f + f_{LO}) - \delta(f - f_{LO})] \end{aligned} \quad (7.27)$$

$$\begin{aligned} \Rightarrow X(f) &= \frac{1}{4} [\delta(f_0 + f_{LO}) + \delta(f_0 - f_{LO}) + \delta(-f_0 + f_{LO}) + \delta(-f_0 - f_{LO})] \\ &\quad + \frac{1}{4} [\delta(f_0 + f_{LO}) - \delta(f_0 - f_{LO}) - \delta(-f_0 + f_{LO}) + \delta(-f_0 - f_{LO})] \end{aligned} \quad (7.28)$$

$$\Rightarrow X(f) = \frac{1}{2} [\delta(f_0 + f_{LO}) + \delta(-f_0 - f_{LO})] \quad (7.29)$$

Eq. (7.29) is in perfect harmony with eq. (7.25), and Figure 7.4.

7.3.1 IQ Imbalance and the error model

The previous analysis in an ideal scenario delivers perfectly well located complex signals spread in the desired spectrum region. However, in the presence of the tiniest of imperfection in the signal path or the mixers itself, the history is completely different: interference products occur as the assumption of the perfect 90° offset, suppressing the image frequencies components during the mixing process [90] is not true anymore. There are several error models for the IQ imbalance analysis [192–196], but in general it can be described by the following modification to eq. (7.17) and (7.18):

$$x_I(t) = \alpha \cos(2\pi ft) \quad (7.30)$$

$$x_Q(t) = \sin(2\pi ft + \psi) \quad (7.31)$$

where α represents the gain imbalance, and ψ the phase imbalance. Doing the same analysis as before, the consequences of this imbalances can be deduced:

$$\begin{aligned} X(f) &= \frac{\alpha}{2} [\delta(f + f_0) + \delta(f - f_0)] * \frac{1}{2} [\delta(f + f_{LO}) + \delta(f - f_{LO})] \\ &\quad - \frac{j}{2} [\delta(f + f_0)e^{j\psi} - \delta(f - f_0)e^{-j\psi}] * \frac{j}{2} [\delta(f + f_{LO}) - \delta(f - f_{LO})] \end{aligned} \quad (7.32)$$

$$\begin{aligned} \Rightarrow X(f) &= \frac{\alpha}{4} [\delta(f_0 + f_{LO}) + \delta(f_0 - f_{LO}) + \delta(-f_0 + f_{LO}) + \delta(-f_0 - f_{LO})] \\ &\quad + \frac{1}{4} [\delta(f_0 + f_{LO})e^{j\psi} - \delta(f_0 - f_{LO})e^{j\psi} \\ &\quad - \delta(-f_0 + f_{LO})e^{-j\psi} + \delta(-f_0 - f_{LO})e^{-j\psi}] \end{aligned} \quad (7.33)$$

Eq. (7.33) shows the mentioned problem when gain and phase imbalances appears: there are components that are not removed by the mixing process, hence, appearing with some relative power on the other side of f_{LO} . From eq. (7.30) and (7.31), a quality factor can be deduced [193, 197] named as Image Rejection Ratio (IMRR) (or IRR depending on the bibliography), see Figure 7.5:

$$IMRR = \frac{\alpha^2 + 1 - 2\alpha \cos(\psi)}{\alpha^2 + 1 + 2\alpha \cos(\psi)} \quad (7.34)$$

The IMRR value should be in principle, the same as the ADC SNR of ~ 64 dB. This is required as any component below the ADC SNR level will be indistinguishable.

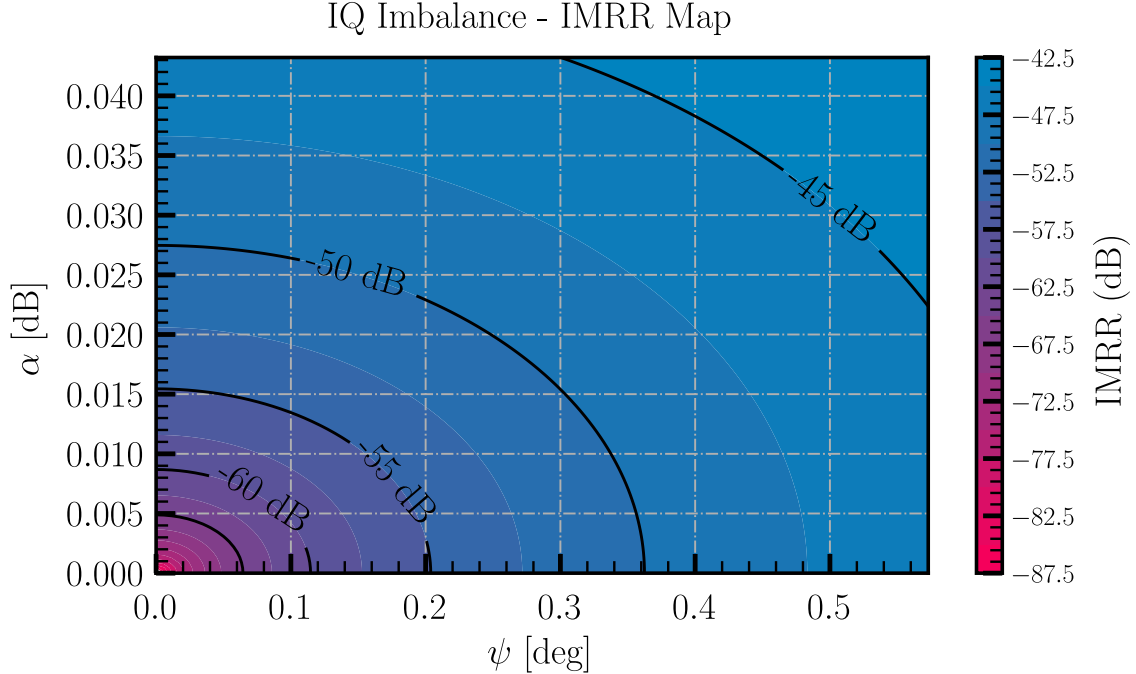


Figure 7.5: IMRR Map: this plot gives insight on how much phase and gain imbalance is tolerable, and how the tiniest of the imbalances can generate a comparable image component (in terms of power). We should be able to control step values of less than 0.1° for the phase imbalance compensation parameter, and less than 0.01 dB for the gain imbalance compensation parameter; in order to achieve an IMRR of less than 60 dB.

7.3.2 Considerations

Correcting the IQ Imbalance in this kind of systems is quiet intricate. The digital backend is connected to a second set of warm electronics which is the RF front-end as was explained in section 4.4 and Figure 4.6, and after it, to the cryostat and the internal electronics. The cryostat can be considered (as a simple two port device) as a completely adapted system (in terms of impedance matching). The transmission path (DAC towards the cryostat) and the reception path (the cryostat towards the ADC) are then, two totally independent paths in terms of signal integrity. It is clear that due to the up-conversion and down-conversion stages in the RF front-end it does not matter that the output signal from the RF front-end to the cryostat is perfectly balanced up to the desired IMRR, when this signal is down converted once is returning from the cryostat, the mixer will introduce a new imbalance to the signal. Then two correction stages take place: for the transmission path and for the reception path. This work only covers the analysis and solution for the transmission path. The reception correction is the same as [118]. Meanwhile, the calibration procedure for the transmission path is based on the works by [118, 198].

7.4 Computational simulations

In the following, a set of simulations are presented. The enumerated PAPR optimization methods were used. The simulation constraints were assigned as a function of the real generation requirements: $F_s = 1$ Gsps, a frequency resolution of 7629.39 Hz (as will be explained in 8.1) and a test signal of 80 tones spanning from -400 MHz to 400 MHz with a local oscillator (LO) guard region from -20 MHz to 20 MHz. Figure 7.6 shows this simulation together with the Probability Distribution Function (PDF) of their amplitude values.

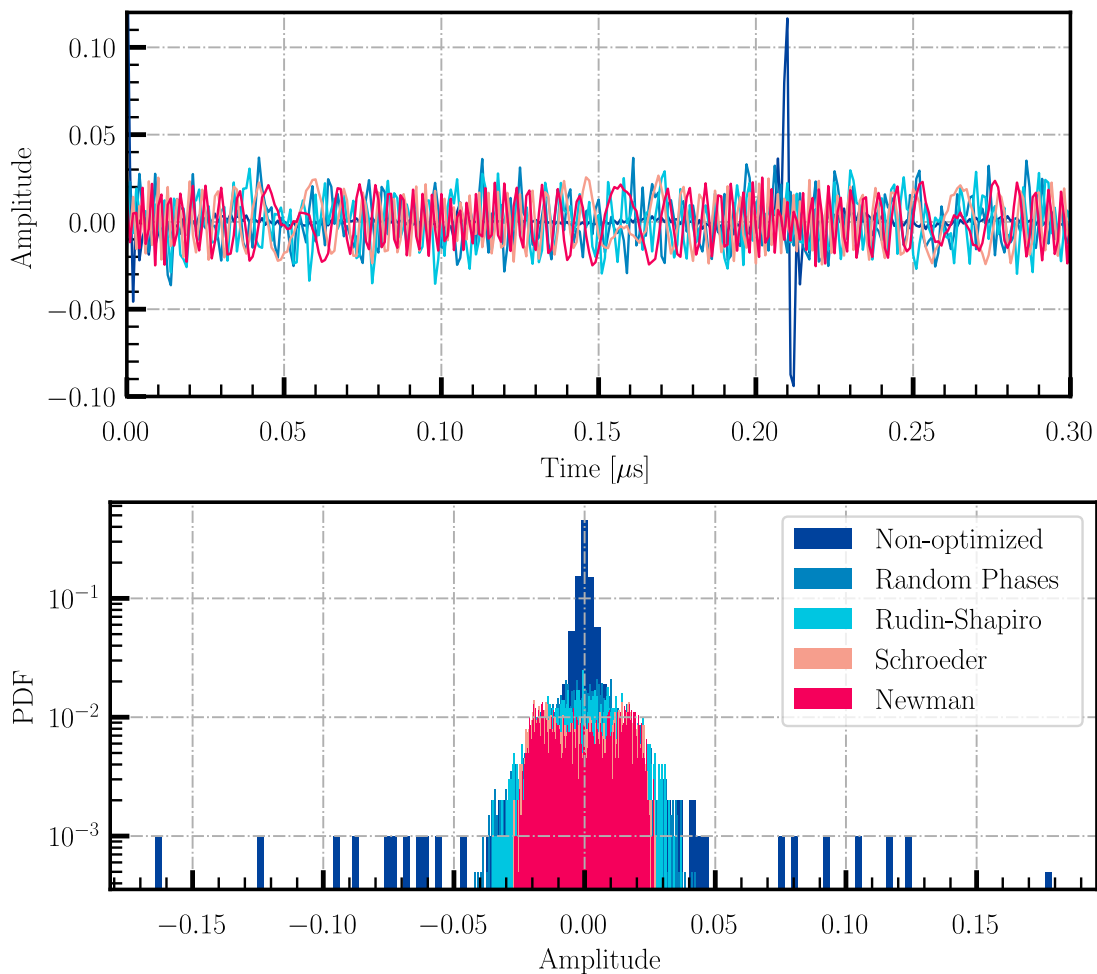


Figure 7.6: 80 tones multitone signal, generated by 5 different methods: no phase optimization, Rudin-Shapiro, Newman, Random Phases and Schroeder. The plot at the bottom represents the amplitudes' PDF.

Figure 7.7 depicts the CCDF already introduced in formula (7.6). The expected poor performance of the non-optimized method is now completely clear: this plot together with the PDF in Figure 7.6 showing that the signal is expending most of its time in very low amplitude values and then an instant in the highest values.

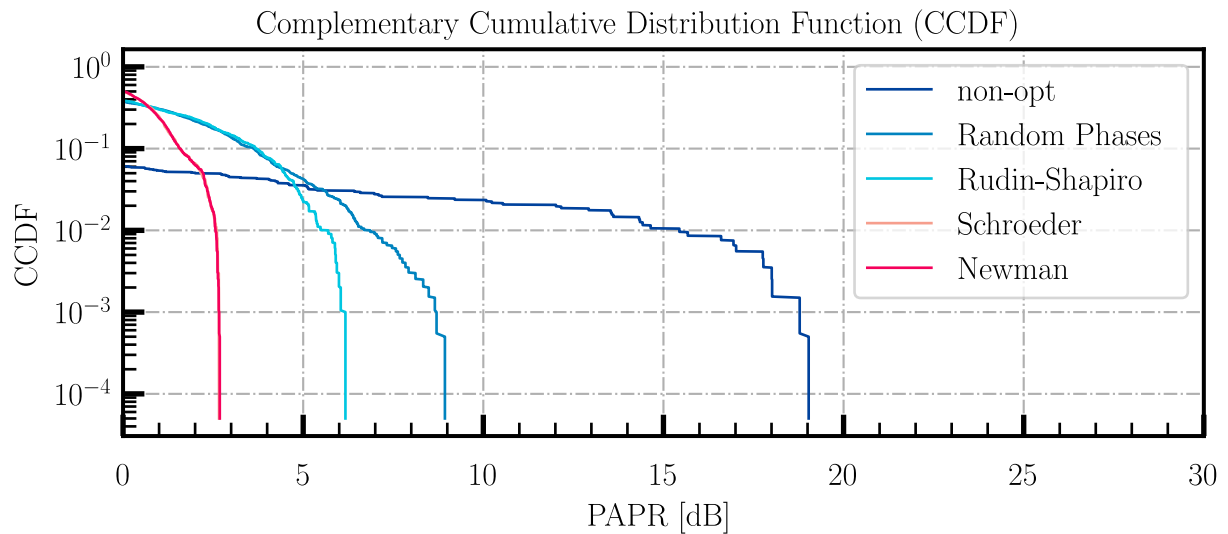


Figure 7.7: CCDF of the 80 tones signal for each PAPR reduction algorithm. The Newman and Schroeder methods performance is quite similar (their curves are indistinguishable at this scale).

Finally, Figure 7.8 shows the evaluation of this algorithms in a more realistic scenario where the distance between the frequency components (Δf) is not constant. These simulations were performed using the modifications enumerated in equations (7.11) and (7.12). It is remarkable to see that as the range for the randomness in this value increases, the PDFs and PAPR of the aforementioned methods (except the non-optimized) exhibits a trend to a *random phases* performance a-like.

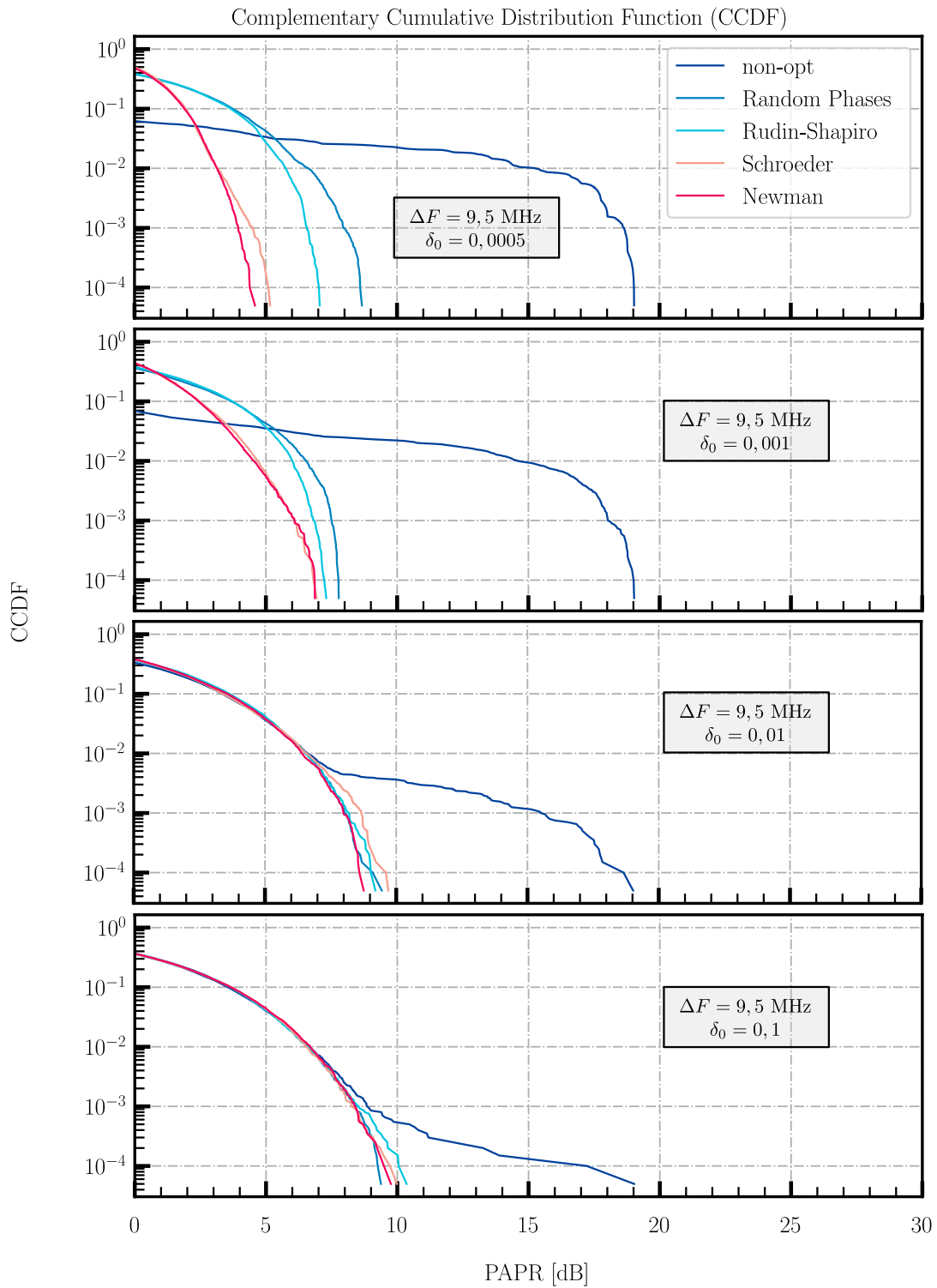


Figure 7.8: CCDF for different randomization values for the frequency assignment in each tone. It is interesting to note that as the relative variation of the frequency values increases there is an apparently convergence value of roughly 10 dB for all the methods, except for the non-optimized one.

Chapter 8

Firmware Implementation and Readout Electronics integration

8.1 Signal Generation

The used stimulation module was developed in [118]. It consists of a dual-port asynchronous Block RAM (BRAM) memory, see Figure 8.1. One port is connected to an AXI4-Lite interface operated by an AXI4-Lite clock, from which it can be written. The access to the memory is not address-based: the data is written to a constant address on the AXI4-Lite interface and the memory is sequentially filled with the 32-bit data words. The other port is connected to the DAC, and can be greater than 32-bits forwarding several samples to the DAC at the same time. These samples are 16 bits wide, and the memory size is N . Finally, the playback process is implemented by counters and a state machine. The frequency resolution is determined by:

$$\Delta f = \frac{f_{clk}}{N} \quad (8.1)$$

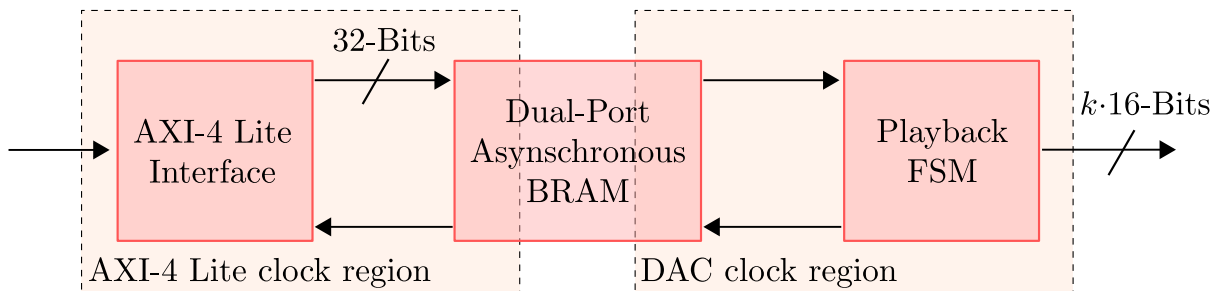


Figure 8.1: Overview of the implemented stimulation module for the multi-tonal signal generation. k is related with the frequency operation in the logic and the sampling frequency of the DAC. The module requires the definition of how many octets (8-bit samples) and that value relates with k .

The DACs sampling frequency is 1 Gsps, and the logic works at 250 MHz; which

means that the module needs to deliver 4 samples per clock. This is done by packaging the samples in octets: 16 octets is the required configuration for this module [118]. Now the definition of how many slices (memory depth N) depends on the required resolution. For the purposes of this Thesis, a suitable frequency resolution is desired as this module plays a critical role in the performance evaluation of designed channelizer. The used resources for this module is depicted in table 8.1.

CLB LUTs	CLB Registers	BRAM	DSP
645	721	128	-

Table 8.1: Resource requirements for one stimulation module working at 250 MHz configured for a frequency resolution of 7629.39 Hz (SLICES = 32768, OCTETS_PER_CLK = 16).

8.2 Goertzel Filter Bank

The proposed channelizer based on a Goertzel Filter consists of several stages, summarized in Figure 8.2.

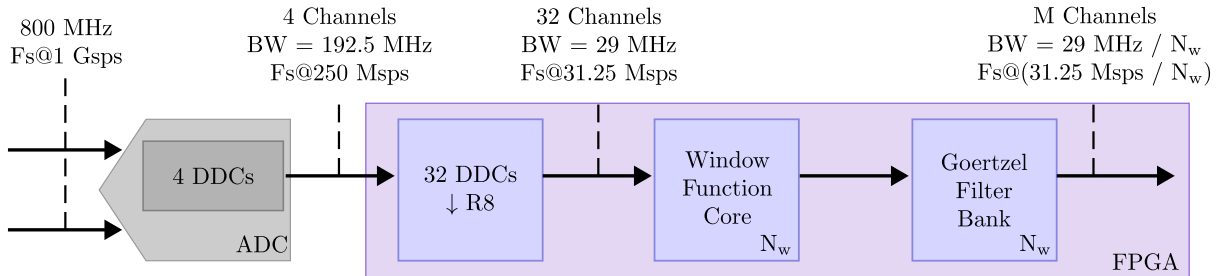


Figure 8.2: Overview of the first frequency demodulation cascade.

Each block will be explained in detail in the following sections. The chosen ADC for the prototype operates at 1 Gsps (IQ sampling). For this implementation it was decided to work with $f_{logic} = 250$ MHz. In addition, to save resources, also one of the ADC features was used that implements a decimation by 4, giving a resulting F_s of 250 Msps and four sub bands of 192.5 MHz each. In particular, for the GF approach, the output BW (or final sampling frequency, F_s) will depend on the length of the window function, N_w .

The channelization process from the ADC to the DDCs outputs described so far, can be seen in Figure 8.3. The output is fed into the GFB for the final channelization step, where each GF is connected to four DDCs. The interconnection between the DDCs and the GFB is explained later in section 8.2.2.

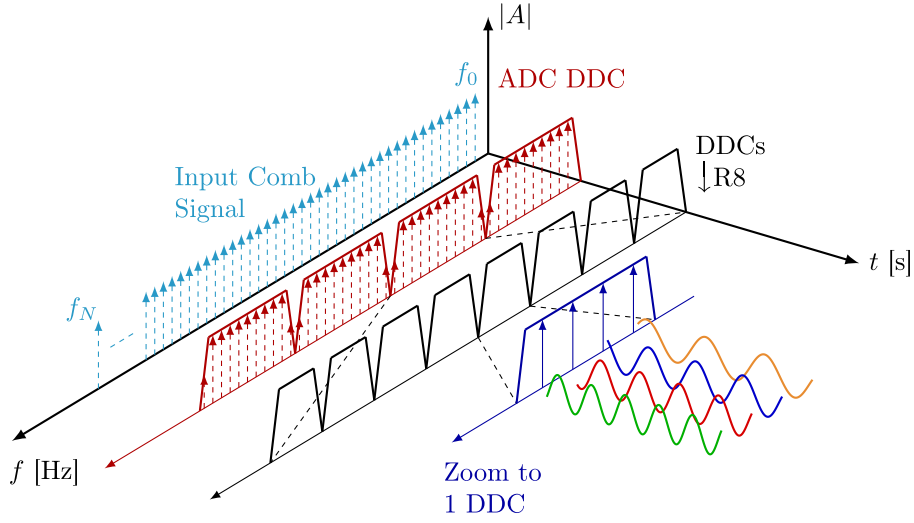


Figure 8.3: Channelization process from the ADC to the DDC stages in the proposed firmware.

8.2.1 Goertzel Filter Core

The ease reading and understanding, algorithm 4 is rewritten here. Highlighted there are two main parts, an iterative section and a non-iterative section.

Algorithm 4: Goertzel algorithm generalized to non-integer multiples of fundamental frequency k

```

1  $\alpha = \frac{2\pi k}{N}$ 
2  $\beta = \frac{2\pi k(N-1)}{N}$ 
3  $a = \cos(\beta)$ 
4  $b = -\sin(\beta)$ 
5  $c = \sin(\alpha) \sin(\beta) - \cos(\alpha) \cos(\beta)$ 
6  $d = \sin(2\pi k)$ 
7  $\omega_0 = \omega_1 = \omega_2 = 0$ 
8 for  $N = 0$  to  $N - 1$  do ▷ Iterative Section
9      $\omega_0 = x[n] + 2 \cos(\alpha)\omega_1 - \omega_2$ 
10     $\omega_2 = \omega_1$ 
11     $\omega_1 = \omega_0$ 
12  $X_k = a\omega_1 + c\omega_2 + j(b\omega_1 + d\omega_2)$  ▷ Non-iterative Section
13  $|X_k| = \sqrt{(a\omega_1 + c\omega_2)^2 + (b\omega_1 + d\omega_2)^2}$ 
14  $\Phi(X_k) = \arctan\left(\frac{b\omega_1 + d\omega_2}{a\omega_1 + c\omega_2}\right)$ 
    
```

From the iterative part, $\omega_0 = x_{in} + 2 \cos(\alpha)\omega_1 - \omega_2$, was mapped to two DSP Slices and their interconnection can be appreciated in Figure 8.4. Two clock cycles are required for determining one ω_0 value which in principle states that the ratio between the logic operation frequency, f_{logic} , and the sampling frequency of the incoming samples, F_S , needs to be at least two. However, adding the appropriate pipeline stages to the architecture

removes this limitation, allowing $F_S = f_{logic}$. The module that calculates $X[k]$ in the Non-Iterative section of the Figure 8.5 uses 12 DSP Slices and handles 32 IQ components when connected to eight Goertzel Algorithm Mapping modules.

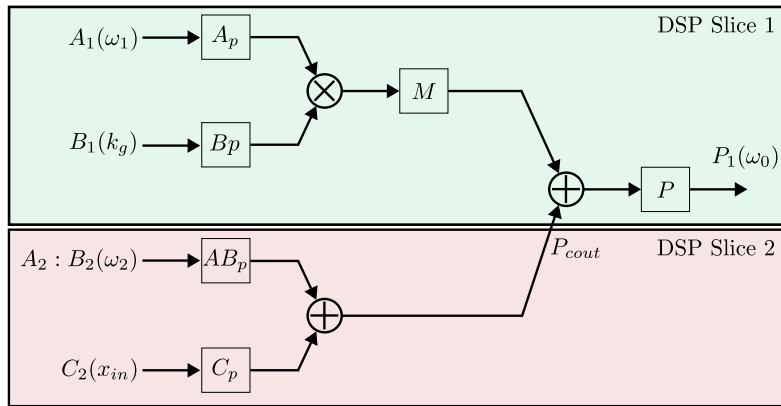


Figure 8.4: Goertzel Algorithm Mapping module. Two DSP Slices are used: A_p , B_p , AB_p , C_p , M and P refers to the pipeline level within the DSP Slice configuration for AMD’s DSP48E2. As P_{cout} is configured to be used, the two DSP Slices are neighbours in the chip. This is applied to all the used DSP Slices involved in the GF mapping.

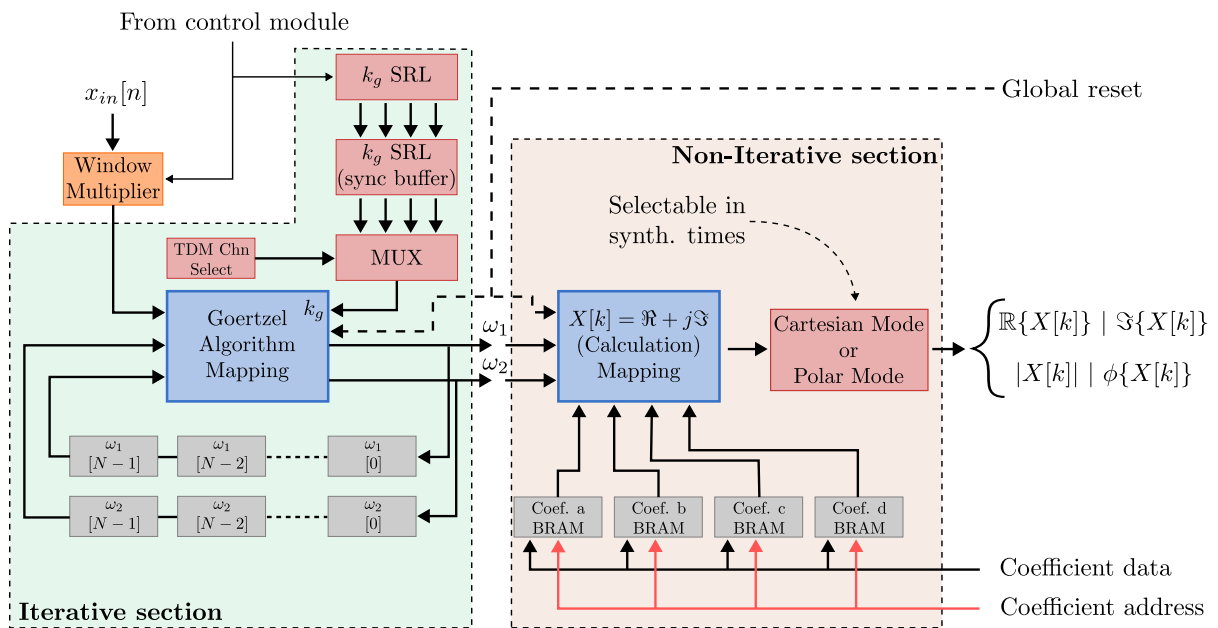


Figure 8.5: Block Diagram of the implemented GF structure.

The *Cartesian Mode* is directly supplied by the algorithm 4 (line 12), while the *Polar Mode* (lines 13 and 14) requires the addition of a CORDIC module for the translation of the cartesian (or rectangle) representation of the complex DFT bin to the polar representation. The used resources for the Goertzel Filter core are depicted in table 8.2.

	CLB LUTs	CLB Registers	BRAM	DSP
G.F. kernel	1	32	-	2
G.F. I.S.	369	528	-	-
G.F. N.I.S.	889	414	-	16

Table 8.2: Resource requirements for the GF Core at 250 MHz, capable of processing four complex tones. I.S. stands for *Iterative Section* and N.I.S. for *Non-Iterative Section*. The resources of the kernel already presented, are repeated in this table for completeness.

8.2.2 Digital Down Converter design

A second decimation stage by 8 was implemented using a DDC, resulting in a final sampling frequency of 31.25 Msps. This DDC is based on a CIC filter as was explained in chapter 5. It uses 3 DSP slices for the complex mixer and 16 DSP slices for the CFIR filter (considering the two channels, I and Q). The decision to use a second DDC stage is based on exploiting and exploring the combination of the defined f_{logic} and the necessity to introduce a register in the feedback path of the GF as will be seen later. The implementation is sketched in Figure 8.6. A Direct Digital Synthesis (DDS) core implements the generation of the complex signal for doing the frequency translation.

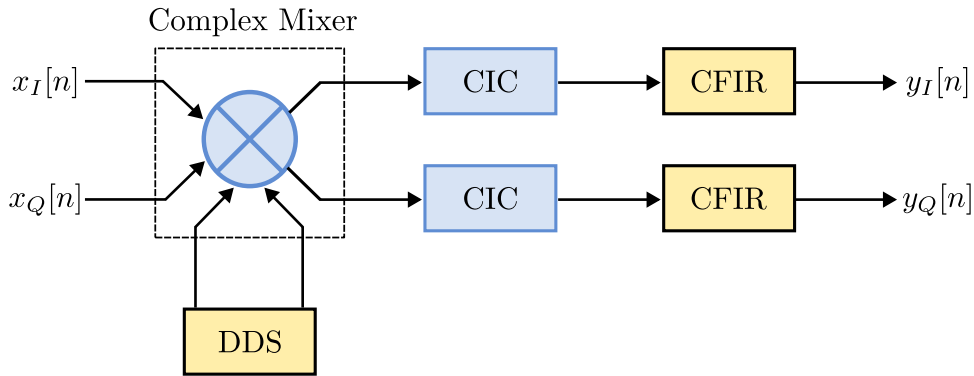


Figure 8.6: Digital Down Converter schematic. $x_I[n]$ and $x_Q[n]$ are multiplied by a complex signal generated by a DDS using a complex mixer. These signals arrive from two ADCs which deliver the I and Q components. The LPF presented in Figure 5.1 is comprised by the CIC and CFIR filters.

The GF structure presented in Figure 8.4 only works for one signal component when $F_S = f_{logic}$ (no second DDC stage). When working with complex signals in quadrature modulation, two structures are required (one for I and one for Q) and therefore a total of four DSP slices:

$$GF_{DSP_0} = 4N_{CT} \quad (8.2)$$

where N_{CT} is the number of Complex Tones to process. When the GF is combined with the DDC stage, the expression to calculate the number of DSP Slices used is:

$$GF_{DSP_1} = \frac{4N_{CT}}{R} + R \left(\frac{128}{R} + 3 \right) = \frac{4N_{CT}}{R} + 3R + 128 \quad (8.3)$$

where R stands for *Decimation Ratio*. $R \left(\frac{128}{R} + 3 \right)$ represents the relationship between the required DSP Slices in the CFIR, the input F_s (after the CIC filter), $f_{logic} = 250$ MHz, the filters order and the quantization parameters, according to Xilinx's FIR Compiler tool [199]. The optimum value for this expression is determined by analyzing its derivative:

$$\frac{\partial GF_{DSP_1}}{\partial R} = -\frac{4N_{CT}}{R^2} + 3 \quad (8.4)$$

For example, for a fixed value of $N_{CT} = 64$, $GF_{DSP_0} = 256$ DSP slices, however the optimum R value in eq. (8.4) is ~ 9.24 , resulting in 183.4 DSP Slices. $R = 8$ is the closest feasible value to work with [166]. The simulated frequency response of the designed DDC can be appreciated in the next Figure 8.7:

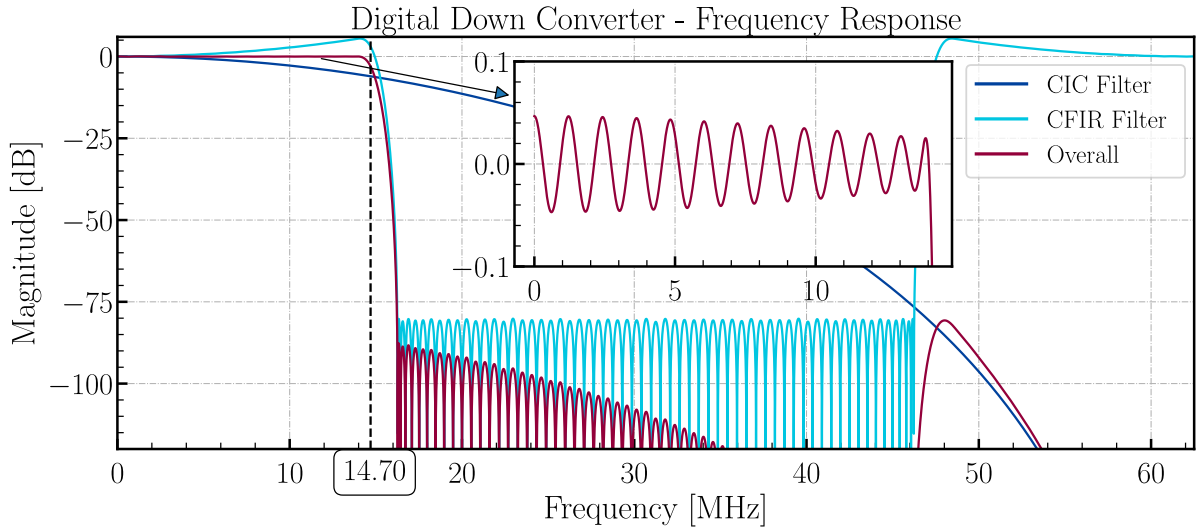


Figure 8.7: Digital Down Converter: python simulated frequency response of the whole filter chain where the CIC, CFIR and overall response are plotted. The 3 dB frequency cut, f_{cut} , marked with the dashed black vertical line is 14.70 MHz and a ripple of less than 0.1 dB can be observed.

Adding this decimation ratio introduces the capability of the designed GF architecture of Figure 8.4 to process four complex DFT bins (or 8 real DFT bins). This is achieved by serially supplying the samples from four different DDCs. The interconnection structure between the GFs and the DDCs is depicted in Figure 8.8, and the used resources for one DDC are listed in table 8.3.

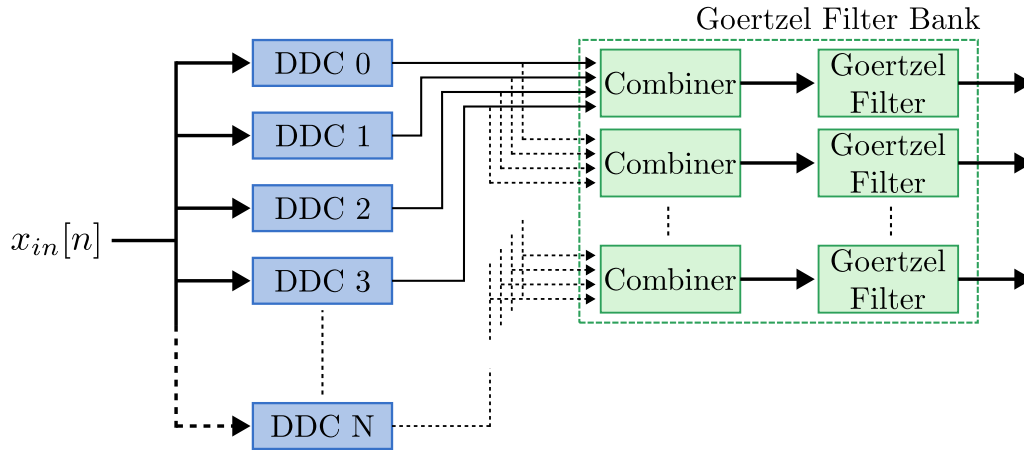


Figure 8.8: Block Diagram of the interconnection between DDCs and GF Cores (the core is composed by the combiner and the GF). Each GF core handles 4 DDCs. The combiner will collect the samples for the DDCs and serialize them to the GF. Each DDC is connected to several GF cores.

CLB LUTs	CLB Registers	BRAM	DSP
1772	3055	2	19

Table 8.3: Resource requirements for one DDC working at 250 MHz for $R = 8$, a bandwidth efficiency of 94% (sampling frequency vs cut-off frequency) and 80 dB of alias rejection.

8.2.3 Window Function

The Window Function block cyclically applies the desired window to the input signal, x_{in} . A block diagram can be appreciated in the next Figure 8.9. Each Window Multiplier is connected to four DDCs as it can be appreciated from Figure 8.8 by means of the combiner module. The required resources are shown in table 8.4.

	CLB LUTs	CLB Registers	BRAM	DSP
AXI Controller and Memory	87	285	4	-
Window Multiplier	51	147	-	2

Table 8.4: Resource requirements for the controller and one Window Multiplier working at 250 MHz.

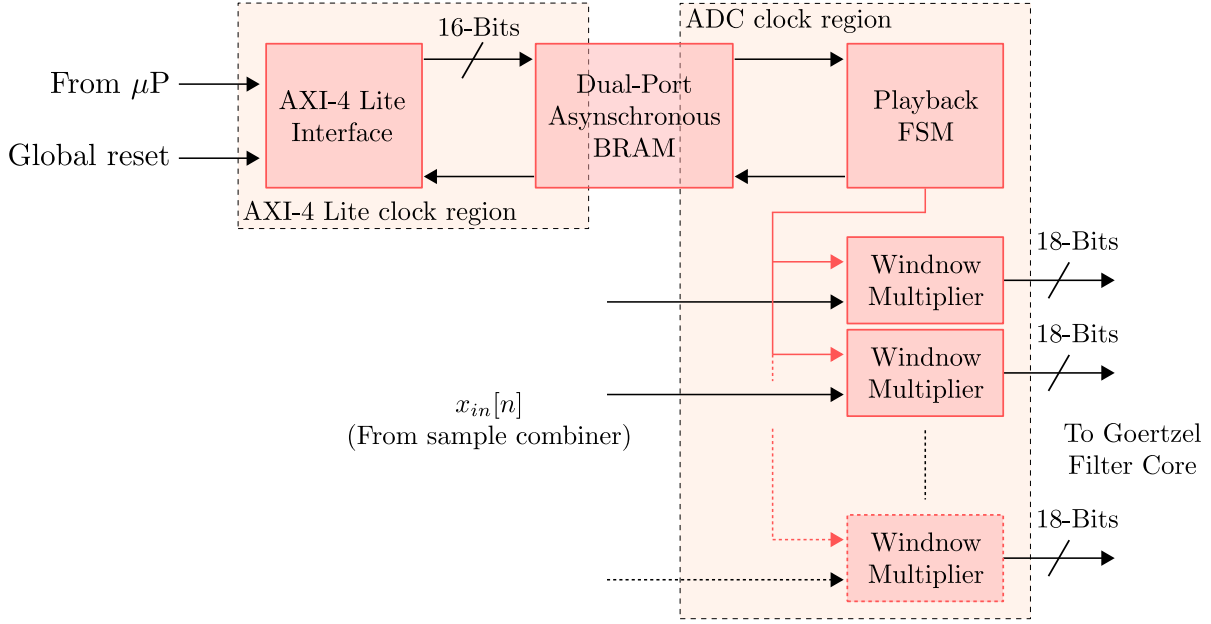


Figure 8.9: Window function block diagram. The AXI-4 Lite and the dual-port BRAM are common cores to all window multipliers. Each window multiplier is then connected to one GF core.

The *global reset* signal (also present in 8.5) performs the synchronization between all modules and is triggered by another core every time that N_w samples (the window size) where processed by the GF core. This cleans and prepare the pipeline for the next following N_w samples that are continuously arriving.

8.3 Signal-to-Noise Ratio (SNR)

The selected ADC samples at 1 Gps and has an ENOB of 10.3 bit at $f_{in} = 450$ MHz, which is used as the starting data width for the following calculations, and a protected aliasing bandwidth of 192.5 MHz for $R_{ADC} = 4$ (R_{ADC} is the decimation ratio configured in the ADC). The estimated SNR is calculated as:

$$\text{SNR} = 6.02N + 1.76\text{dB} + 10 \log_{10}\left(\frac{Fs}{2BW}\right) \quad (8.5)$$

The decimation stage adds a Processing Gain (PG) to the base SNR of the ADC of ≈ 4.145 dB (in accordance with the datasheet specification of 4 dB), giving an SNR ≈ 67.91 dB which requires 11 Bits for data width according to eq. (8.5). Taking into account the impact of the clock jitter on the SNR, a correction of the previous value is necessary:

$$\text{SNR}_{jitter} = -20 \log_{10}(2\pi f_{in} t_j) \quad (8.6)$$

$$\text{SNR}_0 = 10 \log_{10}\left[10^{\left(-\frac{\text{SNR}_{ADC}}{10}\right)} + 10^{\left(-\frac{\text{SNR}_{jitter}}{10}\right)}\right] \quad (8.7)$$

This gives an initial $\text{SNR}_0 \approx 67.60$ dB which also requires 11 Bits for $t_j = 55$ fs rms (for AD9680). Afterwards, the second decimation stage takes place and introduces a new PG relative to the effective BW of this stage, which is about 29 MHz. The PG is defined by the term: $10 \log_{10}(\frac{F_s}{2BW})$ in eq. 8.5. After the second decimation stage, an $\text{SNR}_1 \approx 74.01$ dB is achieved which requires 12 bits as data width. Finally, the GF is applied. Now the PG depends on the size and type of the selected window:

Window Function	PG [dB]	SNR [dB]	NBits
Modified Flat-top	15.34	89.36	15
Dolph-Chebyshev	18.42	92.43	16
Rectangular	21.55	95.56	16

Table 8.5: Window functions PG, final SNR and final number of bits, for window size of $N = 256$ samples.

From this analysis, an estimation of the SNR performance of the entire channelizer can be done, as a function of the input frequency and the necessary number of bits for each stage in order to preserve the expected SNR. These results are shown in Figure 8.10 and in table 8.6.

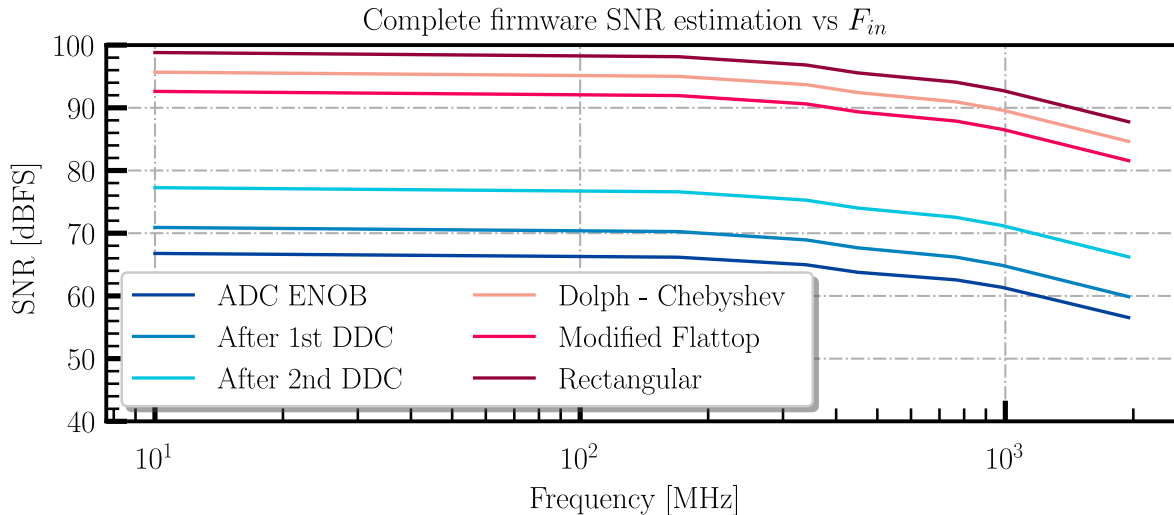


Figure 8.10: Signal-to-Noise Ratio as a function of the input frequency. ADC ENOB refers to the SNR of the ADC before the first decimation stage, considering the jitter contribution. The following curves for the DDCs are obtained by adding the Processing Gain. Finally, three different windows are evaluated.

ADC Converter	ADC DDC	DDC (firmware)	Goertzel Filter
16	16	18	32

Table 8.6: Data width after each stage. *ADC Converter* refers to the ADC block within the chip previous to the internal DDC. *ADC DDC* refers to the internal DDC of the ADC. *DDC firmware* refers to the described hardware within the FPGA.

8.4 Arithmetic treatment

8.4.1 Window function compensation and Goertzel Filter overflow control

The use of window functions to improve the channelizer performance also distorts the signal as can be seen in Figure 8.11, where it is possible to appreciate that the energy and the amplitude of the signal were affected.

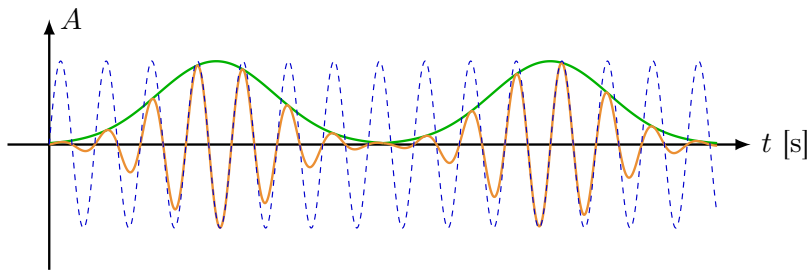


Figure 8.11: Window function (green) applied to a signal (dashed blue).

Since in this work the scientific data is retrieved by analyzing the amplitude of the input tones the amplitude compensation is necessary. This can be corrected by performing the following calculation, which makes the process compatible with any type of window:

$$ACF = \frac{1}{\sum_{i=0}^{N-1} w[n]} \quad (8.8)$$

where *ACF* is the window *Amplitude Correction Factor*, which is also the inverse of the *Coherent Gain*. This compensation is applied in the non-iterative section after the real and imaginary parts of $X[k]$ are calculated.

One of the major considerations during the algorithm implementation is the fixed-point arithmetic treatment. As the GF is an IIR Filter type, the arithmetic growth within the internal registers must be controlled. Several works such as [200–202] suggest different scaling considerations in order to minimize or avoid the overflow situations in the calculation process. The scaling process is applied at the input of the iterative section

to w_1 and w_2 , and not to the input signal, because this has a negative impact on the SNR, when they are reintroduced into the Goertzel algorithm mapping module (see Figure 8.12) by an arithmetic shift (saving FPGA resources), and is configurable by software. The scaling applied is:

$$ASF = \frac{4N}{\pi} \quad (8.9)$$

where ASF stands for *Arithmetic Scaling Factor* and N is the size of the window. This result is then converted to a defined number of bits to be shifted doing a ceiling of the following expression:

$$ASF_{bits} = \lceil \log_2(ASF) \rceil \quad (8.10)$$

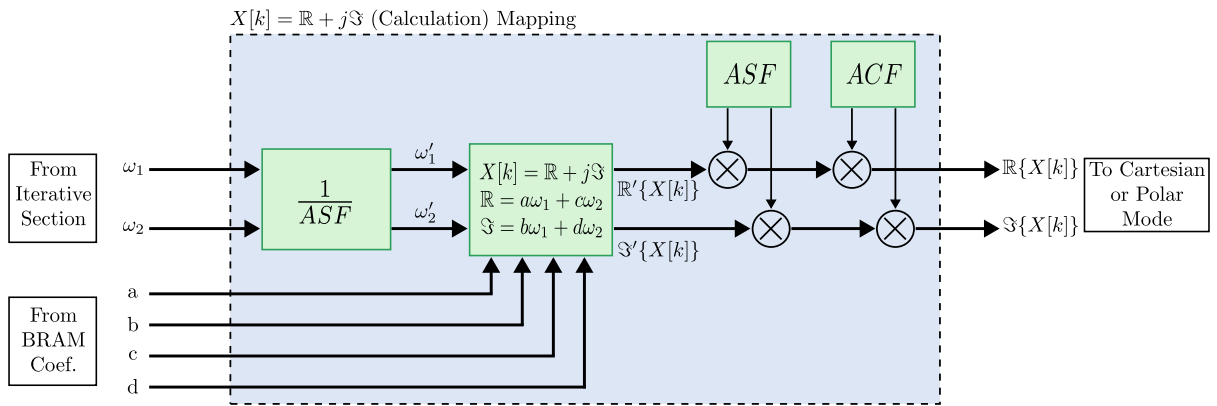


Figure 8.12: Arithmetic treatment. The multiplications symbols were actually performed by arithmetic shifting in order to save resources in the corresponding modules.

8.4.2 Fixed Point arithmetic

Fixed point arithmetic is a critical aspect of the acquisition systems. As this work is proposing a different approach targeting an optimized mapping of the Goertzel Filter, there are no already solved cores for the different required modules of the system (apart from using the FIR Compiler, DDS Compiler and the CORDIC core from AMD's Vivado), as was presented in the previous sections. The selection of the wordlength for each stage of the acquisition chain and the binary point place, was carefully designed: i) accounted from the SNR analysis performed before (the minimum register length), ii) achieve a high data precision and dynamic range.

The Q notation, for $Qm.n$, varies among developers depending on which brand definition they use, from Texas Instruments or ARM. In this work, the ARM convention was used where the wordlength is defined by $m + n$, with m bits for the integer part including the sign bit (for a two's complement representation) and n bits for the fractional part. This gives a more intuitive reading. AMD's Vivado IP Cores uses the Texas Instruments convention where the integer part, m , does not include the sign bit so the wordlength

is calculated as $m + n + 1$. Figure 8.13 shows the evolution of the wordlength and its fixed-point representation.

In general terms, each rational value will be given by a subset contained in:

$$P = \left\{ \frac{p}{2^n} \mid -2^{N-1} \leq p \leq 2^{N-1} - 1, p \in \mathcal{Z} \right\} \quad (8.11)$$

The value of an specific N-bit binary number in $Qm.n$ is given by:

$$x = \frac{1}{2^n} \left[-2^{N-1}x_{N-1} + \sum_{i=0}^{N-2} 2^i x_i \right] \quad (8.12)$$

with i being the i -th bit of x . The range is described by:

$$-2^{N-1-n} \leq x \leq 2^{N-1-n} - \frac{1}{2^n} \quad (8.13)$$

The ranges and other specifications for each stage are expressed in the next table:

Stage	Precision	Range	Resolution	Dynamic Range
DDC	16	$[-2^{15}; 2^{15} - 0.000031]$	0.000031	2^{15}
WF	18	$[-2^{16}; 2^{16} - 0.000031]$	0.000031	2^{18}
GFB	32	$[-65536.0; 65535.999969]$	0.000031	2^{32}
CORDIC	32	$[-4.0; 3.999...355]$	$1,862645e^{-9}$	2^{32}

Table 8.7: Precision, range, resolution and dynamic range for each stage according to its fixed-point representation. The accuracy can be calculated as the resolution divided by two. WF stands for Window Function.

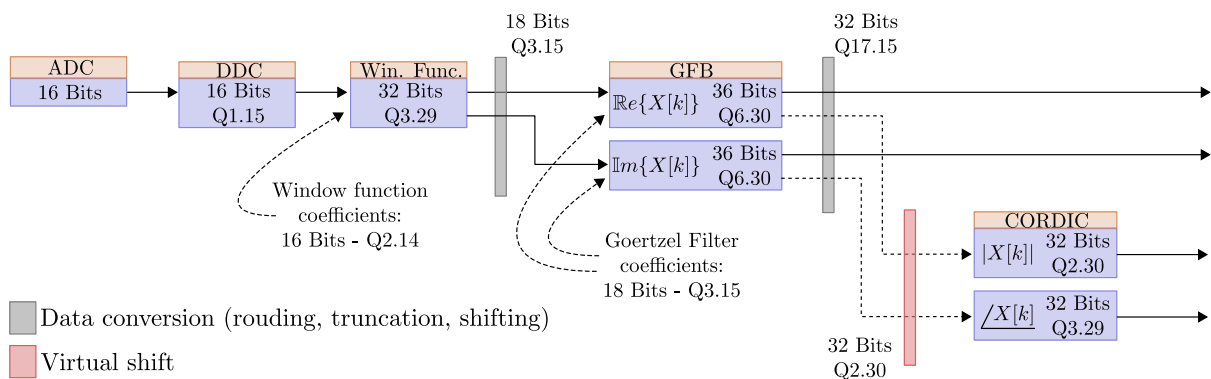


Figure 8.13: Fixed-point arithmetic for each module in the acquisition chain. The representation can start from the DDC output after the FIR Compensation filter. In this figure, the CORDIC Core fixed-point notation was translated to the ARM notation. The 18-bit wordlength in the GFB is due to the minimum bit width of the DSP Slices DSP48E smaller register.

8.5 Complete prototype firmware implementation

The complete prototype firmware is depicted in Figure 8.14. This minimum implemented firmware consists of four DDCs after the receiver JESD204B core, giving one available sub-band from the ADC (of the four available ones); one Goertzel Filter Core detecting one tone in each DDC, which allows the processing of four different frequency tones. The DDC can be tuned in run-time, spanning the whole selected sub-band (from DC to 250 MHz) yielding a coarse tuning of the channelization process, while the fine tuning is achieved with each GF from the GFB (one Goertzel Filter Core represents four GF). The JESD204B modules (the PHY and the core) are AMD's IP Cores for both the receiver and transmitter paths.

The IQ correction and the flux-ramp demodulation modules (in grey) were not implemented yet. The latter one is currently done in a Python script in a post-processing step, doing a quadrature demodulation as proposed by Mates [99, 106].

The GFB output gives a unique 64-bit width stream from where 32 bits belongs to the real part or magnitude of $X[k]$, and the other 32 bits to the imaginary part or phase of $X[k]$. Each of the modules that calculates $X[k]$ in the *non-iterative* section handles 32 channels in a TDM scheme.

After it, the samples are delivered to a DMA for storing the process and calibration data in the main memory, so they can either be further processed on site or forwarded to a server system via an ethernet connection. Depending on how it was configured (and the connected memory), the memory areas where the DMA will work can be in the DDR memory of the processing system or in the programmable logic [118].

The multi-carrier I&Q signal is generated by the transmitter path thanks to the Stimulation module with a resolution frequency of 7629.39 Hz (depending on the memory depth, which can be increased until 131 072 elements because is not using the Ultra RAM slices, giving a minimum resolution of 1907.35 Hz).

All firmware modules that can be configured in run-time are connected to the main processor system via an AXI4-Lite bus (red). The Platform Information and Management Core (PIMC), is a firmware module that provides information about the platform status and control options.

The final resources consumption estimation per complex tone for the implemented channelizer are displayed in table 8.8, with a disaggregation of the two principal parts (the DDC and the GF parts) and a comparison with ECHO's firmware from [118]. The comparison is done for processing 128 complex tones. The ECHO's firmware runs at 500 MHz and the one from this work runs at 250 MHz. The individual channel complex bandwidth in this approach lies between 0.61 MHz to 3.9 MHz, which depends on the size and type of the window function and is re-configurable in run-time. In the case of ECHO, the individual channel complex bandwidth lies between 1 MHz to 3.2 MHz and is not re-configurable in run-time.

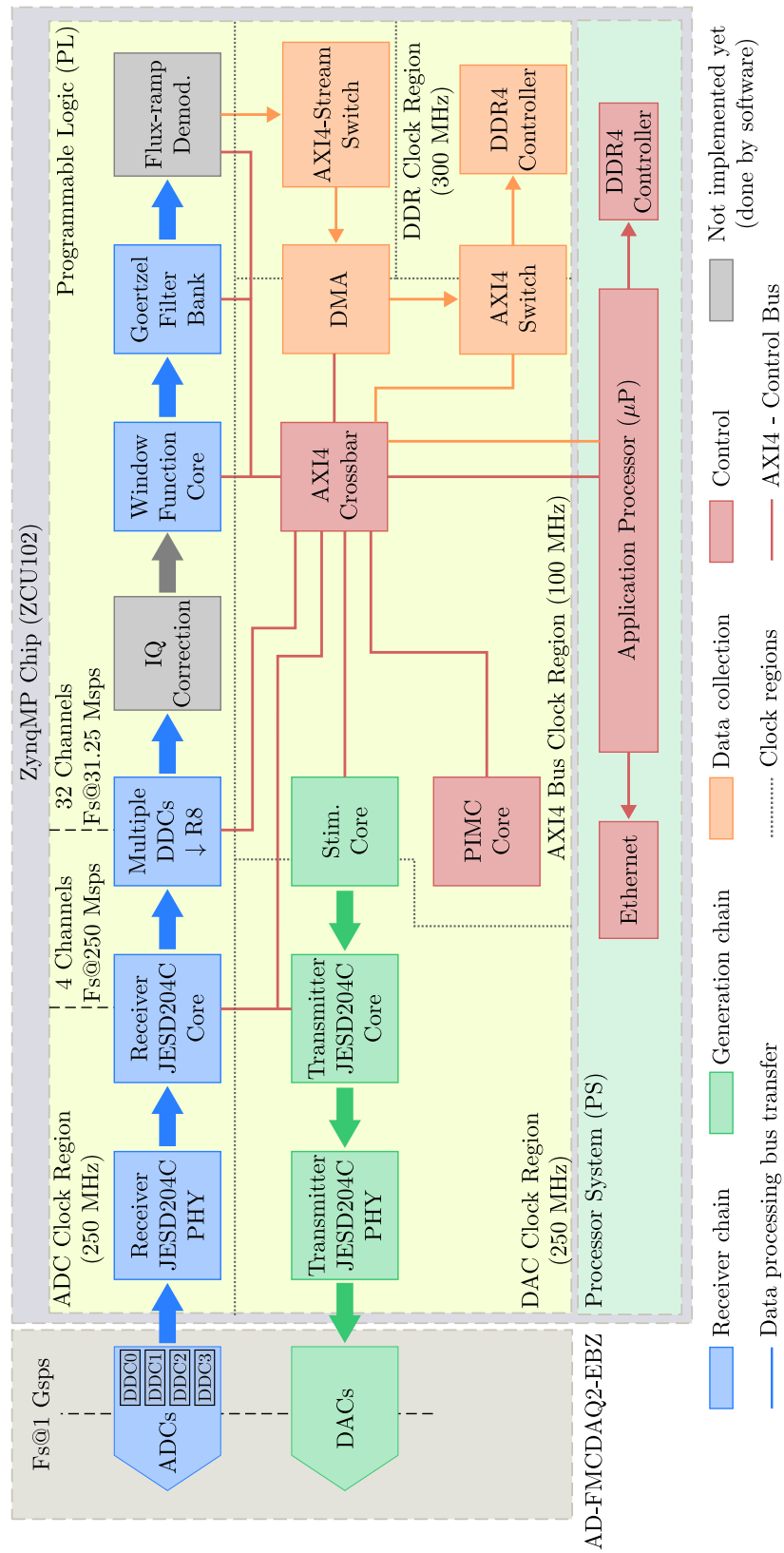


Figure 8.14: Complete Firmware implementation.

		CLB LUTs	CLB Registers	BRAM	DSP
This work	DDC	110.75	190.94	0.125	1.19
	GF	77.39	130.47	0.0625	0.75
	Total	188.14	321.41	0.1875	1.94
ECHO	PFB	63.28	99.98	0.0078	1.30
	MDDC	73.84	139.19	0.25	0.53
	Total	137.12	239.17	0.2578	1.83

Table 8.8: Resource requirements per complex tone for the different approaches with a disaggregation of the main parts. The estimation is for 128 complex tones. The ECHO's firmware runs at 500 MHz and the one from this work runs at 250 MHz. MDDC stands for Multi-channel DDC.

Chapter 9

Prototype Measurements

9.1 Goertzel Filter Bank Channelizer validation

9.1.1 Channelizer Frequency response

A profiling of the designed DDC and GF was performed by means the use of frequency sweeps. In these measurements, the output from the signal generation module was directly routed within the FPGA to the channelizer, as shown in Figures 9.1 and 9.3.

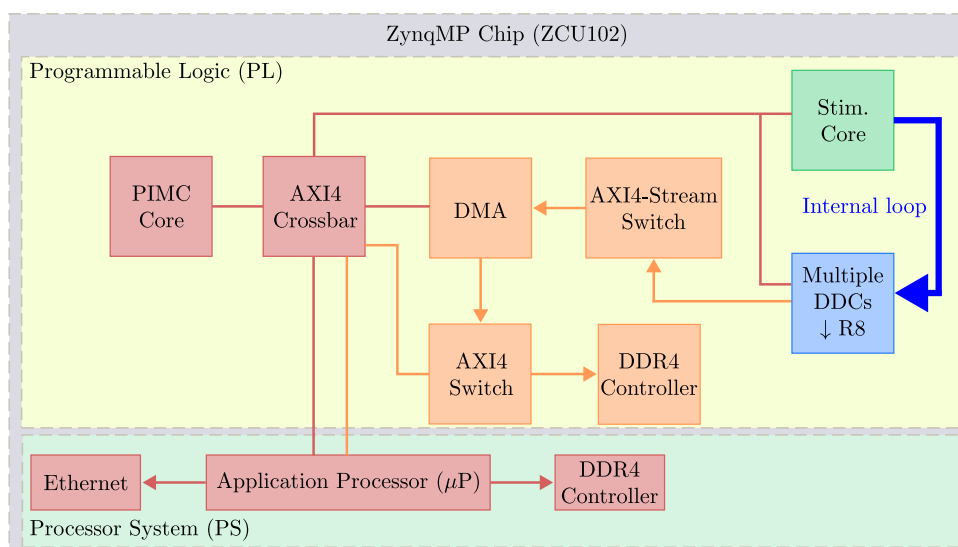


Figure 9.1: Digital Down Converter test firmware (simplified sketch). An internal loopback (blue arrow) connects the stimulation module with the DDC.

This approach was adopted for excluding any contribution from the A/D converters. The frequency sweep was from 15.625 MHz to 78.125 MHz, with a Δf of 65 kHz, at 0 dBFS. Figure 9.2 shows the results which are consistent with the DDC simulations and expected magnitude response shown in Figure 5.7.

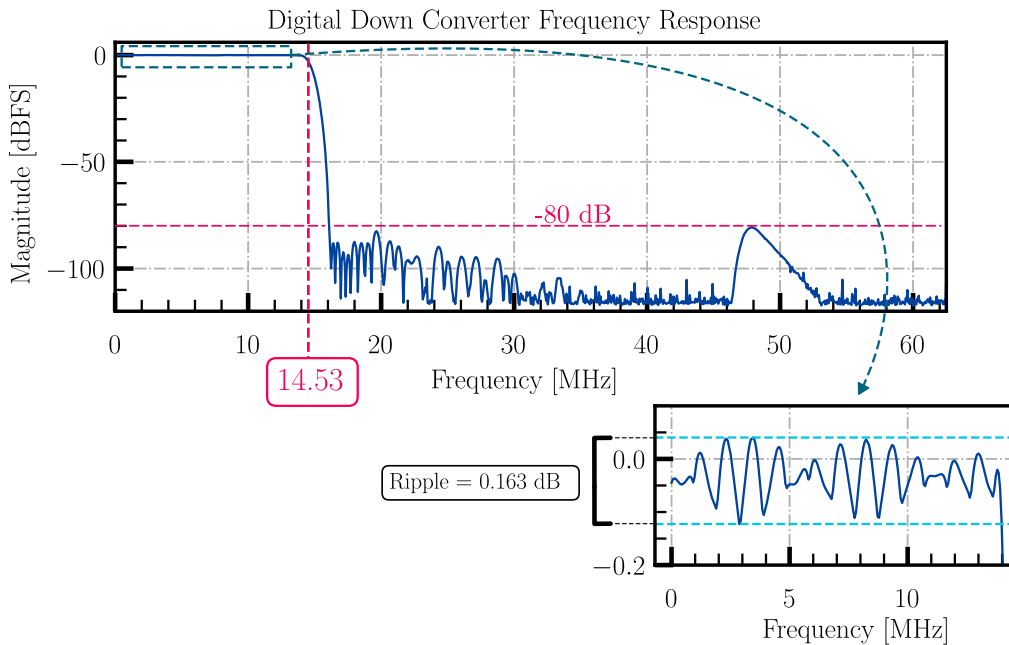


Figure 9.2: Digital Down Converter frequency response. A maximum ripple of 0.163 dB in the bandpass and a 3 dB cut-off frequency at 14.53 MHz are observed.

The discrepancy between the simulation and the implementation, is mainly related with the quantization noise: while the simulation was performed in Python using full precision data, floating point arithmetic, the implementation in the FPGA uses only 16 bits with a fixed point arithmetic. A second contribution is related to the spectral resolution.

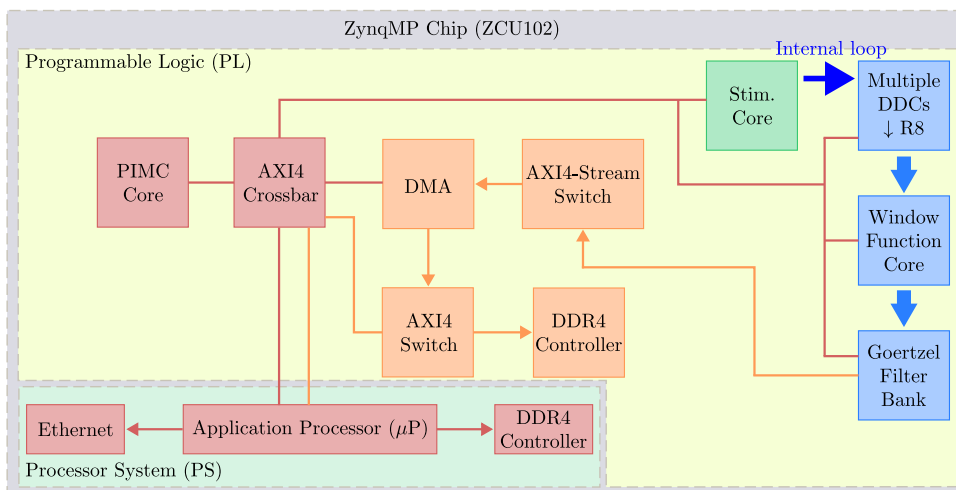


Figure 9.3: Digital Down Converter with Goertzel Filter test firmware (simplified sketch). An internal loopback (blue arrow) connects the stimulation module with the DDC.

For the GF a frequency sweep was carried out from 0 Hz to 15 MHz, with a Δf

of 65 kHz, at 0 dBFS. All the implemented filters will differ in their center frequency (the DFT bin to detect), but will have the same profile. This measurement is shown in Figure 9.4, which shows a consistent profile with the window function used.

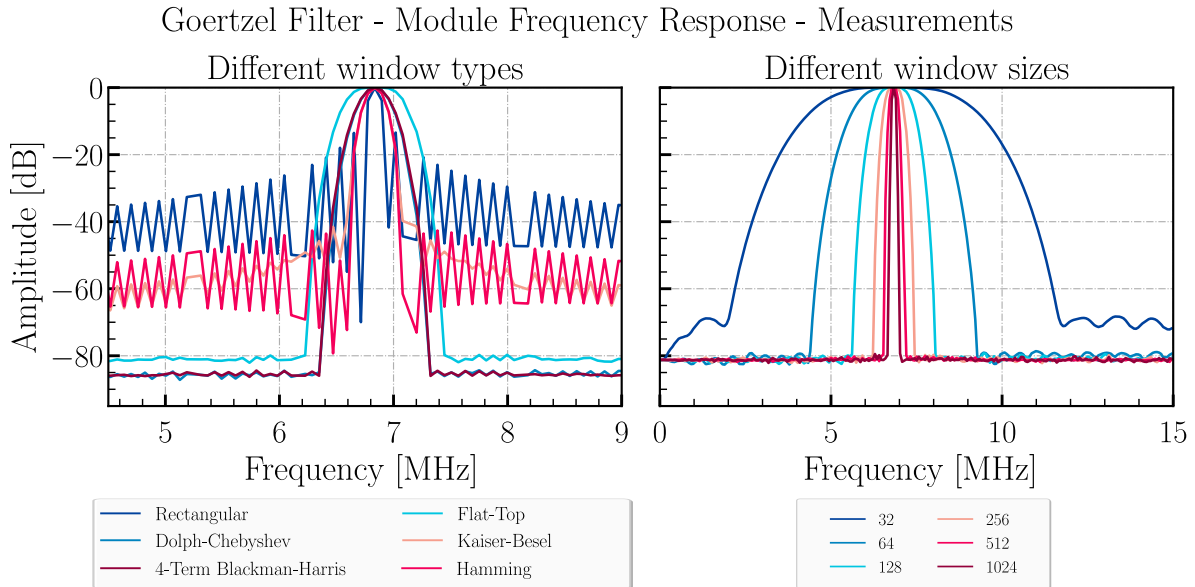


Figure 9.4: Channelizer frequency response for different window types for a 256 samples window size (left). Different window sizes for a flattop window type (right).

9.1.2 Demodulation capabilities

To evaluate the demodulation capabilities a setup was built, whose block diagram is sketched in Figure 9.5. A resonator at room temperature was employed, featuring a varicap that permits the adjustment of the device’s resonance frequency by varying the applied voltage, as illustrated in Figure 9.6.

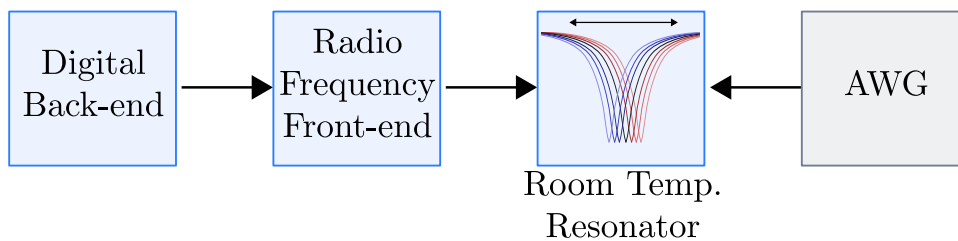


Figure 9.5: Experimental setup for the demodulation capabilities tests. Placing a modulating signal (sinusoidal, triangular, square, etc.) in the resonator’s voltage control terminal using an Arbitrary Wave Generator (AWG) makes changes it resonance frequency. To reach a full dynamic range, the used signals have a DC offset of 5 Vdc, with an amplitude of ± 2 Vdc.

For the tests in the following subsections, the digital backend generated a tone at -239 MHz with a power of -10 dBm in order to monitor the behavior of the resonator, located between 4.2 GHz and 4.3 GHz.

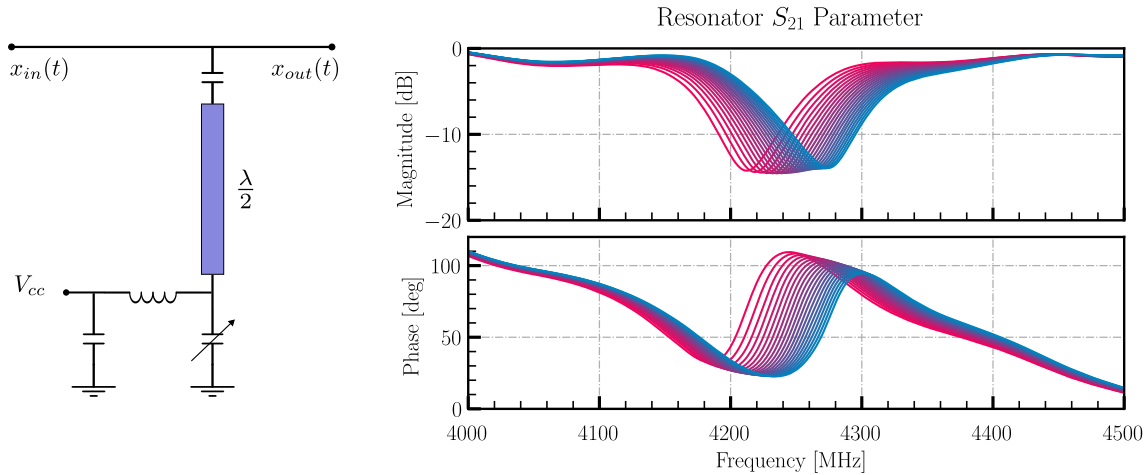


Figure 9.6: Resonator’s schematic. The right and left terminals are the input/output (bi-directional), and the V_{cc} terminal is the Voltage Control which defines the resonance frequency of the device. The voltage range for this terminal goes from 0 Vdc to 10 Vdc (left). Resonator’s S_{21} parameter, characterized using a Vector Network Analyzer for different Vdc values, from 0 Vdc to 10 Vdc with a step size of 0.5 Vdc (right).

The realization of the aforementioned setup is shown in Figure 9.7, where ① is a HMC629 digital attenuator, ② are two LTC5549 real mixers, ③ is a TRF372017 I&Q

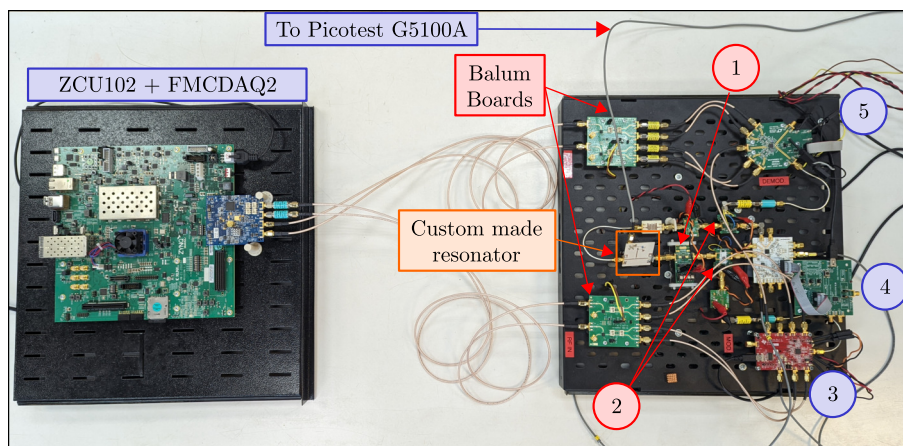


Figure 9.7: Experimental setup for first validation tests with custom resonator. The digital backend placed at the left encompassed by the ZCU102 and the FMCDAQ2 evaluation boards. The modulation of the resonator’s operation point was performed using a signal generator Picotest G5100A.

modulator, ④ is a LMX2594 wideband synthesizer and ⑤ is LTC5586 I&Q demodulator.

Modulation Type I: Amplitude Modulation

The main goal of this first experiment is to recover the amplitude modulated signal, which corresponds to an AM demodulation process. The experimental setup is sketched in Figure 9.8.

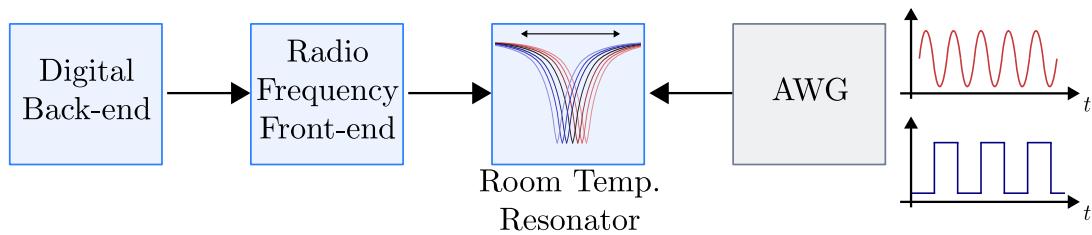


Figure 9.8: Experimental setup for the AM demodulation capabilities tests. placing a modulating signal (sinusoidal, triangular, square, etc.) in the resonator’s voltage control terminal using an AWG.

Different signals were generated (sinusoidal, square, ramp and exponential decay), at different frequencies (from 100 Hz to 50 kHz) in order to validate the GF’s bandwidth and performance. Some of them are shown in Figure 9.9, whose result are in agreement with the developed theory in 6.5 and the performed simulations.

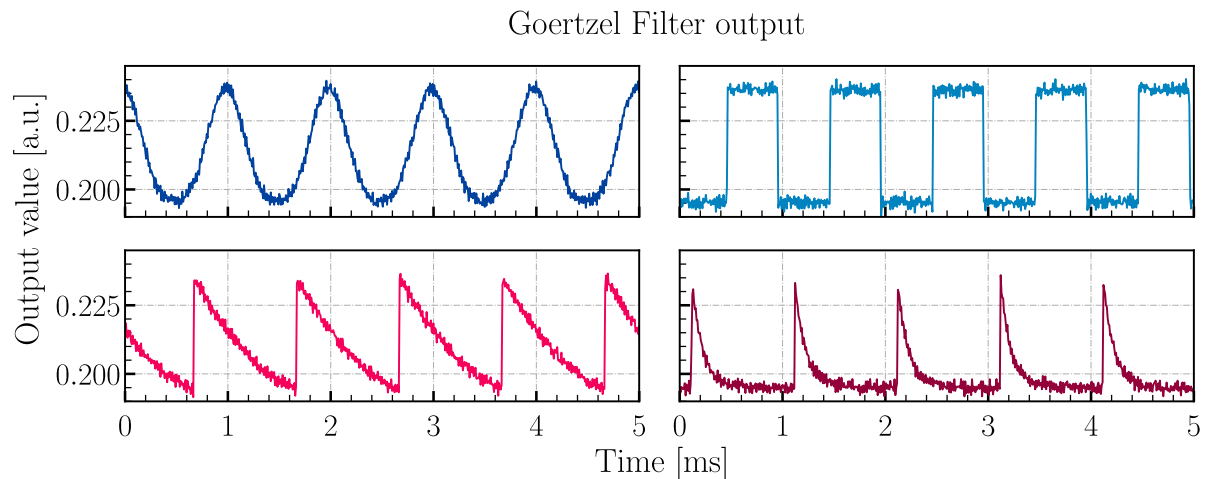


Figure 9.9: GF output for four different modulation signals: sinusoidal, square, ramp and exponential decay. Only the case for a $f_{\text{mod}} = 1$ kHz is shown, for presentation purposes.

Figure 9.10 shows the frequency spectrum of the previously presented signals. There are some artifacts (spurious) related to two main things: i) the performance of the used AWG, and ii) the inherent resonator nonlinearities.

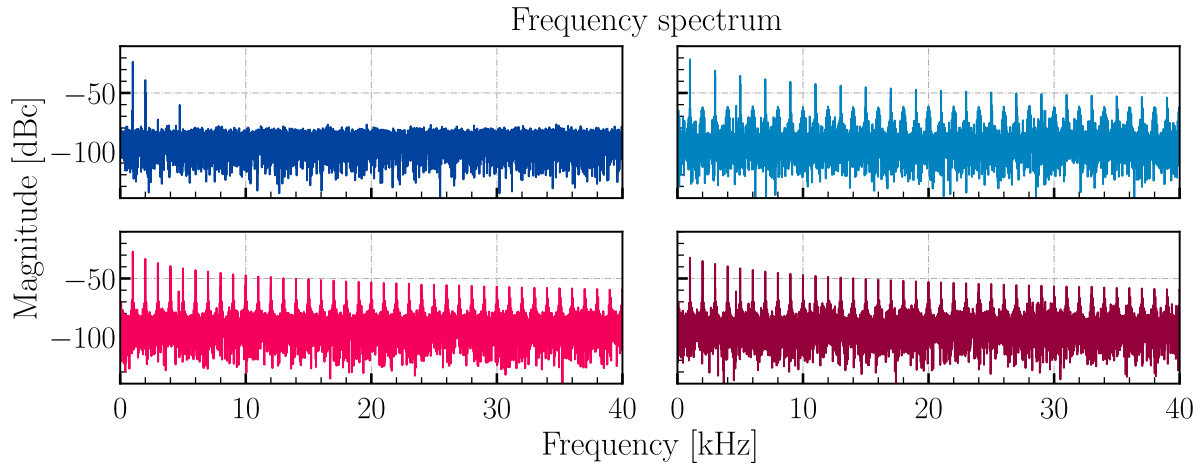


Figure 9.10: Frequency spectrum of Figure 9.9 signals. The $f_{\text{mod}} = 1$ kHz component is clearly visible. There are some artifacts related with the AWG performance, which can be seen more clear in the square signal spectrum between the main components.

Modulation Type II: Amplitude + Phase Modulation

As was explained in Section 3.4, working with a μMUX demands the use of the Flux-Ramp Modulation technique [106]. This means that the problem can be analyzed as one where both AM and PM modulation are present in the carrier signal, based on what was explained in Section 6.5. The same AM modulated signals stimulating the resonator were generated as before, but a PM modulation was added to them. Figure 9.11 shows a sketch of the experimental setup, where $\Delta\phi$ is the introduced phase deviation due to the PM.

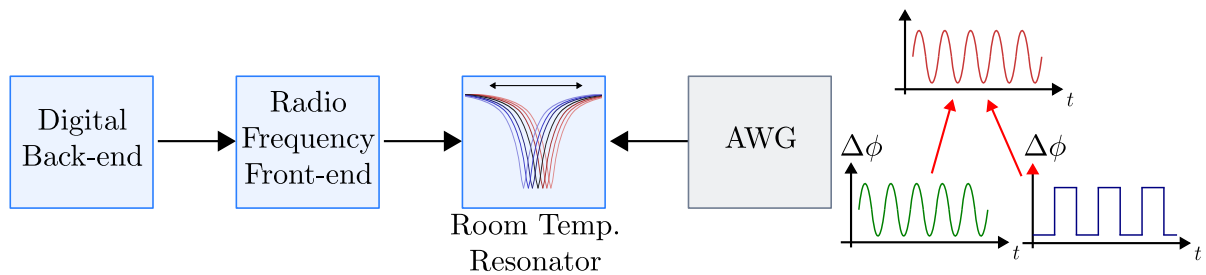


Figure 9.11: Experimental setup for the AM + PM demodulation capabilities tests. placing a sinusoidal signal for emulating the AM and adding a PM to it (square, triangular and sinusoidal too) in the resonator's voltage control terminal using an AWG.

The aim was to retrieve this PM modulated signal, which should represent the information from the sensors. The demodulation method is based on a typical IQ demodulation technique as shown before also in Section 6.5 and performed afterwards in a python script:

$$x'(t) = x(t) * w(t) \quad (9.1)$$

$$\phi = \arctan \left[\frac{\sum x'(t) \cos(w_c t)}{\sum x'(t) \sin(w_c t)} \right] \quad (9.2)$$

where $x(t)$ is the output of the GF and $w(t)$ is a window function which performs a filtering using a Dolph-Chebyshev window (configured to attenuate the Highest Side Lobe -200 dB). For the experimental setup, a 30 kHz sinusoidal signal emulating the SQUID response was generated; and on top of this, a *phase modulation* of 60° at 200 Hz of 2 different types, sinusoidal and square, and 30° at 200 Hz for the triangular case. Figure 9.12 shows the results. This last result consolidates the simulations performed in Section 6.7.3.

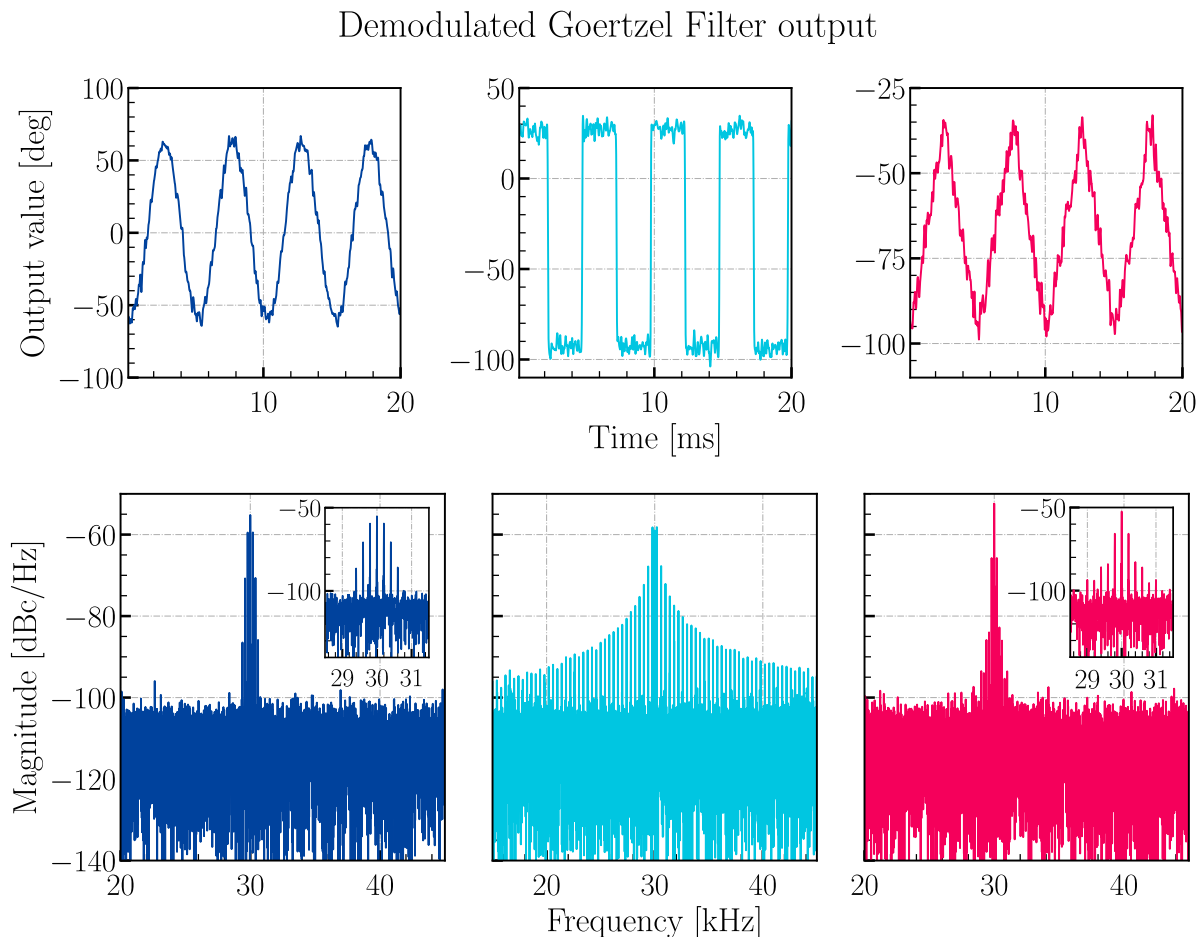


Figure 9.12: PM demodulation from the demodulated AM signal, emulating a detector signal. Total phase shift of 120° as expected (top). Power Spectral Density of the top plot, showing the consistency of the visualized signal and its spectrum; where the main component is located at 200 Hz (bottom).

9.2 Power calibration

A new experimental setup was built for this task and the following ones, consisting of the installation of the racks, instruments, local network (LAN) configuration, the cryostat and cabling (see Figure 9.13). This is the minimum setup necessary for the characterization of a μ MUX working at mK temperatures and its associated read-out electronics. The cryogenic circuit inside the cryostat will be explained later in section 9.5.1.

The cryostat has two different types of input-output lines for the user, DC and RF. The DC lines are mainly used for connecting the LNAs' power supplies in the rack to the LNAs in the 4 K stage inside the cryostat, the feed of the modulation line (the flux-ramp signal path), etc. The RF lines are used for the read-out and characterization of the cryogenic devices, and are connected to the different instruments or the RF front-end through a RF patch (see bottom right in Figure 9.13).

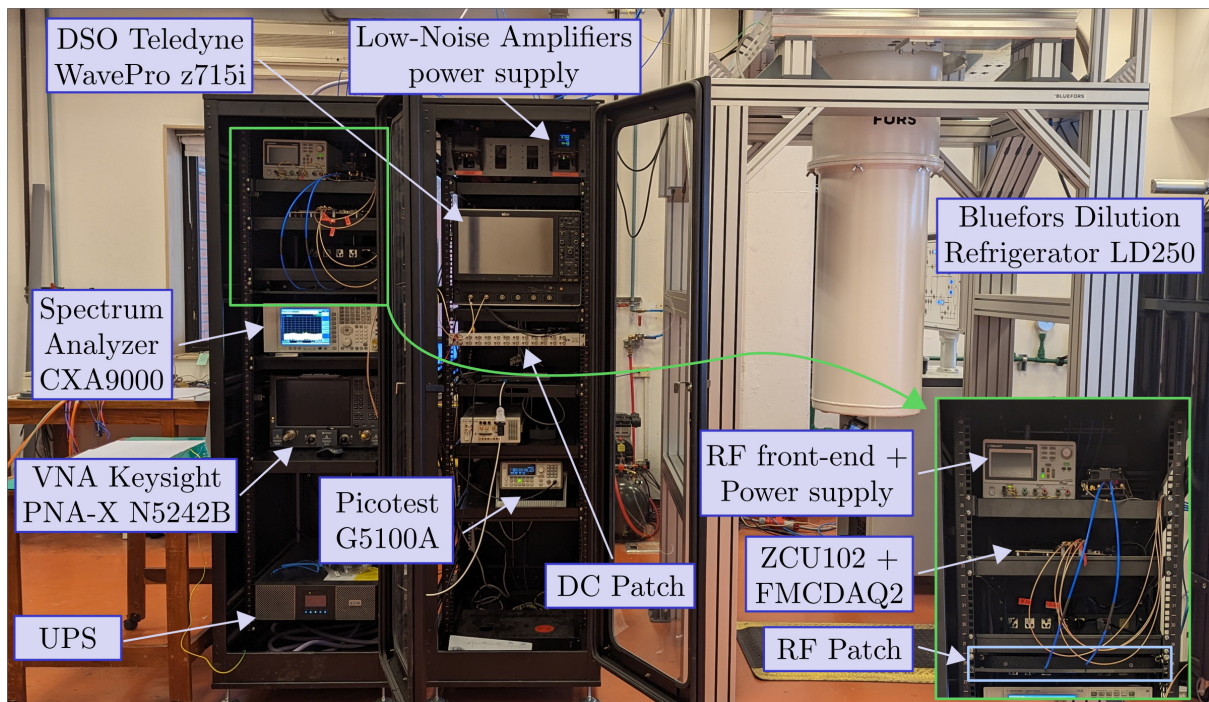
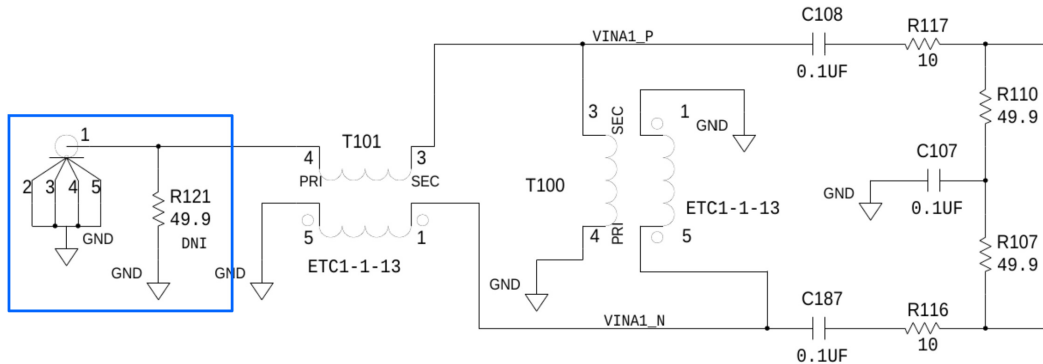


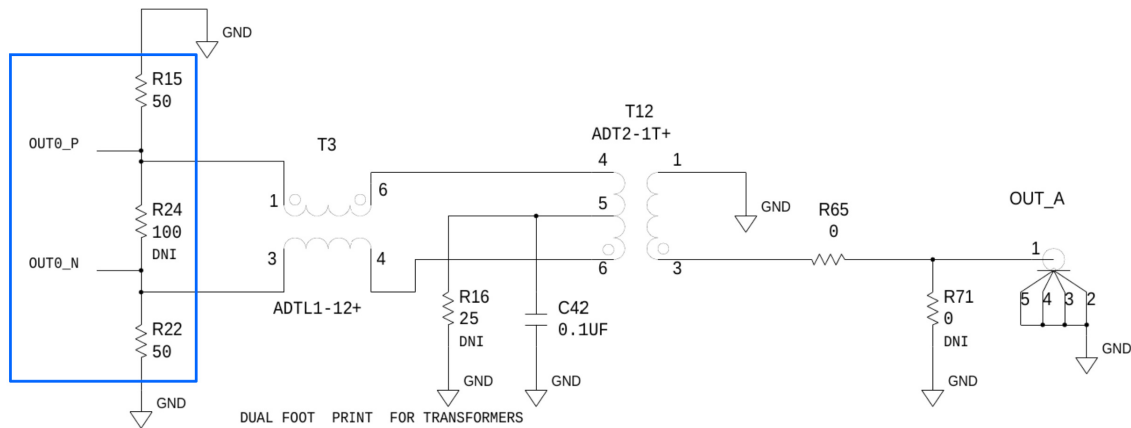
Figure 9.13: Second experimental setup where the RF front-end from [161] was used. This setup was utilized for the power calibration procedure, the DAC characterization and the μ MUX measurements.

The fundamental concept in this step involves establishing the existing relationships between the desired output power from the Digital Backend and its connection to the Cryostat RF input connectors. To accomplish this task, a Digital Oscilloscope (DSO) Teledyne WavePro z715i [203] and a Spectrum Analyzer (SA) Agilent CXA9000 (now Keysight) [204] were utilized at various locations to monitor the transmitted power from the DACs through the Cryostat. The input and output circuits for both, ADC and DAC are depicted in Figure 9.14 and should be taken into account at the moment of generating

the signals for the instruments input/output impedance configuration.



ADC input impedance



DAC output impedance

Figure 9.14: In these schematic circuits the input impedance is matched to 50 Ω. These schematics were taken from the FMCDAQ2 evaluation board documentation [157].

9.2.1 Frequency response of the DAC

For the power calibration, the initial step involved the characterization of the AD9144 DAC’s slope within its usable bandwidth. The experimental setup is illustrated in Figure 9.15. The test comprised a frequency sweep with the DAC operating at full scale. The ADC was terminated with 50 Ω loads, for protecting the chips. A pair of Crystek low-pass filters with a 500 MHz cutoff frequency were employed in the DAC output channels, for removing the components above $F_s/2$ (limit the spectral content to the 1st Nyquist zone) and not introduce them to cryogenic setup. The result is presented in Figure 9.16, where Channel A provides the I component, and Channel B provides the Q component of the complex envelope.

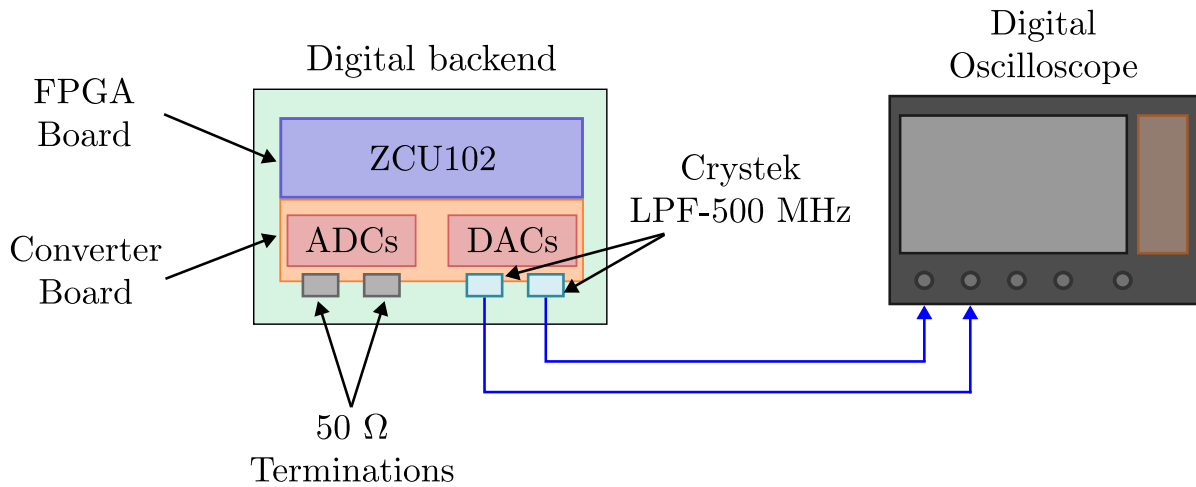


Figure 9.15: Experimental setup for DAC slope / roll-off characterization. The DSO was configured to sample at 1 Gsps, a total acquisition time (horizontal time base) of 2 seconds and each channel coupled to $50\ \Omega$.

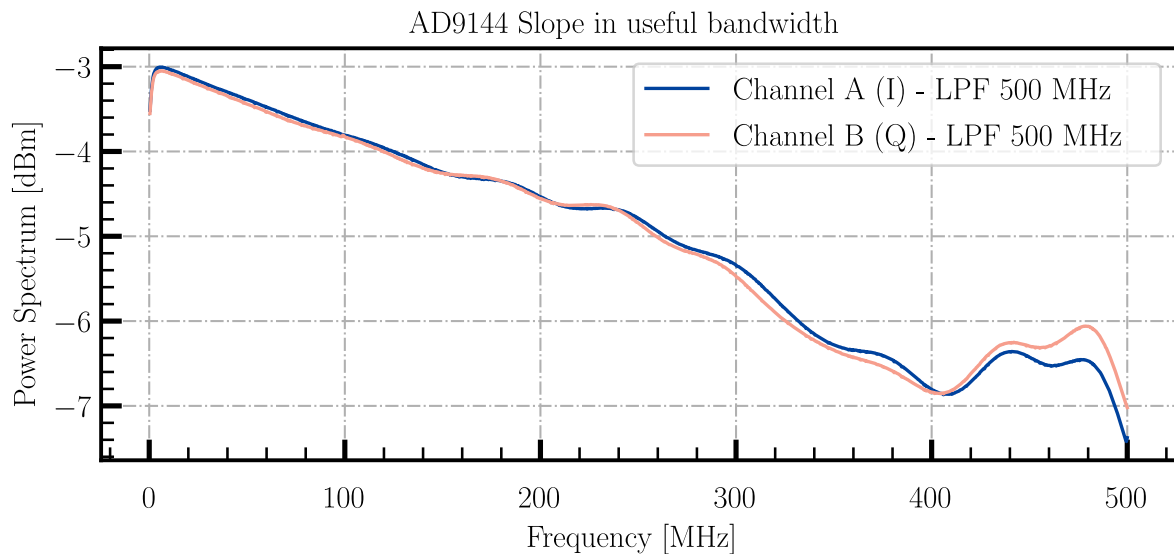


Figure 9.16: DAC roll-off performed by a frequency sweep with $\Delta f = 7629.39\ \text{Hz}$. The complex envelope will be 3 dB above these curves by definition, and can be seen in the following sections.

The $\Delta f = 7629.39\ \text{Hz}$ is related with the memory depth and word length of the stimulation module implemented in the firmware.

9.2.2 Output power calibration

The calibration consisted of a sweep in the generated power of a tone at 145.8 MHz. This frequency value was selected because it will be used in the μMUX measurements

in the next sections. The presented power values in Figure 9.17 consisted of the complex envelope reconstruction using two channels of the DSO: $C = Ch_1 + jCh_2$, and performing a FFT in python.

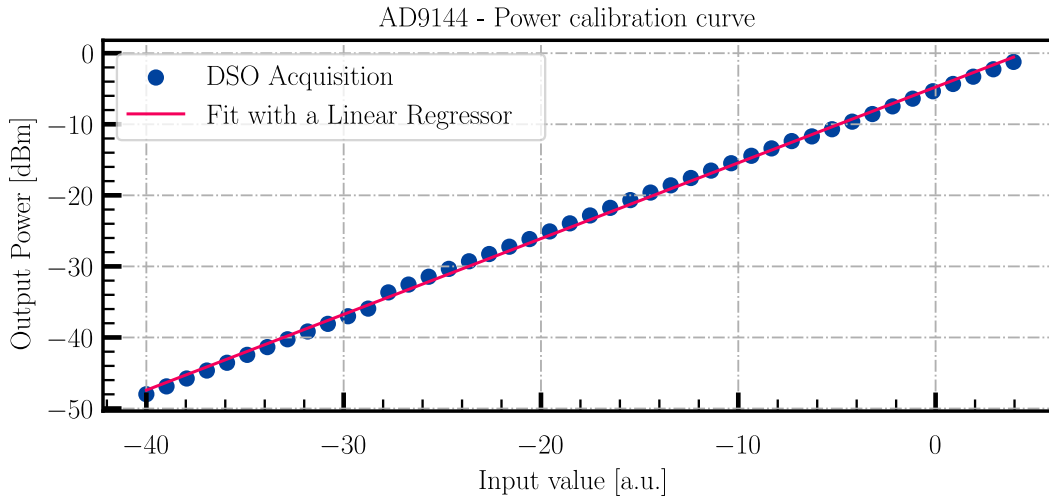


Figure 9.17: Output power calibration. In blue the DSO acquisition points and in red a lineal regression fit. This plot corresponds for the power sweep done to a single tone at 145.8 MHz. The arbitrary unit of the x-axis relates with the value sent to the DAC with the software.

The *jumps* that can be appreciated in two parts of the plot in the DSO acquisition are due to a change in the vertical scale of the instrument. The DSO was configured with a $50\ \Omega$ input impedance in order to match the FMCDQAQ2 board output impedance. The experimental setup was the same as the one of Figure 9.15.

From now on, the input power values for the following measurements will be obtained using the fitted model output.

The same power sweep was performed three more times but with the Spectrum Analyzer connected in different places. The steps were as follow and are depicted in Figures 9.18, 9.19 and 9.20:

1. the TX output of the RF frontend connected to the SA,
2. the baseband RX output of the RF front-end connected to the DSO, and a loop-back in the high frequency connectors with a short cable (for minimum possible attenuation),
3. the TX output was connected to the patch panel with SMA Female - Female mount panel connectors [205], then to the two cables that go to the cryostat (for the TX and the RX) which were connected with a through adapter.

The cables connecting the RF front-end with the cryostat (and vice-versa) are a custom made of 4.064 m (160") based on the P300 version [206]. This cables presents an insertion loss (IL) of 0.85 dB/m at 5 GHz. The connectors introduce an IL of roughly

$0.05\sqrt{f}$ dB (with f in GHz) [206]. There is another IL present in the interconnection RF patch between the RF front-end and these cables (as shown in Figure 9.13).

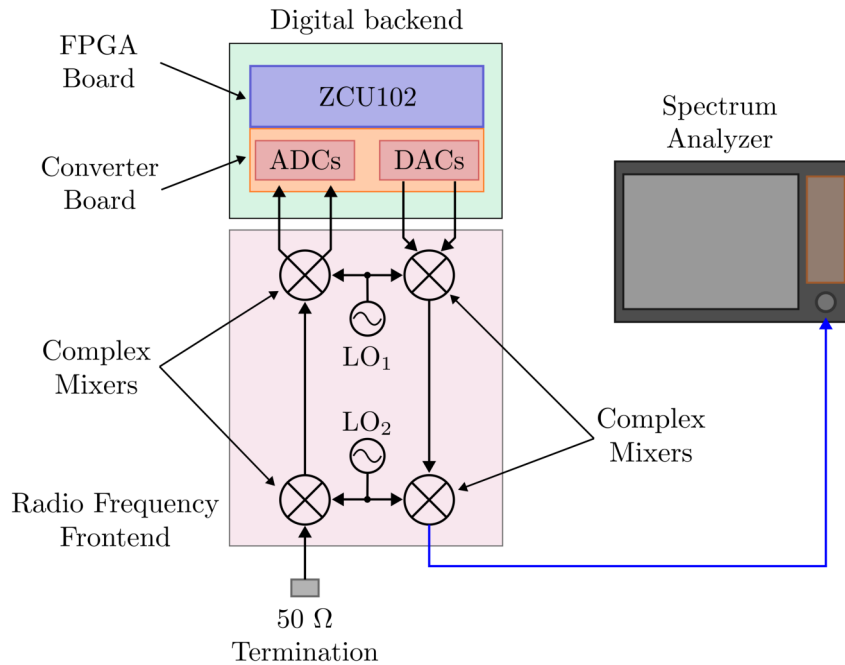


Figure 9.18: Experimental setup for power calibration at the RF front-end high frequency output.

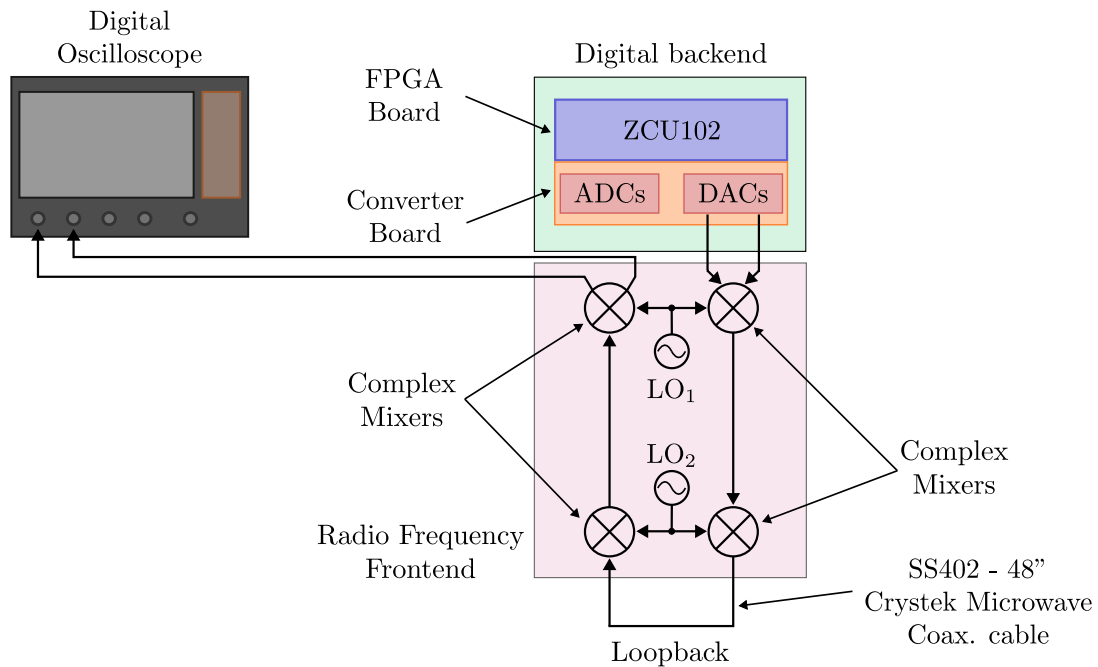


Figure 9.19: Experimental setup for power calibration at the RF front-end base-band output.

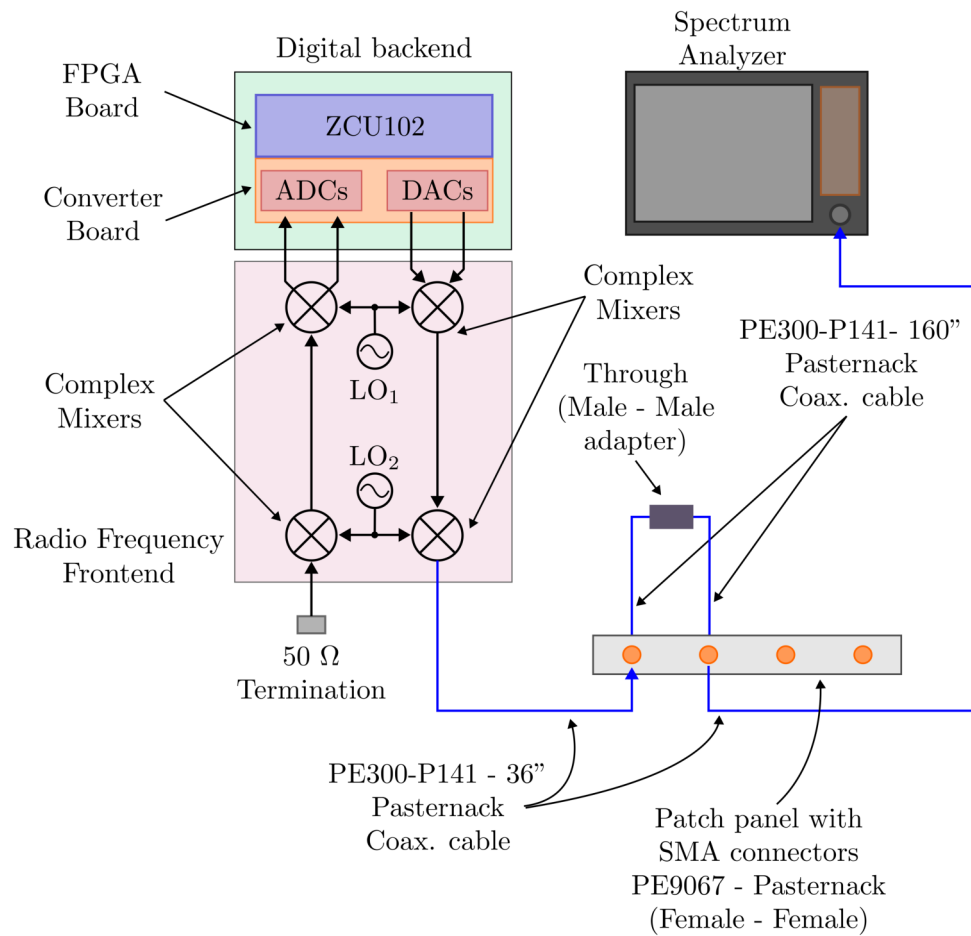


Figure 9.20: Experimental setup for power calibration at the RF front-end high frequency output at the end of the transmission path, the input of the cryostat and then back to the RF front-end.

Figure 9.21 shows the results for this measurements, which are consistent with the built setup specifications (the different cables and connectors IL) and in [161]. Figure 9.22 shows the attenuation introduced by both the RF front-end and the cabling. This curves were obtained by an arithmetic difference of the results presented in Figure 9.21.

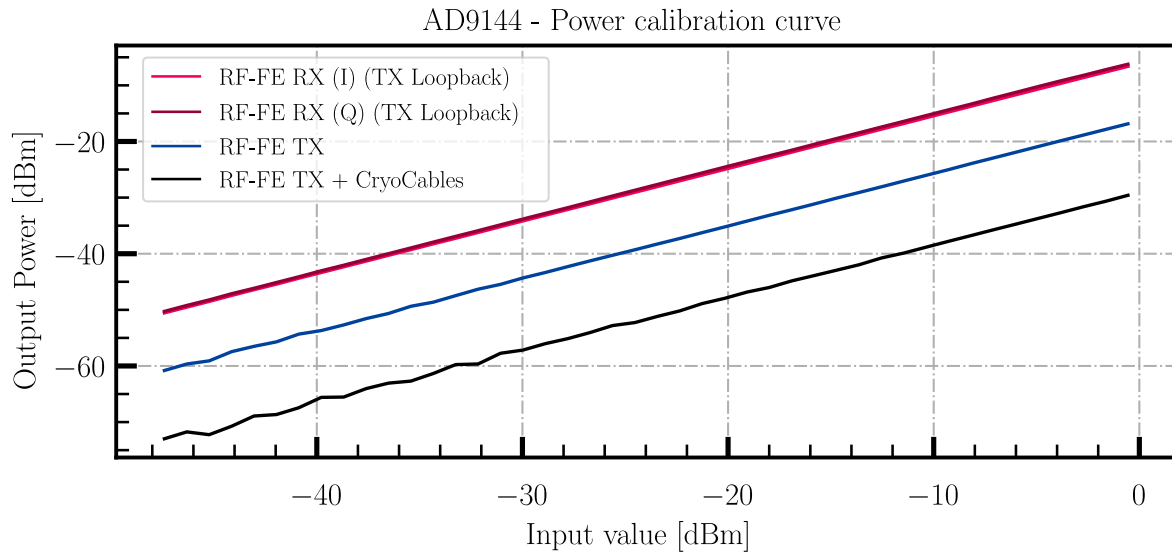


Figure 9.21: Results of the different measurements. The input value is related with the calibrated output power of the DAC. The blue curve is related with the first experimental setup. The black curve is from the third experimental setup. The I&Q components of the complex envelope for the TX Loopback of the second experimental setup, where the gain of the RF front-end can be seen.

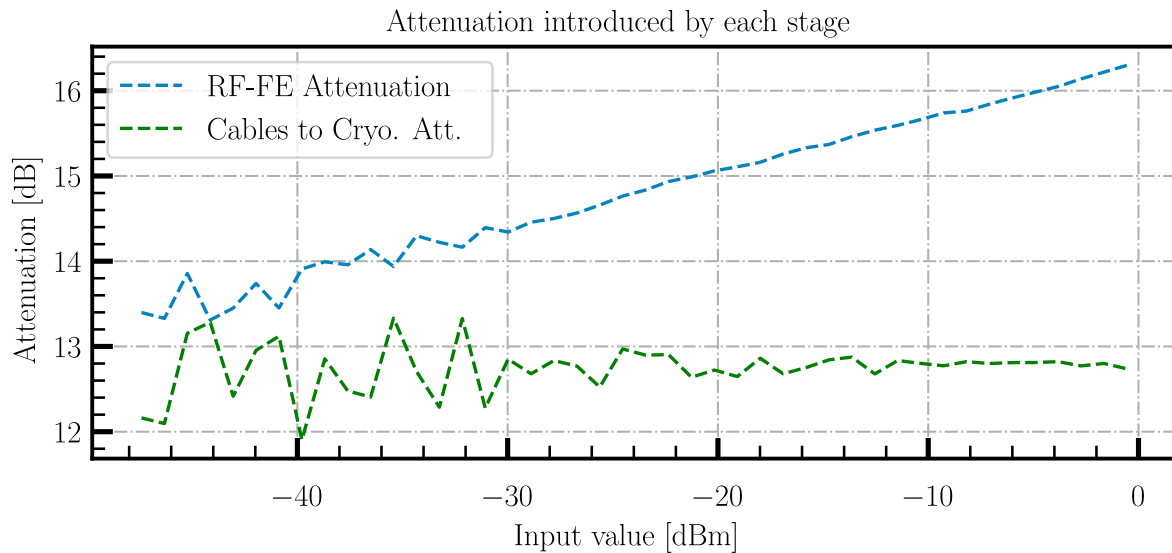


Figure 9.22: Attenuation introduced by the RF frontend and the cables setup. The green curve comprises from the TX of the RF front-end, through the RF patch panel towards the cryostat cable and the return path. The light blue curve was obtained by the difference of the TX RF front-end output and the calibrated input value for the DAC power.

9.3 Power Spectral Density

The Power Spectral Density (PSD) of the signal is shown in Figure 9.23. A loop-back measurement connecting the DACs with the ADCs in the digital back-end to emphasize its noise contribution in blue. Then the RF front-end was added and another loop-back connection between the TX and RX terminals for performing the same measurement was done, in light red. The used window for the GF was a flattop one with a size of 32 samples.

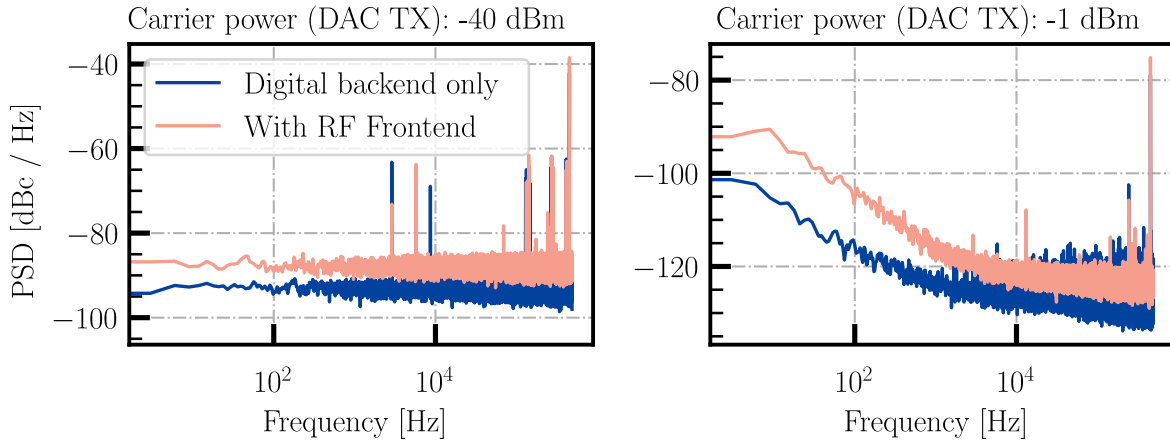


Figure 9.23: Digital backend with the RF Frontend. A 32 samples window size was utilized in this case, with two different power levels generated with the DACs, -1 dBm and -40 dBm.

It is possible to estimate the attenuation introduced by the RF Front-end. From the figure, the noise floor of the digital back-end is around -93.5 dBc and with the front-end addition increases to -87.5 dBc, for the low power input case of -40 dBm. From these, the contribution due to the RF circuit can be obtained as follows:

$$P_{tot} = \sqrt{P_{DB}^2 + P_{RF}^2} \quad (9.3)$$

where P_{DB} refers to the noise floor power level of the Digital back-end and P_{RF} for the RF front-end. As the PSD is referred to the carrier input power, the used values are indeed a relationship between them. The attenuation due to the RF front-end can be established by determining the noise floor level due to it:

$$1.778 \cdot 10^{-9}W = \sqrt{(0.4467 \cdot 10^{-9}W)^2 + P_{RF}^2} \Rightarrow \quad (9.4)$$

$$\Rightarrow P_{RF} = 1.7209 \cdot 10^{-9}W \quad (9.5)$$

The RF front-end attenuates around 5.86 dB in this setup, consistent with the measurement shown in Figure 9.22 (the relationship between the attenuation of the TX path and the gain of the RX path).

9.4 Signal Generation

9.4.1 Slope / Ripple correction

In Figure 9.16, it is observed that it is necessary to equalize the power of the generated tones to ensure uniform power distribution to all resonators. To address this requirement, a simple algorithm was employed, involving the generation of an initial version of the desired signal. The algorithm then measured the actual magnitude using an SA, as depicted in Figure 9.24.

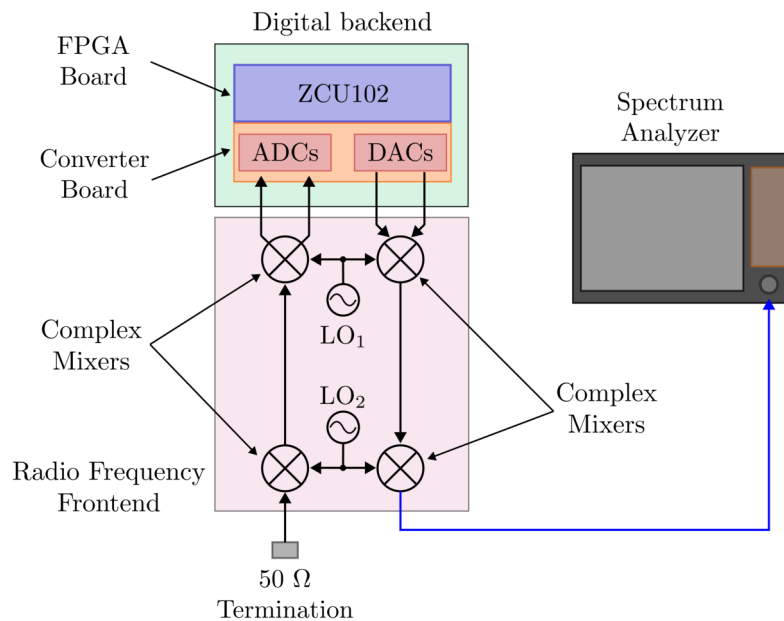


Figure 9.24: Slope compensation and IQ imbalance TX correction experimental setup. In this case, the SA was replaced by the PNA-X N5242B [207] with the SA function mode because of the speed in the acquisition (sweep time) this instrument presents when compared to the former one; making the iterative process for the imbalance correction faster.

Subsequently, the difference between the desired values sent to the DAC and the measured actual values was calculated. This difference was then used to adjust the original desired values. The result of this operation is displayed in the next section together with the IQ imbalance correction in Figure 9.27.

9.4.2 IQ Imbalance correction

The criterion is to improve the IMRR at least to a value equal or greater than the ADC SNR. Figure 9.24 illustrates the setup for the correction, and Figure 9.25 a phase imbalance sweep of 1200 steps, from -0.6 rad to 0.6 rad, in order to visualize how its image counterpart for each tone of the multi-tonal signal was evolving. Nash's method [198] consists of sweeping in phase imbalance and in gain imbalance, calculating the IMRR,

finding the local maximums for that iteration, adjusting a set of new limits accordingly (a little bit tighter and independent pairs of them for each tone), reducing the step size of the sweep and repeating. This iteration should be repeated no less than four times in order to ensure a reliable result. Figure 9.26 is a repetition of the Figure 9.25 but it was highlighted (in different colors) in the image power plot a conceptual representation on how this process evolves

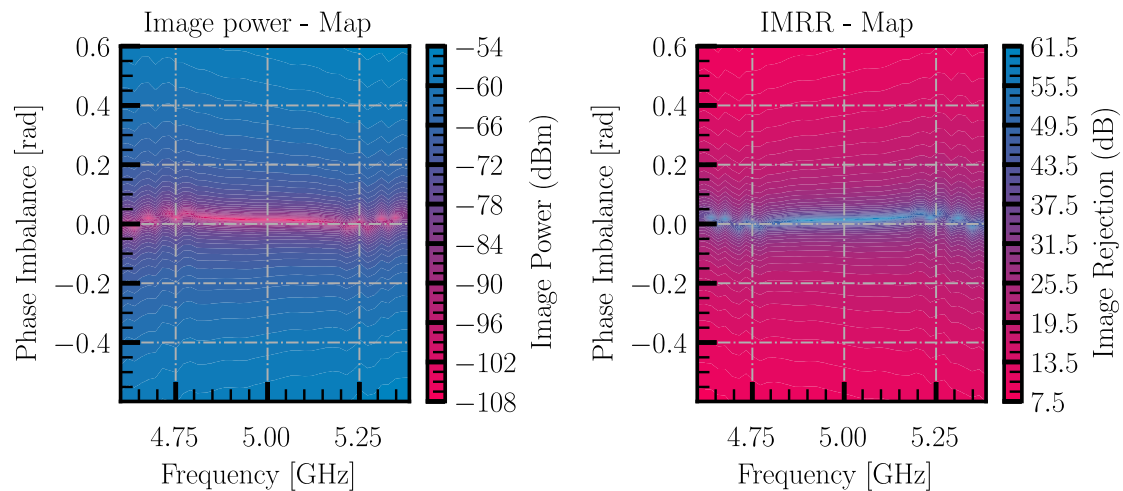


Figure 9.25: IQ imbalance: image power and IMRR illustration of how the images are affected as we sweep in the phase imbalance plane. A set of 40-tone signal distributed between 4.5 GHz - 5.5 GHz was generated. The sweep was from -0.6 rad to 0.6 rad and a measurement with the PNA-X was performed in each iteration.

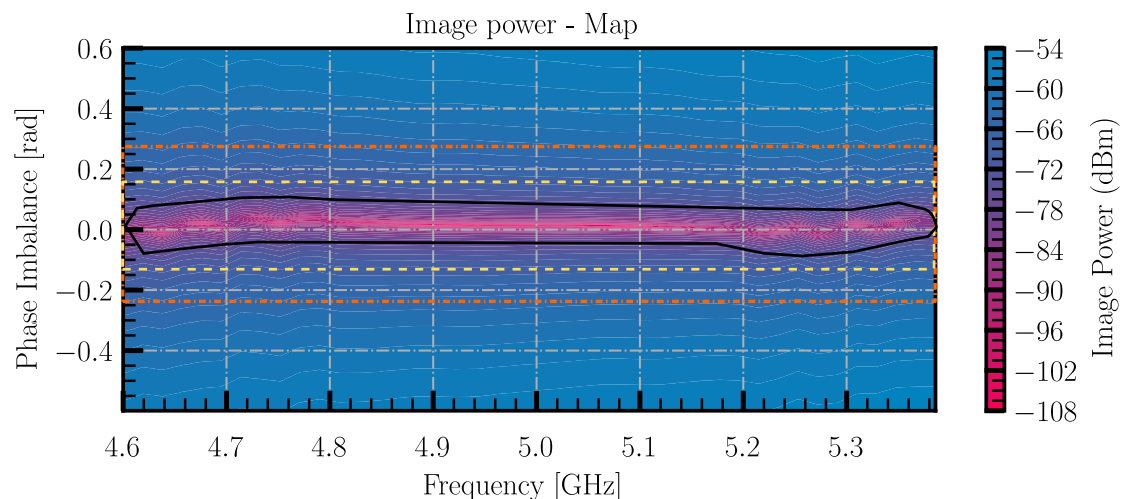


Figure 9.26: IQ imbalance compensation procedure concept: the change in the sweep limits is marked by the different color marks. Every iteration step reduces the search area and should converge to the minimum value for the image power.

Figure 9.27 shows the slope and IQ imbalance compensations result for an 80 tones multitone signal. The PAPR was optimized utilizing random phases.

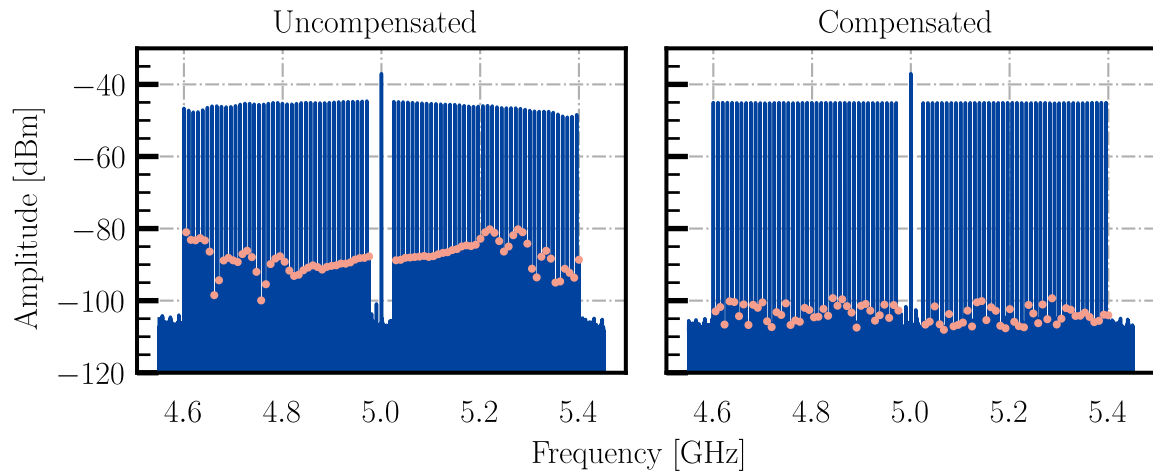


Figure 9.27: 80-tone multitone signal, non-equally spaced, with guard bandwidth near the LO. The LO was tuned to 5 GHz, and the multitone signal span from -400 MHz to 400 MHz. The target power was -46 dBm. The main limitation here was the noise level of the instrument, which established the lower limit to the algorithm for converging to better IMRR values (or lower images power).

9.5 Cryostat measurements

9.5.1 Experimental setup

The setup consists of a Bluefors Dilution Refrigerator LD250 [208], several attenuators for signal conditioning, a directional coupler to the μ MUX input and a circulator at the output followed by an LNA[209] in the 4 K stage. The setup is depicted in Figure 9.28.

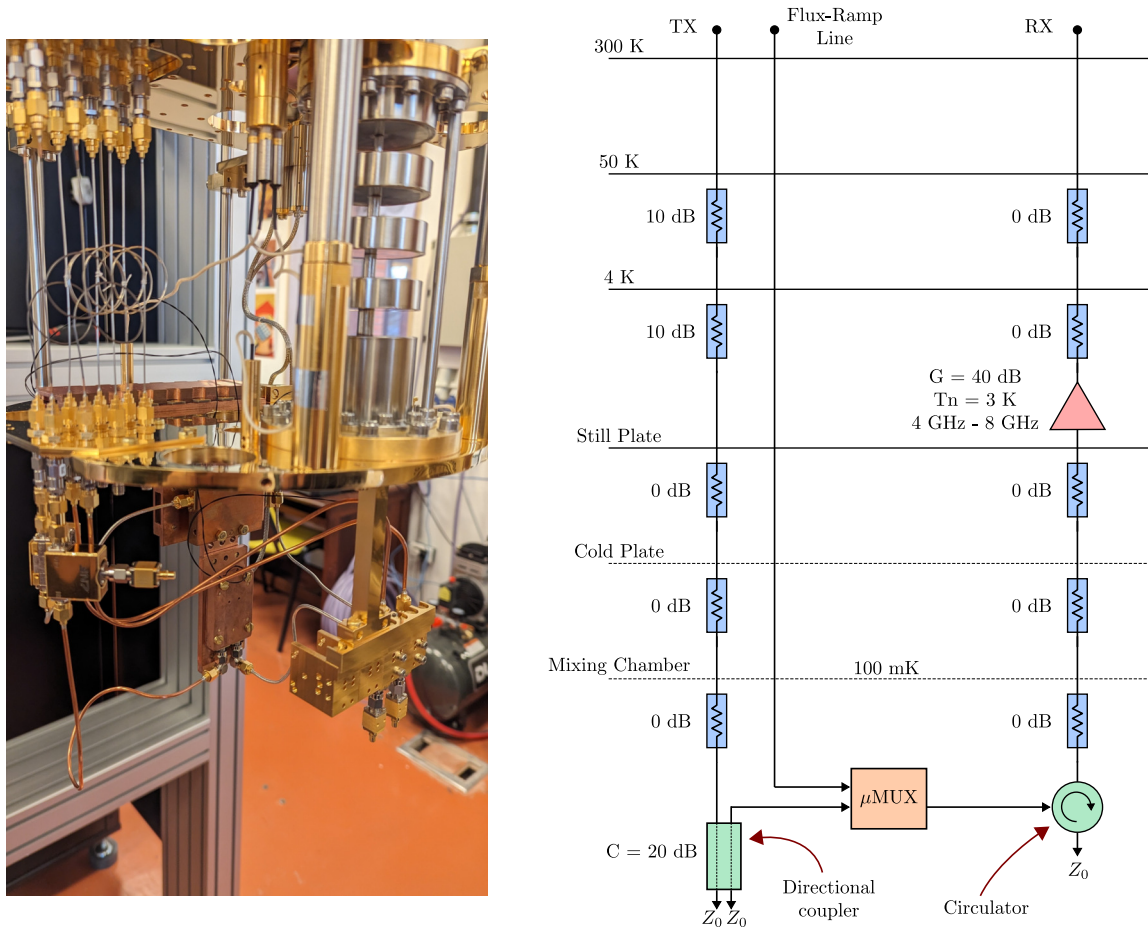


Figure 9.28: Mixing chamber (MXC) with the sample holders placed on it. In the left bottom region, the circulators with the 50Ω loads can be appreciated. At the bottom part the MXC one of the sample holders houses the μ MUX. The directional couplers are in the bottom right of the picture, but unfortunately they are behind the visible brackets where they are fixed (left). A simplified sketch of the cryogenic circuit for the tests (right).

For this stage, the 9 channel μ MUX was placed without attached sensors to it in the 10 mK stage, but set to work at 100 mK. For the FRM a Picotest G5100A generator [210] was used. The μ MUX under test was design for bolometric applications, therefore the experiments where focused on the QUBIC project.

9.5.2 Microwave SQUID Multiplexer characterization

Concluding with the measurements step, a 9 channel μ MUX was used, see Figures 9.29 and 9.30, to characterize the demodulation capabilities of the channelizer like in the previous section 9.1.2 but with a cryogenic device at a temperature of 100 mK. The SQUID resonators in the used μ MUX have a period of $189.76 \mu\text{A}$ per flux-quanta, Φ_0 , and a bandwidth of roughly 200 kHz. The device operating region is depicted in the figure 9.30. The channel located at approx. 3.9656 GHz was used and monitored with a tone power of -40 dBm (-80 dBm at the chip input). This channel did not have an input coil, so the rf-SQUID has a coupling inductor terminated with a resistor and open circuit. This acts like an antenna, thus introducing undesired signals (spurious signals) as will be seen in Figure 9.31 after the channelization process.

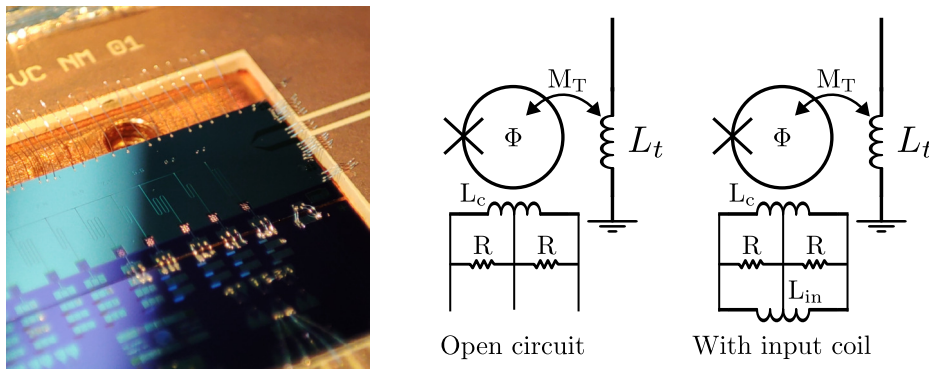


Figure 9.29: 9-channel μ MUX, developed by the IMS and ITeDA placed in the sample holder. Some channels have an input coil and others are terminated in an open circuit.

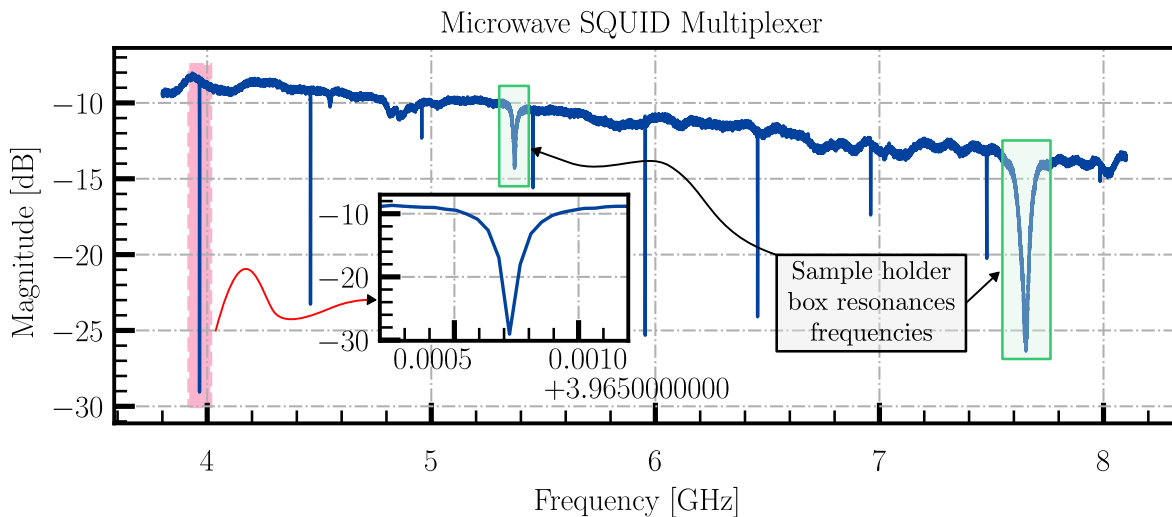


Figure 9.30: μ MUX for the tests. The sample holder resonance frequencies can be appreciated. The first channel of the array was selected and highlighted in the plot.

An update on the PSD was carried out and is shown in Figure 9.31, including the path from the RF front-end, through the cryostat and the μ MUX, and the path back to the front-end. The input power to the cryostat was of -40 dBm, yielding a total power in the μ MUX of roughly -80 dBm, see the input path in Figure 9.28. The return path has approximately 35 dB of gain due to the LNA, and around 6 dB of gain in the RF front-end demodulation.

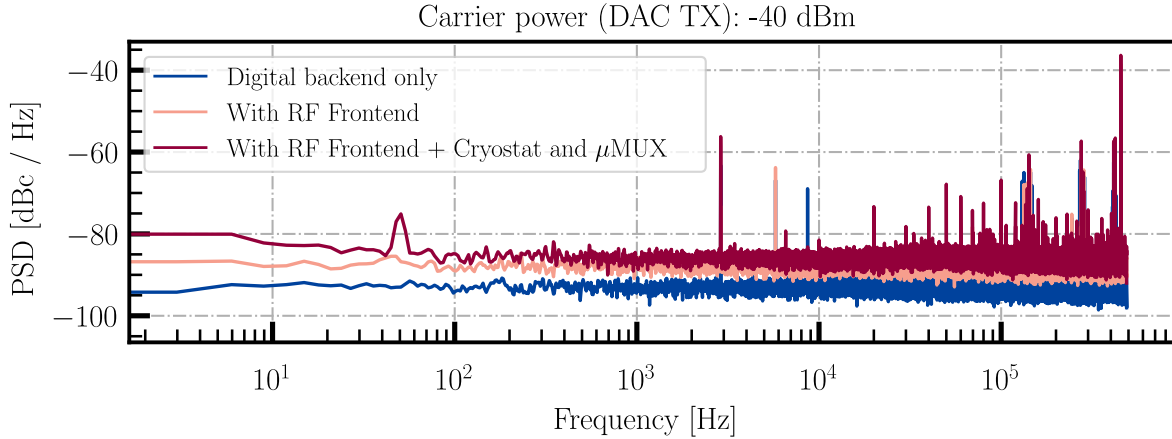


Figure 9.31: Digital backend with the RF frontend and the cryostat. A 32 samples window size was utilized. The input power to the cryostat (third new measurement) was of -40 dBm. The spurious signals that can be seen in the new acquisition are related with the open circuit termination of the coupling inductor of the input circuit in the rf-SQUID.

Different reset frequencies, f_{reset} (referred to the sawtooth frequency or flux-ramp frequency), were generated for the ramp signal, with different amplitudes in order to increase the number of flux-quanta, and then again but adding a phase modulation to the ramp signal. The different combination of f_{reset} and ramp amplitude, will generate different SQUID frequencies, f_{SQUID} . The results of the measurements are depicted in the following figures 9.32, 9.33, 9.34 and 9.35.

Figure 9.32 shows the GF output for a sawtooth signal with a frequency of 1 kHz. Three different maximum amplitude values were used matching one, two and four Φ_0 ; delivering consistent f_{SQUID} of 1 kHz, 2 kHz and 4 kHz respectively. The mean value of the GF was removed (the carrier input power) for visualization purposes and clarity of the result.

Figure 9.33 illustrates the FFT of the signals depicted in Figure 9.32.

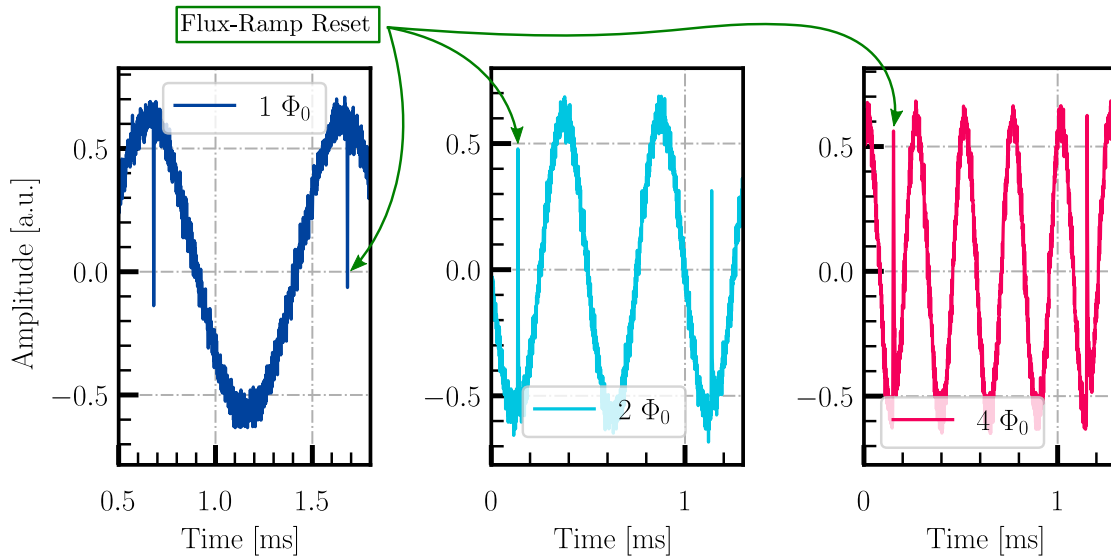


Figure 9.32: GFB output. A sawtooth of $f_{\text{reset}} = 1$ kHz was generated with different amplitudes: for one, two and four quantum-flux (Φ_0). The expected result is that the f_{SQUID} is N_{Φ_0} times the sawtooth frequency. The sawtooth reset can be appreciated in the images.

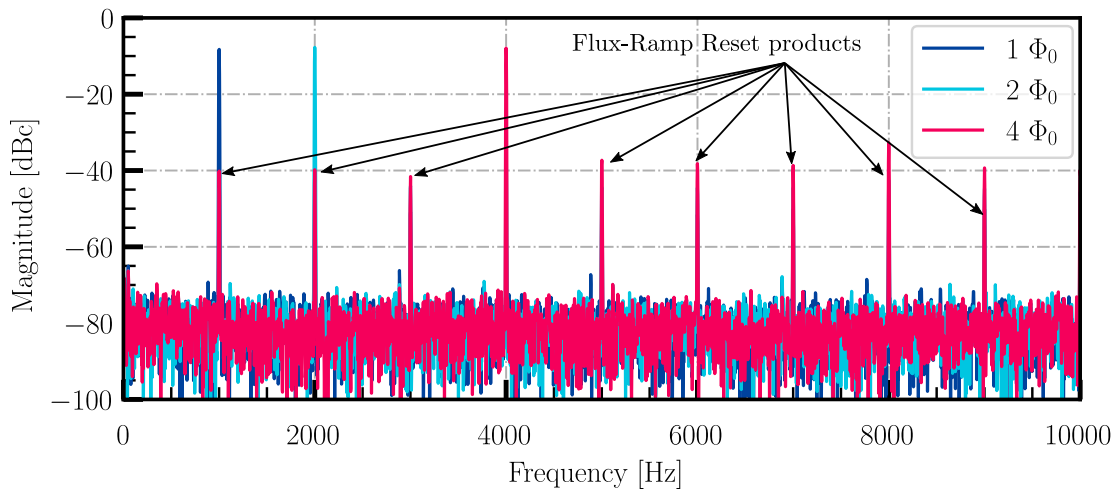


Figure 9.33: Frequency Spectrum of the channelized signals. The sawtooth reset products, marked in the plot, are consistent with signal processing theory: a Dirac delta, $\delta(t)$, in the time-domain has a comb frequency spectrum: each component is spaced f_{reset} . The stronger components belong to the f_{SQUID} : 1 kHz, 2 kHz and 4 kHz.

Figure 9.33 shows the impact of the f_{reset} in the system due to the phase jumps that the sawtooth introduces, appreciated like a train of Dirac Deltas equally spaced every f_{reset} , being 1 kHz for this test. Meanwhile, the stronger components belong to the f_{SQUID} : 1 kHz, 2 kHz and 4 kHz due to the f_{SQUID} .

Figure 9.34 shows the GF output for a sawtooth signal with a frequency of 14 kHz.

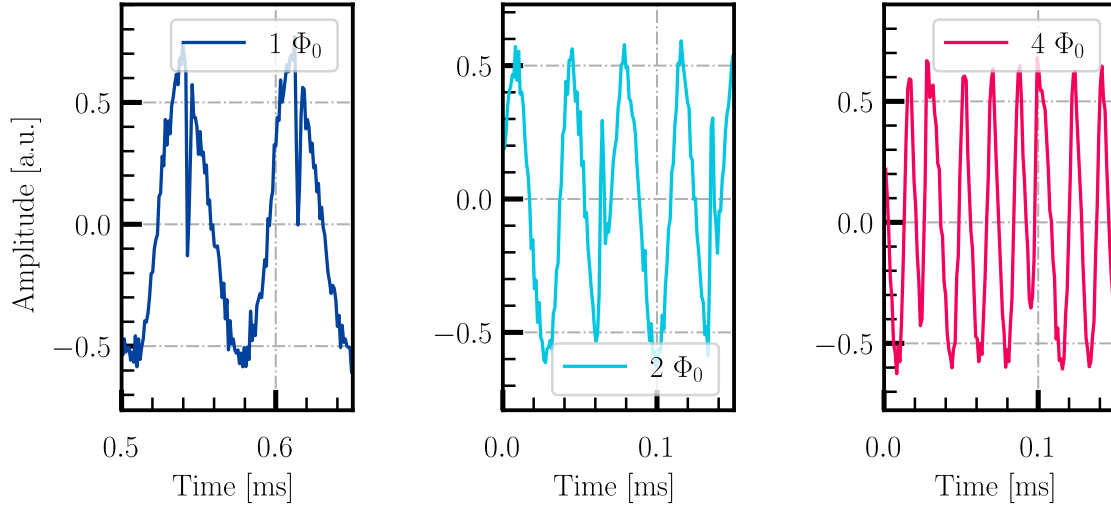


Figure 9.34: Goertzel Filter Channelizer output. A sawtooth of 14 kHz was generated with different amplitudes: for one, two and four quantum-flux (Φ_0).

The visualization of the phase jumps turns out to be a little bit complicated for the case of four Φ_0 , due to sampling reasons. However, Figure 9.35 shows the spectral content with the same outcome of the $f_{\text{reset}} = 1$ kHz case regarding the FRM products, but in this case for $f_{\text{reset}} = 14$ kHz.

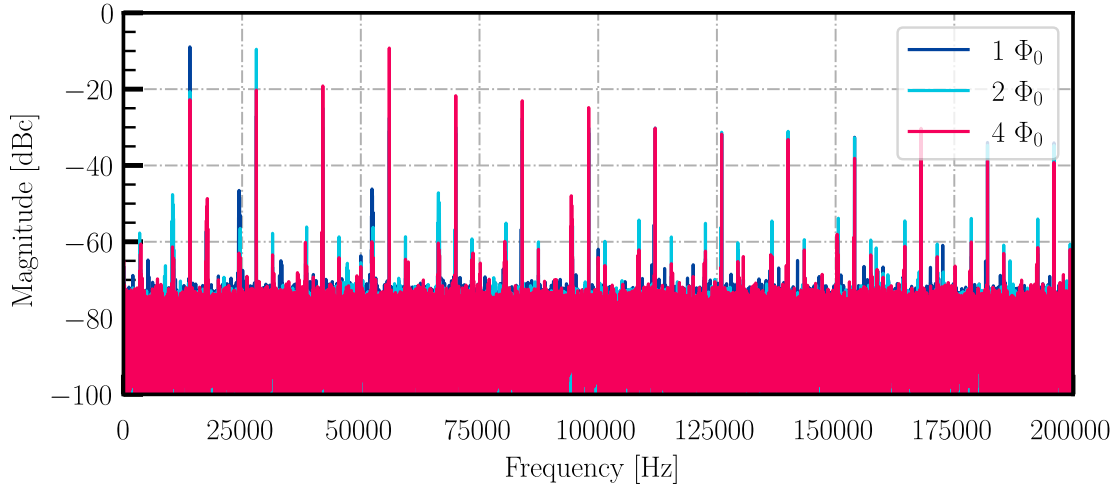


Figure 9.35: Frequency Spectrum of the channelized signals. The stronger components belong to the f_{SQUID} : 14 kHz, 28 kHz and 56 kHz. The spurious components due to the flux-ramp modulation are at the expected distance of 14 kHz

These results illustrate the importance on the selection of the f_{reset} and its amplitude,

as the detector signal will be located between the f_{SQUID} and between the two f_{reset} nearest products.

The ultimate test would have been carried out by coupling a detector to the μMUX . However, during the course of this Thesis work, no detector was available for this test. Instead, a signal $d(t)$ was added to modulate the previously analyzed sawtooth, thereby emulating the presence of a detector. This approach was implemented in two different ways: the introduction of a PM modulating signal and the performance of arithmetic addition with another signal (which emulates a more realistic scenario).

$$y_1(t) = A \cdot \text{ramp}[2\pi f_{\text{reset}}t + d(t)] \quad (9.6)$$

$$y_2(t) = A \cdot \text{ramp}(2\pi f_{\text{reset}}t) + d(t) \quad (9.7)$$

The emulated detector signal, $d(t)$, was a sinusoidal one at different frequencies and modulation indexes. The result of these experiments are depicted in the following set of figures. The results from applying eq. (9.6) are presented in figures 9.36, 9.38 and 9.37; while for formula (9.7) is presented in Figure 9.39.

The GF outputs are not shown in their time domain form as they are visually the same as the already presented plots, but instead, their FFT is presented in Figure 9.36. There, the highlighted FFT bin represents the SQUID frequency, f_{SQUID} , where around it is possible to appreciate the components of the generated PM of 135 Hz.

An f_{reset} of 28 kHz with an amplitude for four Φ_0 was generated, yielding an f_{SQUID} of 112 kHz, visible in Figure 9.36.

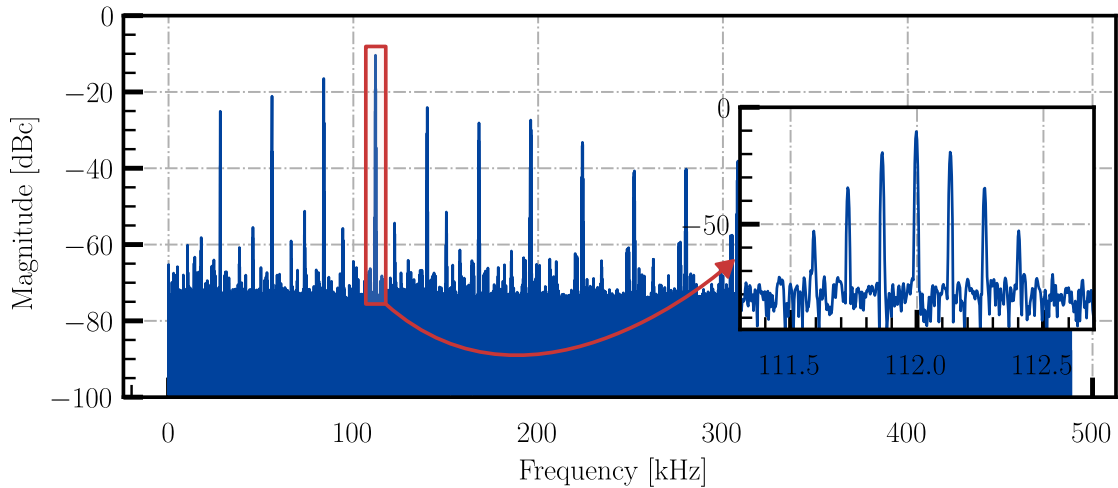


Figure 9.36: FFT of one of the acquisitions with detector emulation: the reset frequency was of 28 kHz, with an amplitude for four Φ_0 . The highlighted FFT bin represents the SQUID frequency, where around it is possible to visualize the components of the generated PM. In this particular plot, for a PM of 135 Hz.

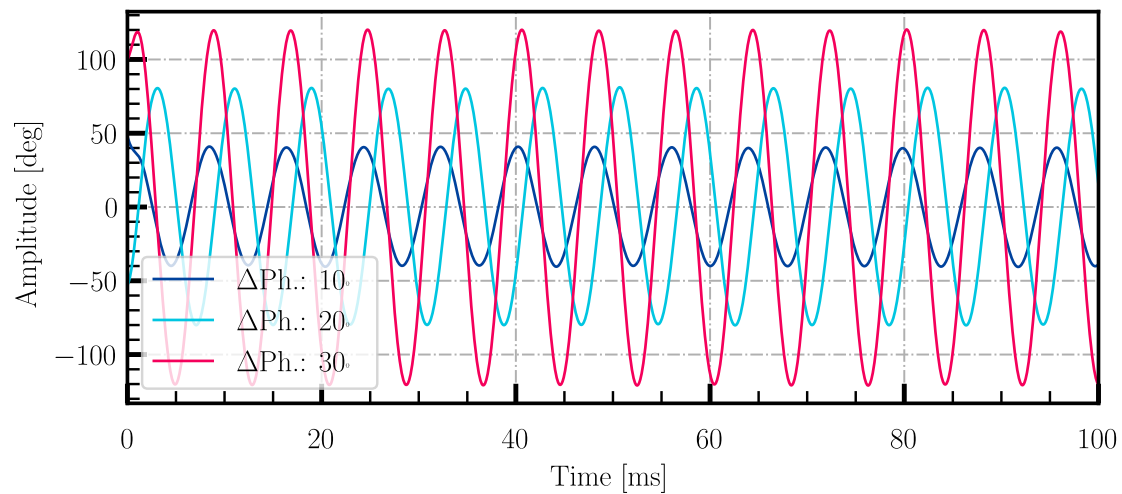


Figure 9.37: Quadrature demodulation of three different detector amplitudes (phase deviation), for four Φ_0 . The result is consistent with the expected value of four times the detector signal, retrieving the generated 135 Hz sinusoidal detector signal. The output of the quadrature demodulation was passed through a digital Butterworth low pass filter of 4th order and a f_{cut} at 500 Hz, in order to remove the high frequency components.

Performing a quadrature demodulation of this component to retrieve the 135 Hz modulating signal, and applying a Butterworth low pass filter with a f_{cut} at 500 Hz allows the recovery of the emulated detector signals, as shown in Figure 9.37 for three different cases. Figure 9.38 presents the same results for a detector signal of 10 Hz.

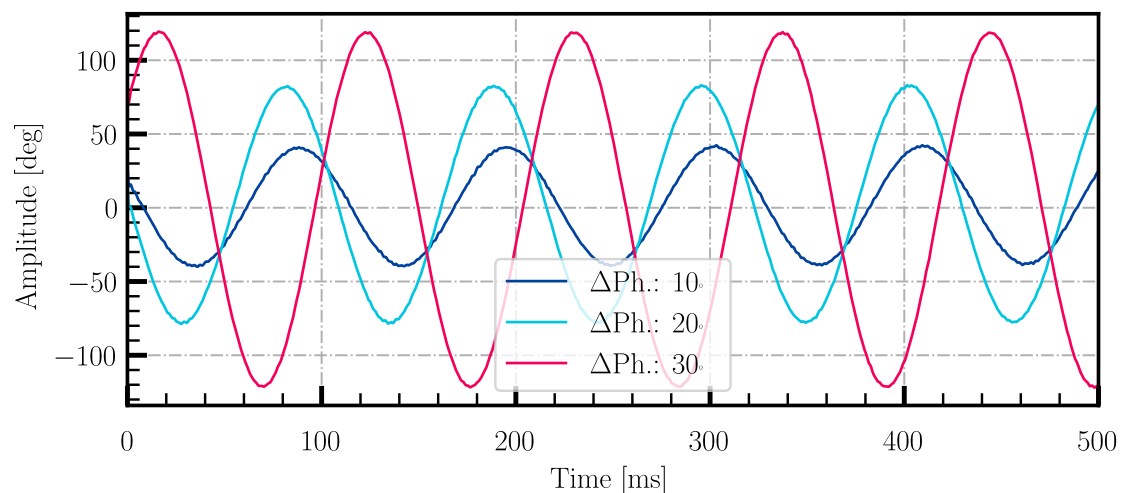


Figure 9.38: Quadrature demodulation of three different detector amplitudes (phase deviation), for four Φ_0 . The result is consistent with the expected value of four times the detector signal, retrieving the generated 10 Hz sinusoidal detector signal. The output of the quadrature demodulation was passed through a digital Butterworth low pass filter of 4th order and a f_{cut} at 500 Hz, in order to remove the high frequency components.

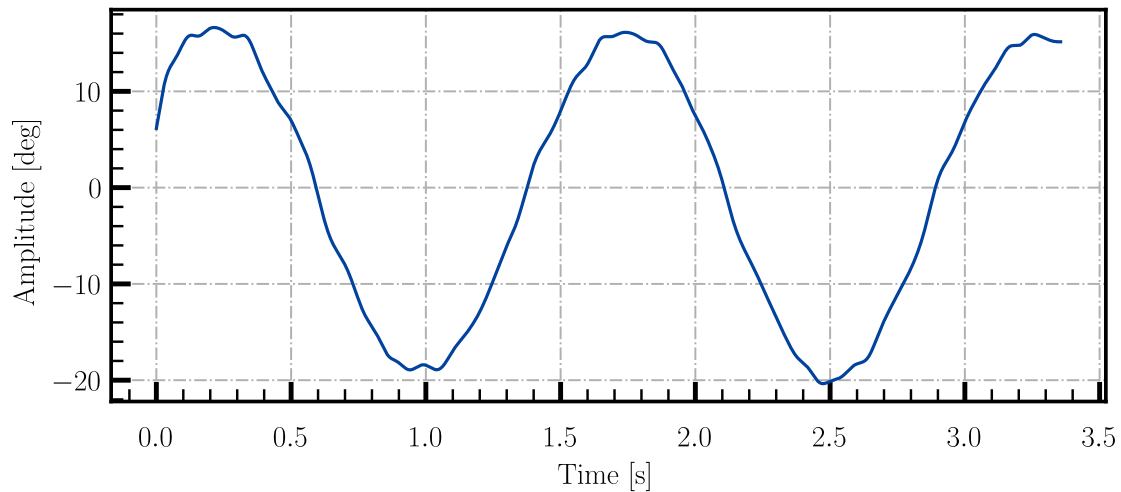


Figure 9.39: The generated 665 mHz sinusoidal detector signal was recovered. The output of the quadrature demodulation was passed through a digital Butterworth low pass filter of 4th order and a f_{cut} at 10 Hz, in order to remove the high frequency components.

It is important to note that the μMUX used in these tests has been optimized for CMB experiments, which is why its bandwidth is approximately 200 kHz. This limited the frequency of the sawtooth and, consequently, the number of quantum fluxes that could be employed. This resulted in a SQUID response frequency of less than 100 kHz. Additionally, the experiment faced a significant constraint when using the arbitrary waveform generation feature of the Picotest instrument, given its limited memory depth of 256 K, equivalent to 262.144 samples, when attempting the emulation using eq. (9.7).

Due to the relationship between the sawtooth and the desired detector signals, the sawtooth had a frequency of 2 kHz with an amplitude of four Φ_0 , while the detector signals ranged from a few mHz to several Hz. These factors contributed to the impossibility to emulate exponential decays with rapid rise times, similar to those encountered in calorimetric experiments. As a result, such scenarios were not tested.

Chapter 10

Summary and perspective

The Electron Capture in ^{163}Ho (ECHO) experiment aims to investigate the neutrino mass in the sub-Ev region, analyzing the end-point region of the ^{163}Ho electron capture spectrum. Large arrays of Magnetic Microcalorimeters (MMCs), loaded with ^{163}Ho , are planned to be used for this purpose operated in parallel to ultimately acquire a statistically significant volume of data. The Q&U Bolometric Interferometer for Cosmology (QUBIC) will contribute in the quest of finding the so called *smoking gun* of inflation, by detecting and characterizing the Cosmic Microwave Background Radiation (CMB) B-modes polarization. B-modes are tensorial perturbations in the metric, product of gravitational waves. As the inflation model predicts the existence of primordial gravitational waves, QUBIC attempts to measure, in particular, primordial B-modes using superconducting bolometers.

These experiments present challenges to be addressed, not only in the low temperature detectors but also in the warm electronics; driving improvements constantly in both cases. These improvements include achieving higher sensitivity, reducing dissipation at mK stages, and increasing multiplexing factors, among others. The pursuit of a higher multiplexing factor naturally leads to Microwave SQUID Multiplexing (μMUX), which involves the injection and subsequent reading of a multi-tonal signal.

Single tone detection methods used to detect each individual frequency component of the aforementioned multitoneal signal, turn out to be an attractive approach as it mainly improves the configuration flexibility and the control of the spectral leakage in this kind of systems.

In this work, a novel method based on a bank of Goertzel Filters (GF) for the channelization of multitoneal signals was presented. The GF is an IIR filter resonating around the bin of interest of a Discrete Fourier Transform (DFT) bin array. Accurate Python simulations of the whole acquisition chain were performed, which included: the Digital Down Converter (DDC) simulation using its transfer function model, the evaluation of several window functions for improving the GF response and the GF itself. These simulations were validated with room temperature measurements presented in chapter 9.

A simple modulation model for the context of cryogenic detectors was presented and used for the analysis of the proposed channelizer, which yielded results accurate enough for the development of the filter bank. This also helped to realize that the GF as it is described in the literature is not enough when implemented in real-time processing, as was explained in Section 6.6. In turn, a new approach is proposed here for targeting a Sliding GF which is more resource efficient when implemented in a Field Programmable Gate Array (FPGA) than the Comb Filter proposal.

The proposed and implemented channelizer performance was evaluated regarding its noise, linearity and demodulation capabilities, showing remarkable characteristics comparable with the Polyphase Filter Bank (PFB) state-of-the-art implementations. The arithmetic treatment, which was thoroughly analyzed and accurately simulated, proved to be of vital importance. It delivered precise results, as confirmed by the measurements. Furthermore, the current state of development, with the necessary resources, was achieved using an FPGA logic operation frequency of 250 MHz. In contrast, other works cited within this thesis operate at 500 MHz. One clear next step is to transition to this higher frequency operation, which will significantly reduce FPGA resource consumption. Also exploring the combination of a PFB + GF (with the idea of replacing the DDC stages) sounds tempting and actually, surprisingly promising. This will be explored and implemented eventually, as part of an extension of this work.

Radio Frequency System-on-Chip (RFSoc) devices definitely are the next generation for the instrumentation of the read-out electronics for cryogenic particle detectors multiplexed in the frequency domain. These devices simplify the overall complexity of the system by removing the requirement of mixers for doing the frequency translation, working with direct synthesis with the DACs and direct sampling with the ADCs. A future migration of the developed firmware in this Thesis will be a part of an extension of this work.

An interesting feature, and perhaps one of the most powerful in this approach, is the flexible configuration capabilities the channelizer has. A bank of Goertzel filters was created, each filter reading the same input signal while selecting, with their unique and non-shared tuning frequency, a well-defined component of that input signal. This tuning frequency can be changed in run-time through the ServiceHub application service, without the necessity of a reboot of the hardware, or a re-flashing of the FPGA. Thus the channelizer can track each tone in the input frequency if its necessary or just reconfigure the system for a different μ MUX.

The signals to be measured for CMB experiments fall within the range from DC to 2.5 MHz. These values are quite complicated to recover as the flicker noise ($1/f$) in the DAQ systems plays an important role here in detriment of the signal integrity. However, both the RF front-end designed for ECHO and the GF approach implemented in the ZCU102 using the same converters as the ECHO electronics (but without the specific improvements applied [118]) could recover a weak signal with a frequency of only 665 mHz.

This could be done with extremely low effort (by only adding a post-processing step of a 4th order Butterworth low pass filtering in python after the typical quadrature demodulation). These results show that the ECHo hardware could be used for CMB experiments.

Multitonal signal generation is still an open research topic in these kind of systems and, in this particular application. In this work we showed that even when the separation between frequency tones is not equidistant the performance is similar to the random phases method. Yet, there is a tolerance value as was demonstrated up to where the Newman and Schroeder phases are still the superior methods. The utilization of PFB for the generation of multi-tonal signals will be explored, as they present lower requirements in terms of memory and allows sub-Hz resolution.

A power calibration method was also proposed which encompassed the measurement of the transmitted signals in different stages of the system. This characterization should be useful for improving the generation algorithms making these algorithms aware of the conditions of the hardware system. Hence in principle, after this procedure is applied it should be possible to generate almost calibrated signals, thus making the fine tuning a much more relaxed process: skipping the slope compensation and reducing the number of required iterations for the TX IQ imbalance correction. This was verified in the sense of the traceable value for the power of the signal that was delivered to the resonators in the cryostat, for the shown results.

In light of all of these, this work has contributed with a novel channelization approach using the Goertzel Filter, giving rise to the Goertzel Filter Bank channelizer (GFB). This method is very efficient in hardware resource consumption, and can be used for the readout of large arrays of MMCs and MMBs multiplexed in the frequency domain. This innovative approach is now open for testing, expansion, and improvement by the wider scientific community working in this field.

List of Figures

1.1	Planck Results 2018	4
1.2	The QUBIC Telescope	5
1.3	Electron Capture in Holmium process	5
1.4	ECHo Energy Spectrum and endpoint	6
1.5	ECHo Energy Spectrum and endpoint with pile-up	7
2.1	Discovery of superconductivity	9
2.2	Electron-Phonon interaction	11
2.3	Josephson Junction diagram	11
2.4	Superconducting Quantum Interference Device	13
2.5	DC- and RF-SQUID	15
2.6	TES transition and model	16
2.7	Microwave Kinetic Inductance Detector	18
2.8	MMC Model	19
2.9	TLS Au:Er and MMC Canonical ensemble	20
2.10	MMB expected signal	21
2.11	MMB conceptual detector layout	22
3.1	TDM schematic	23
3.2	TDM for the QUBIC project	24
3.3	CDM schematic	25
3.4	FDM schematic	26
3.5	FDM schematic for MHz case	26
3.6	Quarter-wave resonator	27
3.7	μ MUX single channel	28
3.8	Microwave SQUID Multiplexer	29
4.1	Basic A/D conversion steps	32
4.2	Quantization noise - Processing gain	34
4.3	MPSoC and RFSoc simplified block diagram of the PS and PL regions [118, 139].	38
4.4	DSP48E2 Slice schematic and basic functionality.	39
4.5	RFSoc RF Data Converter [147]. Each DAC and ADC symbol represents two of them (therefore the two arrows).	40
4.6	Proposed read-out system	41

4.7	Digital Electronics - ZCU102	43
4.8	Converter Board - FMCDAQ2 Board	44
4.9	High Frequency Electronics	45
4.10	ServiceHub Client - Plugin - Hardware sketch	45
5.1	Digital Down Conversion concept	47
5.2	CIC decimator filter	48
5.3	CIC interpolator filter	48
5.4	CIC filter magnitude response simulation	50
5.5	CIC filter cut-off frequency vs number of stages	50
5.6	Compensation FIR filter response	53
5.7	Digital Down Converter python simulation	53
6.1	Goertzel Filter block diagram	59
6.2	Goertzel Filter State Space Variables	61
6.3	Goertzel Filter block diagram with Window function	64
6.4	DFT Circular Shift property	68
6.5	Goertzel Filter with Comb Filter for targeting a sliding version	69
6.6	Goertzel Filter frequency response with different window functions, and window sizes	70
6.7	Goertzel Filter circular shift problem	71
6.8	Goertzel Filter circular shift problem solution	71
6.9	GF demodulation capabilities - Input signal	72
6.10	GF demodulation capabilities - Input signal FFT	72
6.11	GF demodulation capabilities - GF FFT output	73
6.12	GF demodulation capabilities - Quadrature demodulation	73
7.1	Multi-tonal signal without PAPR reduction	77
7.2	FFT of the previous Multi-tonal signal	77
7.3	IQ modulation	80
7.4	IQ modulation frequency shift	81
7.5	IMRR map	83
7.6	80 tones multi-tonal signal simulation with different PAPR reduction algorithms	84
7.7	Analysis of the CCDF for different PAPR reduction algorithms	85
7.8	Analysis of the CCDF for different perturbation factors	86
8.1	Stimulation module diagram	87
8.2	Demodulation cascade overview	88
8.3	Channelization process sketch	89
8.4	Goertzel Algorithm Mapping module	90
8.5	Goertzel Filter core	90
8.6	Implemented Digital Down Conversion	91
8.7	Implemented Digital Down Converter	92
8.8	DDCs and GF interconnection diagram	93

8.9	Implementation of the Window Function	94
8.10	Estimated SNR as a function of the input frequency	95
8.11	Window Caption process	96
8.12	Arithmetic treatment implementation	97
8.13	Fixed-point arithmetic treatment	98
8.14	Complete firmware implementation map	100
9.1	DDC firmware loopback mode	103
9.2	DDC frequency response measurement	104
9.3	DDC and GF firmware loopback mode	104
9.4	Goertzel filter frequency response measurement	105
9.5	Demodulation capabilities experimental setup diagram	105
9.6	Room temperature resonator measurement	106
9.7	First experimental setup	106
9.8	AM demodulation capabilities experimental setup diagram	107
9.9	Demodulation results for AM	107
9.10	PSD of the demodulation results for AM	108
9.11	PM demodulation capabilities experimental setup diagram	108
9.12	Demodulation results PM, and PSD	109
9.13	Complete experimental setup	110
9.14	Converters output and input circuits	111
9.15	Experimental setup for DAC slope characterization	112
9.16	DAC roll-off	112
9.17	Output Power Calibration	113
9.18	Experimental setup for power calibration S1	114
9.19	Experimental setup for power calibration S2	114
9.20	Experimental setup for power calibration S3	115
9.21	Power calibration at different stages	116
9.22	Attenuation of different stages	116
9.23	Power Spectral Density of GF	117
9.24	IQ imbalance correction setup	118
9.25	Acquired image power and IMRR maps	119
9.26	IMRR compensation procedure concept	119
9.27	80 Tones compensated signal	120
9.28	Cryogenic setup	121
9.29	μ MUX under test chip.	122
9.30	μ MUX under test.	122
9.31	PSD of the backend, the frontend and the cryogenic setup	123
9.32	Goertzel Filter output for the case with only a flux-ramp applied, up to 4 ϕ_0 , $f_{\text{reset}} = 1 \text{ kHz}$	124
9.33	Frequency Spectrum of the channelized signals for $f_{\text{reset}} = 1 \text{ kHz}$	124
9.34	Goertzel Filter output for the case with only flux-ramp applied, up to 4 ϕ_0 , $f_{\text{reset}} = 14 \text{ kHz}$	125
9.35	Frequency Spectrum of the channelized signals for $f_{\text{reset}} = 14 \text{ kHz}$	125

List of Figures

9.36	FFT of the acquired data	126
9.37	Phase demodulation of the input signal for 135 Hz	127
9.38	Phase demodulation of the input signal for 10 Hz	127
9.39	Phase demodulation of a detector signal for 665 mHz	128

List of Tables

6.1	Fourier Transform for the continuous and discrete cases.	55
8.1	Resource requirements for one stimulation module working at 250 MHz configured for a frequency resolution of 7629.39 Hz (SLICES = 32768, OCTETS_PER_CLK = 16).	88
8.2	Resource requirements for the GF Core at 250 MHz, capable of processing four complex tones. I.S. stands for <i>Iterative Section</i> and N.I.S. for <i>Non-Iterative Section</i> . The resources of the kernel already presented, are repeated in this table for completeness.	91
8.3	Resource requirements for one DDC working at 250 MHz for $R = 8$, a bandwidth efficiency of 94% (sampling frequency vs cut-off frequency) and 80 dB of alias rejection.	93
8.4	Resource requirements for the controller and one Window Multiplier working at 250 MHz.	93
8.5	Window functions PG, final SNR and final number of bits, for window size of $N = 256$ samples.	95
8.6	Data width after each stage. <i>ADC Converter</i> refers to the ADC block within the chip previous to the internal DDC. <i>ADC DDC</i> refers to the internal DDC of the ADC. <i>DDC firmware</i> refers to the described hardware within the FPGA.	96
8.7	Precision, range, resolution and dynamic range for each stage according to its fixed-point representation. The accuracy can be calculated as the resolution divided by two. WF stands for Window Function.	98
8.8	Resource requirements per complex tone for the different approaches with a disaggregation of the main parts. The estimation is for 128 complex tones. The ECHO's firmware runs at 500 MHz and the one from this work runs at 250 MHz. MDDC stands for Multi-channel DDC.	101

List of Algorithms

1	Goertzel Algorithm	56
2	Standard Goertzel Algorithm	62
3	Generalized Goertzel Algorithm for non-integer k values and shortened iteration loop	63
4	Goertzel algorithm generalized to non-integer multiples of fundamental frequency k	63
5	Goertzel algorithm generalized to non-integer multiples of fundamental frequency - Sliding Version	69
4	Goertzel algorithm generalized to non-integer multiples of fundamental frequency k	89

List of Acronyms

μMUX	Microwave SQUID Multiplexer
μP	micro-processor
ADC	Analog-to-Digital Converter
ASIC	Application Specific Integrated Circuit
BB	baseband
BCS	Bardeen, Cooper, and Schrieffer Theory
CCDF	Complementary Cumulative Distribution Function
CDM	Code Division Multiplexing
CFIR	Compensation Finite Impulse Response
CIC	Cascaded Integrator-Comb
CLB	Configurable Logic Block
CMB	Cosmic Microwave Background Radiation
COBE	Cosmic Background Explorer
CS-PFB	Critically Sampled Polyphase Filter Bank
DAC	Digital-to-Analog Converter
DDC	Digital Down Converter
DFS	Discrete Fourier Series
DFT	Discrete Fourier Transform
DMA	Direct Memory Access
DSO	Digital Oscilloscope
DSP	Digital Signal Processing
DTFT	Discrete Time Fourier Transform
DTMF	Dual-Tone Multi-Frequency
DUC	Digital Up Converter
ECHo	Electron Capture in ¹⁶³ Ho Experiment
ENOB	Effective Number-of-Bits
ESPRIT	Estimation of Signal Parameters via Rotational Invariant Techniques
FDM	Frequency Division Multiplexing

FF	Flip-Flop
FFT	Fast Fourier Transform
FIR	Finite Impulse Response
FPGA	Field Programmable Gate Array
FRM	Flux-Ramp Modulation
FS	Fourier Series
FT	Fourier Transform
GF	Goertzel Filter
GFB	Goertzel Filter Bank
GLAG	Ginzburg, Landau, Abrikosov and Gorkov Theory
HLS	High-Level Synthesis
HTS	high-Tc superconductors
IIR	Infinite Impulse Response
IMRR	Image Rejection Ratio
IP	Intellectual Property
ISI	Inter-Symbol-Interference
LNA	Low-Noise Amplifier
LUT	Look-Up Table
MKID	Microwave Kinetic Inductance Detector
MMB	Magnetic Microbolometers
MMC	Metallic Magnetic Calorimeters
MMC	Magnetic Microcalorimeters
MPSoC	Multiprocessor System-on-Chip
MUSIC	MULTiple Signal Classification
NCO	Numerical Controlled Oscillator
NEP	Noise Equivalent Power
OS-PFB	Over Sampled Polyphase Filter Bank
PAPR	Peak-to-Average Power Ratio
PDF	Probability Distribution Function
PFB	Polyphase Filter Bank
PSD	Power Spectral Density
QUBIC	Q&U Bolometric Interferometer for Cosmology Project
RCSJ	Resistively and Capacitively shunted Junction
RFSoc	Radio Frequency System-on-Chip
RMS	Root-Mean-Squared
RVB	Resonating Valence Bond
SA	Spectrum Analyzer

List of Acronyms

SDR	Software-defined Radio
SIS	Superconductor-Insulator-Superconductor
SNR	Signal-to-Noise Ratio
SoC	System-on-Chip
SQUID	Superconducting Quantum Interference Device
SR	Software Radio
TDM	Time Division Multiplexing
TES	Transition Edge Sensor
TLS	Two-Level System

Bibliography

- [1] M. Aker, A. Beglarian, J. Behrens, A. Berlev, U. Besserer, B. Bieringer et al. “Direct neutrino-mass measurement with sub-electronvolt sensitivity.” *Nature Physics*, vol. 18, pp. 160–166. doi:10.1038/s41567-021-01463-1, 2 2022.
- [2] C. Weinheimer. “KATRIN, a next generation tritium β decay experiment in search for the absolute neutrino mass scale.” *Progress in Particle and Nuclear Physics*, vol. 48, pp. 141–150. doi:10.1016/S0146-6410(02)00120-5, 1 2002.
- [3] L. Gastaldo, K. Blaum, K. Chrysalidis, T. D. Goodacre, A. Domula, M. Door et al. “The electron capture in ^{163}Ho experiment – ECHo.” *European Physical Journal: Special Topics*, vol. 226, pp. 1623–1694. doi:10.1140/epjst/e2017-70071-y, 6 2017.
- [4] A. A. Penzias and R. W. Wilson. “A Measurement of Excess Antenna Temperature at 4080 Mc/s.” *The Astrophysical Journal*, vol. 142, p. 419. doi:10.1086/148307, 7 1965.
- [5] J. Mather, M. Hauser, C. Bennett, N. Boggess, E. Cheng, E. R.E. et al. “Early results from the Cosmic Background Explorer (COBE).” *Advances in Space Research*, vol. 11, pp. 181–191. doi:10.1016/0273-1177(91)90489-7, 1 1991.
- [6] D. N. Spergel and M. Zaldarriaga. “Cosmic Microwave Background Polarization as a Direct Test of Inflation.” *Physical Review Letters*, vol. 79, pp. 2180–2183. doi:10.1103/PhysRevLett.79.2180, 9 1997.
- [7] U. Seljak and M. Zaldarriaga. “Signature of Gravity Waves in the Polarization of the Microwave Background.” *Physical Review Letters*, vol. 78, pp. 2054–2057. doi:10.1103/PhysRevLett.78.2054, 3 1997.
- [8] G. Siringo, E. Kreysa, A. Kovács, F. Schuller, A. Weiß, W. Esch et al. “The large APEX BOlometer CAmera LABOCA.” *Astronomy and Astrophysics*, vol. 497, pp. 945–962. doi:10.1051/0004-6361/200811454, 4 2009.
- [9] P. A. Ade, R. W. Aikin, D. Barkats, S. J. Benton, C. A. Bischoff, J. J. Bock et al. “Detection of B-mode polarization at degree angular scales by BICEP2.” *Physical Review Letters*, vol. 112. doi:10.1103/PhysRevLett.112.241101, 6 2014.

- [10] J. R. Bond, P. Ade, A. Balbi, J. Bock, J. Borrill, A. Boscaleri et al. “CMB Analysis of Boomerang & Maxima & the Cosmic Parameters $\Omega_{tot}, \Omega_b h^2, \Omega_{cdm} h^2, \Omega_\Lambda, n_s$.” 11 2000.
- [11] J. E. Carlstrom, P. A. R. Ade, K. A. Aird, B. A. Benson, L. E. Bleem, S. Buseti et al. “The 10 Meter South Pole Telescope.” *Publications of the Astronomical Society of the Pacific*, vol. 123, pp. 568–581. doi:10.1086/659879, 5 2011.
- [12] B. A. Benson, P. A. R. Ade, Z. Ahmed, S. W. Allen, K. Arnold, J. E. Austermann et al. “SPT-3G: a next-generation cosmic microwave background polarization experiment on the South Pole telescope.” In W. S. Holland and J. Zmuidzinas, eds., “SPIE Proceedings,” SPIE, Jul. 2014. doi:10.1117/12.2057305.
- [13] A. Suzuki, P. A. R. Ade, Y. Akiba, D. Alonso, K. Arnold, J. Aumont et al. “The LiteBIRD Satellite Mission: Sub-Kelvin Instrument.” *Journal of Low Temperature Physics*, vol. 193(5-6), pp. 1048–1056. doi:10.1007/s10909-018-1947-7, May 2018.
- [14] Y. Inoue, P. Ade, Y. Akiba, C. Aleman, K. Arnold, C. Baccigalupi et al. “POLARBEAR-2: an instrument for CMB polarization measurements.” In W. S. Holland and J. Zmuidzinas, eds., “SPIE Proceedings,” SPIE, Aug. 2016. doi:10.1117/12.2231961.
- [15] A. Suzuki, P. Ade, Y. Akiba, C. Aleman, K. Arnold, C. Baccigalupi et al. “The Polarbear-2 and the Simons Array Experiments.” *Journal of Low Temperature Physics*, vol. 184(3-4), pp. 805–810. doi:10.1007/s10909-015-1425-4, Jan. 2016.
- [16] J.-C. Hamilton, L. Mousset, E. Battistelli, P. de Bernardis, M.-A. Bigot-Sazy, P. Chaniai et al. “QUBIC I: Overview and science program.” *Journal of Cosmology and Astroparticle Physics*, vol. 2022, p. 034. doi:10.1088/1475-7516/2022/04/034, 4 2022.
- [17] A. Fleischmann, C. Enss, and G. Seidel. *Metallic Magnetic Calorimeters*, pp. 151–216. 7 2005. doi:10.1007/10933596_4.
- [18] A. Fleischmann, L. Gastaldo, S. Kempf, A. Kirsch, A. Pabinger, C. Pies et al. “Metallic Magnetic Calorimeters.” In “AIP Conference Proceedings,” pp. 571–578. AIP Publishing, 12 2009. doi:10.1063/1.3292407.
- [19] K. Irwin and G. Hilton. *Transition-Edge Sensors*, vol. 99, pp. 63–150. 7 2005. doi:10.1007/10933596_3.
- [20] J. A. Chervenak, K. D. Irwin, E. N. Grossman, J. M. Martinis, C. D. Reintsema, and M. E. Huber. “Superconducting multiplexer for arrays of transition edge sensors.” *Applied Physics Letters*, vol. 74(26), pp. 4043–4045. doi:10.1063/1.123255, Jun. 1999.

- [21] M. Dobbs, M. Halpern, K. D. Irwin, A. T. Lee, J. A. B. Mates, and B. A. Mazin. “Multiplexed readout of CMB polarimeters.” *Journal of Physics: Conference Series*, vol. 155, p. 012004. doi:10.1088/1742-6596/155/1/012004, Mar. 2009.
- [22] K. D. Irwin, M. D. Niemack, J. Beyer, H. M. Cho, W. B. Doriese, G. C. Hilton et al. “Code-division multiplexing of superconducting transition-edge sensor arrays.” *Superconductor Science and Technology*, vol. 23(3), p. 034004. doi:10.1088/0953-2048/23/3/034004, Feb. 2010.
- [23] K. M. Morgan, B. K. Alpert, D. A. Bennett, E. V. Denison, W. B. Doriese, J. W. Fowler et al. “Code-division-multiplexed readout of large arrays of TES microcalorimeters.” *Applied Physics Letters*, vol. 109(11), p. 112604. doi:10.1063/1.4962636, Sep. 2016.
- [24] K. D. Irwin and K. W. Lehnert. “Microwave SQUID multiplexer.” *Applied Physics Letters*, vol. 85, pp. 2107–2109. doi:10.1063/1.1791733, 9 2004.
- [25] J. A. B. Mates, G. C. Hilton, K. D. Irwin, L. R. Vale, and K. W. Lehnert. “Demonstration of a multiplexer of dissipationless superconducting quantum interference devices.” *Applied Physics Letters*, vol. 92(2). doi:10.1063/1.2803852, Jan. 2008.
- [26] S. Kempf, M. Wegner, A. Fleischmann, L. Gastaldo, F. Herrmann, M. Papst et al. “Demonstration of a scalable frequency-domain readout of metallic magnetic calorimeters by means of a microwave SQUID multiplexer.” *AIP Advances*, vol. 7(1). doi:10.1063/1.4973872, Jan. 2017.
- [27] B. A. Mazin, P. K. Day, K. D. Irwin, C. D. Reintsema, and J. Zmuidzinas. “Digital readouts for large microwave low-temperature detector arrays.” *Nuclear Instruments and Methods in Physics Research Section A: Accelerators, Spectrometers, Detectors and Associated Equipment*, vol. 559(2), pp. 799–801. doi:10.1016/j.nima.2005.12.208, Apr. 2006.
- [28] K. D. Irwin, B. Young, B. Cabrera, and A. Miller. “Shannon Limits for Low-Temperature Detector Readout.” In “AIP Conference Proceedings,” AIP, 2009. doi:10.1063/1.3292320.
- [29] L. Mousset, M. G. Larena, E. Battistelli, P. de Bernardis, P. Chaniel, G. D'Alessandro et al. “QUBIC II: Spectral polarimetry with bolometric interferometry.” *Journal of Cosmology and Astroparticle Physics*, vol. 2022(04), p. 035. doi:10.1088/1475-7516/2022/04/035, Apr. 2022.
- [30] A. H. Guth. “Inflationary universe: A possible solution to the horizon and flatness problems.” *Phys. Rev. D*, vol. 23, pp. 347–356. doi:10.1103/PhysRevD.23.347, Jan 1981.
- [31] A. Linde. “A new inflationary universe scenario: A possible solution of the horizon, flatness, homogeneity, isotropy and primordial monopole problems.” *Physics Letters B*, vol. 108(6), pp. 389–393. doi:10.1016/0370-2693(82)91219-9, Feb. 1982.

- [32] A. Albrecht and P. J. Steinhardt. “Cosmology for Grand Unified Theories with Radiatively Induced Symmetry Breaking.” *Phys. Rev. Lett.*, vol. 48, pp. 1220–1223. doi:10.1103/PhysRevLett.48.1220, Apr 1982.
- [33] R. Brout, F. Englert, and E. Gunzig. “The creation of the universe as a quantum phenomenon.” *Annals of Physics*, vol. 115(1), pp. 78–106. doi:10.1016/0003-4916(78)90176-8, Sep. 1978.
- [34] A. Starobinsky. “A new type of isotropic cosmological models without singularity.” *Physics Letters B*, vol. 91(1), pp. 99–102. doi:10.1016/0370-2693(80)90670-x, Mar. 1980.
- [35] P. A. R. Ade, N. Aghanim, C. Armitage-Caplan, M. Arnaud, M. Ashdown, F. Atrio-Barandela et al. “Planck 2013 results. XXII. Constraints on inflation.” *Astronomy & Astrophysics*, vol. 571, p. A22. doi:10.1051/0004-6361/201321569, Oct. 2014.
- [36] E. S. A. ESA. “Planck Image Gallery.” <https://www.cosmos.esa.int/web/planck/picture-gallery>.
- [37] E. S. Battistelli, P. Ade, J. G. Alberro, A. Almela, G. Amico, L. H. Arnaldi et al. “QUBIC: The Q&U Bolometric Interferometer for Cosmology.” *Journal of Low Temperature Physics*, vol. 199(1-2), pp. 482–490. doi:10.1007/s10909-020-02370-0, Feb. 2020.
- [38] G. D’Alessandro, L. Mele, F. Columbro, G. Amico, E. Battistelli, P. de Bernardis et al. “QUBIC VI: Cryogenic half wave plate rotator, design and performance.” *Journal of Cosmology and Astroparticle Physics*, vol. 2022(04), p. 039. doi:10.1088/1475-7516/2022/04/039, Apr. 2022.
- [39] S. Masi, E. Battistelli, P. de Bernardis, C. Chapron, F. Columbro, A. Coppolecchia et al. “QUBIC V: Cryogenic system design and performance.” *Journal of Cosmology and Astroparticle Physics*, vol. 2022(04), p. 038. doi:10.1088/1475-7516/2022/04/038, Apr. 2022.
- [40] F. Cavaliere, A. Mennella, M. Zannoni, P. Battaglia, E. Battistelli, P. de Bernardis et al. “QUBIC VII: The feedhorn-switch system of the technological demonstrator.” *Journal of Cosmology and Astroparticle Physics*, vol. 2022(04), p. 040. doi:10.1088/1475-7516/2022/04/040, Apr. 2022.
- [41] C. O’Sullivan, M. De Petris, G. Amico, E. Battistelli, P. de Bernardis, D. Burke et al. “QUBIC VIII: Optical design and performance.” *Journal of Cosmology and Astroparticle Physics*, vol. 2022(04), p. 041. doi:10.1088/1475-7516/2022/04/041, Apr. 2022.
- [42] M. Piat, G. Stankowiak, E. Battistelli, P. de Bernardis, G. D’Alessandro, M. D. Petris et al. “QUBIC IV: Performance of TES bolometers and readout electronics.” *Journal of Cosmology and Astroparticle Physics*, vol. 2022, p. 037. doi:10.1088/1475-7516/2022/04/037, 4 2022.

- [43] S. Eliseev, K. Blaum, M. Block, S. Chenmarev, H. Dorrer, C. E. Düllmann et al. “Direct Measurement of the Mass Difference of ^{163}Ho and ^{163}Dy Solves the Q -Value Puzzle for the Neutrino Mass Determination.” *Phys. Rev. Lett.*, vol. 115, p. 062501. doi:10.1103/PhysRevLett.115.062501, Aug 2015.
- [44] A. De Rújula and M. Lusignoli. “Calorimetric measurements of $^{163}\text{holmium}$ decay as tools to determine the electron neutrino mass.” *Physics Letters B*, vol. 118(4-6), pp. 429–434. doi:10.1016/0370-2693(82)90218-0, Dec. 1982.
- [45] S. Scholl. “Background analysis and reduction for the ECHo experiment.” *Journal of Physics: Conference Series*, vol. 718, p. 062051. doi:10.1088/1742-6596/718/6/062051, May 2016.
- [46] F. K. Ahrens. “Cryogenic read-out system and resonator optimisation for the microwave SQUID multiplexer within the ECHo experiment.” 2022. URL <http://www.ub.uni-heidelberg.de/archiv/32038>.
- [47] G. Goertzel. “An Algorithm for the Evaluation of Finite Trigonometric Series.” *The American Mathematical Monthly*, vol. 65, p. 34. doi:10.2307/2310304, 1 1958.
- [48] R. Lyons. “Goertzel Algorithm for a Non-Integer Frequency Index.” <https://www.dsprelated.com/showarticle/495.php>, October 2013.
- [49] H. K. Onnes. “Research notes.” *Communication Physics Laboratory 120b, 122b 124c, Univ. Leiden*, pp. 261–272, 1911.
- [50] W. Meissner and R. Ochsenfeld. “Ein neuer Effekt bei Eintritt der Supraleitfähigkeit.” *Die Naturwissenschaften*, vol. 21(44), pp. 787–788. doi:10.1007/bf01504252, Nov. 1933.
- [51] C. Enss and S. Hunklinger. *Low-Temperature Physics*. SpringerLink: Springer e-Books. Springer Berlin Heidelberg, 2005. URL <https://books.google.com.ar/books?id=ufM7sPMTGdAC>.
- [52] V. L. Ginzburg and L. D. Landau. “On the Theory of superconductivity.” *Zh. Eksp. Teor. Fiz.*, vol. 20, pp. 1064–1082. doi:10.1016/B978-0-08-010586-4.50035-3, 1950.
- [53] A. A. Abrikosov. “On the Magnetic properties of superconductors of the second group.” *Sov. Phys. JETP*, vol. 5, pp. 1174–1182, 1957.
- [54] L. P. Gor’kov. “Microscopic derivation of the Ginzburg–Landau equations in the theory of superconductivity.” *Sov. Phys. - JETP (Engl. Transl.); (United States)*, 1 1959. URL <https://www.osti.gov/biblio/7264935>.
- [55] J. Bardeen, L. N. Cooper, and J. R. Schrieffer. “Theory of Superconductivity.” *Phys. Rev.*, vol. 108, pp. 1175–1204. doi:10.1103/PhysRev.108.1175, Dec 1957.

- [56] J. G. Bednorz and K. A. Müller. “Possible high T_c superconductivity in the Ba-La-Cu-O system.” *Zeitschrift für Physik B Condensed Matter*, vol. 64(2), pp. 189–193. doi:10.1007/bf01303701, Jun. 1986.
- [57] P. W. Anderson. “The Resonating Valence Bond State in La_2CuO_4 and Superconductivity.” *Science*, vol. 235(4793), pp. 1196–1198. doi:10.1126/science.235.4793.1196, Mar. 1987.
- [58] L. N. Cooper. “Bound Electron Pairs in a Degenerate Fermi Gas.” *Phys. Rev.*, vol. 104, pp. 1189–1190. doi:10.1103/PhysRev.104.1189, Nov 1956.
- [59] B. Josephson. “Possible new effects in superconductive tunnelling.” *Physics Letters*, vol. 1(7), pp. 251–253. doi:10.1016/0031-9163(62)91369-0, Jul. 1962.
- [60] B. D. Josephson. “The discovery of tunnelling supercurrents.” *Rev. Mod. Phys.*, vol. 46, pp. 251–254. doi:10.1103/RevModPhys.46.251, Apr 1974.
- [61] Clarke, J. and Braginski, A.I. *The SQUID Handbook: Fundamentals and Technology of SQUIDS and SQUID Systems*. Wiley, 2006. URL <https://books.google.de/books?id=BsTTM-nU-JkC>.
- [62] P. Lethuillier. “Analysis of the current-voltage characteristic of the rf SQUID.” *Journal of Applied Physics*, vol. 73(11), pp. 7935–7948. doi:10.1063/1.353947, Jun. 1993.
- [63] A. H. Silver and J. E. Zimmerman. “Quantum States and Transitions in Weakly Connected Superconducting Rings.” *Phys. Rev.*, vol. 157, pp. 317–341. doi:10.1103/PhysRev.157.317, May 1967.
- [64] R. C. Jaklevic, J. Lambe, A. H. Silver, and J. E. Mercereau. “Quantum Interference Effects in Josephson Tunneling.” *Physical Review Letters*, vol. 12, pp. 159–160. doi:10.1103/PhysRevLett.12.159, 2 1964.
- [65] W. C. Stewart. “Current-Voltage Characteristics of Josephson Junctions.” *Applied Physics Letters*, vol. 12(8), pp. 277–280. doi:10.1063/1.1651991, 10 2003.
- [66] D. E. McCumber. “Effect of ac Impedance on dc Voltage-Current Characteristics of Superconductor Weak-Link Junctions.” *Journal of Applied Physics*, vol. 39(7), pp. 3113–3118. doi:10.1063/1.1656743, Jun. 1968.
- [67] Langley, S.P. *The Bolometer*. American Journal of Science, 1880. URL <https://books.google.de/books?id=j9olzQEACAAJ>.
- [68] S. P. T. “The Bolometer.” *Nature*, vol. 25(627), pp. 14–16. doi:10.1038/025014a0, Nov. 1881.
- [69] D. J. Benford. “Transition Edge Sensor Bolometers for CMB Polarimetry.” In “Transition Edge Sensor Bolometers for CMB Polarimetry,” 2008. URL <https://api.semanticscholar.org/CorpusID:52905568>.

- [70] A. Giachero, B. Alpert, D. Becker, D. Bennett, M. Biasotti, C. Brofferio et al. “Measuring the electron neutrino mass with improved sensitivity: the HOLMES experiment.” *Journal of Instrumentation*, vol. 12(02), pp. C02046–C02046. doi:10.1088/1748-0221/12/02/c02046, Feb. 2017.
- [71] D. J. Goldie, M. D. Audley, D. M. Glowacka, V. N. Tsaneva, and S. Withington. “Transition edge sensors for bolometric applications: responsivity and saturation.” *Journal of Applied Physics*, vol. 103(8). doi:10.1063/1.2909981, Apr. 2008.
- [72] M. Audley, W. Holland, W. Duncan, D. Atkinson, M. Cliffe, M. Ellis et al. “SCUBA-2: A large-format TES array for submillimetre astronomy.” *Nuclear Instruments and Methods in Physics Research Section A: Accelerators, Spectrometers, Detectors and Associated Equipment*, vol. 520(1-3), pp. 479–482. doi:10.1016/j.nima.2003.11.378, Mar. 2004.
- [73] S. Bandler, E. Figueroa-Feliciano, N. Iyomoto, R. Kelley, C. Kilbourne, K. Murphy et al. “Non-linear effects in transition edge sensors for X-ray detection.” *Nuclear Instruments and Methods in Physics Research Section A: Accelerators, Spectrometers, Detectors and Associated Equipment*, vol. 559(2), pp. 817–819. doi:10.1016/j.nima.2005.12.149, Apr. 2006.
- [74] L. Gottardi and K. Nagayashi. “A Review of X-ray Microcalorimeters Based on Superconducting Transition Edge Sensors for Astrophysics and Particle Physics.” *Applied Sciences*, vol. 11(9), p. 3793. doi:10.3390/app11093793, Apr. 2021.
- [75] B. A. Mazin, P. K. Day, J. Zmuidzinas, and H. G. Leduc. “Multiplexable kinetic inductance detectors.” In “AIP Conference Proceedings,” American Institute of Physics, 2002. doi:10.1063/1.1457652.
- [76] B. A. Mazin, P. K. Day, H. G. LeDuc, A. Vayonakis, and J. Zmuidzinas. “Superconducting kinetic inductance photon detectors.” In H. A. MacEwen, ed., “SPIE Proceedings,” SPIE, Dec. 2002. doi:10.1117/12.460456.
- [77] P. K. Day, H. G. LeDuc, B. A. Mazin, A. Vayonakis, and J. Zmuidzinas. “A broadband superconducting detector suitable for use in large arrays.” *Nature*, vol. 425(6960), pp. 817–821. doi:10.1038/nature02037, Oct. 2003.
- [78] B. A. Mazin. Microwave kinetic inductance detectors. Ph.D. thesis, California Institute of Technology, 2005. doi:10.7907/GZ72-V784. URL <https://resolver.caltech.edu/CaltechETD:etd-10042004-120707>.
- [79] M. Bühler and E. Umlauf. “A Magnetic Bolometer for Single-Particle Detection.” *Europhysics Letters (EPL)*, vol. 5(4), pp. 297–301. doi:10.1209/0295-5075/5/4/003, Feb.
- [80] M. Bühler, T. Fausch, and E. Umlauf. “Measurement of Spin-Lattice Relaxation Times at Millikelvin Temperatures.” *Europhysics Letters (EPL)*, vol. 23(7), pp. 529–534. doi:10.1209/0295-5075/23/7/011, Sep. 1993.

- [81] M. Bühler, E. Umlauf, and J. Mather. “Noise of a bolometer with vanishing self-heating.” *Nuclear Instruments and Methods in Physics Research Section A: Accelerators, Spectrometers, Detectors and Associated Equipment*, vol. 346(1-2), pp. 225–229. doi:10.1016/0168-9002(94)90708-0, Jul. 1994.
- [82] S. R. Bandler, C. Enss, R. E. Lanou, H. J. Maris, T. More, F. S. Porter et al. “Metallic magnetic bolometers for particle detection.” *Journal of Low Temperature Physics; (United States)*, vol. 93:3-4, 11 1993. URL <https://www.osti.gov/biblio/5478445>.
- [83] S. Kempf, A. Fleischmann, L. Gastaldo, and C. Enss. “Physics and Applications of Metallic Magnetic Calorimeters.” *Journal of Low Temperature Physics*, vol. 193(3-4), pp. 365–379. doi:10.1007/s10909-018-1891-6, Mar. 2018.
- [84] M. E. Sjöstrand and G. Seidel. “Hyperfine resonance properties of Er^{3+} in Au.” *Phys. Rev. B*, vol. 11, pp. 3292–3297. doi:10.1103/PhysRevB.11.3292, May 1975.
- [85] A. Abragam and B. Bleaney. *Electron Paramagnetic Resonance of Transition Ions*. International series of monographs on physics. Clarendon P., 1970. URL <https://books.google.com.ar/books?id=SSD7AAAAQBAJ>.
- [86] J. M. Geria, M. R. Hampel, S. Kempf, J. J. F. Bonaparte, L. P. Ferreyro, M. E. G. Redondo et al. “Suitability of magnetic microbolometers based on paramagnetic temperature sensors for CMB polarization measurements.” *Journal of Astronomical Telescopes, Instruments, and Systems*, vol. 9(01). doi:10.1117/1.jatis.9.1.016002, Feb. 2023.
- [87] S. Marnieros, P. Ade, J. G. Alberro, A. Almela, G. Amico, L. H. Arnaldi et al. “TES Bolometer Arrays for the QUBIC B-Mode CMB Experiment.” *Journal of Low Temperature Physics*, vol. 199(3-4), pp. 955–961. doi:10.1007/s10909-019-02304-5, Jan. 2020.
- [88] C. L. Kuo, J. J. Bock, J. A. Bonetti, J. Brevik, G. Chattopadhyay, P. K. Day et al. “Antenna-coupled TES bolometer arrays for CMB polarimetry.” In W. D. Duncan, W. S. Holland, S. Withington, and J. Zmuidzinas, eds., “SPIE Proceedings,” SPIE, Aug. 2008. doi:10.1117/12.788588.
- [89] C. M. Posada, P. A. R. Ade, Z. Ahmed, A. J. Anderson, J. E. Austermann, J. S. Avva et al. “Fabrication of Detector Arrays for the SPT-3G Receiver.” *Journal of Low Temperature Physics*, vol. 193(5-6), pp. 703–711. doi:10.1007/s10909-018-1924-1, May 2018.
- [90] U. Tietze, C. Schenk, and E. Gamm. *Electronic Circuits - Handbook for Design and Application*. Springer Berlin Heidelberg, 2 edn., 2008. doi:10.1007/978-3-540-78655-9.

- [91] W. B. Doriese, K. M. Morgan, D. A. Bennett, E. V. Denison, C. P. Fitzgerald, J. W. Fowler et al. “Developments in Time-Division Multiplexing of X-ray Transition-Edge Sensors.” *Journal of Low Temperature Physics*, vol. 184(1-2), pp. 389–395. doi:10.1007/s10909-015-1373-z, Dec. 2015.
- [92] M. Durkin, J. S. Adams, S. R. Bandler, J. A. Chervenak, S. Chaudhuri, C. S. Dawson et al. “Demonstration of Athena X-IFU Compatible 40-Row Time-Division-Multiplexed Readout.” *IEEE Transactions on Applied Superconductivity*, vol. 29(5), pp. 1–5. doi:10.1109/tasc.2019.2904472, Aug. 2019.
- [93] J. L. Walsh. “A Closed Set of Normal Orthogonal Functions.” *American Journal of Mathematics*, vol. 45(1), p. 5. doi:10.2307/2387224, Jan. 1923.
- [94] M. D. Niemack, J. Beyer, H. M. Cho, W. B. Doriese, G. C. Hilton, K. D. Irwin et al. “Code-division SQUID multiplexing.” *Applied Physics Letters*, vol. 96(16). doi:10.1063/1.3378772, Apr. 2010.
- [95] G. M. Stiehl, W. B. Doriese, J. W. Fowler, G. C. Hilton, K. D. Irwin, C. D. Reintsema et al. “Code-division multiplexing for x-ray microcalorimeters.” *Applied Physics Letters*, vol. 100(7). doi:10.1063/1.3684807, Feb. 2012.
- [96] W. B. Doriese, S. R. Bandler, S. Chaudhuri, C. S. Dawson, E. V. Denison, S. M. Duff et al. “Optimization of Time- and Code-Division-Multiplexed Readout for Athena X-IFU.” *IEEE Transactions on Applied Superconductivity*, vol. 29(5), pp. 1–5. doi:10.1109/tasc.2019.2905577, Aug. 2019.
- [97] K. Hattori, K. Arnold, D. Barron, M. Dobbs, T. de Haan, N. Harrington et al. “Adaptation of frequency-domain readout for Transition Edge Sensor bolometers for the POLARBEAR-2 Cosmic Microwave Background experiment.” *Nuclear Instruments and Methods in Physics Research Section A: Accelerators, Spectrometers, Detectors and Associated Equipment*, vol. 732, p. 299–302. doi:10.1016/j.nima.2013.07.052, Dec. 2013.
- [98] M. A. Dobbs, M. Lueker, K. A. Aird, A. N. Bender, B. A. Benson, L. E. Bleem et al. “Frequency multiplexed superconducting quantum interference device readout of large bolometer arrays for cosmic microwave background measurements.” *Review of Scientific Instruments*, vol. 83(7). doi:10.1063/1.4737629, Jul. 2012.
- [99] J. A. B. Mates. The Microwave SQUID Multiplexer. Ph.D. thesis, University of Colorado Boulder, 2011. URL https://scholar.colorado.edu/concern/graduate_thesis_or_dissertations/gt54kn14d.
- [100] J. Gao, M. Daal, A. Vayonakis, S. Kumar, J. Zmuidzinas, B. Sadoulet et al. “Experimental evidence for a surface distribution of two-level systems in superconducting lithographed microwave resonators.” *Applied Physics Letters*, vol. 92(15). doi:10.1063/1.2906373, Apr. 2008.

- [101] J. Gao, J. Zmuidzinas, A. Vayonakis, P. Day, B. Mazin, and H. Leduc. “Equivalence of the Effects on the Complex Conductivity of Superconductor due to Temperature Change and External Pair Breaking.” *Journal of Low Temperature Physics*, vol. 151(1–2), p. 557–563. doi:10.1007/s10909-007-9688-z, Jan. 2008.
- [102] D. Drung, C. Assmann, J. Beyer, A. Kirste, M. Peters, F. Ruede et al. “Highly Sensitive and Easy-to-Use SQUID Sensors.” *IEEE Transactions on Applied Superconductivity*, vol. 17(2), p. 699–704. doi:10.1109/tasc.2007.897403, Jun. 2007.
- [103] M. Krantz. “Development of a metallic magnetic calorimeter with integrated SQUID readout.” doi:10.11588/HEIDOK.00028776, 2020.
- [104] M. Wegner. Entwicklung, Herstellung und Charakterisierung eines auf metallischen magnetischen Kalorimetern basierenden Detektorarrays mit 64 Pixeln und integriertem Mikrowellen-SQUID-Multiplexer. Ph.D. thesis, 2018. doi:10.11588/HEIDOK.00025741.
- [105] S. Kempf. Entwicklung eines Mikrowellen-SQUID-Multiplexers auf der Grundlage nicht-hysteretischer rf-SQUIDs zur Auslesung metallischer magnetischer Kalorimeter. Ph.D. thesis, 2012. doi:10.11588/HEIDOK.00013620.
- [106] J. A. Mates, K. D. Irwin, L. R. Vale, G. C. Hilton, J. Gao, and K. W. Lehnert. “Flux-ramp modulation for SQUID multiplexing.” *Journal of Low Temperature Physics*, vol. 167, pp. 707–712. doi:10.1007/s10909-012-0518-6, 6 2012.
- [107] F. Hirayama, S. Kohjiro, D. Fukuda, H. Yamamori, S. Nagasawa, and M. Hidaka. “Microwave SQUID Multiplexer for TES Readout.” *IEEE Transactions on Applied Superconductivity*, vol. 23, pp. 2500405–2500405. doi:10.1109/TASC.2012.2237474, 6 2013.
- [108] D. P. Richter. Multikanal-Auslesung von metallischen magnetischen Kalorimetern mittels eines vollständigen Mikrowellen-SQUID-Multiplexer-Systems. Ph.D. thesis, 2021. doi:10.11588/HEIDOK.00030266.
- [109] D. P. Richter. Multikanal-Auslesung von metallischen magnetischen Kalorimetern mittels eines vollständigen Mikrowellen-SQUID-Multiplexer-Systems. Ph.D. thesis, Heidelberg University, 2021. doi:10.11588/HEIDOK.00030266. URL <http://archiv.ub.uni-heidelberg.de/volltextserver/id/eprint/30266>.
- [110] S. W. Henderson, Z. Ahmed, D. Brown, S. Chaudhuri, H.-M. S. Cho, J. M. D'Ewart et al. “Highly-multiplexed microwave SQUID readout using the SLAC Microresonator Radio Frequency (SMuRF) electronics for future CMB and sub-millimeter surveys.” In J. Zmuidzinas and J.-R. Gao, eds., “Millimeter, Submillimeter, and Far-Infrared Detectors and Instrumentation for Astronomy IX,” SPIE, Jul. 2018. doi:10.1117/12.2314435.

- [111] K. H. Park, Y. S. Yap, Y. P. Tan, C. Hufnagel, L. H. Nguyen, K. H. Lau et al. “ICARUS-Q: Integrated control and readout unit for scalable quantum processors.” *Review of Scientific Instruments*, vol. 93(10). doi:10.1063/5.0081232, Oct. 2022.
- [112] W. D. Kalfus, D. Lee, G. J. Ribeill, S. D. Fallek, A. P. Wagner, B. F. Donovan et al. “High-Fidelity Control of Superconducting Qubits Using Direct Microwave Synthesis in Higher Nyquist Zones.” *IEEE Transactions on Quantum Engineering*, vol. 1, pp. 1–12, 2020. URL <https://api.semanticscholar.org/CorpusID:225412495>.
- [113] J. Proakis and D. Manolakis. “Digital Signal Processing: Pearson New International Edition.” In “Digital Signal Processing: Pearson New International Edition,” Pearson Education, 2014.
- [114] H. Nyquist. “Certain factors affecting telegraph speed.” *The Bell System Technical Journal*, vol. 3(2), pp. 324–346. doi:10.1002/j.1538-7305.1924.tb01361.x, 1924.
- [115] H. Nyquist. “Certain Topics in Telegraph Transmission Theory.” *Transactions of the American Institute of Electrical Engineers*, vol. 47(2), pp. 617–644. doi:10.1109/T-AIEE.1928.5055024, 1928.
- [116] C. E. Shannon. “A mathematical theory of communication.” *The Bell System Technical Journal*, vol. 27(3), pp. 379–423. doi:10.1002/j.1538-7305.1948.tb01338.x, 1948.
- [117] U. K. a. Fernando Puente León. *Messtechnik: Systemtheorie für Ingenieure und Informatiker*. Springer, 9 edn., 2012. doi:<https://doi.org/10.1007/978-3-642-30074-5>.
- [118] N. Karcher. *Ausleseelektronik für magnetische Mikrokalorimeter im Frequenzmultiplexverfahren*. Ph.D. thesis, Karlsruher Institut für Technologie (KIT), 2022. doi:10.5445/IR/1000148040. 54.12.02; LK 01.
- [119] W. R. Bennett. “Spectra of Quantized Signals.” *Bell System Technical Journal*, vol. 27(3), pp. 446–472. doi:10.1002/j.1538-7305.1948.tb01340.x, Jul. 1948. URL <https://doi.org/10.1002/j.1538-7305.1948.tb01340.x>.
- [120] W. Kester. *Data Conversion Handbook (Analog Devices)*. Analog Devices series. Elsevier; Newnes, 2005.
- [121] R. W. S. Alan V. Oppenheim. *Discrete-Time Signal Processing*. Prentice-Hall Signal Processing Series. Prentice Hall, 3 edn., 2009.
- [122] S. Boyd. “Multitone signals with low crest factor.” *IEEE Transactions on Circuits and Systems*, vol. 33(10), pp. 1018–1022. doi:10.1109/tcs.1986.1085837, Oct. 1986.
- [123] M. Friese. “Multitone signals with low crest factor.” *IEEE Transactions on Communications*, vol. 45(10), pp. 1338–1344. doi:10.1109/26.634697, 1997.

- [124] B. Brannon and A. Barlow. “Aperture uncertainty and ADC system performance.” Applications Note AN-501. Analog Devices, Inc., 2000. URL <https://www.analog.com/media/en/technical-documentation/application-notes/AN-501.pdf>.
- [125] G. Comoretto, R. Chiello, M. Roberts, R. Halsall, K. Z. Adami, M. Alderighi et al. “The Signal Processing Firmware for the Low Frequency Aperture Array.” *Journal of Astronomical Instrumentation*, vol. 06(01). doi:10.1142/s2251171716410154, Mar. 2017.
- [126] S. A. Kernasovskiy, S. E. Kuenstner, E. Karpel, Z. Ahmed, D. D. V. Winkle, S. Smith et al. “SLAC Microresonator Radio Frequency (SMuRF) Electronics for Read Out of Frequency-Division-Multiplexed Cryogenic Sensors.” *Journal of Low Temperature Physics*, vol. 193(3-4), pp. 570–577. doi:10.1007/s10909-018-1981-5, May 2018.
- [127] J. P. Smith, J. I. Bailey, J. Tuthill, L. Stefanazzi, G. Cancelo, K. Treptow et al. “A High-Throughput Oversampled Polyphase Filter Bank Using Vivado HLS and PYNQ on a RFSoc.” *IEEE Open Journal of Circuits and Systems*, vol. 2, pp. 241–252. doi:10.1109/ojcas.2020.3041208, 2021.
- [128] O. Bourrion, A. Bideaud, A. Benoit, A. Cruciani, J. F. Macias-Perez, A. Monfardini et al. “Electronics and data acquisition demonstrator for a kinetic inductance camera.” *Journal of Instrumentation*, vol. 6(06), pp. P06012–P06012. doi:10.1088/1748-0221/6/06/p06012, Jun. 2011.
- [129] H. Tuttlebee. *Software Defined Radio: Enabling Technologies*. John Wiley and Sons LTD., 2002.
- [130] P. Vaidyanathan. “Multirate digital filters, filter banks, polyphase networks, and applications: a tutorial.” *Proceedings of the IEEE*, vol. 78(1), pp. 56–93. doi:10.1109/5.52200, 1990.
- [131] F. J. Harris. *Multirate Signal Processing for Communication Systems*. Prentice Hall, 1 edn., 2004.
- [132] F. Harris, C. Dick, and M. Rice. “Digital receivers and transmitters using polyphase filter banks for wireless communications.” *IEEE Transactions on Microwave Theory and Techniques*, vol. 51(4), pp. 1395–1412. doi:10.1109/TMTT.2003.809176, 2003.
- [133] P. M. Krishna and T. S. Babu. “Polyphase Channelizer Demystified [Lecture Notes].” *IEEE Signal Processing Magazine*, vol. 33(1), pp. 144–150. doi:10.1109/MSP.2015.2477423, 2016.
- [134] M. Zhang, H.-L. Zhang, Y.-Z. Zhang, J. Wang, S.-C. Guo, and Q. Meng. “Research on Channelization Techniques of Radio Astronomical Wideband Signal with Oversampled Polyphase Filter Banks.” *Research in Astronomy and Astrophysics*, vol. 23(8), p. 085012. doi:10.1088/1674-4527/acd73b, Jul. 2023.

- [135] M. H. Hayes. Statistical Digital Signal Processing and Modeling. John Wiley & Sons, 1996.
- [136] S. Orfanidis. Optimum Signal Processing (2nd edition). McGraw-Hill Publishing Company, 2007.
- [137] L. Kong, T. Huang, Y. Zhu, and S. Yu. Big Data in Astronomy: Scientific Data Processing for Advanced Radio Telescopes. Elsevier, 1 edn., 2020.
- [138] AMD Xilinx. UG1137 - Zynq UltraScale+ MPSoC Software Developer Guide, 2023. URL <https://docs.xilinx.com/r/en-US/ug1137-zynq-ultrascale-mpsoc-swdev>.
- [139] AMD Xilinx. UG1085 - Zynq UltraScale+ Device Technical Reference Manual, 2023. URL <https://docs.xilinx.com/r/en-US/ug1085-zynq-ultrascale-trm/Zynq-UltraScale-Device-Technical-Reference-Manual>.
- [140] AMD Xilinx. DS889 - Zynq UltraScale+ RFSoc Data Sheet: Overview, 2023. URL <https://docs.xilinx.com/v/u/en-US/ds889-zynq-usp-rfsoc-overview>.
- [141] AMD Xilinx. UG479 - 7 Series DSP48E1 Slice User Guide, 2018. URL https://docs.xilinx.com/v/u/en-US/ug479_7Series_DSP48E1.
- [142] AMD Xilinx. UG579 - UltraScale Architecture DSP Slice User Guide, 2021. URL <https://docs.xilinx.com/v/u/en-US/ug579-ultrascale-dsp>.
- [143] AMD Xilinx. UG571 - UltraScale Architecture SelectIO Resources, 2023. URL <https://docs.xilinx.com/r/en-US/ug571-ultrascale-selectio>.
- [144] AMD Xilinx. DS925 - Zynq UltraScale+ MPSoC Data Sheet: DC and AC Switching Characteristics, 2023. URL <https://docs.xilinx.com/r/en-US/ds925-zynq-ultrascale-plus>.
- [145] AMD Xilinx. UG576 - UltraScale Architecture GTH Transceivers, 2021. URL <https://docs.xilinx.com/v/u/en-US/ug576-ultrascale-gth-transceivers>.
- [146] AMD Xilinx. UG578 - UltraScale Architecture GTY Transceivers, 2021. URL <https://docs.xilinx.com/v/u/en-US/ug578-ultrascale-gty-transceivers>.
- [147] AMD Xilinx. PG269 - Zynq UltraScale+ RFSoc RF Data Converter v2.4 Gen 1/2/3, 2020. URL <https://docs.xilinx.com/v/u/2.4-English/pg269-rf-data-converter>.
- [148] E. Venosa, F. J. Harris, and F. Palmieri. Software Radio. Springer New York, 2012. doi:10.1007/978-1-4614-0113-1.

- [149] F. K. Jondral. “Software-Defined Radio—Basics and Evolution to Cognitive Radio.” *EURASIP Journal on Wireless Communications and Networking*, vol. 2005(3). doi:10.1155/wcn.2005.275, Aug. 2005.
- [150] B. Dober, D. T. Becker, D. A. Bennett, S. A. Bryan, S. M. Duff, J. D. Gard et al. “Microwave SQUID multiplexer demonstration for cosmic microwave background imagers.” *Applied Physics Letters*, vol. 111(24). doi:10.1063/1.5008527, Dec. 2017.
- [151] C. Yu, A. Ames, S. Chaudhuri, C. Dawson, K. D. Irwin, S. E. Kuenstner et al. “An impedance-modulated code-division microwave SQUID multiplexer.” *Engineering Research Express*, vol. 2(1), p. 015011. doi:10.1088/2631-8695/ab68a4, Jan. 2020.
- [152] J. D. Gard, D. T. Becker, D. A. Bennett, J. W. Fowler, G. C. Hilton, J. A. B. Mates et al. “A Scalable Readout for Microwave SQUID Multiplexing of Transition-Edge Sensors.” *Journal of Low Temperature Physics*, vol. 193(3-4), pp. 485–497. doi:10.1007/s10909-018-2012-2, Jul. 2018.
- [153] J. van Rantwijk, M. Grim, D. van Loon, S. Yates, A. Baryshev, and J. Baselmans. “Multiplexed Readout for 1000-Pixel Arrays of Microwave Kinetic Inductance Detectors.” *IEEE Transactions on Microwave Theory and Techniques*, vol. 64(6), pp. 1876–1883. doi:10.1109/TMTT.2016.2544303, 2016.
- [154] R. Gebauer, N. Karcher, D. Gusenkova, M. Spiecker, L. Grünhaupt, I. Takmakov et al. “State preparation of a fluxonium qubit with feedback from a custom FPGA-based platform.” In “AIP Conference Proceedings,” AIP Publishing, 2020. doi:10.1063/5.0011721.
- [155] R. Gebauer, N. Karcher, and O. Sander. “A modular RFSoc-based approach to interface superconducting quantum bits.” In “2021 International Conference on Field-Programmable Technology (ICFPT),” pp. 1–9. 2021. doi:10.1109/ICFPT52863.2021.9609909.
- [156] L. Stefanazzi, K. Treptow, N. Wilcer, C. Stoughton, C. Bradford, S. Uemura et al. “The QICK (Quantum Instrumentation Control Kit): Readout and control for qubits and detectors.” *Review of Scientific Instruments*, vol. 93(4). doi:10.1063/5.0076249, Apr. 2022.
- [157] Analog Devices. AD-FMCDQA2-EBZ. URL <https://www.analog.com/en/design-center/evaluation-hardware-and-software/evaluation-boards-kits/eval-ad-fmcdqa2-ebz.html>.
- [158] Analog Devices. AD9144, Quad, 16-Bit, 2.8 GSPS TxDAC Digital-to-Analog Converter, 2019. URL <https://www.analog.com/media/en/technical-documentation/data-sheets/AD9144.pdf>.
- [159] Analog Devices. AD9680 14-Bit, 1.25 GSPS/1 GSPS/820 MSPS/500 MSPS JESD204B, Dual Analog-to-Digital Converter, 2019. URL <https://www.analog.com/media/en/technical-documentation/data-sheets/ad9680.pdf>.

- [160] Analog Devices. AD-FMCDAQ2-EBZ - Clock Distribution. URL https://wiki.analog.com/resources/eval/user-guides/ad-fmcdaq2-ebz/hardware/functional_overview.
- [161] R. Gartmann, N. Karcher, R. Gebauer, O. Krömer, and O. Sander. “Progress of the ECHo SDR Readout Hardware for Multiplexed MMCs.” *Journal of Low Temperature Physics*, vol. 209(3-4), pp. 726–733. doi:10.1007/s10909-022-02854-1, Sep. 2022.
- [162] “Yocto Project.” URL <https://www.yoctoproject.org/>.
- [163] The Linux Foundation. “gRPC Website.” URL <https://grpc.io/>.
- [164] The Linux Foundation. “gRPC Concepts.”, 2018. URL <https://github.com/grpc/grpc/blob/257d0045ab958eb767a3591c88e9d0c2bdf4b916/CONCEPTS.md>.
- [165] N. Karcher, R. Gebauer, R. Bauknecht, R. Illichmann, and O. Sander. “Versatile Configuration and Control Framework for Real-Time Data Acquisition Systems.” *IEEE Transactions on Nuclear Science*, vol. 68(8), pp. 1899–1906. doi:10.1109/tns.2021.3084355, Aug. 2021.
- [166] E. Hogenauer. “An economical class of digital filters for decimation and interpolation.” *IEEE Transactions on Acoustics, Speech, and Signal Processing*, vol. 29, pp. 155–162. doi:10.1109/TASSP.1981.1163535, 4 1981.
- [167] J. Kaiser and R. Hamming. “Sharpening the response of a symmetric nonrecursive filter by multiple use of the same filter.” *IEEE Transactions on Acoustics, Speech, and Signal Processing*, vol. 25(5), pp. 415–422. doi:10.1109/tassp.1977.1162980, Oct. 1977.
- [168] A. Kwentus, Z. Jiang, and A. Willson. “Application of filter sharpening to cascaded integrator-comb decimation filters.” *IEEE Transactions on Signal Processing*, vol. 45(2), p. 457–467. doi:10.1109/78.554309, 1997.
- [169] G. Stephen and R. Stewart. “High-speed sharpening of decimating CIC filter.” *Electronics Letters*, vol. 40(21), p. 1383. doi:10.1049/el:20046387, 2004.
- [170] G. J. Dolecek and S. K. Mitra. “A New Two-Stage CIC-Based Decimation Filter.” In “2007 5th International Symposium on Image and Signal Processing and Analysis,” IEEE, Sep. 2007. doi:10.1109/ispa.2007.4383693.
- [171] G. Jovanovic Dolecek and S. K. Mitra. “On Design of CIC Decimation Filter with Improved Response.” In “2008 3rd International Symposium on Communications, Control and Signal Processing,” IEEE, Mar. 2008. doi:10.1109/isccsp.2008.4537383.
- [172] G. Jovanovic Dolecek and F. Harris. “On design of two-stage CIC compensation filter.” In “2009 IEEE International Symposium on Industrial Electronics,” IEEE, Jul. 2009. doi:10.1109/isie.2009.5213597.

- [173] M. Li, S. Zhang, and X. Diao. “Compensation method for the CIC filter in digital down converter.” In “2011 International Conference on Electrical and Control Engineering,” IEEE, Sep. 2011. doi:10.1109/iceceng.2011.6057242.
- [174] L. Rabiner, B. Gold, and C. McGonegal. “An approach to the approximation problem for nonrecursive digital filters.” *IEEE Transactions on Audio and Electroacoustics*, vol. 18(2), pp. 83–106. doi:10.1109/tau.1970.1162092, Jun. 1970.
- [175] P. Sysel and P. Rajmic. “Goertzel algorithm generalized to non-integer multiples of fundamental frequency.” *EURASIP Journal on Advances in Signal Processing*, vol. 2012, p. 56. doi:10.1186/1687-6180-2012-56, 12 2012.
- [176] J. Proakis and D. Manolakis. *Digital Signal Processing: Principles, Algorithms, and Applications*, 3rd Edition. Prentice-Hall International editions. Prentice Hall, 1996.
- [177] F. Harris. “On the use of windows for harmonic analysis with the discrete Fourier transform.” *Proceedings of the IEEE*, vol. 66, pp. 51–83. doi:10.1109/PROC.1978.10837, 1978.
- [178] P. Crilly and A. Carlson. *Communication Systems: An Introduction to Signals and Noise in Electrical Communication*. McGraw-Hill Education, 2009. URL <https://books.google.com.ar/books?id=-hRGAQAIAAJ>.
- [179] E. Jacobsen and R. Lyons. “The sliding DFT.” *IEEE Signal Processing Magazine*, vol. 20(2), pp. 74–80. doi:10.1109/MSP.2003.1184347, 2003.
- [180] K. Duda. “Accurate, Guaranteed Stable, Sliding Discrete Fourier Transform [DSP Tips & Tricks].” *IEEE Signal Processing Magazine*, vol. 27(6), pp. 124–127. doi:10.1109/MSP.2010.938088, 2010.
- [181] Y. Cho, J. Kim, W. Yang, and C. Kang. *MIMO-OFDM Wireless Communications with MATLAB*. IEEE Press. Wiley, 2010. URL <https://books.google.com.ar/books?id=6HwAoeuMr3kC>.
- [182] H. Ochiai and H. Imai. “On the distribution of the peak-to-average power ratio in OFDM signals.” *IEEE Transactions on Communications*, vol. 49(2), pp. 282–289. doi:10.1109/26.905885, 2001.
- [183] M. Schroeder. “Synthesis of low-peak-factor signals and binary sequences with low autocorrelation (Corresp.).” *IEEE Transactions on Information Theory*, vol. 16(1), pp. 85–89. doi:10.1109/tit.1970.1054411, Jan. 1970.
- [184] W. Rudin. “Some theorems on Fourier coefficients.” *Proceedings of the American Mathematical Society*, vol. 10(6), pp. 855–859. doi:10.1090/s0002-9939-1959-0116184-5, 1959.

- [185] H. S. Shapiro. Extremal Problems for Polynomials and Power Series. Ph.D. thesis, Massachusetts Institute of Technology, 1952.
- [186] D. J. Newman. “An L1 Extremal Problem for Polynomials.” *Proceedings of the American Mathematical Society*, vol. 16, pp. 1287–1290, 1965.
- [187] A. Gersho, B. Gopinath, and A. M. Odlyzko. “Coefficient Inaccuracy in Transversal Filtering.” *Bell System Technical Journal*, vol. 58(10), pp. 2301–2316. doi:10.1002/j.1538-7305.1979.tb02968.x, Dec. 1979.
- [188] A. Horner and J. Beauchamp. “A genetic algorithm-based method for synthesis of low peak amplitude signals.” *The Journal of the Acoustical Society of America*, vol. 99(1), pp. 433–443. doi:10.1121/1.414555, Jan. 1996.
- [189] D. A. Guimaraes. Digital Transmission. Springer Berlin Heidelberg, 2009. doi:10.1007/978-3-642-01359-1.
- [190] M. S. John G. Proakis. Digital Communications, 5th Edition . McGraw-Hill, 5 edn., 2007.
- [191] R. Lyons. “A Quadrature Signals Tutorial: Complex, But Not Complicated.” <https://www.dsprelated.com/showarticle/192.php>, April 2013.
- [192] F. Churchill, G. Ogar, and B. Thompson. “The Correction of I and Q Errors in a Coherent Processor.” *IEEE Transactions on Aerospace and Electronic Systems*, vol. AES-17(1), pp. 131–137. doi:10.1109/TAES.1981.309045, 1981.
- [193] A. I. Sinsky and P. C. Wang. “Error Analysis of a Quadrature Coherent Detector Processor.” *IEEE Transactions on Aerospace and Electronic Systems*, vol. AES-10(6), pp. 880–883. doi:10.1109/TAES.1974.307900, 1974.
- [194] J. Tubbax, B. Come, L. Van der Perre, S. Donnay, M. Engels, H. D. Man et al. “Compensation of IQ imbalance and phase noise in OFDM systems.” *IEEE Transactions on Wireless Communications*, vol. 4(3), pp. 872–877. doi:10.1109/TWC.2004.843057, 2005.
- [195] L. Anttila, M. Valkama, and M. Renfors. “Blind Moment Estimation Techniques for I/Q Imbalance Compensation in Quadrature Receivers.” In “2006 IEEE 17th International Symposium on Personal, Indoor and Mobile Radio Communications,” pp. 1–5. 2006. doi:10.1109/PIMRC.2006.254374.
- [196] L. Anttila, M. Valkama, and M. Renfors. “Blind Compensation of Frequency-Selective I/Q Imbalances in Quadrature Radio Receivers: Circularity -Based Approach.” In “2007 IEEE International Conference on Acoustics, Speech and Signal Processing - ICASSP '07,” vol. 3, pp. III–245–III–248. 2007. doi:10.1109/ICASSP.2007.366518.

- [197] J. Cavers and M. Liao. “Adaptive compensation for imbalance and offset losses in direct conversion transceivers.” *IEEE Transactions on Vehicular Technology*, vol. 42(4), pp. 581–588. doi:10.1109/25.260752, 1993.
- [198] E. Nash. “Correcting imperfections in IQ modulators to improve RF signal fidelity.” *Application Note*, 2009.
- [199] AMD Xilinx. PG149 - FIR Compiler V7.2, LogiCORE IP Product Guide, 2022. URL https://www.xilinx.com/products/intellectual-property/fir_compiler.html.
- [200] J. Beraldin and W. Steenaart. “Overflow analysis of a fixed-point implementation of the Goertzel algorithm.” *IEEE Transactions on Circuits and Systems*, vol. 36, pp. 322–324. doi:10.1109/31.20217, 1989.
- [201] M. Medina-Melendrez, M. Arias-Estrad, and A. Castro. “Overflow analysis in the fixed-point implementation of the first-order Goertzel algorithm for complex-valued input sequences.” In “IEEE Transactions on Circuits and Systems,” pp. 620–623. IEEE, 8 2009. doi:10.1109/MWSCAS.2009.5236016.
- [202] M. Medina-Melendrez, M. Arias-Estrada, and A. Castro. “Using a Scaling Factor in $O(1/N)$ for the fixed-point implementation of the second-order goertzel filter.” In “IEEE Transactions on Circuits and Systems,” pp. 3218–3221. IEEE, 5 2012. doi:10.1109/ISCAS.2012.6272009.
- [203] Teledyne. WavePro 7 Zi-A Series. URL https://cdn.teledynelecroy.com/files/pdf/wavepro_7_zi-a_datasheet.pdf.
- [204] Keysight. N9000A CXA Signal Analyzer, 9 kHz to 26.5 GHz. URL <https://www.keysight.com/us/en/product/N9000A/cxa-signal-analyzer-9khz-26-5ghz.html>.
- [205] Pasternack. Isolated Ground SMA Female to SMA Female Bulkhead Mount Adapter, with Plastic Isolator. URL <https://www.pasternack.com/images/ProductPDF/PE9067.pdf>.
- [206] Pasternack. SMA Male to SMA Male cable using PE-P141 Coax with HeatShrink, LF Solder. URL <https://www.pasternack.com/images/ProductPDF/PE300.pdf>.
- [207] Keysight. N5242B PNA-X Microwave Network Analyzer. URL <https://www.keysight.com/us/en/product/N5242B/pna-x-microwave-network-analyzer-900-hz-10-mhz-26-5-ghz.html>.
- [208] Bluefors. Dilution Refrigerator Measurement Systems - LD250. URL <https://bluefors.com/products/dilution-refrigerator-measurement-systems/>.
- [209] Low Noise Factory. LNF - LNC 4-8 GHz Ultra Low Noise Amplifier. URL https://lownoisefactory.com/product/lnf-lnc4_8f/.

- [210] Picotest. G5100A Waveform Generator. URL https://www.picotest.com/products_G5100A.html.